Characterization of Resistance of Armour Plate against Deformable Projectile with Fracture Mechanics as a Failure Criteria

A Thesis Submitted

By

Vaibhav Gangwar

In Partial Fulfilment of the Requirements for the Degree of

Doctor of Philosophy (Engineering)

Department of Mechanical Engineering
Faculty Council of Engineering & Technology
Jadavpur University
Kolkata, India

March, 2025

CERTIFICATE FROM THE SUPERVISORS

This is to certify that the thesis entitled "**Characterization of Resistance of Armour Plate against Deformable Projectile with Fracture Mechanics as Failure Criteria**" submitted by Shri **Vaibhav Gangwar**, Who got his name registered on **14 Jan, 2022** for the award of **Ph.D (Engineering) degree** of Jadavpur University is absolutely based upon his own work under our supervision and neither his thesis nor any part of the thesis has been submitted for any degree/ diploma or any other academic award anywhere before.

Acharyya 23/09/25

1. ----------

Supervisor: Prof. Sanjib Kumar Acharyya
Professor
Department of Mechanical Engineering
Jadavpur University, Kolkata-700032

Banerjee 23/09/2025

2. ----------

Supervisor: Dr. Arkadeb Banerjee
Scientist- F
Proof and Experimental Establishment (PXE), DRDO
Chandipur, Balasore - 756025

“Statement of Originality”

I **Vaibhav Gangwar** registered on **14 Jan 2022** do hereby declare that this thesis entitled “**Characterization of Resistance of Armour Plate against Deformable Projectile with Fracture Mechanics as a Failure Criteria”** contains literature survey and original research work done by the undersigned candidate as part of Doctoral studies.

All information in this thesis have been obtain and presented in accordance with existing academic rules and ethical conduct. I declare that, as required by these rules and conduct, I have fully cited and referred all materials and results that are not original to this work.

I also declare that I have checked this thesis as per the “Policy on Anti Plagiarism, Jadavpur University, 2019”, and the level of similarity as checked by iThenticate software is **2 %.**

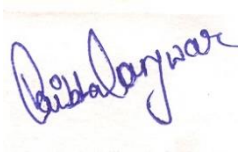

Signature of Candidate:

Date: 23 Sep 2025

Certificate by Supervisors:
(Signature with date)

1. 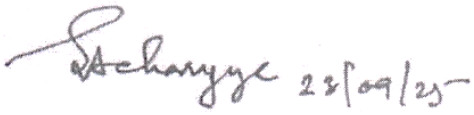

2. 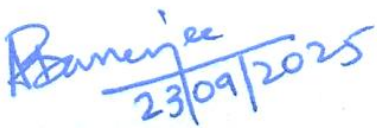

Acknowledgement

The journey of a Ph.D. is filled with challenges, learning, and perseverance, and I am deeply grateful to those who have supported and guided me throughout this endeavour. This thesis is not just a product of my efforts but a reflection of the collective encouragement, wisdom, and contributions of many individuals.

First and foremost, I express my deepest gratitude to my advisor, ***Prof. Sanjib Kumar Acharyya****, for his invaluable mentorship, constant support, and unwavering belief in my potential. His insightful guidance, scientific insights, patience, and constructive feedback have played a crucial role in shaping both my research and academic perspective.*

I am equally grateful to my ***co-supervisor, Dr. Arkadeb Banerjee****, for his valuable advice, encouragement, and technical insights that have enriched my work. His support has been instrumental in refining my research approach and broadening my understanding of the subject.*

A special acknowledgment to ***Prof. (Ret.) Sankar Dhar*** *for his extraordinary contributions, insightful suggestions, and unwavering support throughout this journey. His scientific insights, technical expertise and guidance have significantly impacted my research, and I am truly thankful for his generosity in sharing his knowledge.*

I also extend my sincere appreciation to ***Prof. Prasanta Sahoo*** *and the faculty and staff of the* ***Department of Mechanical Engineering, Jadavpur University****, for providing a nurturing academic environment and essential resources that have supported my research endeavors. Their encouragement and willingness to help have played a vital role in my academic growth.*

I am immensely grateful to ***Proof and Experimental Lab, Chandipur****, for their generous funding and for providing the essential materials for testing. Their support has been crucial in conducting my experimental work and ensuring the successful execution of this research.*

To my colleagues and fellow researchers, I am grateful for the countless discussions, collaborations, and moments of shared learning. Their support has made this journey intellectually stimulating and personally fulfilling.

To my family, no words can truly express my gratitude. Their unconditional love, patience, and sacrifices have been the foundation of my perseverance. Their encouragement in moments of doubt has been my greatest strength.

Finally, I extend my heartfelt appreciation to everyone—both named and unnamed—who has contributed directly or indirectly to this research. Your support, motivation, and kindness have played a vital role in making this milestone a reality.

This thesis is not just an academic achievement but a collective effort. To all of you—thank you.

Vaibhav Gangwar

Contents

Synopsis

Armor steel with a martensitic structure is commonly used because it can absorb a lot of energy when subjected to high-speed impacts. In real-life situations like crashes, explosions, ballistic impacts, and metal forming, factors such as strain (ε), strain rate ($\dot{\varepsilon}$), and temperature (T) change significantly. The material also undergoes major deformation, which is important for designing safe and strong structures. To accurately describe this deformation, a large displacements and large strain approach is used, considering the effects of high strain rates and increased temperature.

This study examines two types of martensitic steel—a typical Rolled Homogeneous Armour (RHA) and PHS1500—under different loading conditions, from slow to intermediate strain rates. Three models were used to predict how these steels behave: the Johnson-Cook model (a commonly used approach), the Rusinek-Klepaczko (R-K) model (a semi-physical model), and a new model based on the Johnson-Cook formulation. Finite element simulations were conducted using ABAQUS CAE Standard/Explicit software, and the results were verified by comparing them with real tensile test data. The research combined extensive experiments with simulations, and the material model was also validated using Charpy V-notch impact tests. Finally, ballistic impact tests were simulated using the three material models. The study closely analyzed how fracture toughness affects the performance of armour plates and showed how the fracture toughness parameter (K_{ID} or K_{IC} (t)) influences ballistic performance. The findings provide crucial insights into the mechanical behaviour and impact resistance of armour steel.

1. Materials

Two materials (steels) are used in study. These are high strength steels.

a) **RHA steel:** Basically medium carbon (~0.35%C) low alloy (0.2%Si, 0.4%Mn, 1.5%Cr, 0.5%Mo, 1.7%Ni) steel containing traces of P, S, Va, Cu and Al**.**

Table 1: Material properties of RHA steel

Young's Modulus E (GPa)	**Yield Stress (MPa)**	**Ultimate Stress (MPa)**	**Elongation (%)**
218	854	963	12%

b) **Projectile steel (PHS 1500):** Medium carbon (~ 0.5%) alloy (1.1% Cr, 0.6% Mn, 0.2% of each of Si, Mo and Ni) steel.

Table 2: Material properties of PHS 1500 steel

Young's Modulus E (GPa)	Yield Stress (MPa)	Ultimate Stress (MPa)	Elongation (%)
210	1450	2100	8%

2. Material Testing

The following test are performed to study the deformation and failure of both the steels means final fracture of specimen during the tensile test.

a. Tensile test (Round specimens, Flat specimens, Notch tensile specimens)

Quasi-static tensile tests at high temperatures, ranging from $27℃ \leq T \leq 500℃$, and strain rates ranging from $10^{-4}\ s^{-1} \leq \dot{\varepsilon_p} \leq 10^{-1}\ s^{-1}$ are performed in an INSTRON 5582 testing machine. Intermediate tests at 27℃ and strain-rates ranging from $0.8\ s^{-1} \leq \dot{\varepsilon_p} \leq 36.439\ s^{-1}$ and temperature 27ºC are carried out in a servo-hydraulic high strain-rate (VHS) testing machine with digital image correlation DIC facility. Above $36.439\ s^{-1}$ this strain-rate the tests are performed on a newly developed testing facility by employing strain gages. The tests are then performed on INSTRON CEAST 9350 testing machine. These tests are performed only for RHA steel because projectile steel is having very high hardness which the greater than the hardness of the grips of the machine. Some of the test results of quasi-static to high strain-rates are shown in Fig. 1. The % of elongation of RHA steel with strain-rates is shown in Fig. 2.

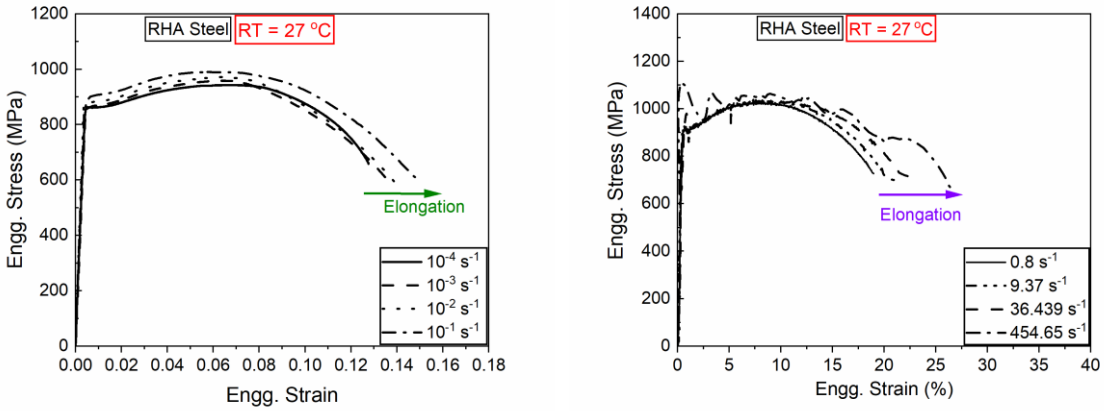

Fig. 1. Engineering stress – strain curves at 27ºC (a) INSTRON 5582 test results and (b) intermediate strain-rate test results obtained from the INSTRON-VHS with DIC.

% Elongation increase only means the material sustain more plastic strain before fracture.

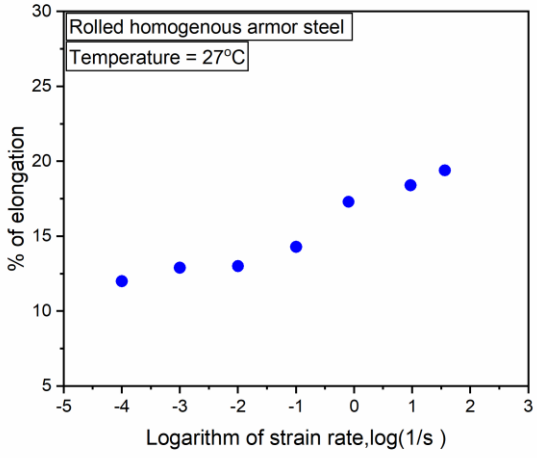

Fig. 2. % of elongation of RHA steel with strain-rate

Elevated temperature experimental data at different strain-rates is shown in Fig. 3. For RHA steel. At high strain rates, adiabatic heating occurs in the material. Understanding how PH 1500 behaves at elevated temperatures helps capture this coupled effect. Like most high-strength steels, PH 1500 loses strength and stiffness with rising temperature. Testing quantifies this reduction for safety design.

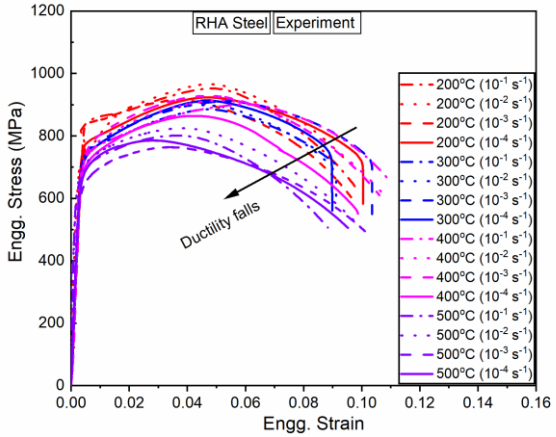

Fig. 3. Stress *vs* strain curve for projectile steel

For projectile steel (PHS 1500) the maximum strain-rate reached was only 3.5 s^{-1} this is because the hardness of the projectile steel is very high. The machine gripping system did not hold the specimen firmly resulting in slippage of the sample. The test results from strain-rates 10^{-4} s^{-1} < $\dot{\varepsilon}$ < 3.5 s^{-1} is shown in Fig. 4a, shows the Young's modulus of the specimen increases and Fig. 4b, depicted the high temperature experimental stress-strain response of projectile steel where the kinks in the graphs show extensometer removal. In Fig. 4a, Although the true elastic modulus of PH 1500 steel is a material constant and does not depend on strain rate, an apparent increase is observed in the stress–strain curves at higher strain rates. This effect is mainly attributed to dynamic testing artifacts such as wave propagation, stress non-equilibrium, and measurement sensitivity in the initial linear region, rather than a genuine change in bond stiffness.

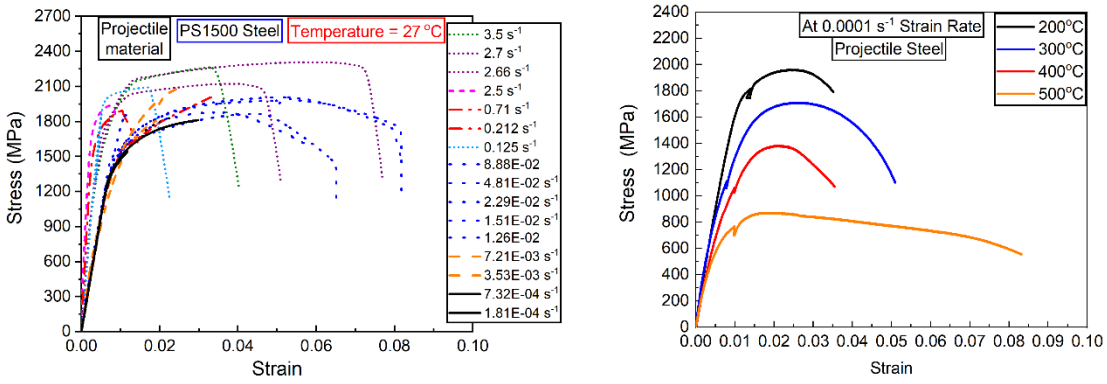

(a) (b)

Fig. 4. Stress *vs* strain curve for projectile steel

b. Charpy V-notch impact testing

Charpy impact tests were conducted at various impact velocities for both RHA and projectile steel. Material model coefficients derived from tensile tests were used to simulate these impact tests. For RHA steel, experiments were performed at room temperature for impact velocities of 3, 4, 5, 6, and 8 m/s (Fig. 5), as well as at elevated temperatures of 100°C and 150°C for impact velocities of 8 m/s and 9 m/s, respectively (Fig. 6). In the case of projectile steel, experiments were carried out at impact velocities of 8, 9, 10, and 11 m/s as shown in Fig. 7a &b.

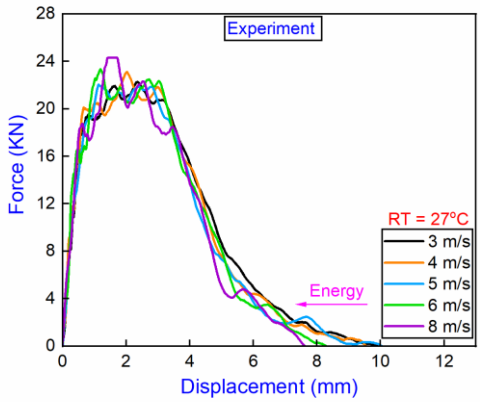

Fig. 5. Force *vs* displacement curve of Charpy V-notch sample.

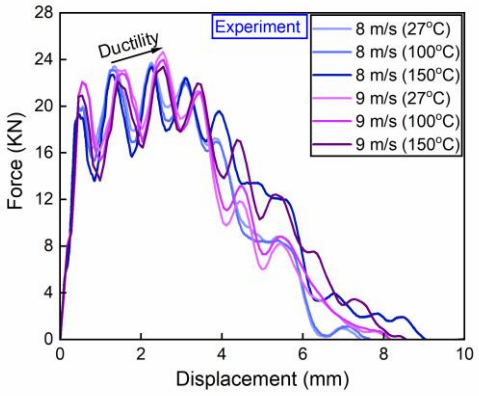

Fig. 6. Force *vs* displacement curve of Charpy V-notch sample at high temperature.

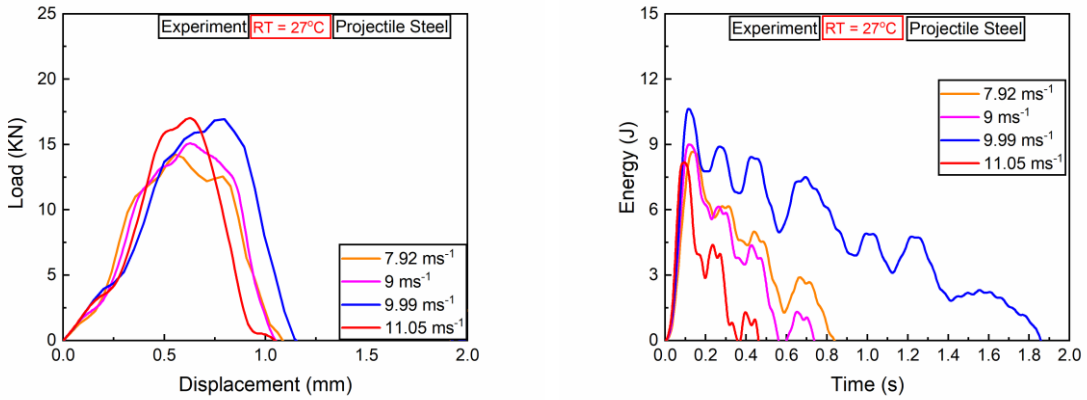

Fig. 7. Projectile steel (a) load vs displacement (b) energy vs time curve

c. Ballistic impact test

Ballistic impact tests are conducted to validate the numerical models. To perform the experiment, the design of a suitable test fixture is crucial. Most important that the target armor plate must be held firmly during the impact, while on the other hand, there must be clearance on all sides for the high-speed cameras and artificial illumination system to have an unobstructed view of the impact event. In this experiment, a suitable holder made of mild steel I-section beams was used to hold the plate in a firm vertical position. The entire setup is depicted in Fig. 8.

This study focuses on the ballistic resistance of a 40 mm thick RHA steel plate. The dimensions of the plates are 500 x 500 x 40 mm. The plates are impacted by stepped shape cylindrical projectiles with a maximum diameter of 30 mm. The projectiles are made of high-strength steel (PHS 1500), featuring high strength and hardness. The projectile has a 1 mm diameter pointed nose shape. Each projectile weighs approximately 300 grams.

The projectile is fired from a typical gun and is propelled by the combustion of the propellant specified. The striking velocities on the target plate are varied by appropriately changing the propellant mass. The striking velocity is measured by typical foil and counter method. Additionally, high-speed video camera is used to capture the impact phenomenon and also estimate the striking velocity & post-perforation residual velocity by frame-by-frame analysis. Provision is also made for artificial illumination on the target keeping in view the high-speed impact event. During the experiment, multiple projectiles were impacted on the target plate at different striking velocities. Above a certain threshold velocity, complete perforation occurred. As the projectile is deformable, deformation and breakage of the projectile after impact could be seen. The residual velocity of the projectile was difficult to estimate due to the disintegration of the projectile and the debris cloud formed during the impact. As a result, the residual velocity of larger debris fragments was considered instead. Table 1 shows the experimental results.

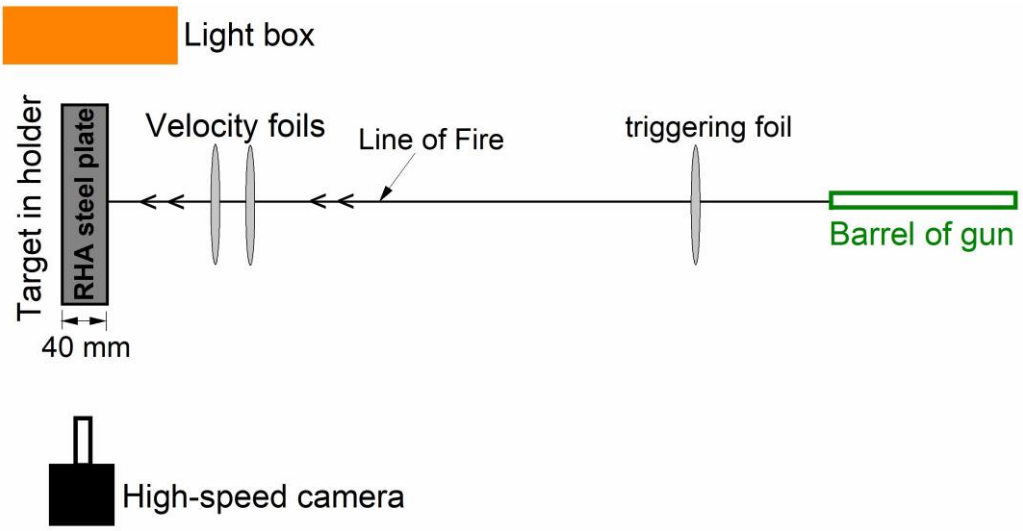

Fig. 8. Schematic of the full experimental setup of the ballistic impact test

Table 1: Experimental results of ballistic impact by deformable projectile

Round No.	V (m/s)	V_r (m/s)	Entry hole Dia		Exit hole Dia		Remarks
			H	V	H	V	
1	806.5	NR	50	52	49	45	Through-hole
2	757.6	0	51	53	NA		Incomplete penetration
3	803.4	166	52	53	45	45	Through-hole
4	757.2	0	50	54	NA		Incomplete penetration
5	775	0	50	50	NA		-do-
6	795	137	53	43	40	35	Through-hole
7	793	128	50	50	45	32	Through-hole

d. Fracture toughness testing

The event of ballistic impact is highly dependent on loading rate and hence the fracture toughness of the armour to be used in simulation is considered as loading rate dependent. The nature of the fracture behaviour may be brittle or ductile depending on the loading rate. Hence both the types of fracture toughness tests (*J-R* and K_{IC}) are explored for the armour material. Test matrix for fracture (*J-R* and K_{IC}) was planned according to the requirement. Due to the constraint of availability of material, one-quarter of CT specimens were designed for testing. One-quarter compact tension (CT) specimens extracted from armour plate are fabricated in accordance with ASTM E-1820. The dimensions of the above-mentioned one-quarter CT specimens are as shown in Fig. 9. All the fracture (*J-R* and K_{IC}) tests were conducted in INSTRON servo-hydraulic machine. The test results are listed in Table 2.

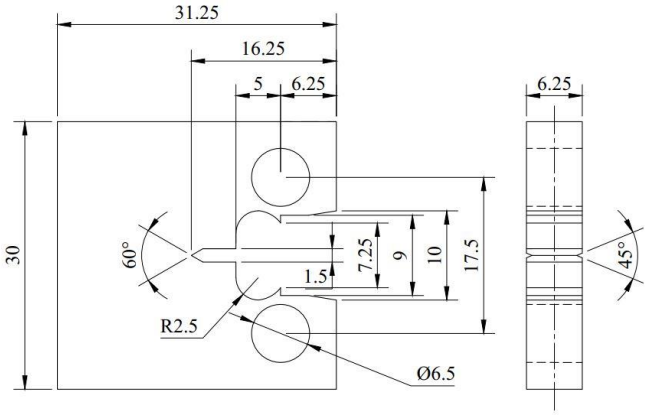

Fig. 9. Geometry of CT specimen used for Fracture Testing.

Table 2. Loading rates vs the fracture toughness parameters

Loading Rate (mm/s)	Test Temperature (°C)	Test Type	Fracture Toughness (J_{IC}) (MPa.mm)	Fracture Toughness (K_{IC}) ($MPa\sqrt{m}$)	Fracture Toughness (K_{JC}) ($MPa\sqrt{m}$)
0.01	27	J-R	30.461	.....	79.59829
0.05	27	J-R and K_{IC}	45.005	90.567	96.75247
0.075	27	J-R	32.12	.....	81.74
0.1	27	J-R	48.965	.....	100.9194
0.5	27	K_{IC}	.....	98.644	
1.0	27	K_{IC}	.....	96.997	
1.5	27	K_{IC}	.....	113.674	
0.01	200	J-R	240.1	.....	223.47
0.01	400	J-R	205.6	.....	206.79

3. Finite element simulation

For accurate finite element simulations, choosing the right material model is crucial to predict how materials behave under different conditions, such as slow loading, high-speed impacts, and high temperatures. There are two main types of material models used for this purpose:

a. **Phenomenological Model** – The **Johnson-Cook (J-C) model** falls into this category. It is a simple and widely used model that effectively describes how materials respond to dynamic forces and high temperatures.

b. **Semi-Physical Model** – The **Rusinek-Klepaczko (R-K) model** is an example of this type. It is commonly used to predict the behavior of materials with a body-centered cubic (BCC) crystal structure, such as some steels.

Additionally, a **Modified Johnson-Cook (MJ-C) model** has been developed to improve the accuracy of the original J-C model by addressing some of its limitations.

The J-C failure model is also used to capture the failure of the material.

a. Tensile test simulation

The tensile test simulation of RHA steel and projectile steel is conducted at differerent strain-rates by using above mentioned material models and failure models. Some of the simulation results are shown in Figs. 10 & 11.

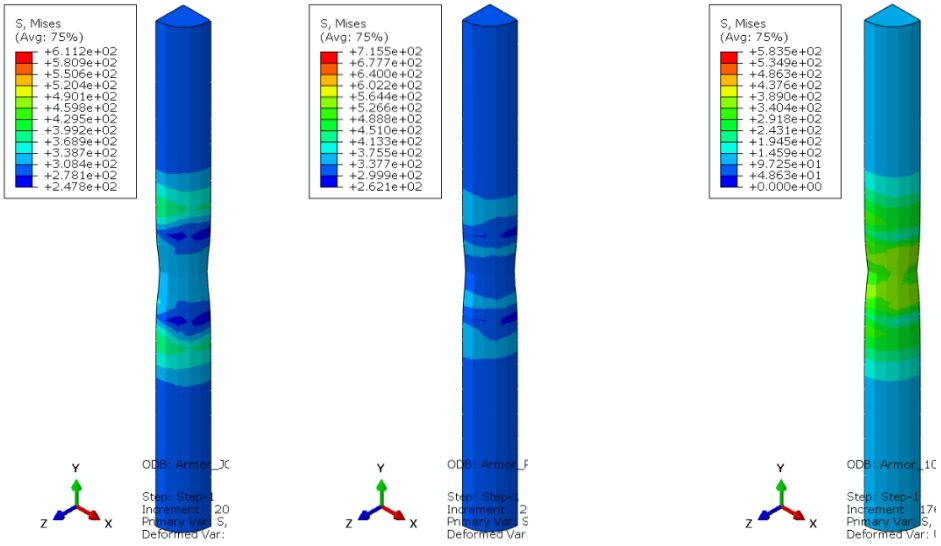

J-C R-K MJ-C

Fig. 10. Deformation patterns by using different material models at $10^{-3}\ s^{-1}$ strain-rate at room temperature

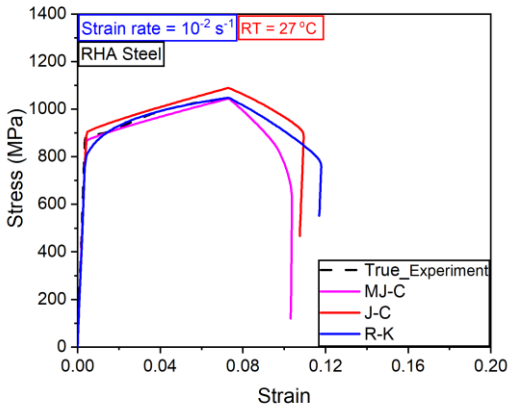

Fig. 11 Load *vs* displacement curves at RT and strain-rates of 10^{-2} s^{-1}

b. Charpy Impact test

The Charpy V-notch impact test of RHA steel and projectile steel is conducted at different velocities by using above mentioned material models and failure models. Some of the experimental and simulation results are shown in Figs. 12 & 13.

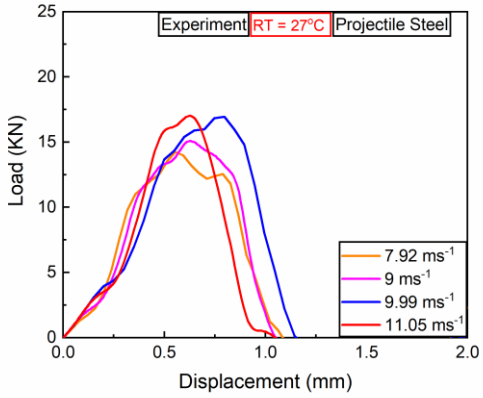

Fig. 12 Charpy V-notch impact test result for projectile steel

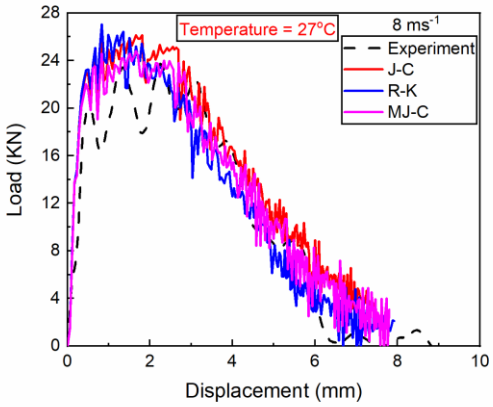

Fig. 13 Charpy V-notch impact test comparison result among material models and experimental results for armour steel.

c. Ballistic impact test

The ballistic impact test was conducted using both rigid and deformable projectiles at different ordinance velocities while keeping the friction coefficient constant. The simulations incorporated the specified material and failure models, and some of the results are shown in Fig. 14.

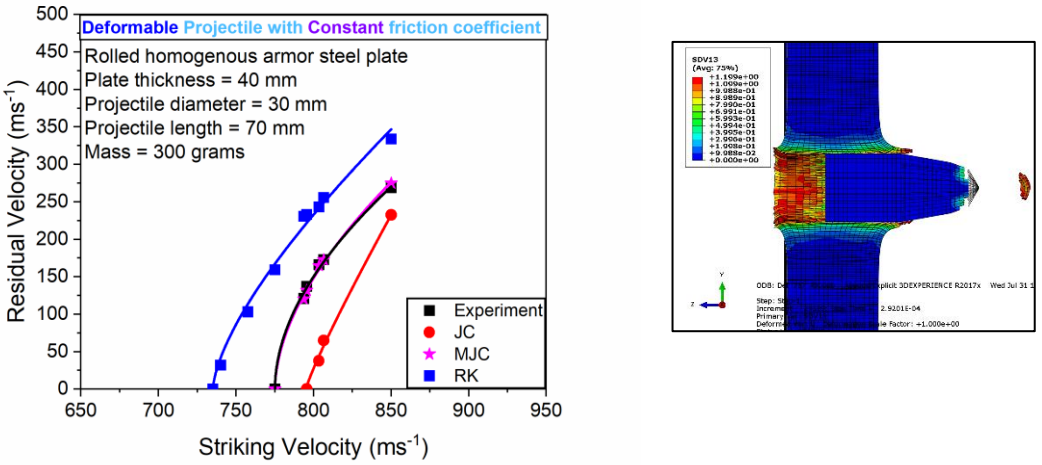

Fig. 14. Simulation plots for deformable projectile of 100 mm in length and 30 mm diameter

d. Ballistic impact test with different nose shapes

The effect of different nose shape in case of deformable projectile also studied at different striking velocities the results are shown in Figs. 15 & 16.

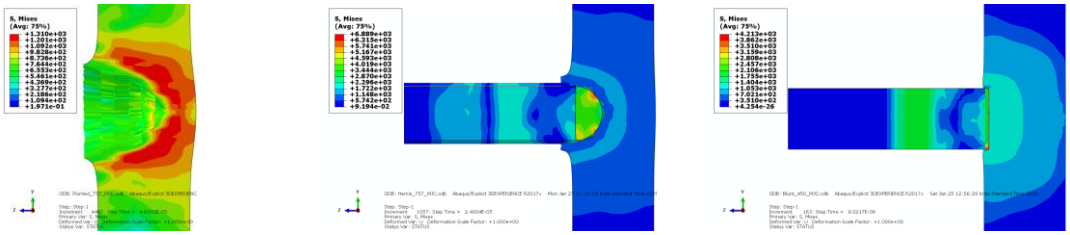

(a) **(b)** **(c)**

Fig. 15. (a) Conical nose shape projectile (b) hemispherical nose shape projectile (c) blunt nose shape projectile

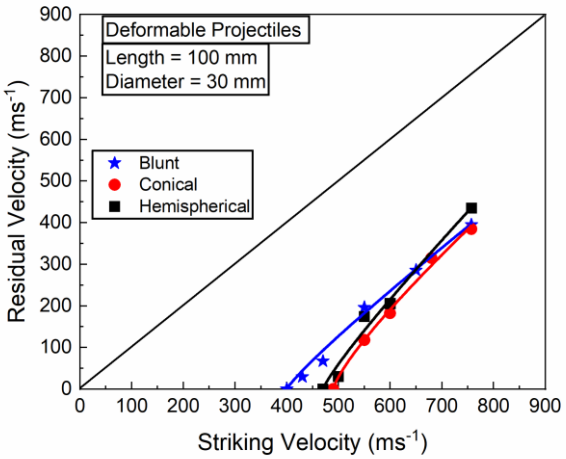

Fig. 16. Lambert-Jonas equation fitting for different nose shapes projectiles

The effect of different heat treatment protocols and beacause of changing microstructure the value of yield stress, plastic modulus and strain hardening changes. The effect of change of these material properties on residual velcoities also studied for only RHA steel. The results are displayed in Fig. 17.

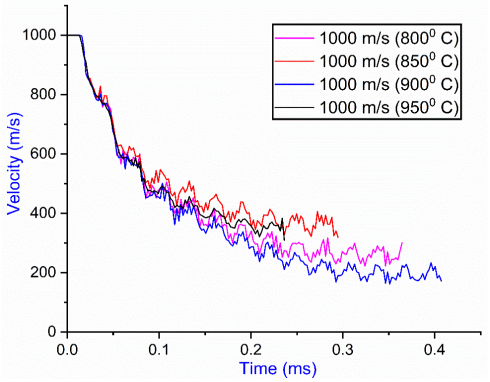

Fig. 17. Velocity vs time plot for as received geometry deformable projectile at 1000 m/s

e. Ballistic impact test with fracture mechanics as failure criteria

The failure of armour plate in this analysis is conducted by taking into account the fracture toughness parameters K_{ID}. Here instead of taking a regular damage model, fracture toughness is taken as a failure criteria. The simulation results are shown in Figs. 18 to 20.

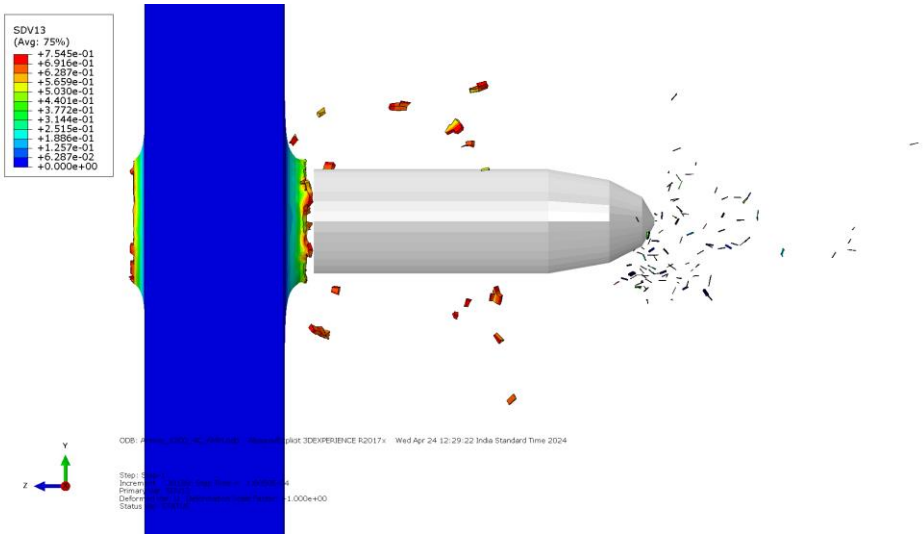

Fig. 18. Striking velocity 1200 ms^{-1}, 40 mm RHA plate, 4 cracks of 6 mm in length

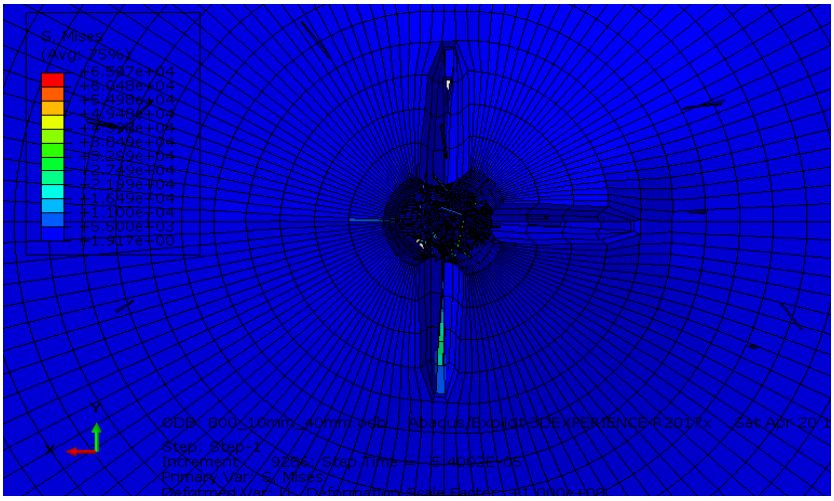

Fig. 19. 4 cracks of 10 mm

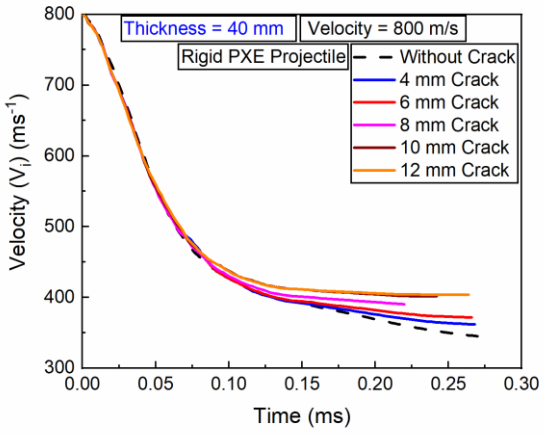

Fig. 20. 40 mm thickness plate

Nomenclature

E	Young's modulus
σ_f	Flow stress
T	Working Temperature
ε	Strain
$\dot{\varepsilon}$	Strain-rate
$\dot{\varepsilon}_s$	Strain rates
ε_p	Plastic strain
σ_μ	Internal stress
σ^*	Stress triaxiality
σ_e	Effective stress
v	Striking velocity
v_r	Residual velocity
v_{bl}	Ballistic limit
K_{IC}	Plain-Strain Fracture Toughness
J_{IC}	Elasto-Plastic Fracture Toughness
K_{ID}	Dynamics Fracture Toughness

List of Figures

S.No. **Page No.**

Chapter -2

Chapter -3

Chapter -4

Chapter -5

Chapter -6

Chapter -7

List of Tables

S.NO. Page No.

Chapter -2

Chapter -3

Chapter -4

Chapter -5

Chapter -6

Chapter -7

Chapter -1

1.1 Introduction:

The Science behind Impact and Fracture Mechanics

In the case of a high-speed projectile striking on an armour plate, a complex chain of events happens in a fraction of millisecond — shock waves spreads, stress builds up, and the material fights to resist penetration. Some armour material plates hold strong and absorbs the impact, while others punctured by the projectile tip leads to crack and fail.

Since ancient times, people have worked to create strong materials—like the steel armor worn by knights or the tough composites used in modern bulletproof gear. But it's not just about making materials stronger; it's also crucial to understand how they break under extreme force.

Impact mechanics is the study of how materials respond to sudden, high-speed forces. Unlike static loads, which are slow and steady, impact forces act in an instant, generating stress waves that travel at the speed of sound within the material. These waves can cause plastic deformation, crack formation, or even complete failure, depending on the material properties.

Over time, scientists have developed computational and experimental methods to understand these interactions. The Johnson-Cook (J-C) model [1] is widely used in the industry to describe how metals behave under sever conditions, incorporating strain (ε), strain-rate ($\dot{\varepsilon}$), and temperature (T) effects. Researchers like Borvik et al. [2] and Camacho and Ortiz [3] further advanced this field by using finite element modelling (FEM) to simulate ballistic penetration and impact resistance, refining our understanding of how materials absorb and dissipate energy.

While impact mechanics explains how materials react to forces, fracture mechanics explains why and how they fail. If you drop a glass cup, it shatters because of the cracks already present in its structure which grow instantaneously. In engineering, tiny defects exist in all materials, but their growth and propagation under load determine whether a structure will survive or fail.

The stress intensity factor (SIF) and fracture toughness K_{IC} are critical parameters in predicting failure. Early studies by A.A. Griffith laid the foundation for linear elastic fracture mechanics (LEFM), while G.R. Irwin expanded it to include plastic deformation [4]. Today, engineers use these principles to predict how cracks grow in aircraft structures, bridges, and even biological implants.

In armour design, both impact and fracture mechanics play a crucial role. Materials like martensitic armour steel [5,6] are preferred because they can absorb impact energy without failing. However, at high $\dot{\varepsilon}$ and elevated temperatures, traditional models like J-C often fail to capture the full complexity of material behaviour. Researchers have modified these models to improve accuracy, incorporating thermal softening, adiabatic heating, and strain rate dependency [7,8].

In real-world scenarios like military combat and vehicle crashes, understanding how materials behave under extreme conditions can save lives. The combination of experimental testing (such as Charpy impact tests) and finite element simulations allows scientists to develop materials that resist penetration, absorb shock, and maintain structural integrity.

Armour steel with a martensitic microstructure is widely used for its energy absorption at high loading rates. Its behavior under high strain rates has been studied [5,9–11]. During practical applications, such as crashes, explosions, ballistic impacts, and metal forming problems, all parameters, such as ε, $\dot{\varepsilon}$ and T, change significantly. Significant plastic deformation also occurs, critical for engineering structures design and safety evaluation. In such deformation processes, the material behavior may accurately be described considering the 'large displacements and large strain' framework, incorporating the influences of a high $\dot{\varepsilon}$ and elevated T.

In this work the behavior of two martensitic steel materials (rolled homogenous armour and PHS 1500) is investigated from quasi-static to intermediate $\dot{\varepsilon}$. The RHA behavior is also investigated at high $\dot{\varepsilon}$. A phenomenological model the J-C, semi-physical material model the Rusinek-Klepaczko (R-K) and a new material model developed based on J-C formulation were used to predict the thermoviscoplastic response of Body centered Tetragonal (BCT) steel. Finite element simulations were performed using ABAQUS CAE Standard/Explicit software. The model's accuracy is validated by comparing its numerical results with experimental data from tensile tests. The research combines extensive experimentation and FE simulations. The material model is also verified through Charpy V-notch impact testing. Finally ballistic impact tests are numerically simulated with three material models. The study also thoroughly examined the effect of fracture toughness on armor plate performance and demonstrated the influence of the fracture toughness parameter K_{ID} on ballistic performance. The findings provide critical insights into the mechanical behavior and impact resistance of typical armour steel material.

1.2 Chronology of impact and fracture mechanics research

Impact mechanics and fracture mechanics are two interrelated fields that have significantly evolved over the past centuries, contributing to our understanding of material behaviour under various loading conditions. Both fields have distinct historical developments, yet they converge in their applications, particularly in areas requiring high reliability and safety, such as aerospace, automotive, and defence industries.

1.3 Literature Review

The resistance of typical armour plates to deformable projectiles is a critical area of study that combines principles of material science, mechanical engineering, and applied physics. This literature review aims to synthesize existing research on this topic, highlighting key developments, methodologies, and findings. The focus is on understanding how fracture mechanics can be applied as a failure criterion to predict and analyse the behaviour of armour materials under high-velocity impacts.

The historical development of impact mechanics and fracture mechanics reflects a continuous effort to understand and predict the behaviour of materials under extreme conditions. From early theoretical foundations laid by pioneers like Galileo, Newton, and Griffith, to modern computational and experimental advancements, both fields have evolved to address increasingly complex engineering challenges. Today, they play a crucial role in ensuring the safety, reliability, and performance of structures in various high-stakes industries.

The most widely used constitutive relations since 1983 is the one proposed by J-C [12] due to its formulation in which all necessary parameters plastic ε, $\dot{\varepsilon}$ and T require for defining dynamic behaviour of metal are present. This model was basically made to capture the dynamic behaviour of FCC material OFHC copper.

In 1985 Zerilli and Armstrong [13] proposed a dislocation-based constitutive relation to investigate dynamic behaviour of FCC material under high $\dot{\varepsilon}$. These constitutive relations are used for ballistic impact event also. In 1999 Borvik et al. [14] applied J-C viscoplasticity material model and the J-C damage model [1] into the non-linear finite element code LS-DYNA to study the ballistic penetration of steel at high $\dot{\varepsilon}$. From this successful modelling of FCC material researchers got the motivation of building material models.

In 1999 Khan and Liang [15] developed a model to study the behaviour of BCC material over a wide range of $\dot{\varepsilon}$ and T. Camacho and Ortiz [3] developed Lagrangian finite element model of ductile penetration and showed that the adaptive meshing plays a key role in alleviating element distortions and modelling accurate regions of high variation in the velocity field. Zukas and

Scheffler [16] focused on computational mesh which leads to the disagreement between the experimental and computational model analysis in problems involving fast and transient loading. They explain the importance of mesh in numerical analysis of armour steel by taking the example of a projectile strikes an armor steel target at a velocity of 0.8 kms^{-1}, causing both projectile and target to exhibit acute mesh discontinuities. They also show the reflection of high frequency waves from the fine and coarse element boundary and effect of L/D ratio.

An experimental and numerical study was reported by Borvik et al. in 2001 [2,17] taking different types of projectiles with flat, hemispherical and conical noses to study the effect of projectile nose shape on the deformation of target. In their experimental work Weldox 460E steel plates of thickness 12mm are penetrated by three different nose configuration penetrators at a velocity of 300m/s for hemispherical and conical projectiles and 185m/s for blunt shape projectiles by gas gun. From experiment they found that blunt projectiles were more efficient penetrators than hemispherical and conical projectiles at low velocities but at higher impact velocities, the conical projectiles require less energy to perforate the target. Their study revealed that the projectile's nose shape significantly affects both the energy absorption mechanism and the failure mode of the target during penetration. In numerical simulation constitutive model of viscoplasticity and ductile damage which they previously developed implemented in finite element code LS-DYNA. They found problem with conventional meshing and the analysis was highly mesh-dependent for impact phenomenon. Therefore, they applied the adaptive meshing concept.

Rusinek and Klepaczko in 2001 [18] a novel experimental methodology was devised to investigate the behaviour of sheet metals across a spectrum extending from low to high strain rates. Their primary objective was to investigate the viscoplastic behaviour of industrial sheet metals. Al-calmed sheet steel is used for applications that require a broad spectrum of strain-rates for eg. drawing and crashworthiness. An additional viscoplastic constitutive relationship was suggested.

For applying correct visco-plastic constitutive relation for a particular material it is better to have knowledge of atomic structure of material like FCC or BCC or some other atomic configuration. Chia-Jung Hu et al. [19] evaluated the performance of a modified rolled homogenous armour (MRHA) steel. A comparison was made with AerMer 100, AISI 1045 and 4130 steels during ballistic impact tests. They found formation of “white”- etched portion of adiabatic shear bands and transformed bands at the front surface of the target plates made of Aermer 100, 4130 and MRHA while steel deformed bands for AISI 1045 steel. Transformed bands refer to the occurrence of a crystallographic phase transition inside the adiabatic shear band. On the other hand, deformed bands are characterized by a very tiny zone of deformation with a very high shear strain, reaching up to 100. These can also be found at the tips of the shear band.

Multiple void interactions and void-by-void growth induced the failure of ductile material, as described by Tvergaard and Hutchinson [20]. Peixinho et al.[21] used Cowper-Symonds constitutive equation to describe material behavior of dual-phase and TRIP steel at different $\dot{\varepsilon}$. The numerical model for crushing behavior of thin-walled tubes was investigated with an explicit elasto-plastic finite element code: LS-DYNA. Strain-rate depended properties of automotive sheet steel are very important especially for crashworthiness and impact events. Bruce and David [22] conducted tensile test on different automotive sheet steels, including IF, HLSA, DP, and TRIP steels from $\dot{\varepsilon}$ range from $0.001\ s^{-1}$ to $500\ s^{-1}$. They found that the energy absorption by the different materials was highly dependent upon the strain limit chosen for the calculation. Large plastic deformation take place during dynamic events not only in case of impact and penetration events but also in high speed machining operations Khan et al. [23] worked on Ti-6Al-4V titanium alloy constitutive modelling form quasi-static to dynamic loading. Titanium alloy widely used in aero-engines, gas turbines, armour and lightweight tanks [24] and place where high temperature and resistance for corrosion is required.

Spall fracture and other rapid tensile failures in ductile materials are often dominated by the rapid growth of voids. Research on the mechanics of void growth clearly shows that void nucleation may be represented as a bifurcation phenomenon, wherein a void forms spontaneously followed by highly localized plastic flow around the new void. The rapid expansion of voids frequently governs spall fracture and other forms of rapid tensile failure in ductile materials. Clear evidence from studies regarding the mechanics of void growth indicates that void nucleation can be conceptualized as a branching phenomenon, in which a void spontaneously forms and is subsequently surrounded by a highly localized plastic flow.

These two facts, initiation by bifurcation at a cavitation stress, at which a void first appears, and rapid domination by inertia, are used to postulate a simple, but physically realistic, model for nucleation and early growth of voids in a ductile material under rapid tensile loading. A reasonable statistical distribution for the cavitation stress at various nucleation sites and a simple similarity solution for inertially dominated void growth permit a simple calculation of the initiation and early growth of porosity in the material. Molinari and Wright [25] uses parametric analyses to show the effect that loading rate, peak loading stress, density of nucleation sites, physical properties of the material, etc. have on the applied pressure and distribution of void sizes when a critical porosity is reached.

P.K.C. Wood et al. [26–34] done lot of work on high strain-rate tension testing from developing tensile specimen design to test procedures. Noise factors, which are significant sources of variation in the testing environment, originate from uncertainties in structural properties, joint positions,

boundary conditions and measurement system. Yan et al. [35] recommended practice for dynamic testing of sheet steels. Wood and Yan both extensively worked on dynamic testing of sheet steel because of the application in automotive industry. Sheet steel show positive strain rate sensitivity which ultimately improve the energy absorption capability during the impact and crash events. Material which undergo inelastic deformation timescale of the event have significant effect on the stress-strain relation in addition to this failure pattern also changes accordingly. In other words, the prediction of the crash behavior in numerical simulations requires the information on the materials behavior during a sudden, dynamic impact load. At different locations strain rates are different therefore it is necessary to describe the $\dot{\varepsilon}$ sensitivity of the material for wide range of $\dot{\varepsilon}$ for numerical crash and impact simulation [36].

The shape of the front area of projectile greatly affect the deformation mechanism of the target plates. The thickness of the target plate also have an effect on the ballistic resistance. It happens sometimes that the some nose shape have different ballistic resistance for thin plate and thick plate, and also the deformation pattern [37,38]. The T/D and L/D ratio also determines the ballistic resistance and deformation pattern. Three factors are prime L/D ratio, nose shape and thickness of the plate. If the nose radius of projectile changes the critical impact energy changes and maximum energy observed at nose radius where mode of failure changes from shear plugging to tensile stretching. Several researchers [38,39] found that the blunt shape penetrators penetrate the target more efficiently than ogive and hemispherical projectiles while others [40] found that the conical projectiles are more efficient penetrators and as the nose angle decrease the perforation resistance of the target tends to drop for thick carbon steel plates. N.K Gupta et al. [41] used target plates of thickness 0.5, 0.71, 1, 1.5, 2, 2.5 and 3 mm and projectile of different nose shapes hemispherical, ogive and blunt shape. The diameter and length of all the projectile are same i.e. 19 mm and 50.8 mm. The study revealed that projectiles with hemispherical noses induced the most significant overall deformation (dishing) on the target plates. For plates up to 1.5 mm thick, those with ogive-shaped noses penetrated most effectively, whereas blunt-nosed projectiles required the least energy to perforate plates between 2 and 3 mm in thickness. Additionally, the hemispherical-nosed design exhibited the highest ballistic limit velocity compared to the other configurations. For numerical model Johnson-cook strength and damage model was used in their simulations.

In 2007 Rusinek and Klepaczko [42] proposed a constitutive relation that encompass strain hardening, wide range of $\dot{\varepsilon}$ and temperature sensitivity and applied to mild steel. The model is phenomenological thermo-visco-plastic and to some extent on the concept of physical modelling.

For ballistic impact phenomenon dynamic behaviour of high strength armor steel material should be known carefully. Nahme and Lach [4] worked on dynamic properties of Mars 190, Mars 240

and Mars 300 armor steel from strain rate 10^{-3} s^{-1} to 10^{6} s^{-1} they also showed the influence of the loading process on the microstructure and the fracture mechanism. Kasonde and Waldo [43] carried out systematic analysis of the microstructure and the fracture surfaces of 13 laboratory melted tempered martensitic armour steels to understand the improved ballistic performance of these steels. In their observation they found that the detrimental effect of inclusion on ballistic performance depends on the tempering T and on the $\dot{\varepsilon}$.

In 2008 Arias et al. [44] conducted a numerical investigation into the normal perforation of thin steel plates impacted by projectiles of various shapes. Their simulation, which utilized adaptive meshing, examined impact velocities between 190 and 600 m/s. The study evaluated the effects of adiabatic shear bands, plastic work, and temperature gradients on the plates. It was found that blunt-nosed projectiles tend to fail by propagating adiabatic shear bands that ultimately eject a plug, while conical projectiles induce a persistent radial compressive state that enlarges the perforation. Hemispherical projectiles, on the other hand, displayed a combination of these failure modes depending on the impact velocity.

Huh et al. [45] carried intermediate strain rate experiment on mild steel and advanced high strength steel at $\dot{\varepsilon}$ range from 1 s^{-1} to 200 s^{-1} with the specially designed jig fixture to reduce load-ringing phenomenon induced by unstable stress wave propagation at high $\dot{\varepsilon}$.

In 2009 Rusinek et al. [46] examine the normal impact of hemispherical projectile. Experiments spanned a broad range of impact speeds, and the effect of friction in the perforation process was evaluated under both dry and lubricated conditions. Three material model are chosen for numerical analysis J-C, P-L, and R-K.

In 2009 Klepaczko et al. [47] modelled the thermo-viscoplastic behaviour of DH-36 and Weldox 460-E structural steel at wide ranges of $\dot{\varepsilon}$ and T especially for impact analysis, by applying three constitutive relations J-C, PB and R-K. For these material R-K constitutive relation was found to be more precise.

In 2010 P.K Jena et al. [48] studied how heat treatment alters both the mechanical and ballistic characteristics of high-strength armour steel. The ballistic behaviour of the heat-treated plates was evaluated by impacting against non-deformable hard-core projectiles at 840±15 m/s at normal angle of attack.

In 2011 Behzad et al. [49] checked the ballistic resistance of multi-layered targets impacted by a blunt nosed shape projectile. They used aluminium-aluminium, steel-aluminium, aluminium-steel, steel-steel plates of thickness 1 mm. A compressed gas gun was used to launch projectile within the velocity range from 50 to 400 m/s. A slightly modified version of the J-C constitutive equation

and fracture criterion was used to simulate material behavior. The experimental outcomes were benchmarked against the predictions provided by the Ipson and Recht analytical model.

In 2012 Farid and Fadi [50] compares the four well known constitutive relations (J-C, R-K, ZA,VA) for HSLA-65 and DH-36 steel over the wide range of $\dot{\varepsilon}$ and T. They pointed out the inaccurate assumptions used in developing J-C, R-K and ZA model. For the mentioned materials VA model prediction is the most accurate.

In 2012 Xu and Huang [51] compares the physically based constitutive models (PB, NNL, ZA, VA and R-K) for armour steel over the wide range of $\dot{\varepsilon}$ and T. They focused on the description and prediction capabilities of material models. For 603 steel R-K and NNL models have better description capability while PB and VA models have better prediction capabilities. It is also found that the description capability of a model is dependent to a large extent on both its form and the number of its constitutive parameters, while the precision of prediction relies largely on the performance of description. In the selection of constitutive models, the experimental data and the constitutive models should be considered synthetically to obtain a better efficiency in material behaviour characterization.

In 2013 Jankowiak et al. [52] explored how sheet steel responds dynamically when perforated by a conical projectile. Their study accounted for factors such as target thickness, the material model used for the target, the projectile's mass, the friction between the projectile and target, and the projectile's geometry.

In 2013 Holmen et al. [53] studied the ballistic properties of AA6070 aluminium alloy at different tempers using target plates of 20 mm thickness. In the material tests it was shown that the O-temper was most ductile and almost no fragmentation took place during the ballistic impact tests. The T6-temper proved to be least ductile, and fragmentation was commonly seen. The experiments show that despite fragmentation, strength is a more important feature than ductility in ballistic impact for this alloy, at least for the given projectile and within the velocity range investigated.

In 2014 Qing Yin et al. [54] describes the three different shear tests for sheet metals in order to enhance the knowledge of the material behaviour under shear conditions. The test set- ups are different in terms of the specimen geometry and the fixture.

In 2014 An He et al. [55] modified the Zerilli-Armstrong constitutive model to predict the hot deformation behavior of 20CrMo alloy steel.

In 2014 Whittington et al. [5] studies the behaviour of RHA (Rolled Homogenous armour) steel at 25^{o}C and 300^{o}C and at $\dot{\varepsilon}$ of 10^{-3} s^{-1} and 1000 s^{-1} the stress state on plasticity and fracture.

In 2014 Kabirian et al. [56] studied the behaviour of 5xxx series of aluminium alloy and detected a critical temperature where the material shows negative to positive $\dot{\varepsilon}$ sensitivity. A constitutive model is proposed to predict the stress–strain response of the alloy over the studied $\dot{\varepsilon}$ and T ranges.

In 2014 Motra et al. [57] quantitatively compare the strain measurement technique by three devices strain guage, extensometer and machine crosshead motion. Three techniques of strain measurement are compared in quantitative manner based on the calculation of mechanical properties (modulus of elasticity, yield strength, tensile strength, percentage elongation at maximum force) of structural steel. A statistical information was used for evaluating the results. It is seen that the extensometer and strain gauge provided reliable data, however the extensometer offers several advantages over the strain gauge and crosshead motion for testing structural steel in tension. Furthermore, estimation of measurement uncertainty is presented for the basic material parameters extracted through strain measurement.

In 2014 Molinari et al. [58] analyse how inertia influence fracture and strain localization. They proposed a multiscale model to predict the behaviour of voided visco-plastic material.

In 2015 Tria et al. [59] study the effectiveness of four ductile fracture models: Modified Johnson-cook (MJC), the Cockcroft-Latham (CL), the maximum shear stress and the constant failure strain model. These models are used to capture material fracture properties and shear plugging failure in 30PM steel plates.

In 2015 Zerbst and Madia [60] introduced a cyclic R-curve analysis method to estimate the initial flaw size, a critical parameter for predicting fatigue crack propagation.

In 2015 Trajkovski et al. [61] study the flow and fracture properties of high-strength armour steel PROTAC 500. The J-C strength and fracture model are used for numerical simulation.

In 2015 Kpenyigba et al. [62] explored how the shape of a projectile's nose influences the ballistic resistance of IF steel. Their study spanned impact velocities from 35 to 180 m/s and utilized the Rusinek-Klepaczko (RK) thermoviscoplastic material model for numerical simulations. The results confirmed that the model reliably represents the physical mechanisms involved in the perforation process.

In 2015 A.Banerjee et al. [63] proposed the modification in the Johnson-cook damage model and validated by simulation the behaviour of typical armour steel through Charpy impact testing.

In 2016 Joo et al. [64] establish experimental technique to conduct tension/compression tests at intermediate $\dot{\varepsilon}$ upto 50 s^{-1}. The hardening curve obtained from tension/compression tests with variation of $\dot{\varepsilon}$. The notable observation are: the Bauschinger ratio is increased with the increase of

$\dot{\varepsilon}$. During the loading reversal phase, there is a gradual drop in the tangent modulus as the $\dot{\varepsilon}$ increases. Consequently, the extent of permanent softening decreases as the $\dot{\varepsilon}$ increases.

In 2016 Jena et al. [65] describe and analyse the effect of tempering time on the ballistic and mechanical properties of a high strength armour steel. The marginal variation is observed in strength and hardness with increasing tempering time at 2, 24 and 48 h. The Charpy impact values are found to be decreasing. Ballistic performance also decreased with increasing tempering time.

In 2016 Wang et al. [66] modified the Johnson-cook fracture criterion to study the effect of $\dot{\varepsilon}$, temperature and stress triaxiality (σ^*) on the fracture behaviours of a single-crystal Nickel-base super alloy.

In 2016 Kim et al. [67] characterized Charpy impact energy of three tempered martensitic steels at room and low temperatures. The interpretation was done by fracture initiation and propagation mechanisms in relation with microstructural evolution of dynamically compressed specimens. According to microstructural analyses adiabatic shear bands were formed in the 400 °C and 500 °C tempered steels. It works as preferred fracture propagation paths to critically reduce the fracture propagation energy. At 600°C tempered steel, the deformation energy due to the pendulum impact was effectively absorbed by the combination of fine spheroidized carbides and softened tempered martensitic matrix without forming adiabatic shear bands, thereby leading to the relatively homogeneous deformation in the impacted region and the very large increase of fracture propagation energy.

In 2016 Nie et al. [68] study the dynamic behaviour of martentistic stainless steel in a complete thermal cycle. They presented the phase-based constitutive model to describe the behaviour of material of turbine blade. The temperature range was selected from 20^oC to 1000^oC, and $\dot{\varepsilon}$ ranging from 10^{-3} s^{-1} to 16,000 s^{-1}.

In 2017 Wang et al. [69] studied the behaviour of 35CrMo steel through compression testing across the wide range of temperature (1123 K – 1423 K) and $\dot{\varepsilon}$ (0.1-10 s^{-1}). They modified the Johnson-cook material model to predict the flow stress of the alloy.

In 2017 Tria and Trebinski [70] presented a novel methodology for experimental verification of constitutive models and numerical algorithms used in terminal ballistics of small arms ammunitions. The methodology comprises of the following elements: identification of material models in a set of independent tests, terminal ballistics testing of conditions covering the most important cases of bullet-target interactions, while providing enough data to assess the scatter of parameters measured in the experiments and to create a measure characterizing deviation of modelling results from the experiments.

In 2017 Banerjee et al. [71] investigated the ballistic resistance of typical armour steel plate of medium thickness by ogive-nosed projectile striking at ordinance velocity. The J-C material model was used for numerical simulation.

In 2017 McDonald et al. [72] evaluated two steels, a high hardness steel (HHA) and a Rolled homogenous armour steel (RHA). A series of 30 blast experiments are carried. In terms of deformation resistance and rupture threshold the HHA steel outperform a more ductile RHA steel.

In 2017 Piao et al. [73] characterize the dynamic behavior of metallic material at ultra-high $\dot{\varepsilon}$ ranging from 10^4 to 10^6 s^{-1}. Three kinds of metallic materials are selected for body-centered cubic (BCC) 4130 steel, face-centered cubic (FCC) OFHC copper, and hexagonal close-packed (HCP) Ti6AL4V alloy. A constitutive model is used for interpolation and extrapolation of stress-strain data. By employing a hybrid experimental-numerical methodology and utilizing the results of the Taylor impact tests, the extrapolated hardening behaviors at extremely high strain rates are precisely calibrated. Significant improvements are observed in the precision of numerical estimations regarding the deforming morphologies of projectiles subjected to extremely high $\dot{\varepsilon}$ when the stress-strain curves are calibrated.

In 2018 Wang et al. [74] investigated the high specific strength steel (HSSS) with dual microstructure. The mechanical properties were found to increases with the $\dot{\varepsilon}$ range from 0.0006 s^{-1} to 56 s^{-1}. These properties makes this steel an excellent candidate for energy absorber in automobile industries. Smaller dimple size and a higher density of phase interfaces in final fracture surface are observed.

In 2018 Avila et al. [75] uses small punch test, SPT for mechanical characterization of nuclear material 316L steel one “hardened” and another “annealed”. The analysis is performed by FEM model. The determination of instantaneous strain rate during the test is still under investigation. The strain and instantaneous strain rate, are not linear as the SPT testing proceeds.

In 2019 Liu and Soares [76] conducted low velocity impact tests and quasi-static punching tests to examine the plastic response and failure of clamped rectangular steel plates struck by hemispherical indenters. They propose to characterize the material strain rate sensitivity and critical fracture strain. The simulation and experimental results are compared. This is the contribution in the research to enhance industry practice in impact simulation of steel when only quasi-static data are available.

In 2019 Murugesan and Jung et al. [77] formulated the flow stress model to characterise the flow behaviour of AISI-1045 medium carbon steel. The selected T and $\dot{\varepsilon}$ range are (650-950^{o}C) and

(0.05-1.0 s^{-1}) respectively. The J-C flow-stress (σ_f) model and a surrogate model are developed for modelling and predicting the material flow behaviour at elevated temperature.

In 2019 Peng et al. [78] studied the effect of σ^* on plastic damage evolution and failure mode of 316L notched specimen with different notch sizes are investigated by digital image correlation (DIC). Authors' found that the plastic damage evolution and failure mode are closely related with notch radius and stress triaxiality (σ^*).

In 2019 Saxena et al. [79] conducted a comparative study to predict the T and $\dot{\varepsilon}$ dependent flow behaviour of Armox 500T steel through physical-based model modified Zerilli-Armstrong (M-ZA), and phenomenological-based model like Cowper Symonds (CS), modified Johnson-cook (M-JC), Arrhenius (Arr) and khan-Huang-Liang (KHL) constitutive model. Isothermal compression tests at low $\dot{\varepsilon}$ (10^{-3} s^{-1} – 10^{-1} s^{-1}) and dynamic compression tests at high $\dot{\varepsilon}$ (600 s^{-1} to 3000 s^{-1}) are performed. An artificial neural network (ANN) model that works on multilayer perceptron (MLP) based back propagation neural network (BPNN) has also been developed.

In 2019 Ho H.C. et al. [80] model tensile tests of high strength S690 and S275 steel materials undergoing large deformations. Standard tensile tests are performed on two steels. The data of the tests are analysed using three different transformation rules: i) Power Law Method, ii) Linear Law Method, and iii) Instantaneous Area method, three different true stress-strain curves are derived. These curves are then incorporated in finite element models to simulate large deformations. The proposed true stress-strain curve determined with instantaneous area method are shown to be highly acceptable for numerical analysis steel undergoing large plastic deformation up to fracture.

In 2019 Paul S. et al. [81] developed a phenomenological model to describe the flow behaviour of 20MnMoNi55 low carbon reactor pressure vessel steel (RPV) steel at sub-zero temperature (-80^{o}C to -140^{o}C) under different $\dot{\varepsilon}$ (10^{-4} s^{-1} to 10^{-1} s^{-1}).

In 2019 T.Fras et al. [82] investigated armour steel of high hardness 600-640 HB plate failure by striking the deformable projectile at velocity 300 ms^{-1}.

In 2019 G.D. kumar et al. [83] studied the effect of T (700^{o}C to 900 ^{o}C) and $\dot{\varepsilon}$ (10^{-4} s^{-1} to 10^{-1} s^{-1}) on the tensile flow behaviour of Fe-0.3 pct C-CrMoV graded steel.

In 2020 Choi et al. [84] studied the effect of addition of Ti as well as Ta on the strength and impact toughness of 9Cr-1W reduced activation ferritic/martensitic steel (RAFM) steel. The ductile-brittle transition temperature (DBTT) of TaTi-RAFM was found to decrease markedly.

In 2020 Kim et al. [85] introduced a numerical approach to simulate fracture patterns involving both ductile and cleavage fracture, validated using API X80 Charpy test data. The study employed a stress-modified fracture strain damage model for ductile fracture, while the maximum principal stress criterion was used for cleavage fracture. By integrating these two models, a method for simulating the interaction between ductile and cleavage fracture was developed. The numerical predictions were validated by comparing them with experimental Charpy test data at ductile-to-brittle transition temperatures. The analysis of fracture surfaces and impact energy exhibited strong agreement with experimental results.

In 2020 B.Jia et al. [86] investigated the strain-induced martensitic transformation (SIMT) in 304 austenitic stainless steel. They extended the Rusinek-Klepaczko (RK) model to incorporate SIMT effects, which enabled them to simulate the material's deformation behavior accurately. Their model successfully captured the flow stress curve for 304 ASS steel at temperatures above -60°C. Additionally, numerical simulations of ballistic impact tests were conducted across various temperatures, and the outcomes closely matched the experimental results.

In 2020 T.Bhujangrao [87] wrote a review paper on intermediate strain rate testing devices. They are divided based on the loading mechanism; it includes the high-speed servo-hydraulic testing machines, hybrid testing apparatus, the drop tower, and the flywheel machine.

In 2020 E.Konca [88] studied the ballistic performance of various microstructures in MIL-A-12560 armour steel. The steel material was subjected to isothermal heat treatments at three different temperatures, 360^{o}C was above the martensitic formation start (Ms) temperature of 336^{o}C while the other two 320^{o}C and 270^{o}C were below the Ms temperature. The promising nature of the bainite microstructure was confirmed as the sample isothermally treated at 360 ◦C provided approximately 10% higher ballistic protection as compared to the regular RHA sample of tempered martensite microstructure.

In 2020 P.K.Jena et al. [89] studied the impact resistance of rolled homogenous steel of five different thickness i.e. 20, 30, 40, 50, and 80 mm through continuous casting route. The microstructure, mechanical and ballistic properties of the continuous cast steel is compared with the steel produced by conventional ingot cast route.

In 2020 S.Choudhary et al. [90] conducted experimental and numerical research on a newly developed high-strength armor steel plate. Their numerical simulations incorporated four ductile fracture criteria: Modified Johnson-Cook (MJC), Cockcroft-Latham (CL), Constant Failure Strain (CFS), and Maximum Shear (MS) stress failure criteria. The study compared these simulation results with impact test data from a 1000 × 1000 × 6 mm steel plate subjected to 7.62 × 51 mm

NATO ball ammunition, meeting National Institute of Justice Level 3 protection standards. The Modified Johnson-Cook, Cockcroft-Latham, and Constant Failure Strain criteria closely matched the experimental findings, whereas the Maximum Shear stress failure criterion did not accurately predict the observed behavior.

In 2020 T.Chiyatan et al. [91] examined the plastic deformation, $\dot{\varepsilon}$ sensitivity, and fracture mechanisms of ferritic-martensitic dual phase steels (grades 780 and 1000) used in automotive structures. They performed tensile tests at quasi-static (0.0001 s^{-1}), medium (0.5–1 s^{-1}), and high (1500–2500 s^{-1}) $\dot{\varepsilon}$, and conducted finite element simulations with 2D representative volume elements (RVEs) to investigate how the microstructure affects local deformation and damage under various $\dot{\varepsilon}$.

In 2020 Y.Cao et al. [92] conducted finite element simulations to determine the Johnson–Cook constitutive and failure parameters for X80 pipeline steel. They validated their model by simulating the Charpy impact test, achieving good agreement with experimental results. Their study further examined the effects of pendulum velocity, specimen width, and striker radius on Charpy impact test outcomes. The findings indicated that pendulum velocity had a negligible influence on the results, while both maximum force and absorbed energy exhibited a linear relationship with specimen width. Additionally, the geometry of the striker significantly affected the test outcomes, with a 2 mm striker yielding notably lower results compared to an 8 mm striker. Based on these observations, the researchers developed a correlation model to relate the absorbed impact energy between sub-size and standard full-size specimens, as well as transformation rules for different striker geometries. These methods and results offer valuable insights for studying dynamic behavior, impact design, and risk assessment of high-grade pipeline steel.

In 2020 Saurav and Rajeev [93] studied the effect of strain-induced austenite to ά- martensite transformation of 304L austenitic steel. Compression tests were carried out at room T in the $\dot{\varepsilon}$ range of 10^{-3} to 10^{3} s^{-1} and the evolution of martensite was quantified using a ferritoscope.

In 2020 Nan Su et al. [94] investigated the tensile flow behaviour of 17-4PH stainless steel sheet from 650^{o}C to 850^{o}C at $\dot{\varepsilon}$ of 10^{-4} to 10^{-1} s^{-1}. The experimental results indicate that work hardening and dynamic recovery are exhibited in the tensile test in the temperature lower than 750^{o}C. A steady stage of stress occurs higher than 750^{o}C because of dynamic recrystallization. Considering the strain compensation, several revised constitutive models of Arrhenius-type were constructed with statistical optimization and multi-strain correction. The comparison shows perfect accurate flow predictions through multi-strain modified models. Meanwhile, the flow behavior of random conditions is predicted accurately by a single correction model with Tikhonov regularization.

In 2020 Z.Qiang et al. [95] investigated the hot deformation behavior of 7A04 aluminum alloy through isothermal compression tests at temperatures between 350 °C and 480 °C and strain rates from 0.002 s^{-1} to 20 s^{-1}. They developed an extended Voce equation [96], incorporating Arrhenius-type modifications, to predict flow stresses under these conditions. The model demonstrated high accuracy, with an average absolute relative error of 4.9%, a root mean square error of 4.8 MPa, and a correlation coefficient of 0.997. Microstructural analysis revealed that dynamic recovery was the primary softening mechanism during hot deformation.

In 2021 J.M.P Martins et al. [97] proposed a novel calibration method for thermo-elasto-viscoplastic constitutive models, reducing the need for extensive testing. Using the Virtual Fields Method with a thermo-mechanical test on a Gleeble 3500 system, they calibrated a modified J-C model for DP 980 steel. Tests at $\dot{\varepsilon}$ of 10^{-4}, 10^{-3}, and 10^{-2} s^{-1} were combined to improve accuracy. While a single test was insufficient to capture strain rate sensitivity, the combined dataset effectively predicted material behavior, demonstrating the method's potential to streamline calibration processes.

In 2021 M.A.O. Vrienlink et al. [98] developed a predictive model to assess the brittle-to-ductile transition in neutron-irradiated tungsten, crucial for plasma-facing components in nuclear fusion reactors. Using a cluster dynamics model to analyze defect production, they integrated the data into a crystal plasticity framework. Simulations closely matched experimental results for yield stress across temperatures and irradiation levels, with a probabilistic cleavage model effectively capturing the transition temperature behavior.

In 2021 A.Sela et al. [99] developed a methodology to measure plastic strain and strain rate in orthogonal machining under plane strain conditions. By creating a physical micro-grid on a workpiece and analyzing its distortion, the method enables localized strain measurement in the primary shear zone using a single image. Applied to Ti-6Al-4V cutting, results were validated through Digital Image Correlation (DIC), analytical models, literature data, and numerical simulations with AdvantEdge-2D, improving accuracy in machining process analysis.

Ji-Su Kim et al. [100] developed a numerical method to simulate interacting ductile and cleavage fractures in drop-weight tear tests (DWTT). The approach combines the stress-modified fracture strain (SMFS) model for ductile fracture and the maximum principal stress criterion for cleavage fracture, incorporating element size effects. Validation against six API X80 datasets at T from -97 ℃ to -20℃ showed strong agreement between experimental and simulation results for load-displacement curves and fracture surfaces.

E.Polatidis et al. [101] investigated the effect of σ^* on deformation-induced martensite in low-alloyed Q&P TRIP Bainitic Ferrite (TBF) steel using in situ neutron diffraction under multiaxial loading. Transformation behavior varied with loading conditions, showing similar martensite formation in uniaxial and equibiaxial tension but significantly less in tension/compression. A kinetic model incorporating stress state, austenite stability, and particle size was used to describe the transformation process. Findings indicate that stress triaxiality alone does not fully explain transformation kinetics, as nucleation sites depend on the stress state.

In Ganjiani and Homayounfard et al. [102] extended an anisotropic failure model to predict ductile fracture, incorporating stress triaxiality and Lode angle effects. Using Hill's 48 yield function, they developed a failure locus and Fracture Forming Limit Diagram (FFLD) for validation. Implemented in Abaqus/Standard via UMAT, simulations assessed proportional and non-proportional loading effects. Results showed strong agreement with experimental data, demonstrating the model's accuracy in predicting ductile failure, particularly for anisotropic materials.

V.Bratov [103] briefly reviews progress in numerical simulations of dynamic crack propagation and fracture of initially intact media and presents examples of simulations utilizing finite element method with embedded dynamic fracture criterion based on the concept of incubation time of brittle fracture introduced by Petrov and Morozov. The examples include dynamic fracture initiation, propagation arrest, and evolution of fracture zones in initially intact media. It is demonstrated that this approach is capable to give an accurate description of all the variety of phenomena associated with dynamic fracture. An important feature of the approach, distinguishing it from the majority of other dynamic fracture criteria is the necessity to introduce but one additional material parameter, easily evaluated experimentally, in order to predict dynamic fracture.

Sha Li et al. [104] extended the quasi-static Material Point Method (MPM) to simulate crack behavior, overcoming meshing challenges and allowing arbitrary crack growth modeling. Stress intensity factors were accurately determined using the interaction integral method and validated with a cracked plate under uniaxial tension. Crack propagation was predicted using the maximum circumferential stress criterion and applied to a compact tension test on clay. The study highlights this method as an effective approach for modeling soil crack behavior beyond small deformations.

Alfonso F.Canteli et al. [105] proposed a phenomenological approach using stochastic processes to model cumulative damage leading to failure. By normalizing damage evolution to cumulative distribution functions (cdfs) of the generalized extreme value (GEV) family, they enabled full damage process reconstruction from partial test data. This method allows extrapolation beyond

experimental limits, aiding failure prediction in fatigue and fracture studies. The approach demonstrated strong model fitting, physical parameter interpretation, and potential applications in probabilistic damage analysis.

J.M.Robles et al. [106] analyzed fatigue crack growth in Al 2024 alloy using the Christopher-James-Patterson (CJP) model. This model accurately characterizes crack tip displacements, stress fields, and plastic zone formation. Integrated with Digital Image Correlation (DIC), it incorporates real-time experimental data and correlates results with Paris law through SEM fracture surface analysis. The study examines crack length and load effects, validating findings with fatigue crack growth rate measurements.

In 2021 Y.Xiong et al. [107] studied the surface roughness, residual stress, and fatigue life of machined in-situ TiB_2/7050Al metal matrix composites. Their analysis showed that three-dimensional roughness better represents the machined surface profile. Cutting temperature significantly influenced residual stress, while increased cutting force slowed the transition from compressive to tensile stress below 270 °C. An exponential relationship between roughness and fatigue life was identified, with brittle fracture characterized by shellfish veins, river patterns, and wave-shaped features.

In 2021 W.Macek et al. [108] analyzed the impact of multiaxial loading on the fracture surface of S355J2 steel under non-proportional bending and torsion. Using a high-resolution optical 3D profilometer, they measured surface roughness and fractal dimension to quantify fracture characteristics. Their study examined shear stress effects, loading conditions, and fatigue life influences, demonstrating the value of advanced topography analysis for fracture evaluation and material assessment.

In 2021 S.Khare et al. [109] studied the deformation behavior of armor steel under high strain and large deformations. The J-C flow stress and failure models were used to predict material behavior, with parameters determined from experiments across strain rates (10^{-4}–1550 s^{-1}) and temperatures (25–600°C). Finite element simulations on notched specimens (2–20 mm radii) showed strong agreement with experimental load-strain curves, and triaxiality values matched those reported in the literature.

In 2021 M.A. Moretti et al.[110] investigated the deformation and recrystallization of alloy 718 in annealed and aged states using Split-Hopkinson pressure bar tests at high $\dot{\varepsilon}$ (1000–3000 s^{-1}) and T from 20°C to 1100°C. Optical microscopy and EBSD analysis revealed that flow stress decreased with higher temperatures and lower strain rates. The aged material exhibited greater strength, with a 200 MPa higher yield strength than the annealed state. Dynamic and meta-dynamic

recrystallization occurred at 1000–1100°C, with discontinuous recrystallization as the dominant mechanism, leading to finer microstructures at higher temperatures.

In 2021 W.Wang et al.[111] developed a mathematical model to evaluate impact energy based on Charpy V-notch specimen response. By analyzing geometry, material properties, and impact energy, they established quadratic and linear relationships for ligament length and thickness, respectively. Experimental validation confirmed the model's accuracy, enabling impact resistance assessment for structures of varying specimen sizes.

In 2021 H.Kosuge et al. [112] studied the impact of cyclic pre-strain on the toughness of ferrite/pearlite two-phase microstructures to improve damage resistance in steel structures exposed to natural disasters. Using strain gradient plasticity (SGP) theory and conventional damage analysis, they identified variations in material damage across different microstructures. A parametric study provided insights for designing steels with reduced brittle fracture risk, leading to the development of stronger, more damage-resistant materials.

In 2021 C.Wang et al. [113] proposed a methodology for using Charpy impact tests to measure fracture toughness and determine reference temperature in low-alloy ferritic steels for reactor pressure vessels. Based on ASTM E1820 and E1921 standards, the method analyzes fracture behavior, load-time curves, and specimen parameters to directly calculate fracture toughness using linear elastic fracture mechanics. Corrections for loading rate and specimen differences improved accuracy, aligning results with compact tension tests. This approach aids in assessing reactor vessel integrity and lifespan in nuclear power plants.

In 2022 K.R.Limmer et al. [114] proposed a shift in ultrahigh-strength steel design, focusing on preventing shear localization rather than enhancing global formability. Their study aimed to: (1) identify mechanisms that resist shear-dominated failure in ballistic impacts, (2) demonstrate crack mitigation strategies in multiphase armor steels, and (3) establish a framework for future armor-steel development through computational and experimental analysis under extreme loading conditions.To accomplish these objectives, they designed a microstructure that will activate mechanisms to locally short-circuit catastrophic failure during ballistic impact: TWIP will activate to suppress the propagation of shear localization bands and TRIP will activate to blunt fast-propagating crack tips. Shear localization will further be affected by the design of dispersion-strengthening agents through the tailoring of morphology, distribution, and interface strength of secondary and tertiary phases.

In 2022 T.C.Moleko et al. [115] presents fractographic and microstructural analysis of as-built and stress relieved DMLS Ti6Al4V (ELI) plates with thicknesses of 8 mm, 10 mm, 12 mm, and 14

mm, impacted by high velocity projectiles. Fractography was performed through scanning electron microscopy on the surfaces of the projectile holes, while microstructural analysis of specimens extracted from the plates close to and far from the projectile holes was conducted by way of optical microscopy. Fractography revealed brittle behavior at the entry points of the penetration holes and ductile behavior at the exit points of the penetration holes. Micro- structural analysis revealed microstructural changes in the alloy and a gradual increase of the β-phase fraction toward the edge of the projectile holes through all the plate thicknesses.

In 2022 W.Zhu et al. [116] This paper presents fractographic and microstructural analysis of as-built and stress relieved DMLS Ti6Al4V (ELI) plates with thicknesses of 8 mm, 10 mm, 12 mm, and 14 mm, impacted by high velocity projectiles. Fractography was performed through scanning electron microscopy on the surfaces of projectile holes, while microstructural analysis of specimens extracted from plates close to and far from the projectile holes was conducted by way of optical microscopy. Fractography revealed brittle behavior at the entry points of the penetration holes and ductile behavior at the exit points of the penetration holes. Micro- structural analysis revealed microstructural changes in the alloy and a gradual increase of the β-phase fraction toward the edge of the projectile holes through all the plate thicknesses.

In 2023 Xue Yin et al. [117] investigated the impact toughness of TiVTaNb high-entropy alloy, highlighting the benefits of Nb addition. Compared to TiVTa, TiVTaNb showed a 67.3% increase in crack initiation energy and a 24.9% rise in propagation energy, enhancing crack resistance. Improved impact toughness was attributed to deeper dimples, more secondary cracks, and greater shear lip bending. While TiVTa deformation was mainly dislocation-driven, TiVTaNb exhibited both dislocation activities and deformation twinning, contributing to superior energy dissipation and impact resistance.

In 2023 Jungwan et al. [118] investigated impact toughness at ambient and cryogenic temperatures with systematic fracture analyses for CuFeMn and Al15(CuFeMn)85 immiscible medium-entropy alloys. These two types of alloys exhibited different impact toughness behavior at different temperatures, while exhibiting higher impact toughness values than those of dual-phase steels with a similar strength level.

In 2023 L. Zhang et al. [119] examined the impact toughness of Ti–5Al–1V–1Sn–1Zr-0.8Mo alloy, highlighting its decline with decreasing temperature under Charpy impact conditions, despite increased strength and elongation in tensile tests. Their findings suggest that strengthening strategies effective under quasi-static tensile deformation may not translate to impact toughness improvements. The study analyzed surface deformation morphologies to explain this discrepancy and established corresponding deformation mechanisms.

In 2023 Yimian Chen et al. [120] developed machine learning models to predict Charpy impact toughness (CIT) in low-alloy steel. Three feature construction strategies were evaluated: alloy composition alone, composition with heat treatment, and composition with heat treatment and physical properties. The third approach provided the most accurate predictions. A genetic programming-based symbolic regression model was then formulated to derive a meaningful relationship between key material properties and CIT, improving toughness estimation for engineering applications.

In 2023 Zhao Zhang et al. [121] conducted finite element simulations to examine the impact of σ^* cut-off values on the ballistic behavior of Al2024-T351 plates struck by projectiles with different nose shapes. Using a modified J-C model and DF2021 criterion in ABAQUS/Explicit, they varied the σ^* cut-off parameter and analyzed ballistic limit velocities, residual velocities, and failure patterns. Results showed that the ballistic limit velocity increased for blunt projectiles but varied for hemispherical and ogival shapes. DF2021 with a 0.1 cut-off parameter best matched experimental data, highlighting the significance of stress triaxiality in fracture predictions.

In 2023 Zhen Zhang et al. [122] investigated the temperature-dependent ductile-brittle transition (DBT) in low-carbon martensitic steel under various stress states. Tensile and three-point bending tests were conducted over a temperature range of 77 K to 423 K at different loading rates. Results showed that ductile-brittle transition temperature (DBTT) is significantly influenced by stress triaxiality, with uniaxial tension having a ~142 K lower DBTT than plane strain conditions. Dynamic strain aging reduced ductile resistance at temperatures above 323 K. Tensile strength and ductility increased as temperature decreased, altering failure modes. A new parameter was introduced for toughness estimation in tensile tests.

In 2023 Yimian Chen et al. [123] examined the impact behavior of Ti-5Al-7.5V-0.5Si-0.25Fe-0.2O (Ti575) alloy with trimodal (TM) and lamellar (LM) microstructures using Charpy U-notch tests and microstructural analysis. LM exhibited superior impact toughness (47.8 J/cm^2) compared to TM (38 J/cm^2), attributed to enhanced intrinsic and extrinsic toughening mechanisms. EBSD analysis showed that LM promoted tensile twin formation, improving crack resistance, while TM's smaller α phases led to stress concentration and reduced plasticity. Crack propagation in LM followed a tortuous path, dissipating more energy, whereas TM allowed easier crack growth, resulting in lower toughness.

In 2023 Nariman et al. [124] studied duplex stainless steels for use in corrosive and low-temperature environments, such as steel bridges, where brittle fracture must be avoided. As part of the German FOSTA project "P 1390," they conducted Charpy-V and fracture toughness tests to establish toughness requirements for new duplex steel grades. Their research assessed the Master

Curve concept and transition temperature correlations, providing insights into fracture resistance and material selection for structural applications.

Jinhua Dai et al. [125] examined the impact behavior of Ti-5Al-7.5V-0.5Si-0.25Fe-0.2O (Ti575) alloy with trimodal (TM) and lamellar (LM) microstructures using Charpy U-notch tests and microstructural analysis. LM exhibited higher impact toughness (47.8 J/cm²) than TM (38 J/cm²), attributed to enhanced intrinsic and extrinsic toughening. EBSD revealed that LM promoted tensile twin nucleation, aiding crack resistance, while TM's smaller α phases led to stress concentration and reduced plasticity. Crack propagation in LM followed a tortuous path, dissipating energy, whereas TM facilitated easier crack growth. These findings improve understanding of Ti575's fracture mechanisms.

Peng Gao et al. [126] studied the repeated impact behavior of TC18 titanium alloy, widely used in aerospace structures. Drop hammer impact tests and microscopic analysis revealed that impact fatigue life (N_f) decreases exponentially with impact energy. Cracks initiate at 40–50% of N_f, propagate steadily until 90%, and rapidly lead to failure in the final stage. Repeated impacts induce complex stress states, grain refinement, phase transitions, and texture strengthening. These findings enhance understanding of TC18's damage mechanisms and contribute to developing a life prediction model.

In 2024 Hongbo Liu. et al. [127] investigated the impact toughness of Q235 steel and its butt-welded joints under low temperatures and corrosion. Using accelerated salt spray corrosion and Charpy impact tests, they analyzed fracture behavior through SEM imaging. Results showed a significant reduction in impact energy as temperature dropped and corrosion progressed, with the combined effect exacerbating material degradation. These findings contribute to the fracture-resistant design of steel structures in harsh offshore environments.

This literature review synthesizes decades of research to conclude that the resistance of armour plates to deformable projectiles is a complex, multi-factorial problem governed by the intricate interplay between material properties, projectile characteristics, and loading conditions. A key outcome is that no single material property determines performance; instead, ballistic resistance is a systems-level property that depends on accurately modeling the material's dynamic behavior under extreme strain rates and temperatures using advanced constitutive models (e.g., Johnson-Cook, Zerilli-Armstrong, Rusinek-Klepaczko), which must be carefully selected based on the material's atomic structure. Furthermore, the review establishes that failure mechanisms—whether adiabatic shear banding, ductile fracture, or plugging—are highly sensitive to projectile nose shape and target thickness, with blunt projectiles often excelling at lower velocities while conical shapes are more efficient at higher speeds. Critically, the synthesis underscores that reliable prediction

requires sophisticated numerical simulations mitigated against mesh dependency by adaptive techniques, all of which must be rigorously validated by experimental data from high-strain-rate tests and microstructural analysis, highlighting a continued evolution towards integrated computational and experimental methodologies for future armour design.

1.4 Motivation of thesis work

The study of typical Rolled Homogeneous Armor (RHA) and PHS 1500 steel material under high loading rates is of significant importance for the defence industry. However, the availability of experimental data and numerical simulation methodologies for these steels under such conditions is limited. Various material models have been developed in the past, including phenomenological, semi-physical, and purely physical models. While these models exhibit different levels of computational efficiency across different materials, none have been able to fully capture the material response of RHA and PS 1500 steel, particularly at high strain rates.

The primary objectives of this research are to develop a reliable material model for these steels at high loading rates and to validate it with experimental data obtained from cost-effective, yet reliable, high-rate tensile tests. Furthermore, this material model will be utilized to investigate the ballistic impact response of the armour steel under study at ordnance velocities. Additionally, the influence of fracture toughness parameters, particularly K_{ID}, will be examined to assess the effect of pre-existing cracks in the plate on the ballistic performance index.

1.5 Objective of present work

a. Development of a Reliable Material Model for high strain rate
- Formulate an effective and accurate material model for the RHA and PHS 1500 steel materials, capable of capturing their behaviours under high loading rates.
- Ensure simulation efficiency while maintaining accuracy across different strain-rate regimes.

b. Experimental Validation
- Conduct high loading rate and high temperature tensile tests on the armour and PHS 1500 steel.
- Conduct tensile tests at high strain-rate in a drop weight impact machine.
- Extraction of material model parameters from tensile tests data.
- Validate the developed material model and model parameters with experimental data to ensure reliability of those over a wide range of $\dot{\varepsilon}$.

c. Application of material model for simulation of Charpy impact tests and validation.

- Simulation of Charpy impact tests at various impact velocities using material models developed through tensile tests.
- Conduct experiment of Charpy impact tests with varied impact velocities in a drop weight impact machine and validation of simulated results.

d. Ballistic Impact Investigation
- Utilize the validated material model to study the ballistic impact response of the armour steel plate at ordnance velocities by using rigid and deformable projectile made from PHS 1500 steel.
- Analyze the effect of $\dot{\varepsilon}$ - dependent material properties on impact resistance.
- Study the effect of different nose shape on failure pattern of the target plate.
- Study the effect of microstructure on ballistic resistance and optimisation of heat treatment protocol.

e. Use of Fracture Toughness in simulation and assessment of Crack Influence on ballistic performance.
- Investigate the role of fracture toughness parameter (K_{ID}) in ballistic performance.
- Determination of fracture toughness (K_{IC}), (J_{IC}) and (K_{ID}) at varying loading rate.
- Simulation of ballistic resistance of armour plate having prescribed cracks within it.
- Assess the effect of pre-existing cracks on the ballistic performance index of the armour plates.

This research aims to enhance the understanding of high $\dot{\varepsilon}$ behaviour in RHA and PHS 1500 steel, contributing to improved material modelling and ballistic impact protection performance prediction.

1.6 Significance of the study

Understanding the impact and fracture mechanics of armour steels is crucial for several reasons:

a. Material test data: A bunch of material test data will be available at high T and various $\dot{\varepsilon}$ for two types of steels.

b. Building effective material model: Effective material model will capture the thermoviscoplastic response from quasi-static to high-strain rates and at high temperatures also.

c. Cost effective material testing: Because of the costly setup of intermediate to high $\dot{\varepsilon}$ tests, it is necessary to build and calibrate intermediate to high $\dot{\varepsilon}$ test facility.

d. Ballistic performance: By studying how armour steels behave under high-strain-rate impacts, researchers can enhance their ability to withstand various threats scenarios.

e. Informing material selection: Selection of proper armour material based on proper heat treatment schedule by changing its microstructure.

f. Understanding failure pattern: Understanding failure pattern of the target plate help in understanding the lethality of the projectile.

g. Effect of cracks inside the plate: Understanding fracture mechanics helps in predicting failure modes, allowing for the design of armour systems that maintain integrity under extreme conditions, thereby preventing catastrophic failures.

1.7 Research Methodology

The research methodology consists of a systematic approach to understanding the high $\dot{\varepsilon}$ behaviour of RHA and PS 1500 steel through experimental testing, material modelling, and numerical simulations. The key steps involved in this study are as follows:

a. Literature review and gap identification

- Conduct a comprehensive review of previous studies on RHA and PHS 1500 steel under high loading rates.
- Identify gaps in existing literature, particularly in material modelling and high strain-rate material characterization.

b. Micro-Hardness testing

- Perform micro-hardness tests on RHA and PHS 1500 steel to assess their mechanical properties and hardness distribution.

c. Tensile testing at different $\dot{\varepsilon}$ and different T

- Conduct quasi-static tensile tests on as-received RHA and PS 1500 steel at $\dot{\varepsilon}$ ranging from 10^{-4} to 10^{-1} s^{-1}.
- Perform intermediate $\dot{\varepsilon}$ tensile tests on RHA steel within the range of 0.1 to 744 s^{-1}.
- Perform low cost intermediate strain-rate test on drop weight impact testing machine INSTRON CEAST 9350. This includes staring from building the material geometry till the validation of test data at same strain-rate in another test system INSTRON VHS with DIC.
- Due to the high hardness of PS 1500 steel, conduct tensile tests only up to a $\dot{\varepsilon}$ of 0.2 s^{-1}.
- Perform high temperature test from 27^{o}C to 500^{o}C at different $\dot{\varepsilon}$ ranging from 10^{-4} to 10^{-1} s^{-1} for the armour steel.
- Perform high temperature test from 27^{o}C to 500^{o}C at $\dot{\varepsilon}$ 10^{-4} for PHS 1500 steel.

d. Material model parameter extraction

- Extract parameters for the J-C and R-K material models to characterize the tensile behaviour of RHA steel.
- Apply only the J-C material model for PHS 1500 steel due to its material characteristics.

e. Validation of material models

- Compare the numerical simulation results obtained from the material models with experimental tensile test data to evaluate accuracy and reliability.

f. Development of a modified material model

- Identify limitations in the J-C material model and propose necessary modifications.
- Develop a new material model, referred to as the **Modified Johnson-Cook (MJ-C) model**, to improve predictive accuracy.

g. Simulation of Charpy impact test

- Perform numerical simulations of the Charpy V-notch impact test using three different material models.
- Incorporate the Johnson-Cook failure model to analyze material behaviour under impact loading.

h. Experimental validation of Charpy impact tests.

i. Numerical simulation of ballistic impact

- Simulate ballistic impact tests using three material models along with the Johnson-Cook failure model.
- Evaluate the predictive capabilities of each model in capturing the ballistic response.
- Validation of simulation results by data from experimental ballistic impact of armour steel plate by projectile made from PHS 1500 material.
- Simulate ballistic impact tests using different nose shape projectiles using most effective material model.
- Simulation ballistic impact test of the armour steel plate with different microstructure.

j. Fracture toughness testing and implementation in simulation

- Perform fracture toughness tests to determine K_{IC}, J_{IC}, and K_{ID} for the armour steel under study.
- Incorporate the K_{ID} parameter into the numerical simulation to assess its influence on the ballistic performance of armour steel.

1.8 Overview

A new material model was proposed to predict the thermoviscoplastic behavior of rolled homogenous armor steel (martensitic steel). The proposed model was successfully verified. The effect of fracture toughness on the performance of armor plates was thoroughly validated. Additionally, the influence of the dynamic friction coefficient on ballistic resistance was successfully demonstrated.

The thesis work included experimentation and simulation. The experiments included tensile tests from quasi-static to high $\dot{\varepsilon}$ from room (27^{o}C) to elevated temperature ($600\,^{o}$C), Fracture toughness testing (K_{IC}, J_{IC} and K_{ID}), instrumental Charpy V-notch impact testing, Tensile test of notch specimen, Heat treatment, Microstructural analysis (Fractography).

Finite element simulations were conducted using ABAQUS CAE Standard/Explicit software, with model development performed in SolidWorks design software. Programming languages such as Fortran and Python. Custom material and interaction subroutines, including UMAT and VUMAT, were developed to enhance the simulation capabilities. The research objectives were successfully achieved, resulting in two international journal publications and one international conference presentation.

Additionally, a method was developed for conducting intermediate to high $\dot{\varepsilon}$ tensile tests using a drop-weight impact testing machine, encompassing the entire process from modeling to result extraction. The results were successfully validated against tensile test data at comparable $\dot{\varepsilon}$ obtained from other testing machines, such as the Split Hopkinson Bar (SHB) and VHS 65/80. This method offers significant advantages by reducing testing costs and material consumption.

References

[1] G.R. Johnson, W.H. Cook, Fracture characteristics of three metals subjected to various strains, strain rates, temperatures and pressures, Eng. Fract. Mech. 21 (1985) 31–48. https://doi.org/10.1016/0013-7944(85)90052-9.

[2] T. Borvik, O.S. Hopperstad, T. Berstad, M. Langseth, Perforation of 12mm thick steel plates by 20mm diameter projectiles with flat, hemispherical and conical noses - Part II: Numerical simulations, Int. J. Impact Eng. 27 (2001) 37–64. https://doi.org/10.1016/S0734-743X(01)00035-5.

[3] G.T. Camacho, M. Ortiz, Adaptive Lagrangian modelling of ballistic penetration of metallic targets, Comput. Methods Appl. Mech. Eng. 142 (1997) 269–301. https://doi.org/10.1016/S0045-7825(96)01134-6.

[4] H. Nahme, E. Lach, H. Nahme, E.L. Dynamic, H. Strength, A. Steels, J. De Physique, Dynamic Behavior of High Strength Armor Steels To cite this version : HAL Id : jpa-

00255522, 07 (1997).
[5] W.R. Whittington, A.L. Oppedal, S. Turnage, Y. Hammi, H. Rhee, P.G. Allison, C.K. Crane, M.F. Horstemeyer, Capturing the effect of temperature, strain rate, and stress state on the plasticity and fracture of rolled homogeneous armor (RHA) steel, Mater. Sci. Eng. A 594 (2014) 82–88. https://doi.org/10.1016/j.msea.2013.11.018.
[6] B.B. Singh, G. Sukumar, A. Paman, G. Balaji, K. Siva Kumar, V. Madhu, R. Arockia Kumar, A Comparative Study on the Ballistic Performance and Failure Mechanisms of High-Nitrogen Steel and RHA Steel Against Tungsten Heavy Alloy Penetrators, J. Dyn. Behav. Mater. 7 (2021) 60–80. https://doi.org/10.1007/s40870-020-00270-8.
[7] B. Zhang, X. Shang, S. Yao, Q. Wang, Z. Zhang, X. Yang, J. Cai, K. Wang, A Comparative Study on Johnson-Cook, Modified Johnson-Cook, Modified Zerilli-Armstrong and Arrhenius-Type Constitutive Models to Predict Hot Deformation Behavior of TA2, High Temp. Mater. Process. 38 (2019) 699–714. https://doi.org/10.1515/htmp-2019-0026.
[8] R. Bobbili, V. Madhu, Constitutive Modeling of Hot Deformation Behavior of High-Strength Armor Steel, J. Mater. Eng. Perform. 25 (2016) 1829–1838. https://doi.org/10.1007/s11665-016-2001-z.
[9] S.C. Woo, J.T. Kim, J.Y. Kim, T.W. Kim, Correlation of fracture processes and damage mechanisms of armor structural materials under high strain rates with acoustic emission characteristics, Int. J. Impact Eng. 63 (2014) 29–42. https://doi.org/10.1016/j.ijimpeng.2013.07.007.
[10] N.A. Fellows, J. Harding, Localization of plastic deformation during high strain rate torsion testing of rolled homogeneous armour, J. Strain Anal. Eng. Des. 36 (2001) 197–210. https://doi.org/10.1243/0309324011512748.
[11] L.S. Magness, High strain rate deformation behaviors of kinetic energy penetrator materials during ballistic impact, Mech. Mater. 17 (1994) 147–154. https://doi.org/10.1016/0167-6636(94)90055-8.
[12] G.R. Johnson, W.H. Cook, A Computational Constitutive Model and Data for Metals Subjected to Large Strain, High Strain Rates and High Pressures, 1983.
[13] F.J. Zerilli, R.W. Armstrong, Dislocation-mechanics-based constitutive relations for material dynamics calculations, J. Appl. Phys. 61 (1987) 1816–1825. https://doi.org/10.1063/1.338024.
[14] T. Børvik, M. Langseth, O.S. Hopperstad, K.A. Malo, Ballistic penetration of steel plates, 1999. https://doi.org/10.1016/S0734-743X(99)00011-1.
[15] A.S. Khan, R. Liang, Behaviors of three BCC metal over a wide range of strain rates and temperatures: Experiments and modeling, Int. J. Plast. 15 (1999) 1089–1109. https://doi.org/10.1016/S0749-6419(99)00030-3.
[16] J.A. Zukas, D.R. Scheffler, Practical aspects of numerical simulations of dynamic events: Effects of meshing, Int. J. Impact Eng. 24 (2000) 925–945. https://doi.org/10.1016/S0734-743X(00)00012-9.
[17] T. Borvik, O.S. Hopperstad, T. Berstad, M. Langseth, Perforation of 12mm thick steel plates by 20mm diameter projectiles with flat, hemispherical and conical noses Part I:

Experimental study, Int. J. Impact Eng. 27 (2002) 19–35. https://doi.org/https://doi.org/10.1016/S0734-743X(01)00034-3.
[18] A. Rusinek, J.R. Klepaczko, Shear testing of a sheet steel at wide range of strain rates and a constitutive relation with strain-rate and temperature dependence of the flow stress, Int. J. Plast. 17 (2001) 87–115. https://doi.org/10.1016/S0749-6419(00)00020-6.
[19] C.J. Hu, P.Y. Lee, J.S. Chen, Ballistic performance and microstructure of modified rolled homogeneous armor steel, J. Chinese Inst. Eng. Trans. Chinese Inst. Eng. Ser. A/Chung-Kuo K. Ch'eng Hsuch K'an 25 (2002) 99–107. https://doi.org/10.1080/02533839.2002.9670684.
[20] V. Tvergaard, J.W. Hutchinson, Two mechanisms of ductile fracture: Void by void growth versus multiple void interaction, Int. J. Solids Struct. 39 (2002) 3581–3597. https://doi.org/10.1016/S0020-7683(02)00168-3.
[21] N. Peixinho, N. Jones, A. Pinho, Experimental and numerical study in axial crushing of thin walled sections made of high-strength steels, J. Phys. IV JP 110 (2003) 717–722. https://doi.org/10.1051/jp4:20020778.
[22] D.M. Bruce, D.K. Matlock, J.G. Speer, A.K. De, Assessment of the strain-rate dependent tensile properties of automotive sheet steels, SAE Tech. Pap. (2004). https://doi.org/10.4271/2004-01-0507.
[23] A.S. Khan, Y.S. Suh, R. Kazmi, Quasi-static and dynamic loading responses and constitutive modeling of titanium alloys, Int. J. Plast. 20 (2004) 2233–2248. https://doi.org/10.1016/j.ijplas.2003.06.005.
[24] J.S. Montgomery, M.G.H. Wells, Titanium armor applications in combat vehicles, Jom 53 (2001) 29–32. https://doi.org/10.1007/s11837-001-0144-2.
[25] A. Molinari, T.W. Wright, A physical model for nucleation and early growth of voids in ductile materials under dynamic loading, J. Mech. Phys. Solids 53 (2005) 1476–1504. https://doi.org/10.1016/j.jmps.2005.02.010.
[26] P.K.C. Wood, C. a Schley, R. Beaumont, M. a Williams, M. a Buckley, A new strain rate dependent spot weld model for automotive crash applications, (2009) 1–14. http://strathprints.strath.ac.uk/30723/.
[27] P.K.C. Wood, C.A. Schley, M.A. Williams, R. Beaumont, A. Pearce, Progress in high rate tensile testing towards 1000 s -1 on a servo- hydraulic machine, (2009).
[28] P.K.C. Wood, C.A. Schley, M. Williams, R. Beaumont, A. Rusinek, U. Mayer, A. Pearce, A method to calibrate a specimen with strain gauges to measure force over the full-force range in high rate testing, (2009) 265–273. https://doi.org/10.1051/dymat/2009036.
[29] P.K.C. Wood, C.A. Schley, M. Buckley, A new test procedure to validate dynamic tensile mechanical properties of sheet metals and alloys for automotive crash applications, SAE Tech. Pap. 2008-Septe (2008). https://doi.org/10.4271/2008-28-0019.
[30] P.K.C. Wood, C.A. Schley, Strain Rate Testing of Metallic Materials and Their Modelling for Use in CAE Based Automotive Crash Simulation Tools (Recommendations and Procedures), 2009. http://scholar.google.com/scholar?hl=en&btnG=Search&q=intitle:Strain+Rate+Testing+o

f+Metallic+Materials+and+their+Modelling+for+use+in+CAE+based+Automotive+Crash+Simulation+Tools+(Recommendations+and+procedures)#0.
[31] P.K.C. Wood, C. a Schley, R. Beaumont, B. Walker, T. Dutton, M. a Buckley, Modelling and predicting spotweld failures in automotive crash structures, Simulation (2009).
[32] P.K.C. Wood, C.A. Schley, R. Beaumont, M.A. Williams, M.A. Buckley, Improved efficiency and quality control in the manufacture and preparation metallic specimens for high rate tensile testing, (2014) 5–10.
[33] P.K.C. Wood, C.A. Schley, I. McGregor, T. Dutton, M. Bloomfield, R. Bardenheier, Characterising performance of automotive materials at high strain rate for improved crash design, J. Phys. IV JP 134 (2006) 1167–1174. https://doi.org/10.1051/jp4:2006134178.
[34] P.K.C. Wood, C.A. Schley, M. Buckley, L. Rover, B. Walker, F. Iarc, VALIDATING DYNAMIC TENSILE MECHANICAL PROPERTIES OF SHEET STEELS FOR AUTOMOTIVE CRASH APPLICATIONS AUTHORS : T . Dutton , Dutton Simulation CORRESPONDENCE : Dr . Paul Wood ABSTRACT KEYWORDS :, (2013) 33–46.
[35] B. Yan, Y. Kuriyama, A. Uenishi, D. Cornette, M. Borsutzki, C. Wong, Recommended practice for dynamic testing for sheet steels - Development and round robin tests, SAE Tech. Pap. 115 (2006) 147–157. https://doi.org/10.4271/2006-01-0120.
[36] R. Bardenheier, G. Rogers, Dynamic impact testing with servohydraulic testing machines, J. Phys. IV JP 134 (2006) 693–699. https://doi.org/10.1051/jp4:2006134107.
[37] R.F.R. and T.W. Ipson, Ballistic Perforation Dynamics, J. Appl. Mech. 30 (1963) 384–391.
[38] T.W. Ipson, R.F. Recht, Ballistic-penetration resistance and its measurement, Exp. Mech. 15 (1975) 249–257. https://doi.org/10.1007/bf02318057.
[39] A.L. Wingrove, The influence of projectile geometry on adiabatic shear and target failure, Metall. Trans. 4 (1973) 1829–1833. https://doi.org/10.1007/BF02665409.
[40] S.S. Santoshi OHTE, Hiroyasu YOSHIZAWA, Norimasa CHIBA, Impact strength of steel plates struck by projectiles, Bull. JSME 25 (1982) 2278–2281.
[41] N.K. Gupta, M.A. Iqbal, G.S. Sekhon, Effect of projectile nose shape, impact velocity and target thickness on deformation behavior of aluminum plates, Int. J. Solids Struct. 44 (2007) 3411–3439. https://doi.org/10.1016/j.ijsolstr.2006.09.034.
[42] A. Rusinek, R. Zaera, J.R. Klepaczko, Constitutive relations in 3-D for a wide range of strain rates and temperatures - Application to mild steels, Int. J. Solids Struct. 44 (2007) 5611–5634. https://doi.org/10.1016/j.ijsolstr.2007.01.015.
[43] K. Maweja, W. Stumpf, The design of advanced performance high strength low-carbon martensitic armour steels. Part 1. Mechanical property considerations, Mater. Sci. Eng. A 485 (2008) 140–153. https://doi.org/10.1016/j.msea.2007.08.048.
[44] A. Arias, J.A. Rodríguez-Martínez, A. Rusinek, Numerical simulations of impact behaviour of thin steel plates subjected to cylindrical, conical and hemispherical non-deformable projectiles, Eng. Fract. Mech. 75 (2008) 1635–1656. https://doi.org/10.1016/j.engfracmech.2007.06.005.
[45] H. Huh, J.H. Lim, S.H. Park, High speed tensile test of steel sheets for the stress-strain curve at the intermediate strain rate, Int. J. Automot. Technol. 10 (2009) 195–204.

https://doi.org/10.1007/s12239-009-0023-3.
[46] A. Rusinek, J.A. Rodríguez-Martínez, R. Zaera, J.R. Klepaczko, A. Arias, C. Sauvelet, Experimental and numerical study on the perforation process of mild steel sheets subjected to perpendicular impact by hemispherical projectiles, Int. J. Impact Eng. 36 (2009) 565–587. https://doi.org/10.1016/j.ijimpeng.2008.09.004.
[47] J.R. Klepaczko, A. Rusinek, J.A. Rodríguez-Martínez, R.B. Pecherski, A. Arias, Modelling of thermo-viscoplastic behaviour of DH-36 and Weldox 460-E structural steels at wide ranges of strain rates and temperatures, comparison of constitutive relations for impact problems, Mech. Mater. 41 (2009) 599–621. https://doi.org/10.1016/j.mechmat.2008.11.004.
[48] P.K. Jena, B. Mishra, M. RameshBabu, A. Babu, A.K. Singh, K. SivaKumar, T.B. Bhat, Effect of heat treatment on mechanical and ballistic properties of a high strength armour steel, Int. J. Impact Eng. 37 (2010) 242–249. https://doi.org/10.1016/j.ijimpeng.2009.09.003.
[49] B. Babaei, M.M. Shokrieh, K. Daneshjou, The ballistic resistance of multi-layered targets impacted by rigid projectiles, Mater. Sci. Eng. A 530 (2011) 208–217. https://doi.org/10.1016/j.msea.2011.09.076.
[50] F. Abed, F. Makarem, Comparisons of constitutive models for steel over a wide range of temperatures and strain rates, J. Eng. Mater. Technol. 134 (2012) 1–10. https://doi.org/10.1115/1.4006171.
[51] Z. Xu, F. Huang, Comparison of physically based constitutive models characterizing armor steel over wide temperature and strain rate ranges, Model. Simul. Mater. Sci. Eng. 20 (2012). https://doi.org/10.1088/0965-0393/20/1/015005.
[52] T. Jankowiak, A. Rusinek, P. Wood, A numerical analysis of the dynamic behaviour of sheet steel perforated by a conical projectile under ballistic conditions, Finite Elem. Anal. Des. 65 (2013) 39–49. https://doi.org/10.1016/j.finel.2012.10.007.
[53] J.K. Holmen, J. Johnsen, S. Jupp, O.S. Hopperstad, T. Børvik, Effects of heat treatment on the ballistic properties of AA6070 aluminium alloy, Int. J. Impact Eng. 57 (2013) 119–133. https://doi.org/10.1016/j.ijimpeng.2013.02.002.
[54] Q. Yin, B. Zillmann, S. Suttner, G. Gerstein, M. Biasutti, A.E. Tekkaya, M.F.X. Wagner, M. Merklein, M. Schaper, T. Halle, A. Brosius, An experimental and numerical investigation of different shear test configurations for sheet metal characterization, Int. J. Solids Struct. 51 (2014) 1066–1074. https://doi.org/10.1016/j.ijsolstr.2013.12.006.
[55] A. He, G. Xie, H. Zhang, X. Wang, A modified Zerilli-Armstrong constitutive model to predict hot deformation behavior of 20CrMo alloy steel, Mater. Des. 56 (2014) 122–127. https://doi.org/10.1016/j.matdes.2013.10.080.
[56] F. Kabirian, A.S. Khan, A. Pandey, Negative to positive strain rate sensitivity in 5xxx series aluminum alloys: Experiment and constitutive modeling, Int. J. Plast. 55 (2014) 232–246. https://doi.org/10.1016/j.ijplas.2013.11.001.
[57] H.B. Motra, J. Hildebrand, A. Dimmig-Osburg, Assessment of strain measurement techniques to characterise mechanical properties of structural steel, Eng. Sci. Technol. an

Int. J. 17 (2014) 260–269. https://doi.org/10.1016/j.jestch.2014.07.006.
[58] A. Molinari, S. Mercier, N. Jacques, Dynamic failure of ductile materials, Procedia IUTAM 10 (2014) 201–220. https://doi.org/10.1016/j.piutam.2014.01.019.
[59] D.E. Tria, R. Trebinski, On the influence of fracture criterion on perforation of high-strength steel plates subjected to armour piercing projectile, Arch. Mech. Eng. 62 (2015) 157–179. https://doi.org/10.1515/meceng-2015-0010.
[60] U. Zerbst, M. Madia, Fracture mechanics based assessment of the fatigue strength: Approach for the determination of the initial crack size, Fatigue Fract. Eng. Mater. Struct. 38 (2015) 1066–1075. https://doi.org/10.1111/ffe.12288.
[61] J. Trajkovski, R. Kunc, V. Pepel, I. Prebil, Flow and fracture behavior of high-strength armor steel PROTAC 500, Mater. Des. 66 (2015) 37–45. https://doi.org/10.1016/j.matdes.2014.10.030.
[62] K.M. Kpenyigba, T. Jankowiak, A. Rusinek, R. Pesci, B. Wang, Effect of projectile nose shape on ballistic resistance of interstitial-free steel sheets, Int. J. Impact Eng. 79 (2015) 83–94. https://doi.org/10.1016/j.ijimpeng.2014.10.007.
[63] A. Banerjee, S. Dhar, S. Acharyya, D. Datta, N. Nayak, Determination of Johnson cook material and failure model constants and numerical modelling of Charpy impact test of armour steel, Mater. Sci. Eng. A 640 (2015) 200–209. https://doi.org/10.1016/j.msea.2015.05.073.
[64] G. Joo, H. Huh, M.K. Choi, Tension/compression hardening behaviors of auto-body steel sheets at intermediate strain rates, Int. J. Mech. Sci. 108–109 (2016) 174–187. https://doi.org/10.1016/j.ijmecsci.2016.01.035.
[65] P.K. Jena, P. Ponguru Senthil, K. Siva Kumar, Effect of tempering time on the ballistic performance of a high strength armour steel, J. Appl. Res. Technol. 14 (2016) 47–53. https://doi.org/10.1016/j.jart.2016.02.002.
[66] J. Wang, W. Guo, J. Guo, Z. Wang, S. Lu, The Effects of Stress Triaxiality, Temperature and Strain Rate on the Fracture Characteristics of a Nickel-Base Superalloy, J. Mater. Eng. Perform. 25 (2016) 2043–2052. https://doi.org/10.1007/s11665-016-2049-9.
[67] H. Kim, J. Park, M. Kang, S. Lee, Interpretation of Charpy impact energy characteristics by microstructural evolution of dynamically compressed specimens in three tempered martensitic steels, Mater. Sci. Eng. A 649 (2016) 57–67. https://doi.org/10.1016/j.msea.2015.09.099.
[68] Z. Nie, G. Wang, J. Yu, D. Liu, Y. (Kevin) Rong, Phase-based constitutive modeling and experimental study for dynamic mechanical behavior of martensitic stainless steel under high strain rate in a thermal cycle, Mech. Mater. 101 (2016) 160–169. https://doi.org/10.1016/j.mechmat.2016.08.003.
[69] S. Wang, Y. Huang, Z. Xiao, Y. Liu, H. Liu, A modified Johnson-cook model for hot deformation behavior of 35CrMo steel, Metals (Basel). 7 (2017) 1–10. https://doi.org/10.3390/met7090337.
[70] D.E. Tria, R. Trębiński, Methodology for experimental verification of steel armour impact modelling, Int. J. Impact Eng. 100 (2017) 102–116.

https://doi.org/10.1016/j.ijimpeng.2016.10.011.
[71] A. Banerjee, S. Dhar, S. Acharyya, D. Datta, N. Nayak, Numerical Simulation of Ballistic Impact of Armour Steel Plate by Typical Armour Piercing Projectile, Procedia Eng. 173 (2017) 347–354. https://doi.org/10.1016/j.proeng.2016.12.028.
[72] B. McDonald, H. Bornstein, G. Langdon, R. Curry, A. Orifici, Deformation and Rupture of Armour Grade Steel under Localised Blast Loading, Procedia Eng. 197 (2017) 13–22. https://doi.org/10.1016/j.proeng.2017.08.077.
[73] M.J. Piao, H. Huh, I. Lee, L. Park, Characterization of hardening behaviors of 4130 Steel, OFHC Copper, Ti6Al4V alloy considering ultra-high strain rates and high temperatures, Int. J. Mech. Sci. 131–132 (2017) 1117–1129. https://doi.org/10.1016/j.ijmecsci.2017.08.013.
[74] W. Wang, Y. Ma, M. Yang, P. Jiang, F. Yuan, X. Wu, Strain rate effect on tensile behavior for a high specific strength steel: From quasi-static to intermediate strain rates, Metals (Basel). 8 (2018). https://doi.org/10.3390/met8010011.
[75] D. Sánchez-Ávila, R. Barea, E. Martínez, J.R. Blasco, L. Portolés, F. Carreño, Determination of the instantaneous strain rate during small punch testing of 316 L stainless steel, Int. J. Mech. Sci. 149 (2018) 93–100. https://doi.org/10.1016/j.ijmecsci.2018.09.042.
[76] B. Liu, C. Guedes Soares, Effect of strain rate on dynamic responses of laterally impacted steel plates, Int. J. Mech. Sci. 160 (2019) 307–317. https://doi.org/10.1016/j.ijmecsci.2019.06.034.
[77] M. Murugesan, D.W. Jung, Johnson cook material and failure model parameters estimation of AISI-1045 medium carbon steel for metal forming applications, Materials (Basel). 12 (2019). https://doi.org/10.3390/ma12040609.
[78] J. Peng, Y. Wang, Q. Dai, X. Liu, L. Liu, Z. Zhang, Effect of stress triaxiality on plastic damage evolution and failure mode for 316L notched specimen, Metals (Basel). 9 (2019). https://doi.org/10.3390/met9101067.
[79] A. Saxena, A. Kumaraswamy, N. Kotkunde, K. Suresh, Constitutive Modeling of High-Temperature Flow Stress of Armor Steel in Ballistic Applications: A Comparative Study, J. Mater. Eng. Perform. 28 (2019) 6505–6513. https://doi.org/10.1007/s11665-019-04337-z.
[80] H.C. Ho, K.F. Chung, X. Liu, M. Xiao, D.A. Nethercot, Modelling tensile tests on high strength S690 steel materials undergoing large deformations, Eng. Struct. 192 (2019) 305–322. https://doi.org/10.1016/j.engstruct.2019.04.057.
[81] S. Paul, P. Dey, S. Bhattacharjee, S.K. Acharyya, P. Sahoo, J. Chattopadhyay, Phenomenological modelling of flow behaviour of 20MnMoNi55 reactor pressure vessel steel at cryogenic temperature with different strain rates, Def. Technol. 15 (2019) 326–337. https://doi.org/10.1016/j.dt.2018.08.007.
[82] T. Fras, N. Faderl, C.C. Roth, D. Mohr, Strikers with different nose shape impacting an armour steel - numerical modelling, 12th Eur. LS-DYNA Conf. (2019).
[83] G. Dilip Chandra Kumar, V. Anil Kumar, R.K. Gupta, S.V.S. Narayana Murty, B.P. Kashyap, Effect of Strain Rate and Temperature on the Tensile Flow Behavior and

Microstructure Evolution in Fe-0.3 Pct C-CrMoV Grade Steel, Metall. Mater. Trans. A Phys. Metall. Mater. Sci. 50 (2019) 161–178. https://doi.org/10.1007/s11661-018-4963-y.
[84] J.Y. Choi, J. Moon, B.H. Kim, J.H. Jang, T.H. Lee, H.U. Hong, H.C. Kim, C.H. Lee, N.H. Kang, Tensile and Charpy impact properties of reduced activation ferritic/martensitic steel with small amounts of Ta and Ti, J. Nucl. Mater. 528 (2020) 151862. https://doi.org/10.1016/j.jnucmat.2019.151862.
[85] J.S. Kim, Y.J. Kim, M.W. Lee, K.S. Kim, K. Shibanuma, Fracture simulation model for API X80 Charpy test in Ductile-Brittle transition temperatures, Int. J. Mech. Sci. 182 (2020) 105771. https://doi.org/10.1016/j.ijmecsci.2020.105771.
[86] B. Jia, A. Rusinek, R. Pesci, S. Bahi, R. Bernier, Thermo-viscoplastic behavior of 304 austenitic stainless steel at various strain rates and temperatures: Testing, modeling and validation, Int. J. Mech. Sci. 170 (2020) 105356. https://doi.org/10.1016/j.ijmecsci.2019.105356.
[87] T. Bhujangrao, C. Froustey, E. Iriondo, F. Veiga, P. Darnis, F.G. Mata, Review of intermediate strain rate testing devices, Metals (Basel). 10 (2020) 1–24. https://doi.org/10.3390/met10070894.
[88] E. Konca, A comparison of the ballistic performances of various microstructures in mil-a-12560 armor steel, Metals (Basel). 10 (2020). https://doi.org/10.3390/met10040446.
[89] P.K. Jena, M.A.M. Manickam, S. Venketachari, S.C. Srivastava, A. Srivastava, S. Chakrabarty, K. Siva Kumar, Microstructure, mechanical, ballistic property evaluation of RHA steel produced by continuous-casting route, J. Appl. Res. Technol. 18 (2020) 1–13. https://doi.org/10.22201/ICAT.24486736E.2020.18.1.927.
[90] S. Choudhary, P.K. Singh, S. Khare, K. Kumar, P. Mahajan, R.K. Verma, Ballistic impact behaviour of newly developed armour grade steel: An experimental and numerical study, Int. J. Impact Eng. 140 (2020) 103557. https://doi.org/10.1016/j.ijimpeng.2020.103557.
[91] T. Chiyatan, V. Uthaisangsuk, Mechanical and fracture behavior of high strength steels under high strain rate deformation: Experiments and modelling, Mater. Sci. Eng. A 779 (2020) 139125. https://doi.org/10.1016/j.msea.2020.139125.
[92] Y. Cao, Y. Zhen, M. Song, H. Yi, F. Li, X. Li, Determination of Johnson–Cook parameters and evaluation of Charpy impact test performance for X80 pipeline steel, Int. J. Mech. Sci. 179 (2020). https://doi.org/10.1016/j.ijmecsci.2020.105627.
[93] S. Sunil, R. Kapoor, Effect of Strain Rate on the Formation of Strain-Induced Martensite in AISI 304L Stainless Steel, Metall. Mater. Trans. A Phys. Metall. Mater. Sci. 51 (2020) 5667–5676. https://doi.org/10.1007/s11661-020-05968-x.
[94] N. Su, M. Chen, W. Zhang, L. Xie, W. Tang, Constitutive Modeling of 17-4PH Stainless Steel Sheet at Elevated Temperature and Statistical Optimization, J. Mater. Eng. Perform. 29 (2020) 1194–1205. https://doi.org/10.1007/s11665-020-04648-6.
[95] Z. Qiang, C. Wen, L. Jun, H. Shuhai, X. Xiangsheng, Hot deformation behavior of 7A04 aluminum alloy at elevated temperature: constitutive modeling and verification, Int. J. Mater. Form. 13 (2020) 293–302. https://doi.org/10.1007/s12289-019-01486-3.
[96] G. Sainath, B.K. Choudhary, J. Christopher, E. Isaac Samuel, M.D. Mathew, Applicability

of Voce equation for tensile flow and work hardening behaviour of P92 ferritic steel, Int. J. Press. Vessel. Pip. 132–133 (2015) 1–9. https://doi.org/10.1016/j.ijpvp.2015.05.004.
[97] J.M.P. Martins, S. Thuillier, A. Andrade-Campos, Calibration of a modified Johnson-Cook model using the Virtual Fields Method and a heterogeneous thermo-mechanical tensile test, Int. J. Mech. Sci. 202–203 (2021) 106511. https://doi.org/10.1016/j.ijmecsci.2021.106511.
[98] M.A. Oude Vrielink, V. Shah, J.A.W. van Dommelen, M.G.D. Geers, Modelling the brittle-to-ductile transition of high-purity tungsten under neutron irradiation, J. Nucl. Mater. 554 (2021) 153068. https://doi.org/10.1016/j.jnucmat.2021.153068.
[99] A. Sela, G. Ortiz-de-Zarate, D. Soler, G. Germain, P. Aristimuño, P.J. Arrazola, Measurement of plastic strain and plastic strain rate during orthogonal cutting for Ti-6Al-4V, Int. J. Mech. Sci. 198 (2021) 106397. https://doi.org/10.1016/j.ijmecsci.2021.106397.
[100] J.S. Kim, Y.J. Kim, M.W. Lee, K.S. Kim, K. Shibanuma, Finite element simulation of drop-weight tear test of API X80 at ductile-brittle transition temperatures, Int. J. Mech. Sci. 191 (2021) 106103. https://doi.org/10.1016/j.ijmecsci.2020.106103.
[101] E. Polatidis, G.N. Haidemenopoulos, D. Krizan, N. Aravas, T. Panzner, M. Šmíd, I. Papadioti, N. Casati, S. Van Petegem, H. Van Swygenhoven, The effect of stress triaxiality on the phase transformation in transformation induced plasticity steels: Experimental investigation and modelling the transformation kinetics, Mater. Sci. Eng. A 800 (2021). https://doi.org/10.1016/j.msea.2020.140321.
[102] M. Ganjiani, M. Homayounfard, Development of a ductile failure model sensitive to stress triaxiality and Lode angle, Int. J. Solids Struct. 225 (2021) 111066. https://doi.org/10.1016/j.ijsolstr.2021.111066.
[103] V. Bratov, NUMERICAL SIMULATIONS of DYNAMIC FRACTURE. CRACK PROPAGATION and FRACTURE of INITIALLY INTACT MEDIA, Mater. Phys. Mech. 47 (2021) 455–474. https://doi.org/10.18149/MPM.4732021_7.
[104] S. Li, Y. Zhang, J. Wu, J. Yu, X. Gong, Modeling of crack propagation with the quasi-static material point method, Eng. Fract. Mech. 245 (2021) 107602. https://doi.org/10.1016/j.engfracmech.2021.107602.
[105] A. Fernández-Canteli, E. Castillo, S. Blasón, A methodology for phenomenological analysis of cumulative damage processes. Application to fatigue and fracture phenomena, Int. J. Fatigue 150 (2021). https://doi.org/10.1016/j.ijfatigue.2021.106311.
[106] J.M. Robles, J.M. Vasco-Olmo, A.S. Cruces, F.A. Diaz, M.N. James, P. Lopez-Crespo, Combined approach for fatigue crack characterisation in metals, Procedia Struct. Integr. 37 (2021) 865–872. https://doi.org/10.1016/j.prostr.2022.02.020.
[107] Y. XIONG, W. WANG, Y. SHI, R. JIANG, C. SHAN, X. LIU, K. LIN, Investigation on surface roughness, residual stress and fatigue property of milling in-situ TiB2/7050Al metal matrix composites, Chinese J. Aeronaut. 34 (2021) 451–464. https://doi.org/10.1016/j.cja.2020.08.046.
[108] W. Macek, Z. Marciniak, R. Branco, D. Rozumek, G.M. Królczyk, A fractographic study exploring the fracture surface topography of S355J2 steel after pseudo-random bending-torsion fatigue tests, Meas. J. Int. Meas. Confed. 178 (2021).

https://doi.org/10.1016/j.measurement.2021.109443.
[109] S. Khare, K. Kumar, S. Choudhary, P.K. Singh, R.K. Verma, P. Mahajan, Determination of Johnson–Cook Material Parameters for Armour Plate Using DIC and FEM, Met. Mater. Int. 27 (2021) 4984–4995. https://doi.org/10.1007/s12540-020-00895-3.
[110] M.A. Moretti, B. Dalai, P. Åkerström, C. Arvieu, D. Jacquin, E. Lacoste, L.E. Lindgren, High Strain Rate Deformation Behavior and Recrystallization of Alloy 718, Metall. Mater. Trans. A Phys. Metall. Mater. Sci. 52 (2021) 5243–5257. https://doi.org/10.1007/s11661-021-06463-7.
[111] W. Wang, P. Wang, X. Liu, Z. Dong, H. Fang, Mathematical Model for Charpy Impact Energy of V-Notch Specimens, Adv. Mater. Sci. Eng. 2021 (2021). https://doi.org/10.1155/2021/5330068.
[112] H. Kosuge, T. Kawabata, T. Okawa, Microstructural design strategy to maintain the brittle fracture toughness of hard-soft dual phase steel after cyclic plastic strain, Mater. Des. 203 (2021) 109603. https://doi.org/10.1016/j.matdes.2021.109603.
[113] C. Wang, Z. Tong, W. Zhong, H. Lin, G. Ning, C. Zhang, B. Yu, S. Xu, W. Yang, A method for directly measuring fracture toughness and determining reference temperature for RPV steels by Charpy impact test, Eng. Fract. Mech. 243 (2021) 107526. https://doi.org/10.1016/j.engfracmech.2021.107526.
[114] K.R. Limmer, J.T. Lloyd, D.M. Field, D.J. Magagnosc, C. Hornbuckle, T.R. Walter, C.S. Meredith, J.D. Clayton, P.A. Jannotti, Designing Steels to Mitigate Failure during Ballistic Deformation (Summary Technical Report, Oct 2018-Sept 2021), 2022.
[115] T.C. Moleko, M. Maringa, W.B. Du Preez, Fractography and Microstructural Analysis of As-Built and Stress Relieved DMLS Ti6Al4V (ELI) Plates Subjected to High Velocity Impact, Adv. Mater. Sci. Eng. 2022 (2022). https://doi.org/10.1155/2022/9008244.
[116] W. Zhu, W. Liu, Y. Ma, S. Meng, J. Wang, Y. Duan, Q. Cai, Revealing impact failure behavior of tungsten composite using instrumented Charpy impact testing, Mater. Charact. 192 (2022) 112181. https://doi.org/10.1016/j.matchar.2022.112181.
[117] X. Yin, Y.K. Dou, X.F. He, K. Jin, C.L. Wang, Y.G. Dong, C.Y. Wang, Y.F. Xue, W. Yang, Effects of Nb Addition on Charpy Impact Properties of TiVTa Refractory High-Entropy Alloy, Acta Metall. Sin. (English Lett. 36 (2023) 405–416. https://doi.org/10.1007/s40195-022-01494-4.
[118] J. Lee, J.M. Park, J. Moon, H. Park, H.S. Kim, Charpy impact toughness of Cu–Fe–Mn-based immiscible medium-entropy alloys, Mater. Sci. Eng. A 862 (2023) 144464. https://doi.org/10.1016/j.msea.2022.144464.
[119] L. Zhang, Q. Wang, J.Q. Ren, C. Xin, D.J. Chen, X.F. Lu, Comparative study on the effect of test temperature on tensile and charpy impact properties of Ti–5Al–1V–1Sn–1Zr-0.8Mo alloy, Mater. Sci. Eng. A 879 (2023). https://doi.org/10.1016/j.msea.2023.145231.
[120] Y. Chen, S. Wang, J. Xiong, G. Wu, J. Gao, Y. Wu, G. Ma, H.H. Wu, X. Mao, Identifying facile material descriptors for Charpy impact toughness in low-alloy steel via machine learning, J. Mater. Sci. Technol. 132 (2023) 213–222. https://doi.org/10.1016/j.jmst.2022.05.051.

[121] Z. Zhang, Y. Wu, F. Huang, Effect of stress triaxiality cut-off value in the fracture criterion on predicting the ballistic behavior of Al2024-T351 plate impacted by blunt- hemisphere- and ogival-nosed projectiles, J. Mater. Res. Technol. 25 (2023) 138–165. https://doi.org/10.1016/j.jmrt.2023.05.186.
[122] Z. Zhang, F. Shen, H. Liu, M. Könemann, S. Münstermann, Temperature-dependent deformation and fracture properties of low-carbon martensitic steel in different stress states, J. Mater. Res. Technol. 25 (2023) 1931–1943. https://doi.org/10.1016/j.jmrt.2023.06.070.
[123] J. Xu, K. Wang, Q. Ma, H. Li, P. Wang, R. Chen, Y. Qian, D. Zeng, Study on acoustic emission properties and crack growth rate identification of rail steels under different fatigue loading conditions, Int. J. Fatigue 172 (2023) 107638. https://doi.org/10.1016/j.ijfatigue.2023.107638.
[124] N. Afzali, G. Jabour, N. Stranghöner, P. Langenberg, A comparative study into the fracture toughness properties of duplex stainless steels, J. Constr. Steel Res. 212 (2024). https://doi.org/10.1016/j.jcsr.2023.108283.
[125] J. Dai, B. Tang, Y. Chu, K. Liu, G. Zheng, X. Chen, J. Li, P. Zhang, Effect of microstructure on impact fracture mechanism of a high-strength Ti-5Al-7.5V-0.5Si-0.25Fe-0.2O alloy, Mater. Sci. Eng. A 890 (2024) 145900. https://doi.org/10.1016/j.msea.2023.145900.
[126] P. Gao, Y. Zhu, J. Zhu, C. Wang, X. Liu, K. Han, B. Wang, Q. Yang, C. Bai, Studies on the life, damage evolution, and crack propagation behaviors of TC18 titanium alloy under repeated impact loading, Int. J. Fatigue 179 (2024) 108074. https://doi.org/10.1016/j.ijfatigue.2023.108074.
[127] H. Liu, Y. Zhou, F. Wang, Y. Lu, Z. Chen, Experimental study on impact toughness of structural steel and its butt-welded joint at low temperature and corrosion, J. Constr. Steel Res. 212 (2024) 108298. https://doi.org/10.1016/j.jcsr.2023.108298.

Chapter - 2

Experiment on tensile tests at high strain rates and FE simulation using J-C, R-K material model and modification in J-C model

Abstract: This study investigated the intermediate and high-temperature behavior of RHA steel and projectile steel, a material crucial for applications requiring blast, impact, crash, and ballistic resistance. The deformation characteristics are analyzed through tensile tests conducted across a range of $\dot{\varepsilon}$ —from quasi-static $\left(10^{-4}\ \mathrm{s}^{-1} \leq \dot{\varepsilon_p} \leq 10^{-1}\ \mathrm{s}^{-1}\right)$ to intermediate $\left(0.8\ \mathrm{s}^{-1} \leq \dot{\varepsilon}_{\mathrm{p}} \leq 36.439\ \mathrm{s}^{-1}\right)$—and at *T* spanning from room *T* ($27^{o}C$) to $500^{o}C$ for RHA steel. For projectile steel deformation characteristics are analyzed through tensile tests conducted across a range of $\dot{\varepsilon}$ — from quasi-static $\left(10^{-4}\ \mathrm{s}^{-1} \leq \dot{\varepsilon_p} \leq 10^{-1}\ \mathrm{s}^{-1}\right)$ to intermediate ($0.2\ \mathrm{s}^{-1}$)—and at *T* spanning from room *T* ($27^{o}C$) to $500^{o}C$. The research employs phenomenological Johnson-Cook (J-C) models and semi-physical Rusinek-Klepaczko (R-K) models for finite element (FE) simulations of these tensile tests. To simulate the degradation of the load-bearing capacity, a J-C failure model is integrated with a modified damage growth law into the material models, which are all implemented in ABAQUS CAE FE software via a user-defined material subroutine (UMAT). The material parameters necessary for these models are extracted directly from experimental data. The simulated results of the tensile tests using the different material models are then validated against experimental findings, and the accuracy and effectiveness of each model are assessed both qualitatively and quantitatively. This study identifies significant limitations in the current models, particularly in their ability to accurately predict material behavior under tension at intermediate $\dot{\varepsilon}$ and elevated *T*. To address these shortcomings, a modified Johnson-Cook (MJ-C) material model and modified Johnson-Cook failure model are proposed, which more effectively accounts for the influence of *T* on strain hardening and $\dot{\varepsilon}$ sensitivity. This modification greatly improves the predictive accuracy of FE simulations of tensile deformation across the full range of $\dot{\varepsilon}$ and *T* examined, outperforming both the original J-C and R-K models.

2.1 Introduction

The energy absorption capacity of a typical armour steel and with a martensitic microstructure makes it popular for use at high loading rates. On the other hand, the high strength of projectile steel makes it suitable to defect the target. Numerous researchers have examined the behaviour of armour steel at high $\dot{\varepsilon}$ [1–4]. All parameters, such as ε, $\dot{\varepsilon}$, and *T*, change significantly during real-world applications, such as crashes, explosions, ballistic impacts, and metal forming issues. There is also a significant amount of plastic deformation, which is vital for the design of engineering

structures and the assessment of safety. The behaviour of the material in these deformation processes may be precisely characterized by taking into account the "large displacements and large strain" framework, which also takes into account the effects of high $\dot{\varepsilon}$ and increasing *T*.

To correctly simulate how a material behaves during certain processes (such as large deformation, impact, etc.), it is essential to use a proper mathematical model (known as a constitutive description) that accurately represents the material's properties and behavior. Two different methodologies for building a constitutive model are commonly used in the literature [5]. Some groups of researchers consider the flow stress to be a function of $(\varepsilon_p, \dot{\varepsilon}, T)$ [6,7], whereas others consider the rate of strain hardening in relation to $\left(\varepsilon_p, \dot{\varepsilon}, T\right)$ [8–10].

The material models proposed by Johnson and Cook (J-C) [11], Zhao and Gary [12,13], Khan, Huang and Liang (KHL) [14,15], and Paul et al. [16] were developed on the basis of experimental observations following the first approach. This approach is known as 'phenomenological modelling', which does not correlate the macroscopic behaviour with the physical behaviour of material microstructures. Rather, a suitable mechanical model is adopted to fit the experimental observations; in this way, it requires fewer material constants, and a simple model becomes computationally inexpensive. On the other hand, physics-based constitutive models typically include a large number of material constants to capture the physics of the behavior. Although computationally expensive, owing to their superior ability to capture material behavior at the microscopic scale, physics-based models are gaining attraction for complex loading conditions [17]. Combining the advantages of these two approaches, optimum benefits are observed for the Rusinek and Klepaczko (R-K) [18] and Zerilli and Armstrong (ZA) [19] material models. The J-C model was originally proposed for metals. For simplicity, it is preferred in industry as well as in research. The logarithmic strain-rate hardening in the J-C model causes the fitting curve to deviate from the experimental results, in addition to introducing additional complexity in the calculations. Over time, to overcome this problem, some authors have coined a complementary term for strain-rate expression (Peixhino et al.) [20]. However, this phenomenon persists particularly under conditions of elevated strain rates and increasing temperatures, resulting in thermal softening caused by adiabatic heating. The precise impact of this is not adequately defined in the J-C relationship [21]. Rusinek et al. explored the impact of this research on DP 600 steel in 2007 [10], suggesting a novel constitutive relation grounded in a semi-physical methodology. In the R-K constitutive model, the stress changes with strain rate, whether increasing or decreasing, which is a significant advantage. Through experiments, by Klepaczko and Duffy [22], the strain rate sensitivity of stress was observed for BCC metals, in which the R-K constitutive relation was partially accounted for. This behavior can be illustrated through the evolution of the microstructure.

The use of internal variables in phenomenological models has also been proposed to explain the physics behind plastic deformation, such as in physically based cases. Both models effectively simulate the experimental data pertaining to a specific range of $(\varepsilon_p, \dot{\varepsilon}, T)$. However, Follansbee and Kocks [23] reported that the performances of both models are inadequate for comprehending the existing constitutive data across a broad spectrum of strain rates or, more precisely, for predicting stress variations caused by rapid changes in strain-rates. Tong et al. [24], Bodner and Rubin [25], and Frutschy and Clifton [26,27] investigated the impact of the strain rate on strengthening at various temperatures.

In addition, Kotkunde [29] and Tao [28,29] analyzed the predictive accuracy of the J-C, Fields-Backofen (FB) [30], KHL, a modified version of the J-C, and, mechanical threshold stress (MTS) equations for Ti-6AL-4V alloy. In their findings, they reported, that the prediction by the modified version of the J-C model was the best among the material models considered for the Ti-6AL-4V alloy. Recently, Prakash et al. [31] studied the σ_f for the same alloy but at high $\dot{\varepsilon}$ and high T via tensile, compressive and flexural loads. The modified J-C and the J-C models were employed to predict Al7075 behavior at increased temperatures; however, modified J-C models have better predictions owing to adjustments in the temperature term [32]. Fengquan Hu et al. [33] investigated the J-C constitutive and failure-fracture model parameters for Q345C steel. L. Levgen et al. [34] identified the material parameters at elevated strain-rates using ballistic impact tests and performed inverse finite element analysis. Geng et al. [35] investigated the flow stress behavior of a GH4169 superalloy subjected to friction stir welding via modified FB, J-C and Arrhenius [36] models. The Arrhenius model prediction was good for this superalloy. The Arrhenius equation was also used for aluminum alloys by Zhang et al. [37] to predict compressive stress. FB and its modified version, Field-Backofen-Zhang (MFBZ) [38], have been utilized to predict the isothermal tensile flow stress in alpha-Ti tubes. According to these two models, the prediction by the MFBZ is more accurate, with an R-squared value of 0.98 [39].

M.E. Korkmaz et al. [40,41] identified J-C model parameters for a Nimonic 80A superalloy. The parameters were subsequently confirmed via the finite element method [42]. M.E. Korkmaz also verified the J-C model parameters for ferritic stainless steel via the drilling process. Many experimental results have been verified with finite element simulations [43]. The orientation dependent J-C model for selective laser melting manufactured with ALSi10Mg was also investigated by [44]. The deformation behavior and $\dot{\varepsilon}$ sensitivity of 33MnCrB5 boron steel were also studied via a material J-C constitutive equation [45].

In addition to modifying the J-C strength model, researchers have modified the J-C failure model [46], or different methods have been adopted to calibrate the J-C damage model parameters. D.

Rajaman et al. [47] applied a novel calibration procedure to calculate J-C damage model parameters for finite element simulation of scratch abrasion. M. Gerstgrasser [48] analyze two parameter identification methods for the original and modified J-C failure strain models. Some researchers [49] have used a genetic algorithm to calibrate the J-C strength and failure model parameters.

A detailed study on plastic deformation at high $\dot{\varepsilon}$ and T revealed that the mismatch between the J-C simulation and actual material response is due to the complex interaction of $\dot{\varepsilon}$ and T in plastic strain evolution. Significant progress has been made in modelling plastic deformation via microscopic parameters, with various microscale and multiscale mechanisms proposed for strain hardening [50–52].

In the study of armor steel materials known for their resistance against impact loading, the J-C model has been used by many researchers [53–55] because it provides a fairly good simulation of the quasistatic and dynamic behavior of metals [56,57] in a computationally inexpensive way. The existing material models are suitable for elevated temperatures and high strain-rates but cannot accurately predict body-centered tetragonal (BCT)-type armor steel behavior at elevated T [58]. The J-C, the mechanical threshold stress, and the Rusinek-Klepaczko material models each have strengths in specific applications but share common limitations. These include an empirical basis, the need for extensive parameter calibration, limited consideration of microstructural changes, assumptions of isotropic behavior, and challenges in accurately predicting behavior under complex loading paths, high strain-rates, and varying temperatures. Additionally, computational costs and stress state dependencies further limit their applicability in some scenarios. Understanding these limitations is crucial for selecting and refining constitutive models for accurate material behavior prediction under dynamic conditions. Additionally, for the RHA steel material, the coefficient for $\dot{\varepsilon}$ hardening is not independent of the $\dot{\varepsilon}$, and its strain hardening parameter is also temperature dependent and is not considered in the J-C model. This study aims to fill this gap in the existing J-C model, which is necessary for BCT-type RHA steel materials.

This chapter explored the deformation and failure mechanisms of typical rolled homogenous armor steel materials under intermediate strain-rates. Experiments have been conducted from quasi-static $\dot{\varepsilon}$ $\left(10^{-4}\ s^{-1} \leq \dot{\varepsilon}_p \leq 10^{-1}\ s^{-1}\right)$ to intermediate $\dot{\varepsilon}$ $\left(10^{-1}\ s^{-1} \leq \dot{\varepsilon}_p \leq 36.439\ s^{-1}\right)$ and at high temperatures ranging from RT $(27℃)$ to $500℃$. The material parameters determined from the experimental results were used to perform FE simulations of tensile tests via the phenomenological J-C model, MJ-C [59] and the semi-physical R-K model [60].

To simulate the loss of load-bearing capacity, the J-C failure model [61] and modified damage growth law are used. The alternate equations for the J-C failure model were also analyzed to

simulate the loss of load-bearing capacity. The ABAQUS software with user the defined material subroutine UMAT combines the J-C failure model with all three material models to perform finite element simulations of tensile tests at various $\dot{\varepsilon}$ and T. The simulated and experimental results are compared, and each material model's effectiveness—both quantitatively and qualitatively—is assessed.

2.2 Experiments

Experiments are essential for analyzing a material's mechanical response, with tensile tests commonly used to reveal its behavior. Since materials can respond differently under various conditions, this study examines the effects of varying loading rates and temperatures. However, the impact of a corrosive environment has not been explored and may be addressed in future work.

2.2.1 Material

The reference material used in this paper is a typical armour steel that has been the subject of investigation by numerous scholars throughout the past decade [1,56,62–64]. It is also called rolled homogeneous armor (RHA) steel. This material was selected because its intermediate to high strain-rate response and high-temperature response was merely investigated, although it is widely acceptable for armor applications. The heat treatment schedule is listed in Fig. 2.1a. Fig. 2.2a illustrates its microstructure. The main phases present are martensite with some ferrite and pearlite. The ferrite appears as light-colored grains under an optical microscope. The martensite appears as a needle-like or lath-like structure in quenched and tempered RHA steel. The chemical composition of armour steel is listed in Table 2.1a.

Another material studied was the projectile steel (PHS 1500). The material heat treatment schedule is listed in Fig. 2.1b. The material is medium carbon steel. Microstructurally, it has fine martensitic needle like lath. The material chemical composition is listed in Table 2.1b and optical microstructure is shown in Fig. 2.2b.

The vicker hardness impression is shown in Fig. 2.3 and hardness value of the two materials are listed in Table. 2.2.

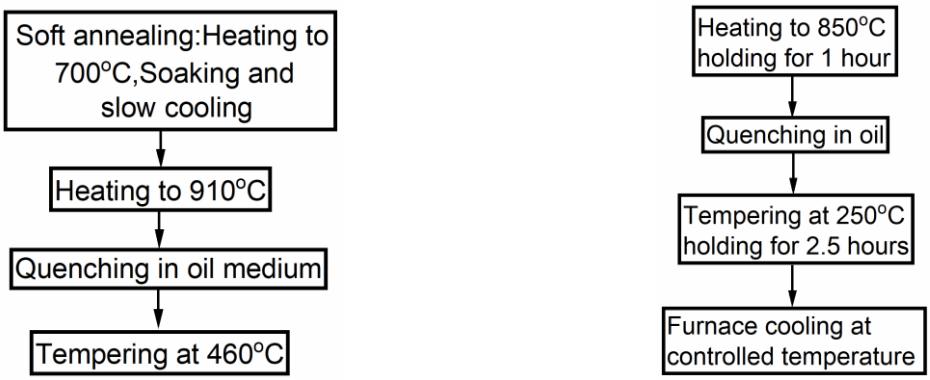

(a) (b)

Fig. 2.1 Heat treatment schedule of (a) RHA, and (b) Projectile steel

Table 2.1a RHA steel chemical composition

C	Si	Mn	P	S	Cr	Mo	Ni	Cu	Al	Fe
0.35	0.23	0.43	0.011	0.007	1.47	0.45	1.65	0.03	0.02	Rest

Table 2.1b Projectile steel chemical composition

C	Si	Mn	P	S	Cr	Mo	Ni	Cu	Al	Fe
0.47	0.26	0.62	0.011	0.006	1.12	0.18	0.22	0.14	0.07	Rest

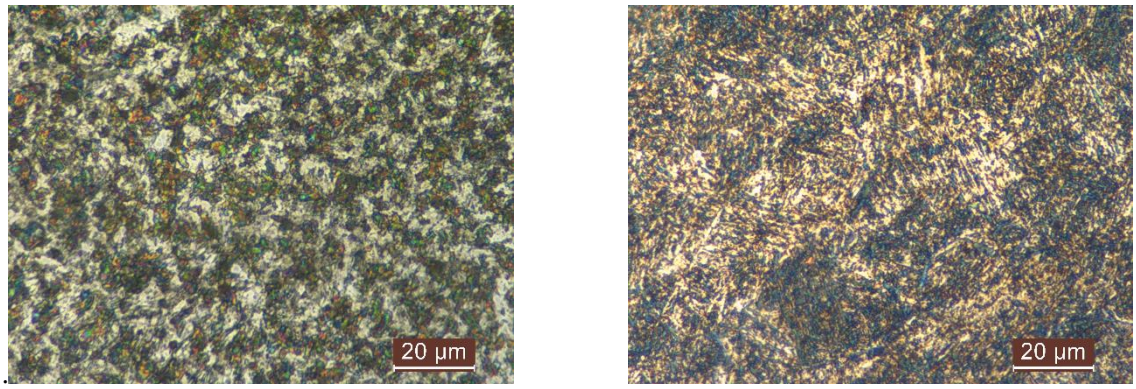

(a) (b)

Fig. 2.2 Optical images of (a) RHA steel (b) Projectile steel

(a) (b)

Fig. 2.3 Vicker hardness impression of (a) RHA, and (b) Projectile steel

Table 2.2 Vickers hardness (HV) of materials at (500 g)

RHA steel	300-320
PHS1500 steel	380-405

2.2.2 Tensile tests

Table 2.3 & 2.4 shows the test matrix for tensile tests performed on the armour steel and projectile steel materials.

Table 2.3 Tensile test matrix for the armor material

Temperature (27°C) $\dot{\varepsilon}$ ***(s^{-1}):***	**10^{-4}**	**10^{-3}**	**10^{-2}**	**10^{-1}**	**0.8**	**9.37**	**36.439**
Temperature (200, 300, 400 and 500°C) $\dot{\varepsilon}$ ***(s^{-1}):***	10^{-4}	10^{-3}	10^{-2}	10^{-1}	_	_	_

Table 2.4 Tensile test matrix for the projectile steel

Temperature* (27°C)** $\dot{\varepsilon}$ ***(s^{-1}):	**10^{-4}**	**10^{-3}**	**10^{-2}**	**10^{-1}**	**0.5**	**-**	**-**
Temperature* (*200, 300, 400 and 500°C*)** $\dot{\varepsilon}$ ***(s^{-1}):	10^{-4}	10^{-3}	10^{-2}	10^{-1}	_	_	_

Quasi-static tests at high temperatures, ranging from $27℃ \leq T \leq 500℃$, and $\dot{\varepsilon}$ ranging from $10^{-4}\ s^{-1} \leq \dot{\varepsilon_p} \leq 10^{-1}\ s^{-1}$ are performed in an INSTRON 5582 testing machine. Intermediate tests at 27℃ and $\dot{\varepsilon}$ ranging from $0.8\ s^{-1} \leq \dot{\varepsilon_p} \leq 36.439\ s^{-1}$ and temperature 27°C are carried out in a servo-hydraulic high strain-rate (VHS) testing machine with DIC facility. The design of all the test specimens are shown in Fig. 2.4. The thickness of intermediate strain-rate sample is 3 mm.

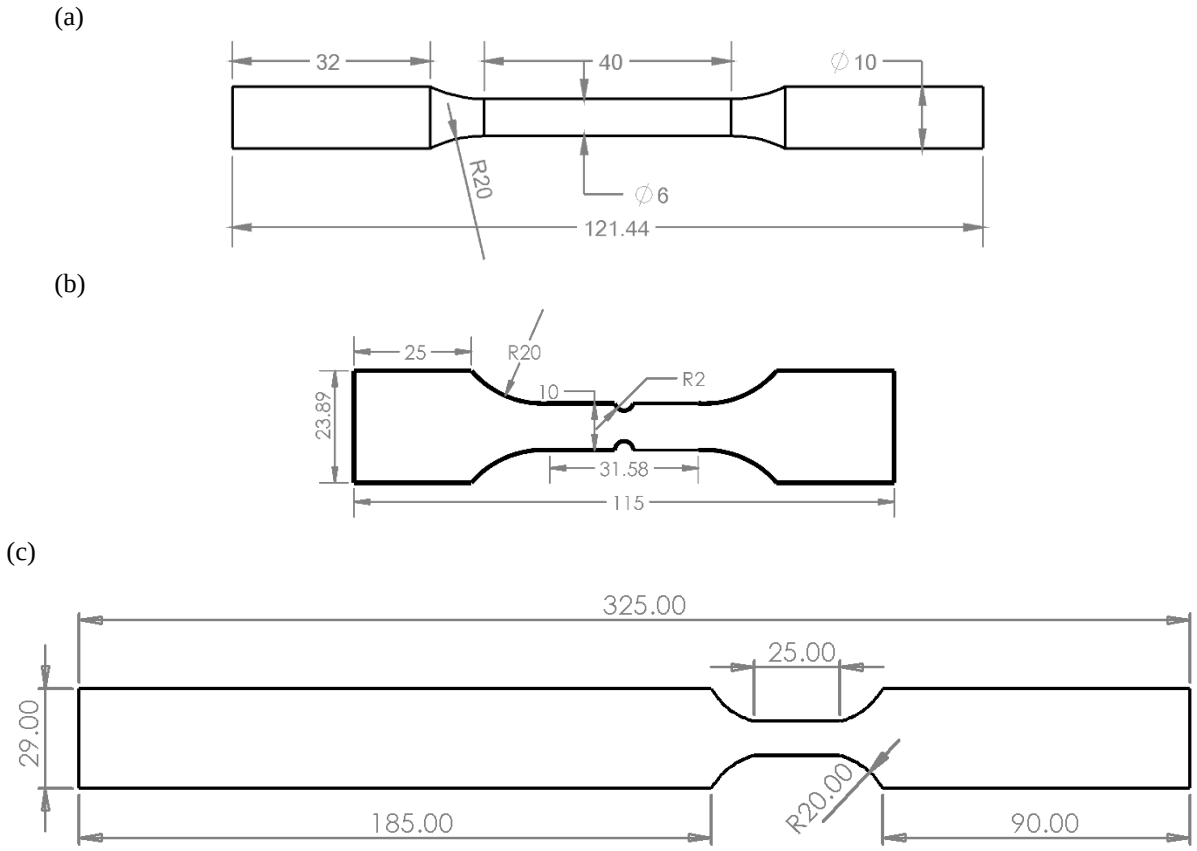

Fig. 2.4 Geometry of a tensile (a) round sample (b) flat round notch sample (c) Long flat tensile test sample for intermediate strain-rate testing.

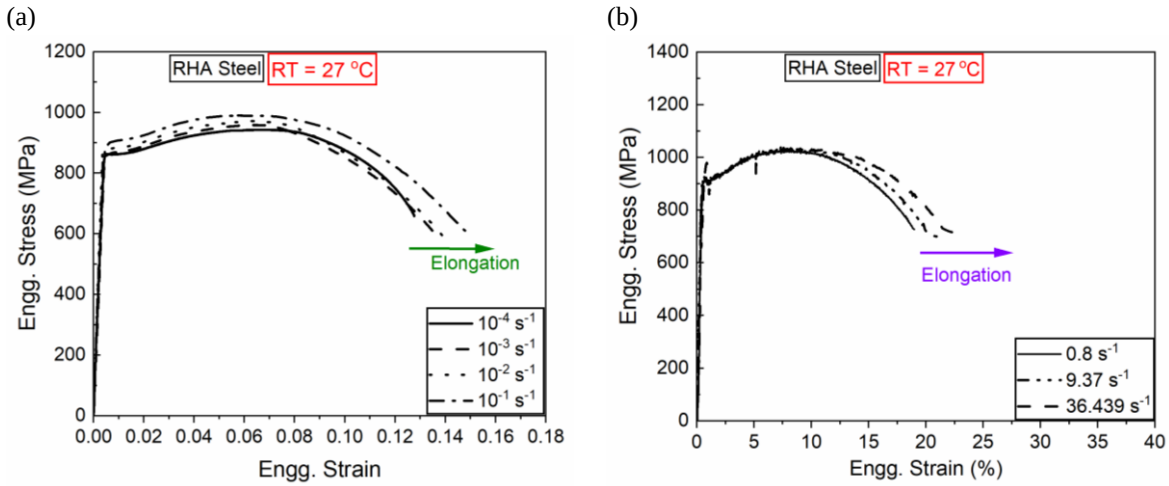

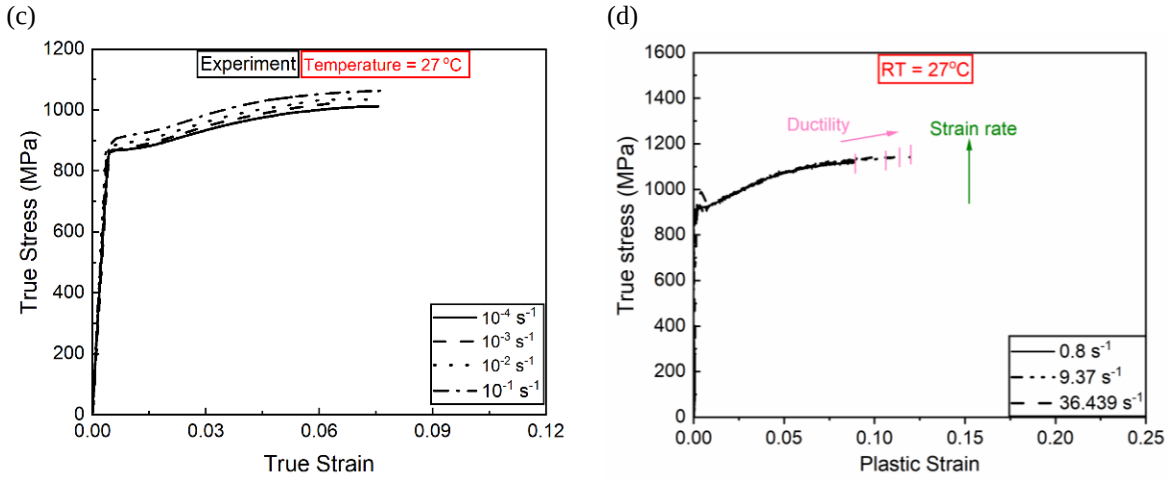

Fig. 2.5 Engineering stress – strain curves at 27°C (a) INSTRON 5582 test results and (b) intermediate test results obtained from the INSTRON-VHS with DIC. True stress – strain curves at 27°C (c) INSTRON 5582 test results and (d) intermediate test results obtained from the INSTRON-VHS with DIC.

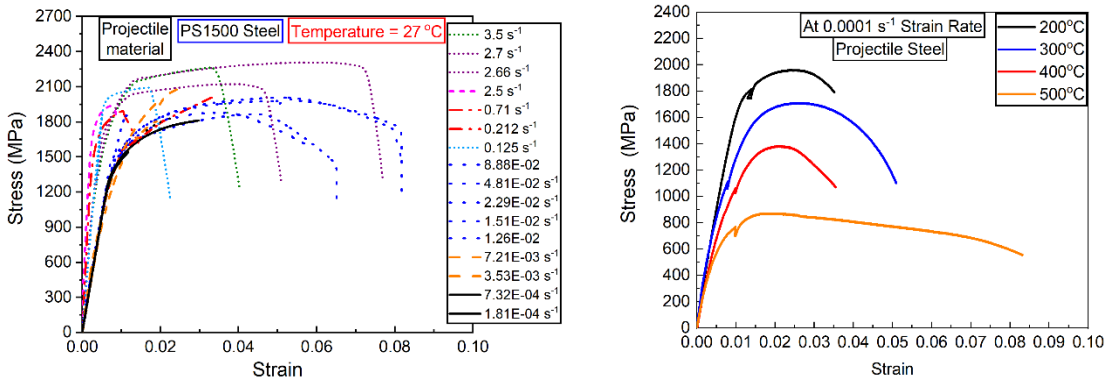

(a) (b)

Fig. 2.6 Stress *vs* strain curve for projectile steel

Before testing, all the samples were annealed via a consistent protocol to ensure material uniformity. Machining was performed with a precision of 100 microns, and wire cutting achieved even greater accuracy at 10 microns. The universal tensile machine (UTM) load-cell, LVDT, extensometer, and furnace temperature controller were calibrated by the manufacturer, ensuring precise control of loading rates and temperature. A Eurotherm controller maintained the furnace temperature within ±2°C. Tests were conducted by an experienced operator to minimize subjective error. The sample rate was optimized on the basis of the strain rate via calibrated sensors, and

standardized testing procedures (ASTM E8M) were followed. Additionally, two tests per condition were performed to ensure statistically significant results. Fig. 2.5a-b shows the engineering stress – strain curves at 27°C, whereas Fig. 2.5c shows the true stress – strain curves for quasi-static $\dot{\varepsilon}$, and Fig. 2.5d shows the true stress – plastic strain curves for intermediate $\dot{\varepsilon}$. The figures clearly show positive strain-rate sensitivity in the quasi-static range, but in the intermediate strain-rate range, the material's post elastic response, until ultimate, exhibits minimal sensitivity to the variations in strain-rates (Fig. 2.5b & d). The reason may be that at high loading rates, due to insufficient time, the interstitial carbon atoms could not settle between dislocations and anchor them. Beyond ultimate stress, where the nature of the material is different and more general, the damage mechanics may have a dominant effect.

At high temperature for projectile steel the strength falls but the ductility increases as shown in Fig. 2.6b.

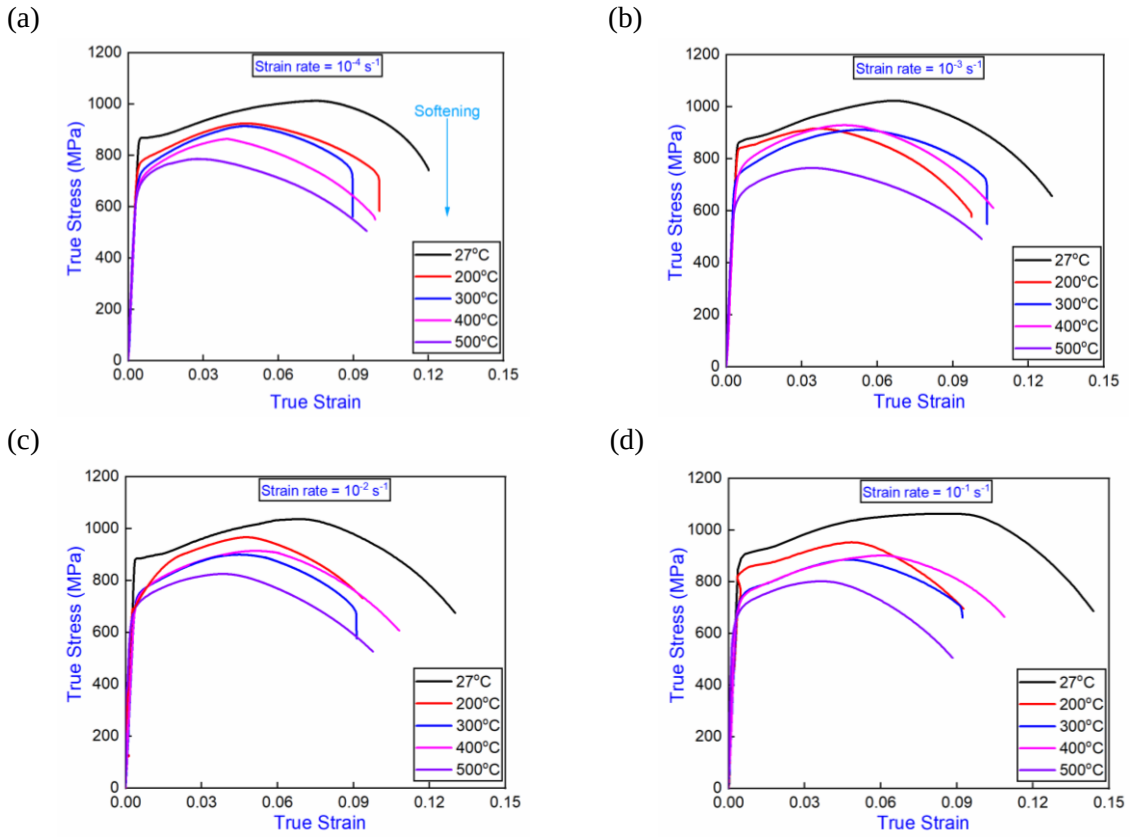

Fig. 2.7 shows that while the $\dot{\varepsilon}$ remained constant, the Young's modulus of the armor steel, *E*, did not vary significantly with temperature, as listed in Table 2.5.

Table 2.5 Elastic modulus (GPa) at different T and $\dot{\varepsilon}$

Strain-rate s^{-1}	Temperature °C				
	RT	200	300	400	500
10^{-4}	204.421	217.83	212.191	211.396	225.496
10^{-3}	201.14	193.856	232.846	222.388	222.08
10^{-2}	248.011	227.022	210.134	188.128	217.57
10^{-1}	225.880	199.266	226.213	230.166	235.65

However, the plastic flow curves exhibit significant variations in response to both the $\dot{\varepsilon}$ and test T. As the temperature increases, the σ_f rapidly decreases, even as the $\dot{\varepsilon}$ remains constant. Conversely, the flow stress is increases at elevated $\dot{\varepsilon}$ when the temperature remains constant. Elongation decreases with increasing temperature because the steel softens, localizes deformation earlier, and may undergo microstructural instabilities or dynamic strain aging that limit ductility.

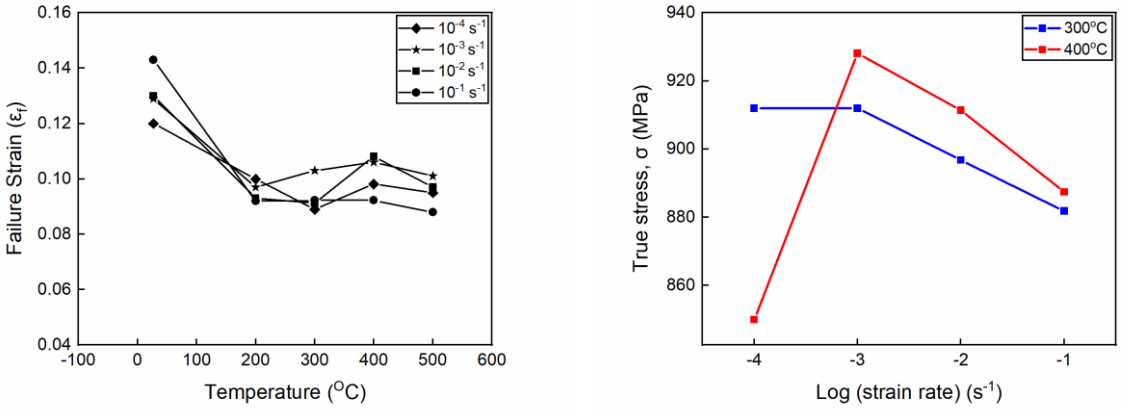

(a) (b)

Fig. 2.8 Negative strain-rate sensitivity (a) plot of failure strain *vs* temperature of armour steel (b) at temperature window 300 ℃ to 400 ℃.

Fig. 2.8 also shows the negative temperature sensitivity in the $\dot{\varepsilon}$ window of 10^{-3} - 10^{-1} s^{-1} for temperatures ranging from 300℃ to 400℃. This phenomenon is clearly visible in Fig. 7a-d, where between 300℃ and 400℃, the stress increases with increasing temperature.

It can be speculated that this is due to dynamic strain aging (DSA). The additional hardening observed at 400℃ may be due to the precipitation hardening of carbide precipitates, which occurs at tempering temperatures of 400℃ – 500℃ [65,66].

The results show that the T has a greater effect on the σ_f than does the $\dot{\varepsilon}$. However, it is interesting

to note that the work-hardening rate is more affected by the applied $\dot{\varepsilon}$ in the intermediate range. It can be speculated that the adiabatic increase in temperature is very small, and hence, the dominating parameter is the loading rate and not the temperature.

Tensile tests were conducted on notched samples to determine the J-C failure parameters [61]. Fig. 2.4b shows a drawing of the sample, and the other dimensions are listed in Table 2.6.

Table 2.6 Geometry of the notch sample

Parameters	$\dot{\varepsilon} = 10^{-4}s^{-1}$							
	Round-notch							
Diameter (mm)	4	4	4	4	8	8	8	8
Thickness (mm)	6	2	4	8	6	4	2	8

2.3 Finite element simulation

Accurate finite element simulations require selecting the right material model to predict material behavior under various conditions, such as slow loading, high-speed impacts, and high temperatures. The **J-C model**, a phenomenological approach, is widely used for its simplicity and effectiveness in describing dynamic and thermal effects on materials. In contrast, the **R-K model**, a semi-physical model, is particularly suited for materials with a body-centered cubic (BCC) crystal structure, such as certain steels. To improve the accuracy of the J-C model, a **Modified Johnson-Cook (MJ-C) model** has been developed, addressing some of its limitations and enhancing predictive capabilities under complex loading conditions.

2.3.1 Material models

The following material models are used to predict the armour steel thermoviscoplastic behavior.

2.3.1.1 Johnson-Cook material model

The J-C model, [1] relies on a phenomenological approach and establishes a connection between stress and strain to encompass the impact of both strain-rate and temperature. This relationship [Eq. (2.1)] is frequently employed in the numerical analysis of quasi-static and dynamic processes [67–69].

$$\sigma_{eq}(\varepsilon_p, \dot{\varepsilon}, T) = [A + B\,\varepsilon_p^n][1 + C\ln(\dot{\varepsilon^*})][1 - T^{*m}] \quad (2.1)$$

where σ_{eq} is the von Mises stress, which is a function of the equivalent plastic strain ε_p; $\dot{\varepsilon^*} = \dot{\varepsilon}/\dot{\varepsilon}_R$ is the dimensionless $\dot{\varepsilon^*}$ ratio, and the working $\dot{\varepsilon}$ is normalized by the reference strain-rate $\dot{\varepsilon}_R$ and the absolute working T in an uncoupled manner. The function is defined via five material parameters: A, B, C, n and m. The third term consists of the homologous temperature, $T^* =$

$(T - T_0)/(T_m - T_0)$, where T_m is the melting T of the material and where T_0 is a reference T.

The material parameters are input into the FE software alongside the field variables. On the basis of the experimental flow curves at various strain-rates at the reference temperature and various temperatures at $\dot{\varepsilon}_R$, these J-C model parameters are determined for the armor steel material and are listed in Table 2.7a. The detailed method of parameter extraction was described previously [54].

2.3.1.2 Modified Johnson-Cook material model

The original J-C model, as described by Eq. (2.1), is easy to implement because of the decoupling of the impact of $(\varepsilon_p, \dot{\varepsilon}, T)$ on the flow stress. In the J-C model, the stress *vs* $\ln(\dot{\varepsilon}/\dot{\varepsilon}_R)$ relation is assumed to be linear. This assumption leads to a constant strain-rate sensitivity coefficient, denoted as *C*. Additionally, the strain hardening exponent, n, is assumed to be insensitive to temperature.

The experimental observations agree with the above assumptions for a range of $\dot{\varepsilon}$ and temperature variations [70]. However, from the experimental results of the investigated steel in this work, the $\dot{\varepsilon}$ and *T* sensitivity of the hardening exponent are visible, especially at intermediate $\dot{\varepsilon}$ and *T*. The J-C model cannot capture the sensitivity due to an increase in the $\dot{\varepsilon}$ at the intermediate $\dot{\varepsilon}$ regime. To enhance the predictability of the J-C model at intermediate $\dot{\varepsilon}$, a modified term was proposed by Hoon Huh et al. [71]. This is done by replacing $\ln(\dot{\varepsilon}/\dot{\varepsilon}_R)$ with $\{\ln(\dot{\varepsilon}/\dot{\varepsilon}_R)\}^r$.

Previous research has established that the strain hardening exponent, *n*, is influenced by both the $\dot{\varepsilon}$ and *T* [18,60]. According to the literature, n decreases with increasing *T* and decreasing $\dot{\varepsilon}$. The experimental results (Figs. 2.5 and 2.7) for the present material show a significant change in the strain hardening rate with temperature but less change with variations in the $\dot{\varepsilon}$. With these observations, only the *T* dependence of *n* is considered in this study. A linear dependence of the strain hardening exponent *n* on *T* is observed for the armour steel, as presented in Fig. 2.9.

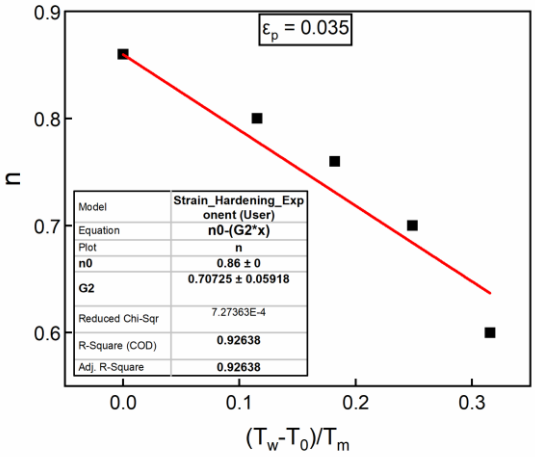

Fig. 2.9 Strain hardening decreases as the temperature increases

Using the modified version of the J-C model, the MJ-C model is represented as:

$$\sigma_{eq}(\varepsilon_p, \dot{\varepsilon}, T) = [A + B\varepsilon_P^n][1 + G_1\{\ln(\dot{\varepsilon}/\dot{\varepsilon}_R)\}^r][1 - G_3 T^{*^m}] \quad (2.2)$$

$$\text{with } n = n_0 - G_2[(T - T_0)/T_m] \quad (2.3)$$

Here, the parameter n is a function of the working T, and is defined in Eq. 2.3. In Eq. 2.3, the parameter n_0 is the strain hardening exponent at the reference temperature, T_0. In this work, room T was used as a reference. G_2 is obtained from the slope of the linear fit, as shown in Fig. 2.9.

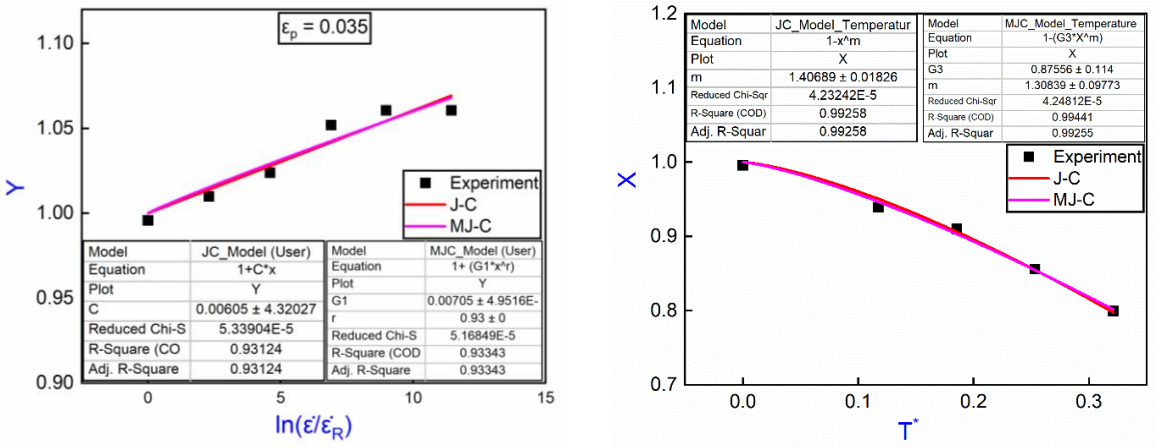

(a) (b)

Fig. 2.10 (a) Variation of Y with logarithm of normalized strain-rate (b) Variation of X with normalized temperature

In Eq. 2.2, the commonly used parameter C is replaced with G_1, as $\ln(\dot{\varepsilon}/\dot{\varepsilon}_R)$ is replaced by $\{\ln(\dot{\varepsilon}/\dot{\varepsilon}_R)\}^r$, where parameter r introduces nonlinearity in the stress *vs*. $\ln(\dot{\varepsilon}/\dot{\varepsilon}_R)$ relation. To estimate the parameters at room temperature, a quantity Y is defined as:

$$Y = \sigma_{eq}/(A + B\varepsilon_P^n) = [1 + G_1\{\ln(\dot{\varepsilon}/\dot{\varepsilon}_R)\}^r] \tag{2.4}$$

Fig. 2.9a is a plot of Y *vs*. $\ln(\dot{\varepsilon}/\dot{\varepsilon}_R)$. The values of parameters G_1 and r are determined by fitting a general allometric power law curve.

In Eq. 2.2, another parameter, G_3, is introduced. Parameters G_3 and m are estimated by defining an intermediate quantity X from Eq. 2.2 as follows:

$$K = [A + B\varepsilon_P^n][1 + G_1\{\ln(\dot{\varepsilon}/\dot{\varepsilon}_R)\}^r] \tag{2.5}$$

$$X = \sigma_{eq}/K = [1 - G_3 T^{*^m}] \tag{2.6}$$

In Fig. 2.9b, the plot of the parameter X *vs* homologous temperature, T^*, is fitted with a general allometric power law curve to obtain the parameters G_3 and m. The fitting functions have an R-square accuracy of 0.99.

In the classical J-C model, the effects of T and $\dot{\varepsilon}$ are decoupled. The MJ-C material model exhibits partial coupling between strain hardening and thermal softening. Eq. 2.2 contains three terms. The first term represents strain hardening, coupled with the temperature effect, whereas the second and third terms represent the T and $\dot{\varepsilon}$ effects, respectively. The imposed nonlinearity in the two later terms made it more adaptable. Additionally, the same amount of experimental data is needed for the extraction of material parameters, as is the case for the R-K model. The model is implemented in ABAQUS FE software through a user-defined material model UMAT, ignoring the dynamic effects. The parameter values are listed in Table 2.7a.

2.3.1.3 Rusinek-Klepaczko material model

The semi-physical material model suggests that strain hardening depends on the T and $\dot{\varepsilon}$. This method utilizes the idea of breaking down the total flow stress (the von Mises equivalent stress) into σ_μ and σ_e. Eq. 2.7 provides the constitutive relation for calculating the flow stress in this model:

$$\sigma = E(T)/E_0\left[\sigma_\mu\left(\varepsilon_p, \dot{\varepsilon}_p, T\right) + \sigma_e\left(\dot{\varepsilon}_p, T\right)\right] \tag{2.7}$$

Here, E_0 represents the Young's modulus at $T = 27℃$. The overall stress is additively contributed by σ_μ or the internal stress and σ_e or the effective stress. The effective stress describes the kinetics

of thermally activated processes [18].

In Eq.7, $\mathrm{E(T)} = \mathrm{E_0}\{1 - (T/T_m)\exp[\theta^*(1 - T_m/T)]\}$ (2.8)

where θ^* and T_m denote the characteristic homologous and melting temperatures, respectively. The thermal softening (the weakening of the modulus) of a material can be defined via Eq. 2.8. However, it is clear from the experimental investigation (Fig. 2.3) that the *E* of the studied armor steel is not significantly dependent on the temperature within the range of temperatures investigated.

The 'internal stress' is defined by Eq. 2.9 as:

$$\sigma_{\mu}\left(\varepsilon_p, \dot{\varepsilon}_p, T\right) = B\left(\dot{\varepsilon}_p, T\right)\left[\varepsilon_0 + \varepsilon_p\right]^{n\left(\dot{\varepsilon}_p, T\right)} \quad (2.9)$$

where ε_0 is the strain value that corresponds to the yield stress. $B\left(\dot{\varepsilon}_p, T\right)$ is the plasticity modulus, and $n\left(\dot{\varepsilon}_p, T\right)$ is the strain hardening exponent. The explicit definitions of these exponents as functions of the *T* and $\dot{\varepsilon}$ are given in Eqs. 2.10 & 2.11:

$$B\left(\dot{\varepsilon}_p, T\right) = B_0\left[(T/T_m)\log(\dot{\varepsilon}_{max}/\dot{\varepsilon}_p)\right]^{-v} \quad (2.10)$$

$$n\left(\dot{\varepsilon}_p, T\right) = n_0\left\langle 1 - D_2(T/T_m)\log(\dot{\varepsilon}_p/\dot{\varepsilon}_{min})\right\rangle \quad (2.11)$$

where, v represents the temperature sensitivity, n_0 is the strain hardening exponent, B_0 is the material constant at $T = 27℃$, D_2 is another material constant and $\dot{\varepsilon}_{\min}$ is the minimum strain-rate. The strain hardening exponent n must be non-negative because a negative n would unrealistically increase the internal stress as the temperature increases at a given strain-rate [72]. The Macaulay operator is defined as follows: $\langle x\rangle = x$ if $\langle x\rangle \geq 0$ or $\langle x\rangle = 0$ if $\langle x\rangle < 0$. The σ_e is calculated via the Arrhenius relation (Eq. 2.12), which combines the *T* and $\dot{\varepsilon}$ and is particularly suitable for describing plastic deformation driven by thermal activation.

$$\sigma_e\left(\dot{\varepsilon}_p, T\right) = \sigma_e^o\left\langle 1 - D_1(T/T_m)\log\left(\dot{\varepsilon}_{max}/\dot{\varepsilon}_p\right)\right\rangle^{m^*} \quad (2.12)$$

where σ_e^o is the effective stress at $T = 27℃$, D_1 is the material constant, $\dot{\varepsilon}_{max}$ is the maximum strain-rate and $m^* = 1/m$ and m are constants that allow the $\dot{\varepsilon}$-*T* sensitivity to be defined. The number of parameters to be determined is eight. The experimental data for $\dot{\varepsilon} = 10^{-4}\ \mathrm{s}^{-1} \leq \dot{\varepsilon}_p \leq 36.439\ \mathrm{s}^{-1}$ and $T = 27℃ \leq T \leq 500℃$ are used to determine all of the parameters for the R-K material model. In the literature [60,73,74], the procedures for parameter extraction are described.

2.3.1.4 Johnson-Cook failure model

To simulate the loss of load-bearing capacity leading to catastrophic failure, it is essential to consider a failure criterion. Johnson and Cook [61] expanded the Hankock and Mackenzie fracture criterion, demonstrating that the strain at failure is influenced by factors such as stress triaxiality (σ^*), temperature (T), and strain-rate ($\dot{\varepsilon}$) and strain path. The equation for the strain at fracture is given in Eq. 2.13:

$$\varepsilon_f = [D_1 + D_2 \exp(D_3\sigma^*)][1 + D_4 \ln \dot{\varepsilon}^*][1 + D_5 T^*] \quad (2.13)$$

for $\sigma^* \leq 1.5$. The dimensionless stress ratio, σ^*, is called the stress triaxiality factor and is defined by $\sigma^* = \sigma_m/\sigma_{eq}$, where σ_m is the hydrostatic stress and σ_{eq} is the von Mises equivalent stress. Fig. 2.11 shows the dependence of the fracture strain on the stress triaxility.

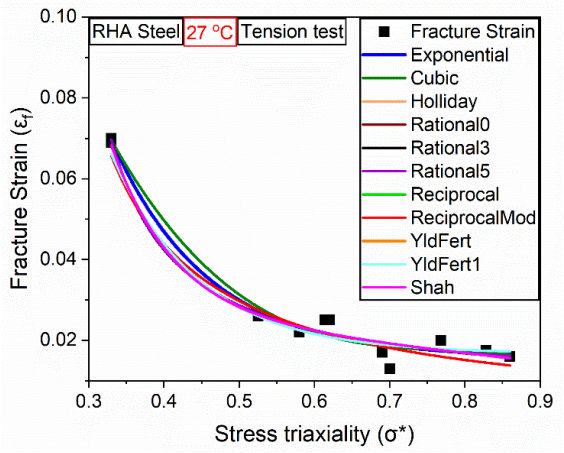

Fig. 2.11 Dependence of fracture strain on stress triaxiality

The $\dot{\varepsilon}^*$and T^* are the same as those defined in the J-C material model (Eq. 2.1). The fracture strain ε_f for different notched samples is determined by experiments and for each such geometry σ^* is evaluated via FE simulations of tensile tests of notched samples. The stress triaxiality is calculated at the ultimate load point. The five constants D_1 ... D_5 are experimentally determined via experimental and FE simulation results and are listed in Table 2.7a.

The first term in the Johnson-Cook failure model has been modified via various empirical relationships. The corresponding fitting equations are illustrated in Fig. 2.11 and provided below.

$$\varepsilon_f = [A + Bx + Cx^2 + Dx^3]\,[1 + D_4 \ln \dot{\varepsilon}^*][1 + D_5 T^*] \quad (\textit{Cubic}) \quad (2.14)$$

$$\varepsilon_f = [A + Bx + Cx^2]^{-1}\,[1 + D_4 \ln \dot{\varepsilon}^*][1 + D_5 T^*] \quad (\textit{Holliday}) \quad (2.15)$$

$$\varepsilon_f = [\frac{b+cx}{1+ax}]\,[1 + D_4 \ln \dot{\varepsilon}^*][1 + D_5 T^*] \quad (\textit{Rational0}) \tag{2.16}$$

$$\varepsilon_f = [\frac{b+x}{a+cx}]\,[1 + D_4 \ln \dot{\varepsilon}^*][1 + D_5 T^*] \quad (\textit{Rational3}) \tag{2.17}$$

$$\varepsilon_f = [\frac{a+bx}{1+cx+dx^2}][1 + D_4 \ln \dot{\varepsilon}^*][1 + D_5 T^*] \quad (\textit{Rational5}) \tag{2.18}$$

$$\varepsilon_f = [\frac{1}{a+bx}]\,[1 + D_4 \ln \dot{\varepsilon}^*][1 + D_5 T^*] \quad (\textit{Reciprocal}) \tag{2.19}$$

$$\varepsilon_f = [\frac{a}{1+bx}]\,[1 + D_4 \ln \dot{\varepsilon}^*][1 + D_5 T^*] \quad (\textit{ReciprocalModl}) \tag{2.20}$$

$$\varepsilon_f = [a + b\rho^x]^{-1}\,[1 + D_4 \ln \dot{\varepsilon}^*][1 + D_5 T^*] \quad (\textit{YldFert}) \tag{2.21}$$

$$\varepsilon_f = [a + be^{-kx}]^{-1}\,[1 + D_4 \ln \dot{\varepsilon}^*][1 + D_5 T^*] \quad (\textit{YldFert1}) \tag{2.22}$$

$$\varepsilon_f = [a + bx + cr^x]^{-1}\,[1 + D_4 \ln \dot{\varepsilon}^*][1 + D_5 T^*] \quad (\textit{Shah}) \tag{2.23}$$

These equations can be applied to different materials, depending on the specific material failure response that needs to be analyzed. The effect of using Shah Equation, compared with the original exponential term in the J-C failure model (first bracket), is analyzed and discussed in Section 2.4, "Results and Discussion". The Shah Equation parameters are listed in Table 2.7b.

Now, the damage of an element is defined by Eq. 2.24:

$$D = \sum\left(\Delta\varepsilon_p / \varepsilon_f\right) \tag{2.24}$$

where $\Delta\varepsilon_p$ is an increment of plastic strain, and the damage variable D is a scalar value that ranges from 0 to 1. The initial damage of 0.001 is considered in this work when manufacturing defects are considered. The equivalent plastic strains at the element integration points are used in the damage estimation. When D reaches a critical value, D_c ($D = D_c \leq 1$), softening will occur.

The investigation revealed that damage is constant during the development of microcracks caused by dislocation pile-up. There is a certain point where damage begins to occur as a result of accumulated plastic strain [54]

$$\dot{D} = \begin{cases} 0 & when, \varepsilon_{pl} < \varepsilon_{p,d} \\ \frac{D_c}{\varepsilon_f - \varepsilon_{p,d}}\,\dot{\varepsilon}_{pl} & when, \varepsilon_{pl} \geq \varepsilon_{p,d} \end{cases} \tag{2.25}$$

where D_c is the critical damage and where $\varepsilon_{p,d}$ is the damage threshold [75].

This failure model prescribed in the J-C model is capable of capturing the nonlinearity present in

the experimental behavior, but the damage growth law is linear. Hence, a nonlinear definition of damage evolution is proposed in this work. The damage is thought to occur in two phases. The rate of damage growth is very slow in the initial phase. This is because void nucleation alone is responsible for the initial damage. The damage growth law, in this phase, is given as a linear function of critical damage:

$$\dot{D}_i = D_c/(D_c - \dot{D}_{Ci}) \tag{2.26}$$

Here, $\dot{D}_{Ci}$ is the damage initiation at necking. $\dot{D}_{Ci}$ is assumed to have a low value of 0.1% when $\varepsilon_{pl} < \varepsilon_{p,d}$ until the ultimate stress is reached. Damage growth is accelerated after the ultimate point during the necking process because of void growth and coalescence. At this stage, the damage growth is nonlinear and is expressed as Eq. 2.27.

$$\dot{D} = \frac{\dot{D}_i\, D_c}{\varepsilon_f - \varepsilon_{p,d}}\, \dot{\varepsilon}_{pl} \tag{2.27}$$

Since damage decreases the material strength during deformation, the equation for the affected material is as follows:

$$\sigma_D = \left(1 - \dot{D}\right) \sigma_{eq} \tag{2.28}$$

where σ_D is the stress in the damaged state and σ_{eq} is obtained from the material models. The damage parameters are extracted from the experimental data of flat-notched samples. The procedure is well explained in the literature [54,76,77]. The strain-rate and temperature affect damage under all kinds of loading, whether it is quasi-static, dynamic or impact.

Table 2.7a displays the material parameters for three material models (J-C, MJ-C, and R-K) and the J-C failure parameters derived from tensile tests conducted at various strain-rates and temperatures.

Table 2.7a Viscoplastic material models and failure model coefficient values

J-C model constants	Value	MJ-C model constants	Value	R-K model constants	Value	J-C Failure model constants	Value
A	854.34 MPa	A	854.34 MPa	B_0	1467.72 MPa	D_1	0.043
B	1789.69 MPa	B	1789.69 MPa	n_0	0.078	D_2	0.91
C	0.0081	G_1	0.005	ε_0	0.0041	D_3	-6.42
n	0.86	G_2	0.58	D_1	0.65	D_4	0.174
m	1.50	r	0.93	v	0.247	D_5	1.22
		G_3	0.707	σ_0^*	656.12 MPa	D_{c2}	0.6
		m	0.77	m	2.94	D_{c1}	0.05
				D_2	0.02		
				θ^*	0.61		
				T_m	1773 K		
				$\dot{\varepsilon}_{max}$	10^7		
				$\dot{\varepsilon}_{min}$	10^{-5}		

Table 2.7b Shah Equation parameter values

a	b	c	r
0.033	-0.02	2.22	5.97e-06

2.3.2 Modelling and simulation

The constitutive model and failure criteria are implemented in ABAQUS FE software through a UMAT subroutine. When an element meets the failure criterion, the material softens, the stress decreases, and the element is eventually removed, reducing its load-bearing capacity to zero. To assess the accuracy of the constitutive models, 29 tensile tests on armor steel specimens at different $\dot{\varepsilon}$ and T were simulated in ABAQUS [78]. All the material models used the same damage model. A round specimen with a 40 mm gauge length and a 6 mm diameter (Fig. 2.12a) was first modelled to validate the parameters by predicting the load *vs* displacement, with the results discussed in section 2.2.2.

For simulation at intermediate strain-rate (0.8 s^{-1}, 9.37 s^{-1} and 36.439 s^{-1}) a flat quarter-section of the specimen with a 25 mm gauge length, 5 mm width, and 1.5 mm thickness (Fig. 2.12c) was modelled for FE simulation [73]. The quarter specimen geometry was discretized into 250 linear hexahedral elements (C3D8) elements, each 1 mm in size, with 468 nodes. Axisymmetric boundary conditions were applied (Fig. 2.12b & d), with a velocity boundary condition at the free

end for loading.

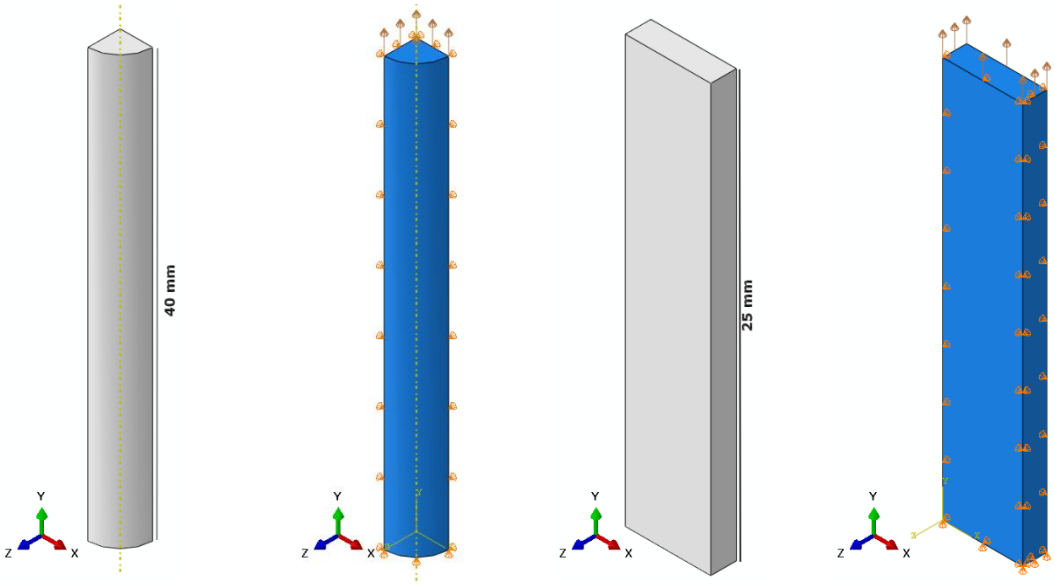

(a) (b) (c) (d)

Fig. 2.12 Tensile test specimen model (a) quarter model of round specimen (b) boundary conditions on round specimen, (c) quarter flat specimen, (d) boundary conditions on flat specimen

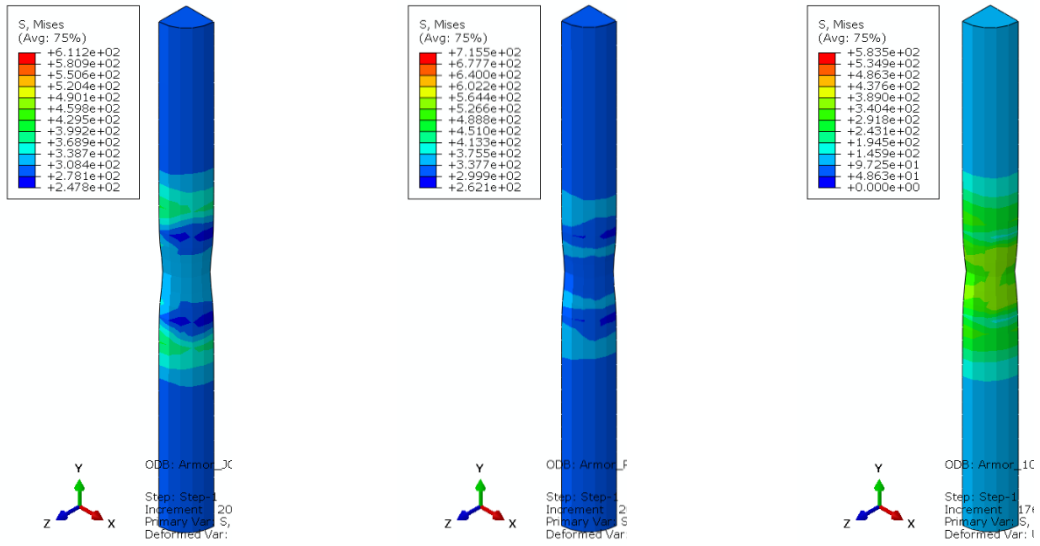

J-C R-K MJ-C

Fig. 2.13 Deformation patterns of round tensile specimen as predicted by different material models at $10^{-3}\ s^{-1}$ $\dot{\varepsilon}$ and at room T

The deformation patterns of the samples from J-C, R-K and MJ-C models are shown in Fig. 2.13

& 2.14. The true stress-strain curves obtained by implementing the J-C, MJ-C and R-K material models are compared with the experimental results. The numerical simulation results of the high-temperature tensile test for strain-rates of $10^{-4}\ s^{-1} \leq \dot{\varepsilon}_p \leq 10^{-1}\ s^{-1}$ are shown in Figs. 2.21-2.24. The simulation results predicted by the MJ-C model at a $\dot{\varepsilon}$ of $10^{-4}\ s^{-1}$ are similar to those of the J-C model because the parameters *A*, *B*, and *n* for the J-C and MJ-C models are the same.

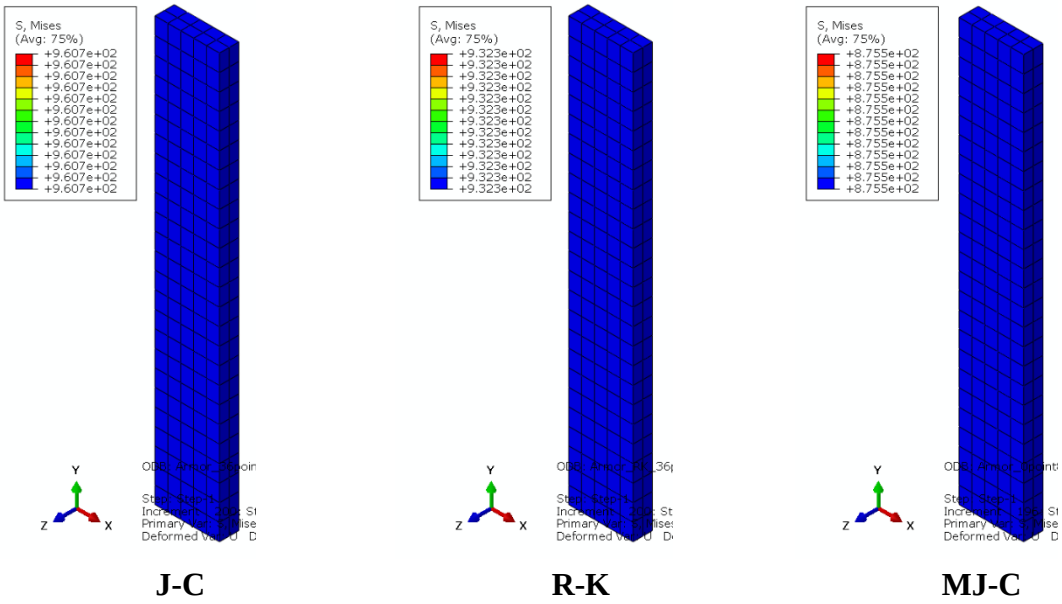

Fig. 2.14 Deformation patterns by using different material models at a strain-rate of 36.439 s^{-1} at room temperature

Figs. 2.17a-g illustrates that the J-C model did not correctly estimate the nature of the flow stress, σ_f within the studied range of strain-rates, especially at strain-rates ranging from 10^{-4} to 10^{-1} s^{-1} and intermediate $\dot{\varepsilon}$ ranging from 9.37 - 36.439 s^{-1}. It also does not correctly estimate the nature of the σ_f at high *T*, such as 200℃ at $\dot{\varepsilon}$ of 10^{-4} s^{-1} and 10^{-1} s^{-1}, 300℃ at $\dot{\varepsilon}$ of 10^{-2} s^{-1} and 10^{-1} s^{-1}, 400℃ at $\dot{\varepsilon}$ of 10^{-3} s^{-1} and 10^{-2} s^{-1}, 500℃ at $\dot{\varepsilon}$ of 10^{-4} s^{-1}, as shown in Figs. 2.21-2.24. Additionally, at high *T*, the work hardening rate is lower than the thermal softening rate, and in the J-C model, the $\dot{\varepsilon}$ coefficient is independent of *T*.

In contrast, the R-K model accurately predicts the material response up to a $\dot{\varepsilon}$ of 0.01 s^{-1} at room temperature, after which it begins to overpredict as shown in Fig. 2.17. The simulations by the J-C model are closer to the experimental results than those by the R-K model, especially when a high strain-rate is involved, and as a consequence, modifications to the J-C model are suggested to make the predictions more in agreement. The failure model is less sensitive to the strain-rate if the value of stress triaxiality is calculated at the fracture point [59] whereas if the value of stress

triaxiality is calculated at the ultimate stress the failure model is sensitive to the strain-rate from room to high temperatures as shown in Fig. 2.21-2.24.

In addition to the ultimate stress at all strain rates, whether at room or high temperatures, with the three-material model adopted, the simulations reveal the different natures of the curve after necking with the same failure and damage model parameters; here, the stress response is predominantly governed by the failure and damage model.

Interestingly, the softening rate due to the damage evolution law adopted is somewhat better when the R-K model is applied at room temperature, but at high temperatures, the MJ-C model is better.

2.3.2.1 Validation of the material models parameters by load *vs* displacement response

Armour steel - The material parameters are derived from experimental stress-strain data. Therefore, comparing the simulated and experimental load-displacement behaviors highlights the effectiveness of the material models in predicting material behavior, the precision of the extracted parameters, and the accuracy of the extraction process. The simulation is conducted on a quarter round tensile specimen part with 40 mm gauge length and a 6 mm diameter, as illustrated in Fig. 2.13 and results are shown in Figs. 2.15 & 2.16.

(a)

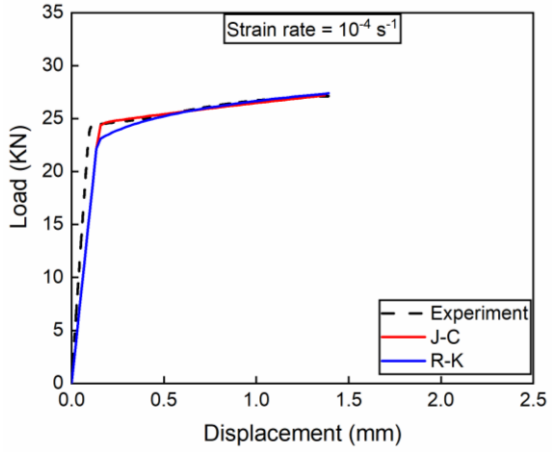

(b)

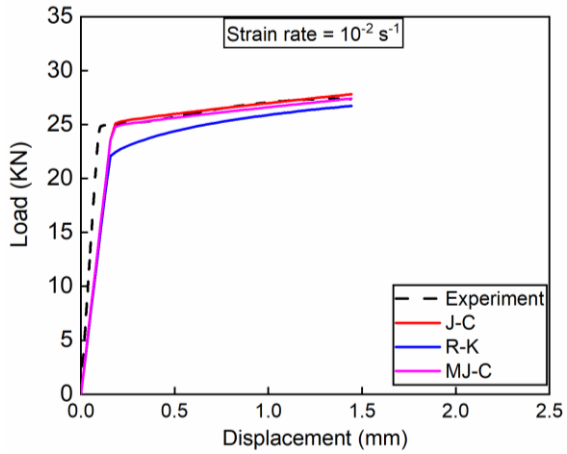

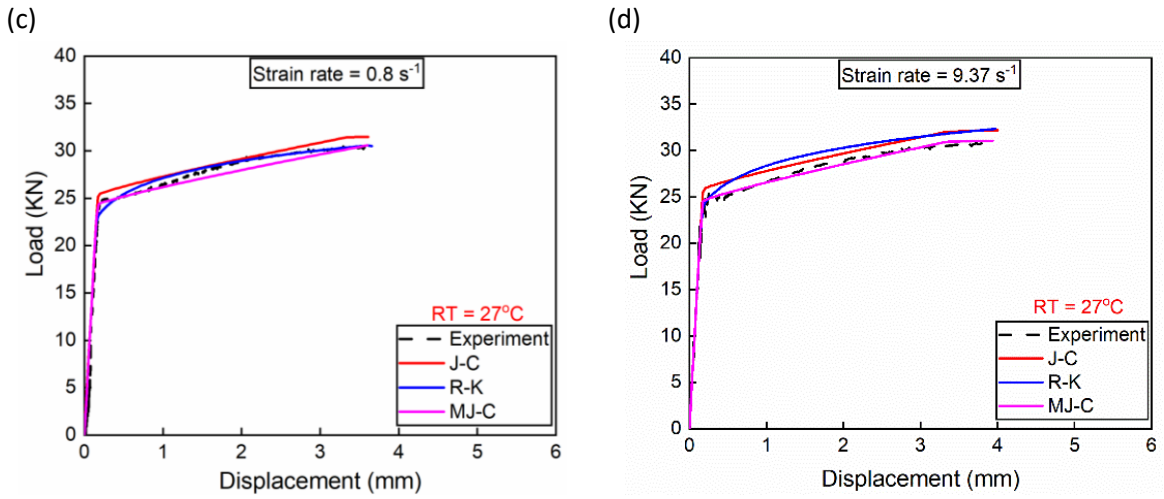

Fig. 2.15 Load *vs* displacement curves at RT and $\dot{\varepsilon}$ of (a) 10^{-4}, (b) 10^{-2}, (c) 0.8 s^{-1} , and (d) 9.37, s^{-1}

In Figs. 2.17a-d, at 27°C, strain rates 10^{-4} s^{-1} and 10^{-2} s^{-1} in the quasi-static range and strain-rates of 0.8 s^{-1} and 9.37 s^{-1} in the intermediate range are compared with the experimental results.

It is evident from the plots that the MJ-C model provides better simulations of the load-displacement behaviors at both low and high plastic deformations than the J-C and R-K models do.

Figs. 2.16a-d show comparisons of the load *vs* displacement responses between the experimental data and the FE simulation. These comparisons were conducted at a $\dot{\varepsilon}$ of 10^{-4} s^{-1} and T varying from 200°C to 500°C. Although the nonlinearity at high temperatures is better captured by the R-K model, the overall prediction is better by the MJ-C model.

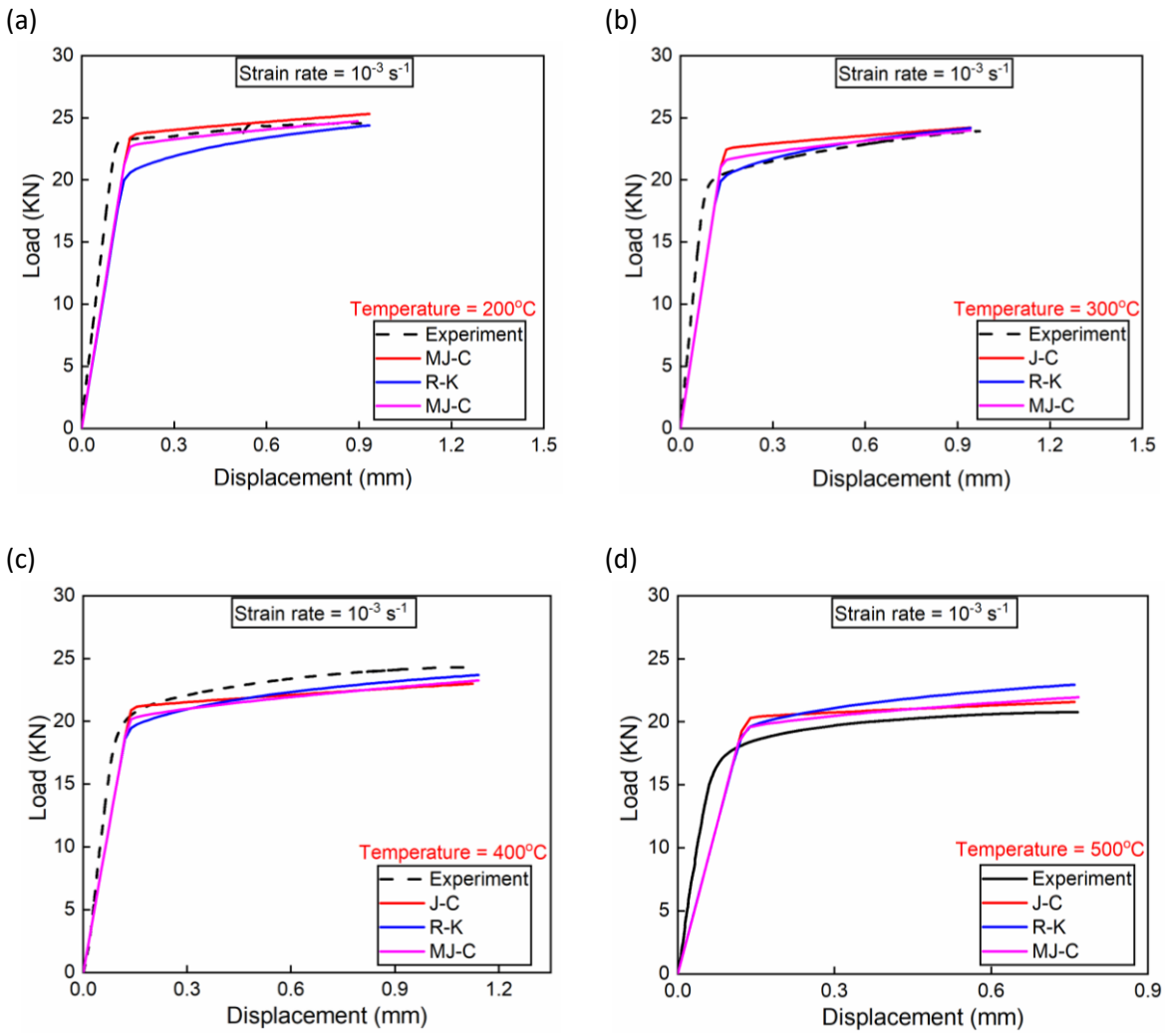

Fig. 2.16 Load *vs* displacement curves at 10^{-3} s^{-1} strain-rate and (a) 200°C, (b) 300°C, (c) 400°C, and (d) 500°C

According to these observations, it is apparent that the MJ-C model outperforms the other two models in terms of predicting the actual deformation behavior of the material. Although the J-C and R-K material model predictions are good for a specific range of temperatures and $\dot{\varepsilon}$ for this material, the MJ-C model captures the material response much better overall, especially at high strain-rates.

(a)

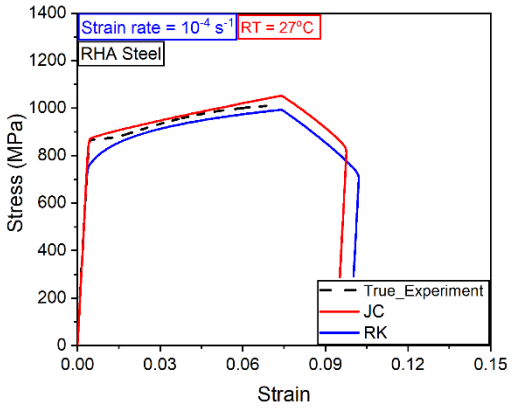
Strain rate = 10-4 s-1
RT = 27°C
RHA Steel
Stress (MPa)
Strain
True_Experiment
JC
RK

(b)

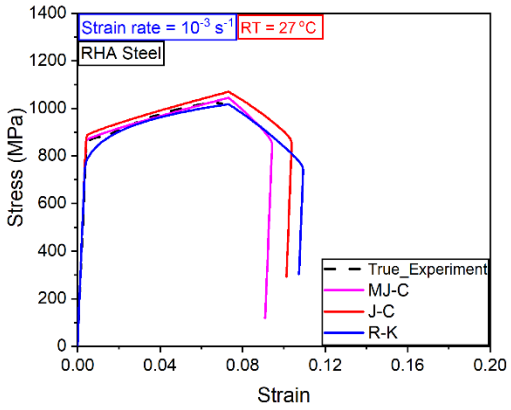
Strain rate = 10-3 s-1
RT = 27 °C
RHA Steel
Stress (MPa)
Strain
True_Experiment
MJ-C
J-C
R-K

(c)

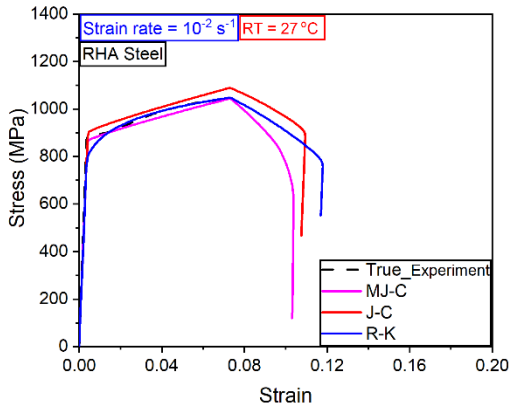
Strain rate = 10-2 s-1
RT = 27 °C
RHA Steel
Stress (MPa)
Strain
True_Experiment
MJ-C
J-C
R-K

(d)

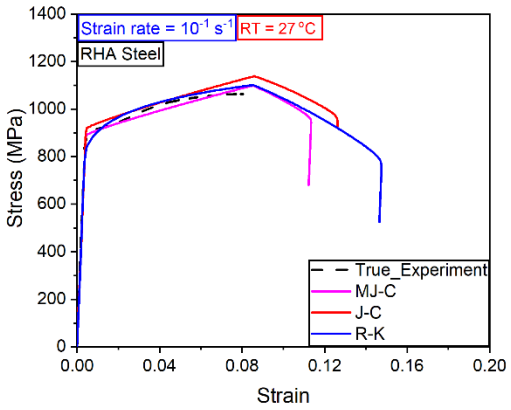
Strain rate = 10-1 s-1
RT = 27 °C
RHA Steel
Stress (MPa)
Strain
True_Experiment
MJ-C
J-C
R-K

(e)

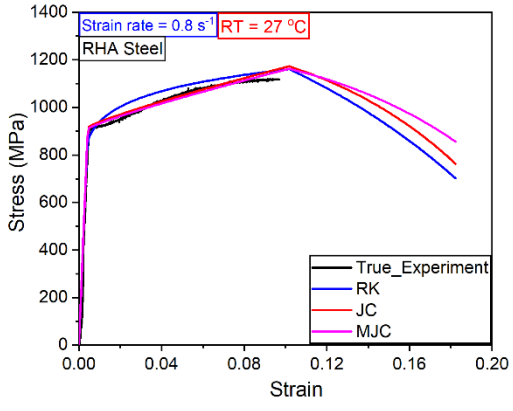
Strain rate = 0.8 s-1
RT = 27 °C
RHA Steel
Stress (MPa)
Strain
True_Experiment
RK
JC
MJC

(f)

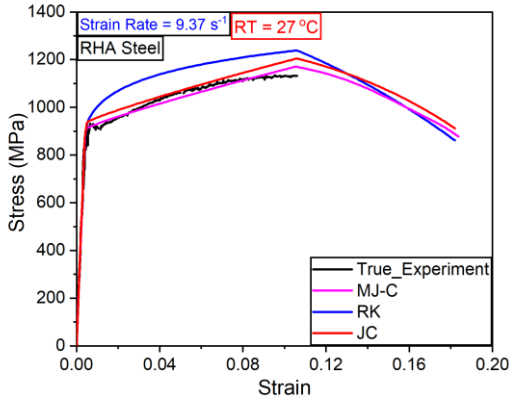
Strain Rate = 9.37 s-1
RT = 27 °C
RHA Steel
Stress (MPa)
Strain
True_Experiment
MJ-C
RK
JC

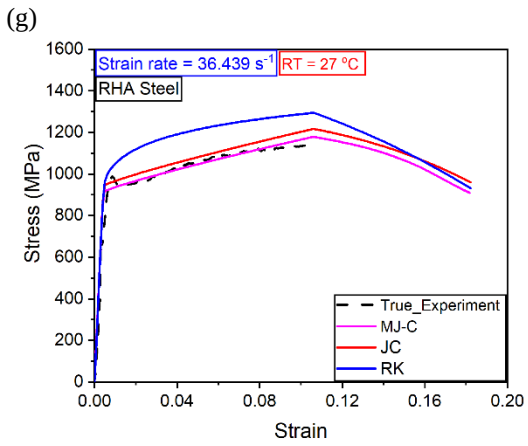

Fig. 2.17 True stress - true strain curves of tensile tests done at RT and $\dot{\varepsilon}$, (a) 10^{-4}, (b) 10^{-3}, (c) 10^{-2}, (d) 10^{-1} ,(e) 0.8 , (f) 9.37 , and (g) 36.439, s^{-1}

Projectile steel – The J-C strength model parameters extracted for PHS 1500 steel are validated by predicting load vs displacement and true stress vs true strain at room and $300^{o}C$ and comparing the same with the experimental results as shown in Fig. 2.18-2.20. The simulated results are closely matching with the experimental results.

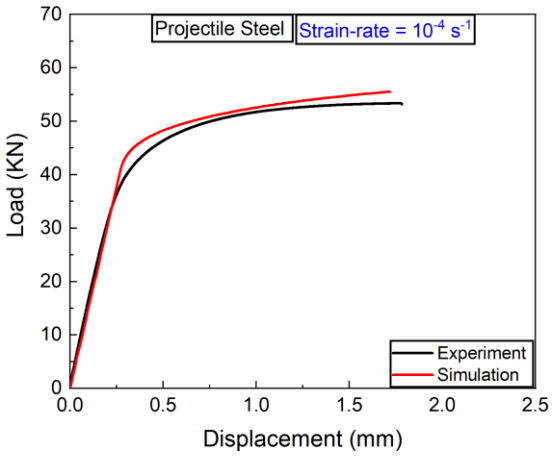

Fig. 2.18 Load *vs* displacement curves at RT and strain-rates of 10^{-4} s^{-1}

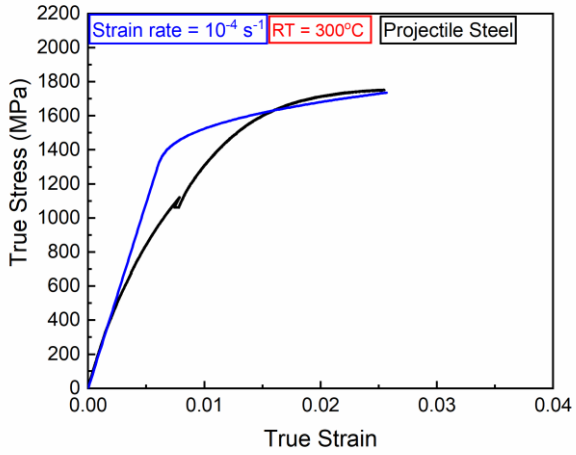

Fig. 2.19 True stress *vs* true strain curves at 10^{-4} s^{-1} strain-rate and 300°C temperature

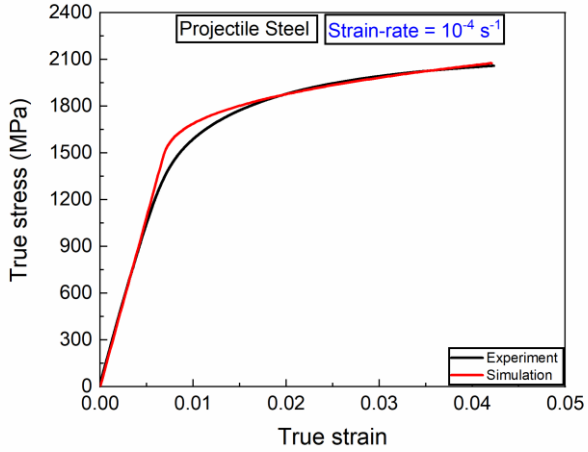

Fig. 2.20 True stress - true strain curves at RT and 10^{-4} s^{-1} strain-rate

2.4 Results and Discussion

To facilitate comparison and quantification, the experimental results and the predictions from the J-C, R-K, and MJ-C models are displayed together in Figs. 2.21-2.24. To more effectively evaluate the performance of these material models across varying degrees of plastic deformation, the yield stresses, the true stress at a specific plastic strain level (4%) Fig 2.25b and the ultimate stresses at different $\dot{\varepsilon}$ and T are plotted individually Fig 2.25c.

(a) (b)

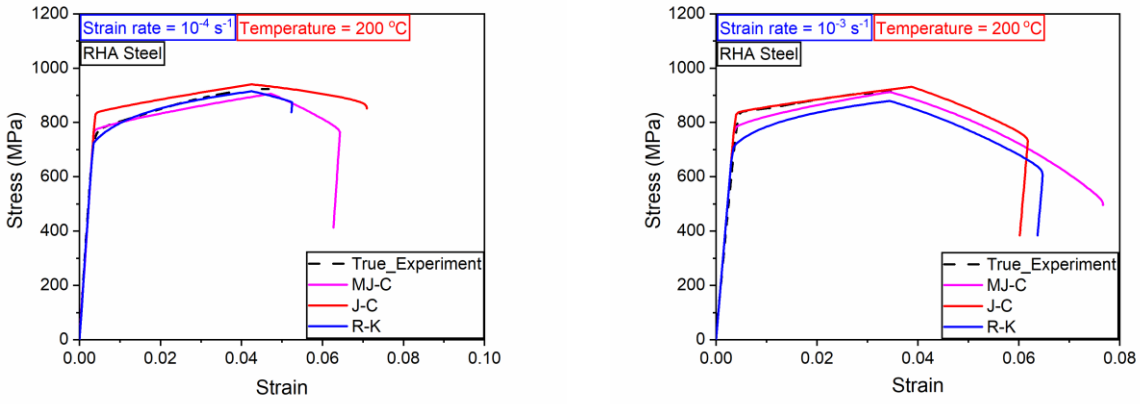

(c) (d)

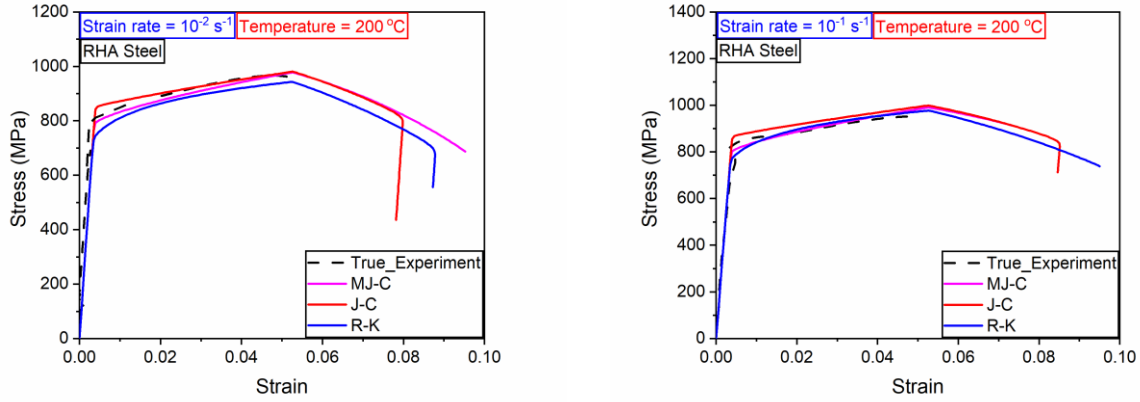

Fig. 2.21 True stress-strain curves at 200℃ for (a) 10^{-4} , (b) 10^{-3}, (c) 10^{-2}, and (d) 10^{-1}, s^{-1}

2.4.1 Strain-rate sensitivity

The $\dot{\varepsilon}$ sensitivity is prominent at higher plastic deformation levels and gradually saturates beyond a certain strain-rate (approximately1 s^{-1}) at room temperature, as shown in experimental curve in Fig. 2.17. For the ultimate stress, the $\dot{\varepsilon}$ sensitivity increases but at a slower rate after (approximately 1 s^{-1}) $\dot{\varepsilon}$.

The first comparison is performed via analysis of the $\dot{\varepsilon}$ effect for quasi-static and intermediate loading [79]. For quasi-static loading, the $\dot{\varepsilon}$ range was $10^{-4}\ s^{-1} \leq \dot{\varepsilon}_p \leq 10^{-1}\ s^{-1}$. From the experimental results, at higher temperatures, between $\dot{\varepsilon}$ of approximately $10^{-3}\ s^{-1}$ and $10^{-2}\ s^{-1}$, a negative $\dot{\varepsilon}$ sensitivity is evident as shown in Fig. 2.8.

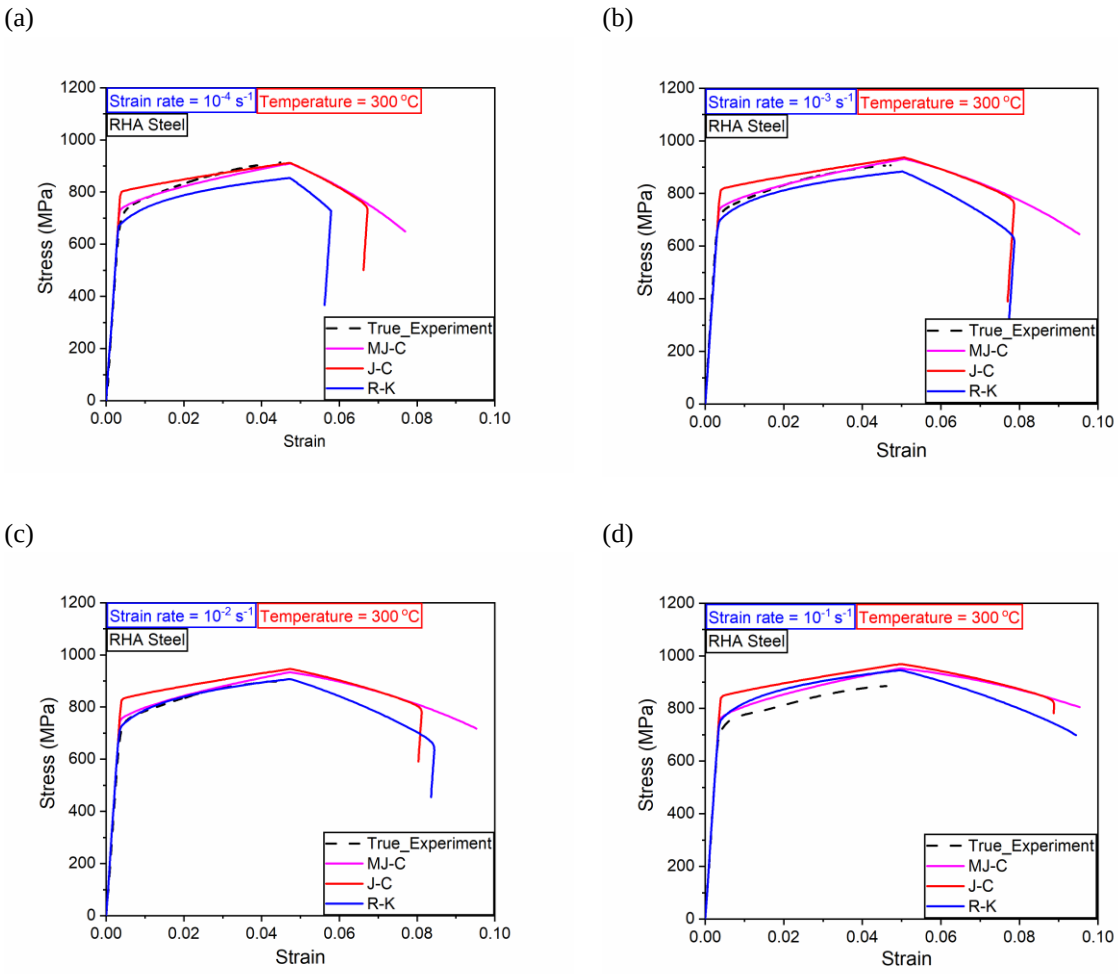

Fig. 2.22 True stress-strain curves at 300°C for (a) 10^{-4}, (b) 10^{-3}, (c) 10^{-2} and (d) 10^{-1} s^{-1}

In the intermediate range, $0.8\,s^{-1} \leq \dot{\varepsilon}_p \leq 36.439\,s^{-1}$, as observed in Figs. 2.17e-g; beyond a strain-rate of approximately $0.8\,s^{-1}$, a lower strain-rate sensitivity is observed. In Figs. 2.17e-g, the MJ-C model predicted the actual flow curve of the armor steel better than the J-C model did and was closest among the models considered until the ultimate point, which can be seen in Fig. 2.17.

Beyond the ultimate stress, the simulated material behavior is a joint contribution of a material model and, predominantly, of a damage model. Before the ultimate point where the material models were predominant, the agreement with the actual data was good. After the ultimate stress the actual response is speculated to be attributed to the damage model, and it is different for all three material models.

At this point, it is important to realize that softening due to damage should be gradual. The nonlinearity of the stress-strain relationships during the damage evolution stage is adequately simulated by all three material models, but the slopes of the softening curves are different.

Although none of the material models accurately captured the negative strain-rate sensitivity, they all predicted the experimental flow stress within 10% accuracy across all test temperatures. At low levels of plastic deformation, near the yield point, the MJ-C model consistently performed well with increasing test temperatures, as demonstrated in Fig. 2.25a. The R-K model has the worst yield stress prediction at room and high temperatures as shown in Fig 2.26 and the J-C model also fails to accurately predict the yield stress.

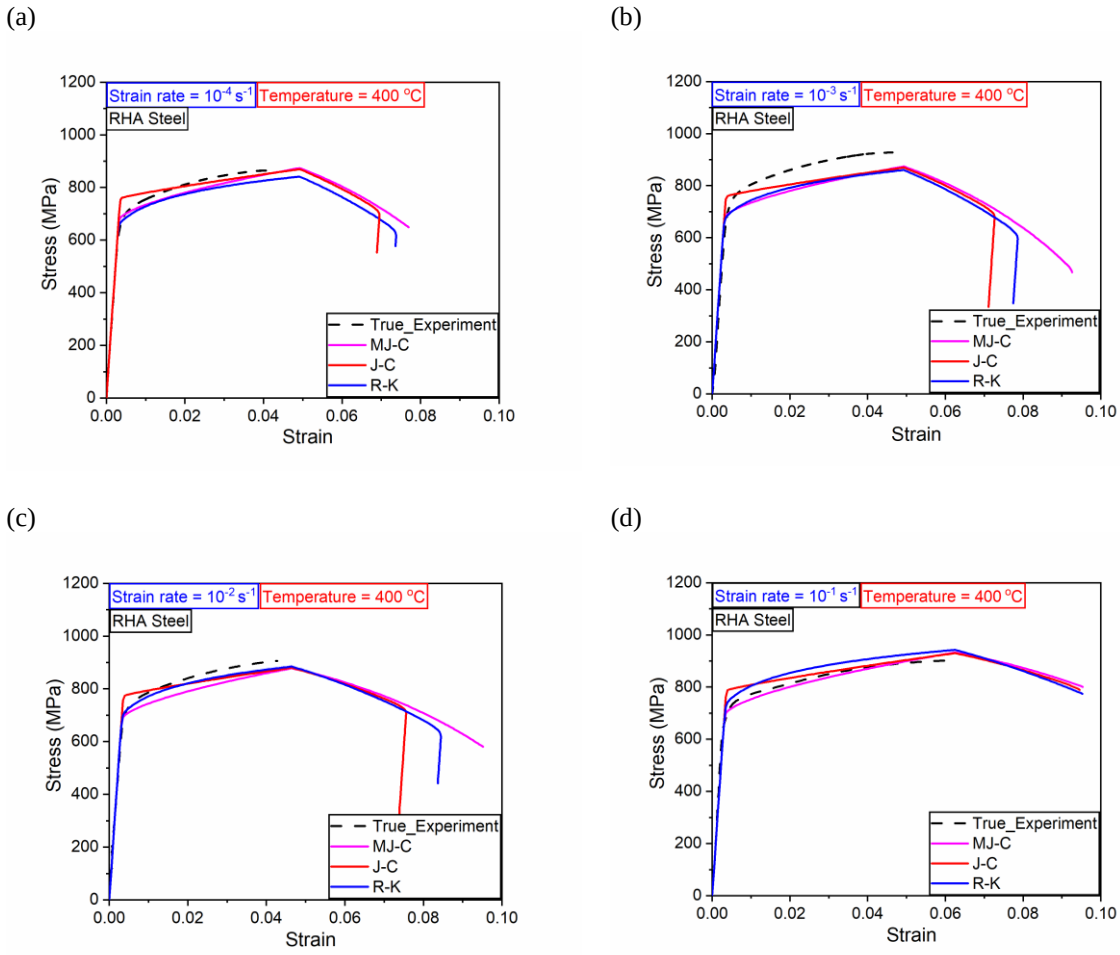

Fig. 2.23 True stress-strain curves at 400℃ for (a) 10^{-4}, (b) 10^{-3}, (c) 10^{-2} and (d) 10^{-1} s^{-1}

(a) (b)

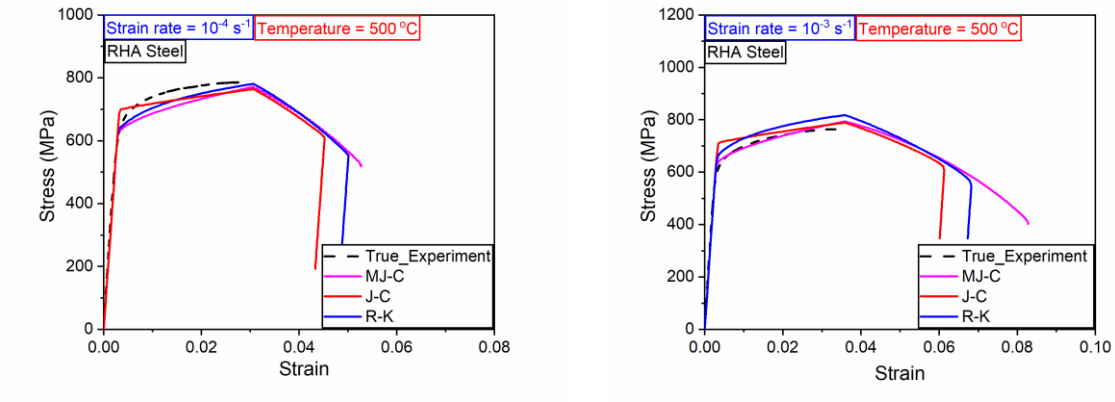

(c) (d)

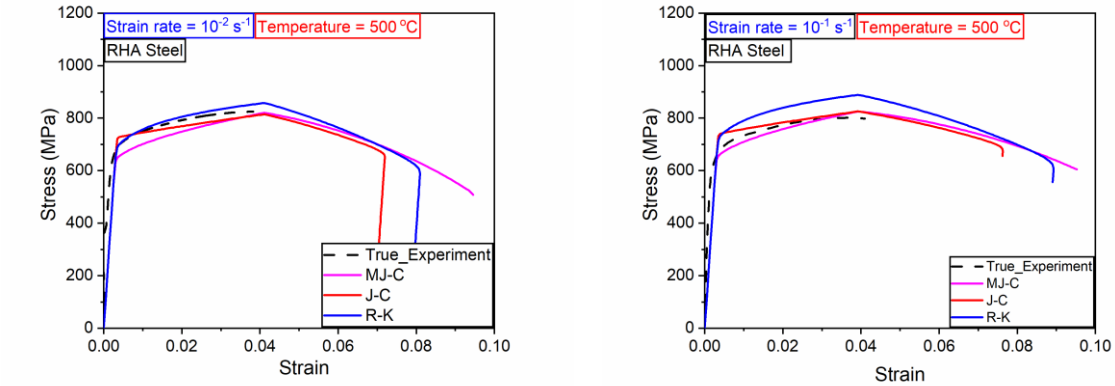

Fig. 2.24 True stress-strain curves at 500°C for (a) 10^{-4}, (b) 10^{-3}, (c) 10^{-2} and (d) 10^{-1} s^{-1}

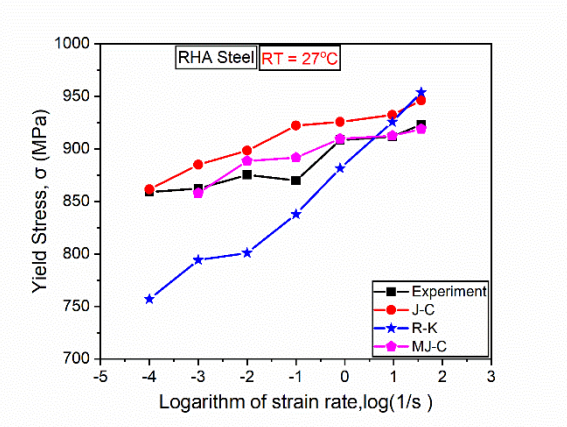

Fig. 2.25a Strain-rates sensitivity at yield stress & RT

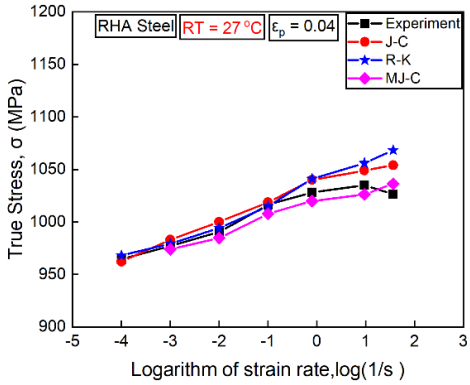

Fig. 2.25b Strain-rates sensitivity at 4% strain & RT

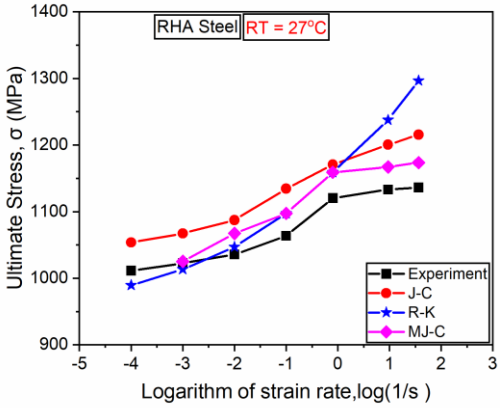

Fig. 2.25c Strain-rate sensitivity at the ultimate stress and RT

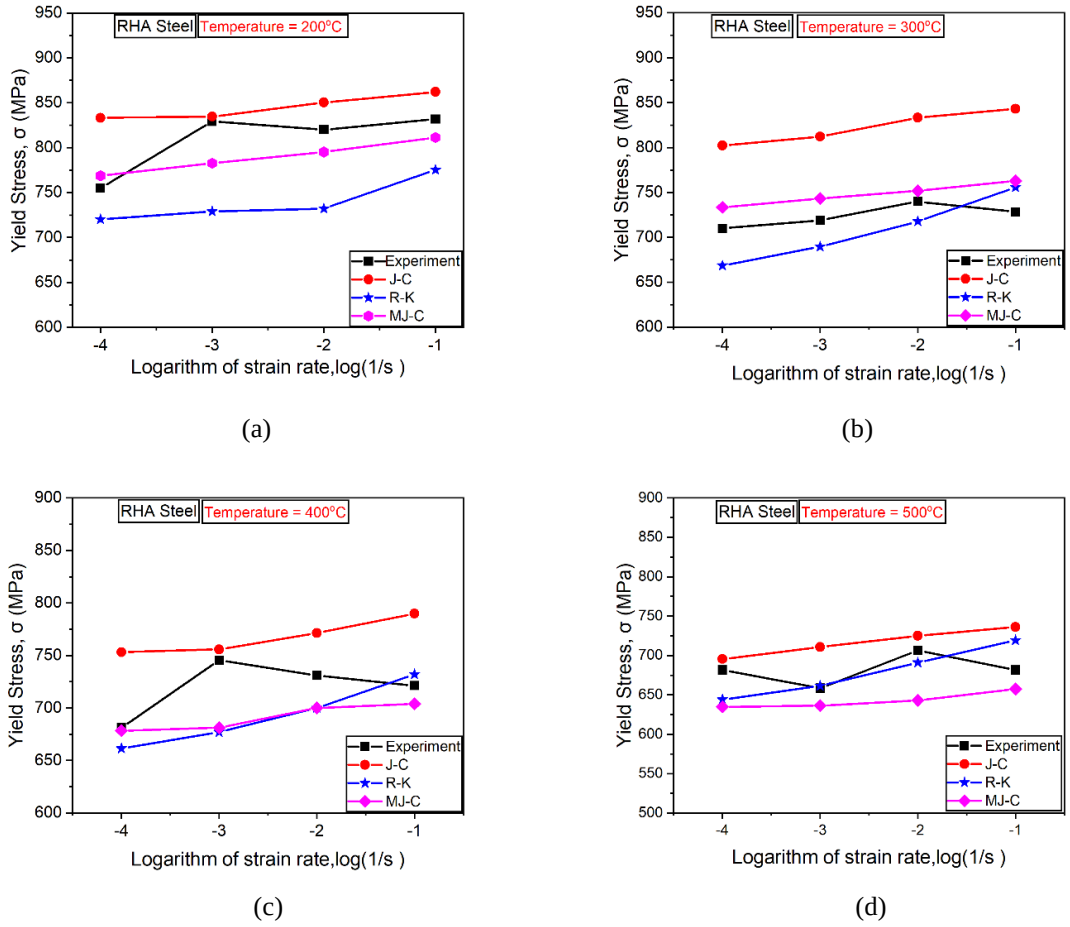

Fig. 2.26 Strain-rate sensitivity at yield at (a) 200°C (b) 300°C (c) 400°C (d) 500°C

The $\dot{\varepsilon}$ sensitivity of the material models at a ε_p of 4% is illustrated in Fig. 2.25b. The R-K model tends to overpredict the $\dot{\varepsilon}$ sensitivity beyond a $\dot{\varepsilon}$ of 0.1 s^{-1}, suggesting limitations in its accuracy at higher $\dot{\varepsilon}$. The Johnson-Cook model provides a more accurate prediction than the R-K model within the same strain-rate range, although slight deviations are still observed. In contrast, the MJ-C model delivers the most accurate predictions, showing the best correlation with experimental data across the $\dot{\varepsilon}$ range.

A similar trend is observed in predictions of ultimate stress, as shown in Fig. 2.25c. The R-K model tends to overestimate the ultimate stress at higher strain rates, whereas the J-C model offers a better but still imperfect fit. The MJ-C model again stands out by providing the most reliable predictions of the ultimate stress, which aligns closely with the experimental results.

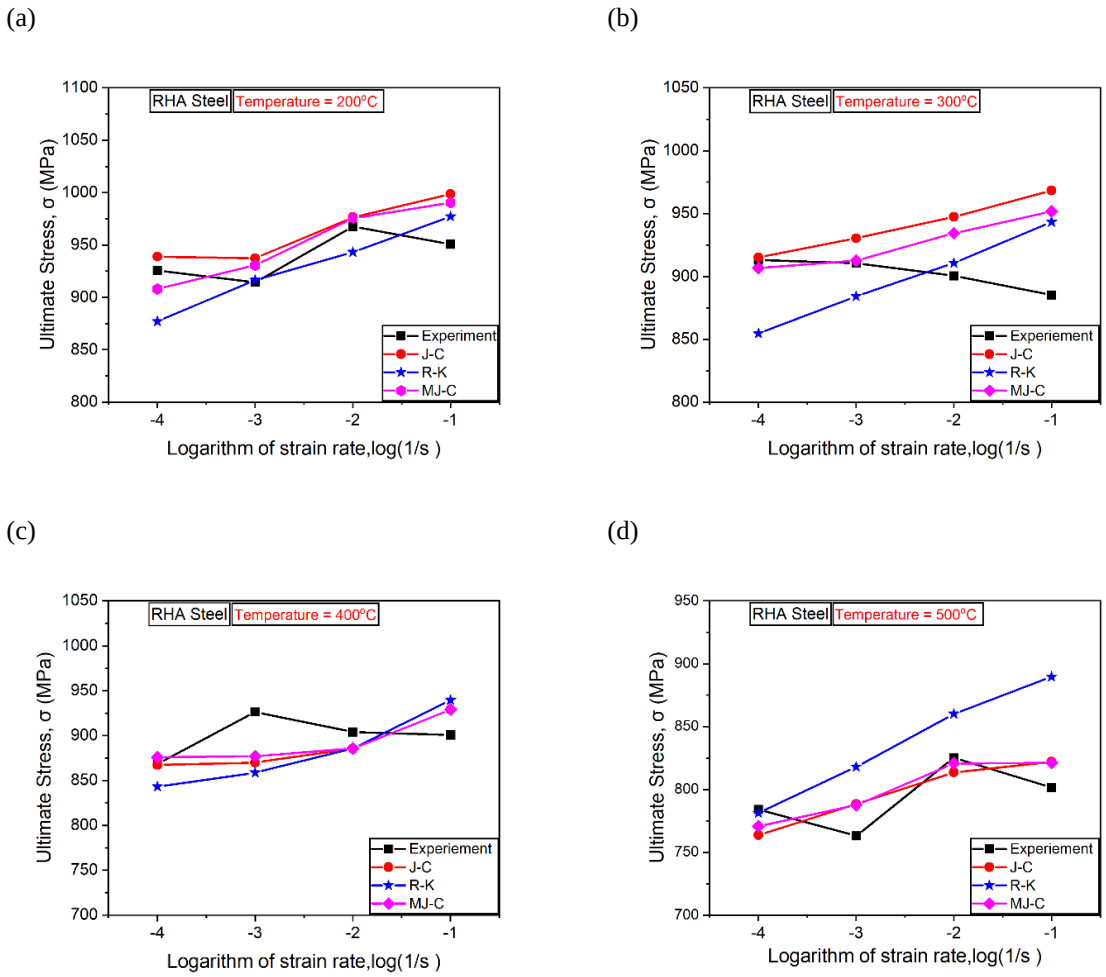

Fig. 2.27 Strain-rate sensitivity at ultimate stress at (a) 200°C (b) 300°C (c) 400°C (d) 500°C

Figs. 2.25-2.27 clearly show that the MJ-C model prediction for yield and ultimate stress is the best among all three material models.

2.4.2 Temperature sensitivity

To validate the J-C, R-K and MJ-C models, different test temperatures are preselected for armor steel ranging from 27 °C $\leq T \leq$ 500°C at quasi-static $\dot{\varepsilon}$ ranging from 10^{-4} s^{-1} $\leq \dot{\varepsilon}_p \leq 10^{-1}$ s^{-1}. The overall trend in the experimental data also indicates a decrease, except for an intermediate temperature range where negative temperature (300°C - 400°C) sensitivity is observed. The simulated results shown in Figs. 2.26-2.27, indicate that the J-C, MJ-C and R-K models predict

yield stresses that decrease as the temperature increases as shown in Fig. 2.28 also. Similar observations are made for the ultimate stresses shown in Figs. 2.26-2.27. Only the R-K model ultimate stress slightly increases from 300℃ to 400℃ at a $\dot{\varepsilon}$ of 10^{-1} s^{-1} as shown in Fig. 2.28.

(a)

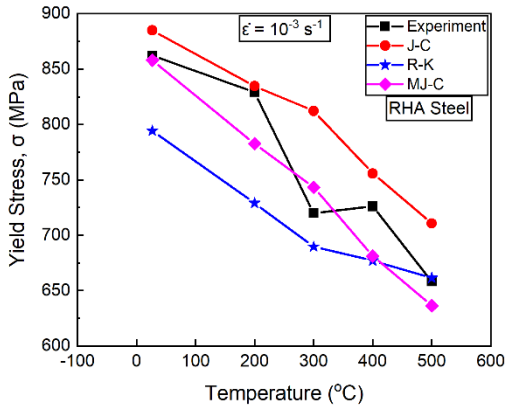

(b)

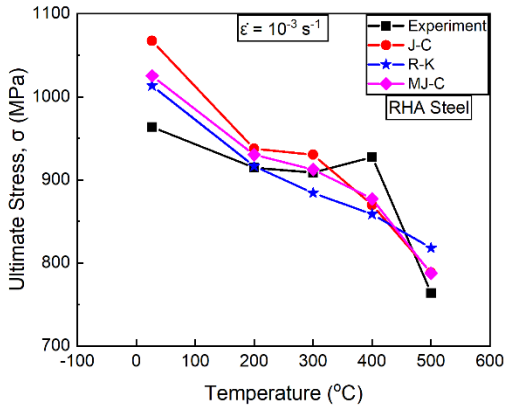

(c)

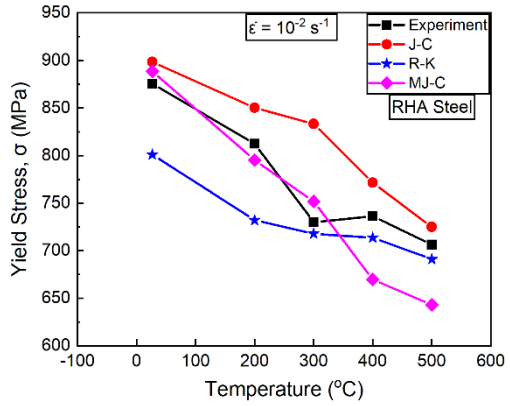

(d)

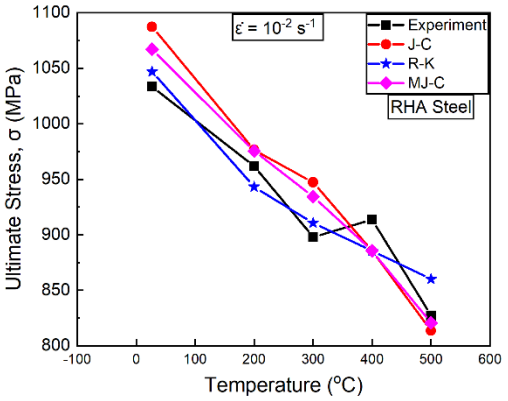

(e) (f)

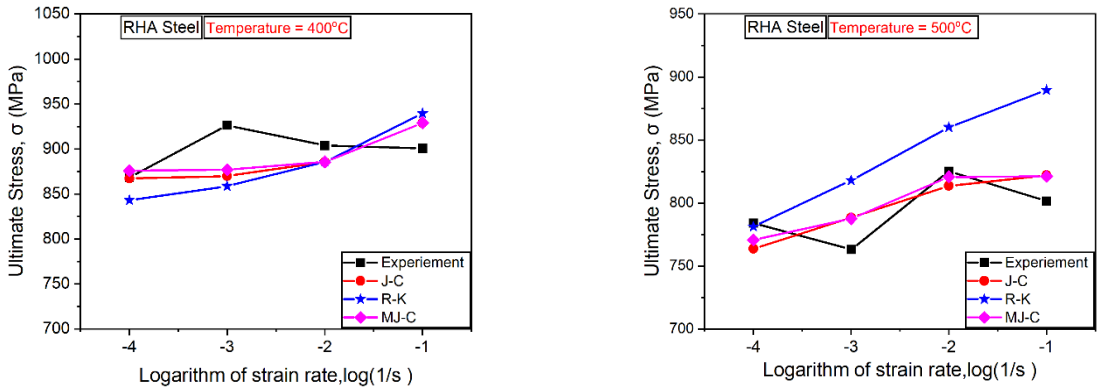

Fig. 2.28 Temperature sensitivity of material models in prediction of yield stress and ultimate stress, at different strain-rates

In the R-K model, temperature and strain-rate effects are interdependent, leading to a trade-off between thermal softening and strain-rate hardening during simulation, which may result in 'negative rate sensitivity' behavior. Although similar outcomes can be predicted by other coupled models, they fail to accurately simulate the underlying physics of this negative sensitivity. On the basis of these observations, the MJ-C model offers more accurate predictions than the other two material models within the temperature range of 27℃ - 500℃.

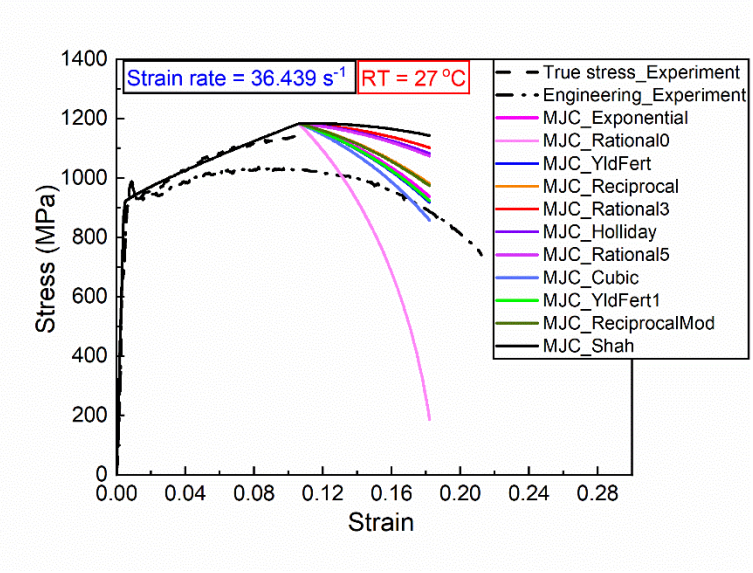

Fig. 2.29 Stress-strain curves at 36.439 s^{-1} strain-rate

2.4.3 Comparative study of different equations in failure model of the Johnson-Cook

The different fitted equations for stress triaxiality with fracture strain are now simulated for a $\dot{\varepsilon}$ of 36.439 s^{-1} as shown in Fig. 2.29. The results indicate that each equation produces distinct failure behaviors. Among them, the exponential and Shah exponential equations were selected for further analysis because of their superior ability as shown in Fig. 2.29 to predict failure behavior in RHA steel, with the Shah equation chosen specifically for its stable failure predictions. To validate these models, additional simulations were conducted via the general exponential equation from the J-C failure model and the Shah exponential equation. These simulations were performed at $\dot{\varepsilon}$ of 0.8 s^{-1}, 9.37 s^{-1}, and 36.739 s^{-1} at 27℃, (see Figs. 2.30a-b) as well as at elevated T ranging from 200℃ to 500℃ with a $\dot{\varepsilon}$ of 0.1 s^{-1} (see Figs. 2.30c-f). The comparison highlights the model's performance across varying $\dot{\varepsilon}$ and T.

(a)

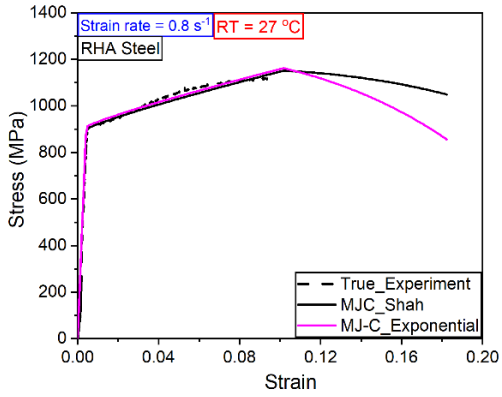

(b)

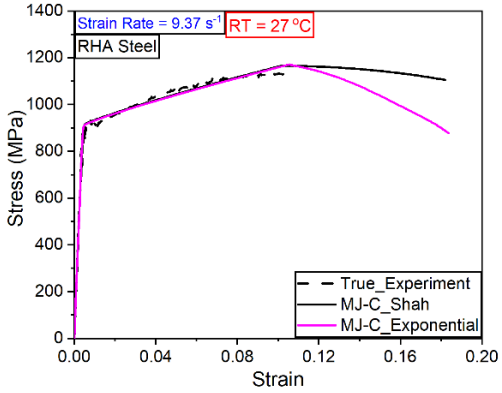

(c)

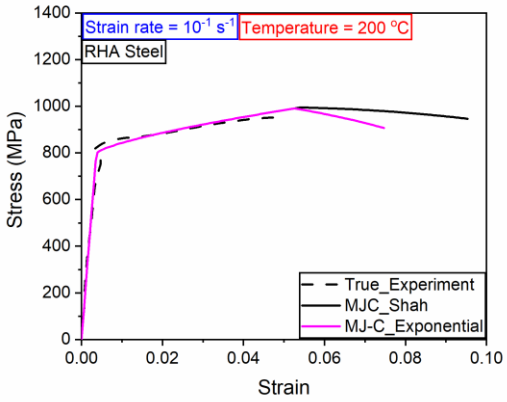

(d)

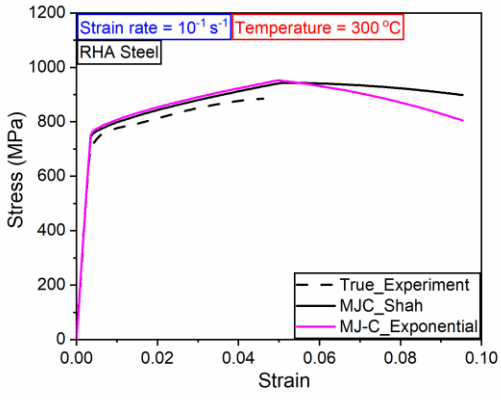

(e) (f)

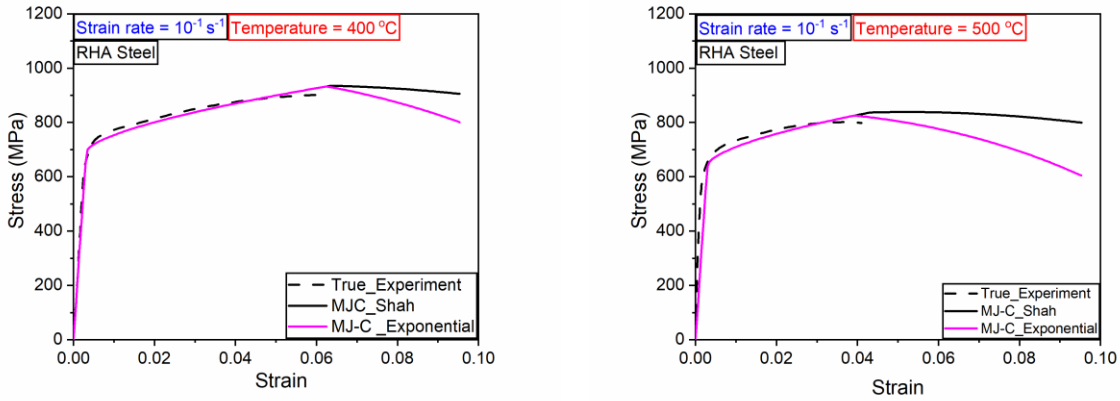

Fig. 2.30 Stress-strain curves at different temperature at $\dot{\varepsilon}$ 10^{-1} s^{-1}

2.5 Quantitative assessments of the material models

By comparing the FE curves simulated using the J-C, R-K and MJ-C material models with the experimental curves, a rudimentary and qualitative assessment of the model efficacy was possible. The errors in the prediction of yield stress and ultimate stress by the three models at RT and at elevated temperatures are quantified and compared [57,72,80].

The prediction error, Δ, is calculated via Eq. 2.29 and used to compare the abilities of various constitutive models quantitatively [57,72,81,82].

$$\Delta = \frac{1}{N}\sum_{i=1}^{N}\left|\frac{\sigma_i^{exp}-\sigma_i^{pre}}{\sigma_i^{exp}}\right| \times 100\% \qquad (2.29)$$

where σ_i^{exp} and σ_i^{pre} denote the experimental and model-predicted stress values, respectively. The description errors for each simulation for each model are first calculated, and then the average percentage errors are obtained separately, as shown in Figs. 2.31a & 2.32a.

It is evident from Figs. 2.31a & 2.32a that the overall MJ-C simulation is better. The intermediate strain-rate simulations are more inaccurate because the dynamic effects are neglected during simulation. Fig. 2.31a shows that considerable error in yield stress prediction by the R-K model is due mainly to its theoretical construction. It is also noticeable from Figs. 2.31b & 2.31b that at approximately 400°C, there are considerable errors when all the material models. It appears that this is due to the negative $\dot{\varepsilon}$ sensitivity, as material models are incapable of capturing, as discussed previously.

(a) (b)

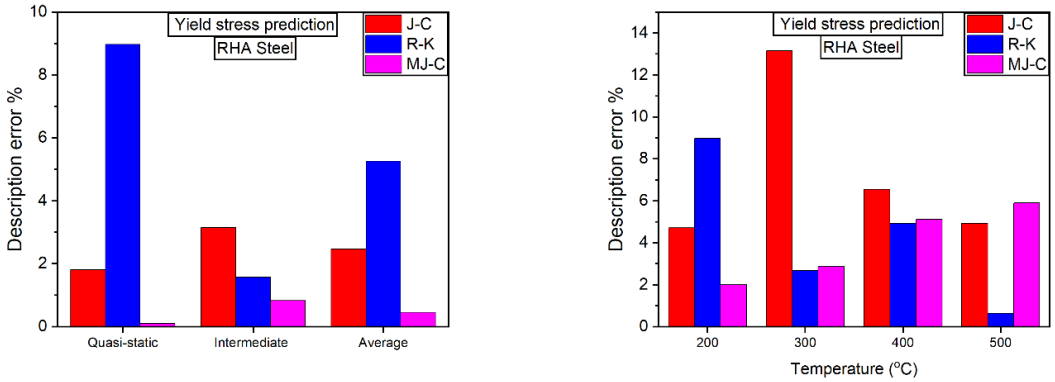

Fig. 2.31 Error in prediction of yield stress at (a) 27°C (b) high temperatures

(a) (b)

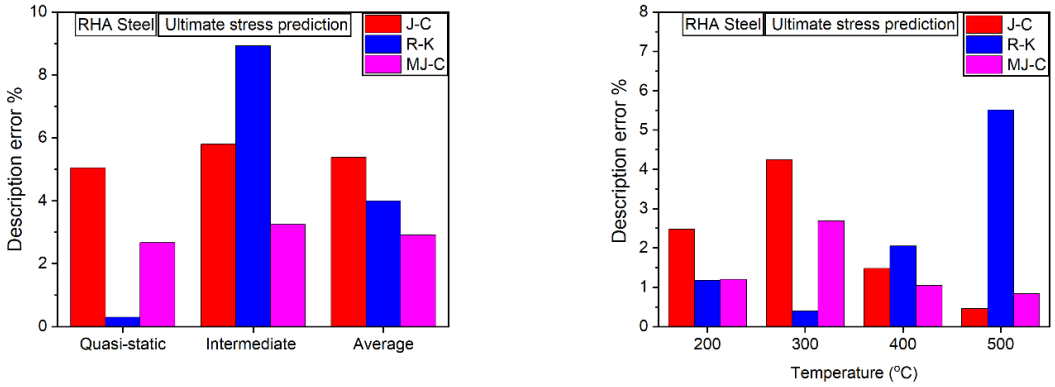

Fig. 2.32 Error in prediction of ultimate stress at (a) 27°C (b) high temperatures

2.5.1 Description capability of different models vs. number of material parameters used

Fig. 2.33 shows the prediction error *vs* material parameter number for all the material models. This plot shows the error-simplicity compromise, if any. The J-C model has the lowest material parameters, but the error is high.

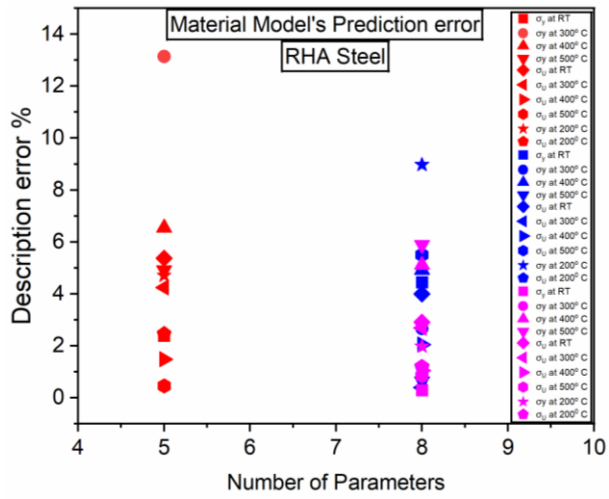

Fig. 2.33 Relationship between each material models parameter count and description error

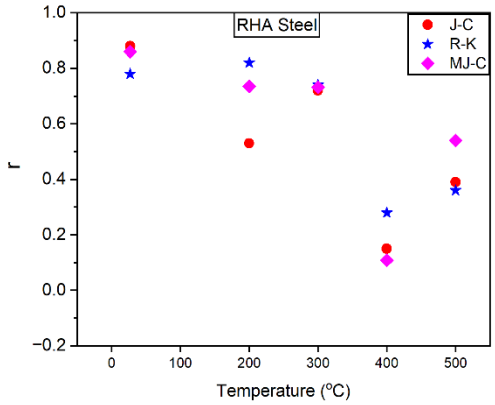

Fig. 2.33 Plot of correlation coefficient values for three material models

Table 2.8 Prediction errors of σ_y at room temperature

Material models	**Percentage of prediction error**	
	Quasi-Static	**Intermediate**
	σ_y	**σ_y**
J-C	1.81	3.14
R-K	8.97	1.56
MJ-C	0.09	0.82

Table 2.9 Prediction error of σ_y at elevated temperatures

Material models	**Percentage of prediction error**			
	σ_y at 200°C	**σ_y at 300°C**	**σ_y at 400°C**	**σ_y at 500°C**
J-C	4.71	13.14	6.55	4.92
R-K	8.97	2.67	4.92	0.63
MJ-C	1.98	2.85	5.12	5.89

Table 2.10 Prediction error of σ_u at elevated temperatures

Material models	Percentage of prediction error				
	σ_u at RT	σ_u at 200°C	σ_u at 300°C	σ_u at 400°C	σ_u at 500°C
J-C	5.05	2.47	4.25	1.48	0.46
R-K	0.30	1.18	0.39	2.05	5.51
MJ-C	2.67	1.20	2.69	1.05	0.84

All model errors at different stresses are listed in Table 2.8-2.10. It is important to note that the R-K and MJ-C models share the same number of parameters (eight) (Fig. 2.33). Despite this, the MJ-C model has better prediction capability, and the equation is simpler.

2.5.2 Correlation coefficients for the models

The Pearson correlation coefficient is calculated to analyze the correlation between the experimental and simulated ultimate stress data extracted by via material models. It is expressed by Eq. 2.30 [83].

$$r = \frac{n(\sum xz) - (\sum x)(\sum z)}{\sqrt{[nx^2 - (\sum x)^2][n\sum z^2 - (\sum z)^2]}} \tag{2.30}$$

where n is the number of experimental values at a particular strain-rate. Here, $n = 4$ and $n = 7$ are taken because the experiments are conducted at four quasi-static $\dot{\varepsilon}$, three are conducted in the intermediate range, and x and z are the experimental value and material model values, respectively.

Table 2.11 Correlation coefficient values for the three material models

Material models	Correlation coefficient values r				
	σ_y at RT	σ_y at 200°C	σ_y at 300°C	σ_y at 400°C	σ_y at 500°C
J-C	0.88	0.53	0.72	0.15	0.39
R-K	0.78	0.82	0.74	0.28	0.36
MJ-C	0.86	0.73	0.73	0.10	0.54

The correlation coefficient values for the three material models are shown in Table 2.11 and are plotted in Fig. 2.33. At room temperature, the coefficient is very weak for the J-C material model and strong for the R-K and MJ-C material models. Overall, the correlation coefficient is strong for the MJ-C model.

2.6 Conclusion

The thermomechanical behaviour of a typical rolled homogeneous armour steel is investigated in this work at temperatures ranging from ambient temperature (27℃) to 500℃, and $\dot{\varepsilon}$ ranging from 10^{-4} s^{-1} to 36.439 s^{-1}. Three material models are employed to simulate steel deformation under high loading conditions: the Johnson-Cook (J-C) model, the Rusinek-Klepaczko (R-K) model, and the modified Johnson-Cook (MJ-C) model, which is derived from the J-C model. From the results of the simulations, the following conclusions are drawn:

- The flow stress predictions from the J-C and R-K material models are in good agreement with the experimental data within specific $\dot{\varepsilon}$ ranges at both room and elevated temperatures. However, their accuracy is limited when they are applied across the entire strain-rate range. In particular, the R-K model, which uses stress decomposition, proves ineffective in capturing the material's behavior at intermediate strain rates, highlighting its limitations for this range of conditions.
- The proposed modification to the J-C material model aims to account for the influence of temperature on strain hardening, sensitivity to strain-rate, and sensitivity to temperature. This modification involves alterations in the strain hardening exponent, the equation for $\dot{\varepsilon}$ sensitivity, and the *T* function.
- The modified damage growth law is applied to simulate the accelerated reduction in load-bearing capacity, which is consistent with experimental observations. The simulation is performed on the tensile test of a specimen using three different material models: the J-C, R-K, and MJ-C models. The results reveal significant differences in the nature of damage evolution across the models, both at room *T* and at elevated *T*. Each model captures distinct aspects of material degradation, with variations in strain hardening, thermal softening, and damage accumulation behavior. These discrepancies highlight the sensitivity of damage growth to the choice of material model, particularly under varying temperature conditions.
- Different fitted equations relating stress triaxiality to fracture strain were simulated for a strain rate of 36.439 s^{-1} (see Fig. 2.24). Each equation results in distinct failure behaviors, suggesting that alternative formulations may provide improved predictions of failure behavior for RHA steel. These variations offer the potential for refining failure predictions under specific conditions, enhancing the accuracy of the material models.
- In terms of computational time, the J-C model is the fastest, the R-K model takes the longest, and the MJ-C model falls in between the other models in terms of analysis time.
- Quantitative analysis of the MJ-C model reveals a prediction error of less than 2% for both yield stress and ultimate tensile stress at room temperature. For high-temperature tensile tests, the prediction error remains under 3% for both yield and ultimate stresses. These

error margins fall within acceptable limits for material model validation, demonstrating the high accuracy of the MJ-C model in capturing the stress-strain behavior of the material across different temperature conditions. This level of precision confirms the model's reliability for simulating both room and elevated temperature deformation responses.

- For RHA steel (body-centered tetragonal, BCT structure), highlighting the suitability of different material models on the basis of $\dot{\varepsilon}$ and T conditions is important. The J-C model is effective for predicting material behavior at quasi-static $\dot{\varepsilon}$, but its accuracy is limited to room temperature conditions. The R-K model, however, is found to be unsuitable for accurately capturing the material's response under these conditions. In contrast, the MJ-C model demonstrates broader applicability, providing reliable predictions across a wider range of $\dot{\varepsilon}$, from quasi-static to intermediate, and for elevated temperature scenarios. This makes the MJ-C model the most appropriate for simulating the deformation behavior of typical armour steel under varying loading and thermal conditions.
- Experimental observations indicate that the material exhibits positive $\dot{\varepsilon}$ and T sensitivity over the majority of the testing range. However, within a narrow window of $\dot{\varepsilon}$ and temperature, a negative $\dot{\varepsilon}$ and temperature sensitivity are observed. While this negative rate effect was not thoroughly investigated in this study, understanding the thermomechanical behavior of RHA steel material remains critical. The observed negative sensitivity could be attributed to dynamic strain aging in the microstructure of the material, which occurs within a specific range of T and $\dot{\varepsilon}$. To fully capture these effects, the current material models should be adjusted to account for such negative sensitivities, enhancing their adaptability and accuracy. Further investigations into this phenomenon would be valuable extensions of the present work.
- Each of the three material models—J-C, R-K, and MJ-C—offers distinct capabilities in describing the mechanical behavior of metallic materials. These models vary in their ability to capture key phenomena such as strain hardening, thermal softening, and damage evolution. Therefore, the selection of an appropriate material model should be based on the specific application and operating conditions, including the strain rate, temperature, and desired accuracy of the predictions. For optimal simulation accuracy and material response prediction, it is essential to match the material model to the relevant environmental conditions and mechanical demands of the intended use.

References

[1] Whittington WR, Oppedal AL, Turnage S, Hammi Y, Rhee H, Allison PG, et al. Capturing the effect of temperature, strain rate, and stress state on the plasticity and fracture of rolled homogeneous armor (RHA) steel. Mater Sci Eng A 2014;594:82–8. https://doi.org/10.1016/j.msea.2013.11.018.

[2] Woo SC, Kim JT, Kim JY, Kim TW. Correlation of fracture processes and damage mechanisms of armor structural materials under high strain rates with acoustic emission characteristics. Int J Impact Eng 2014;63:29–42. https://doi.org/10.1016/j.ijimpeng.2013.07.007.

[3] Fellows NA, Harding J. Localization of plastic deformation during high strain rate torsion testing of rolled homogeneous armour. J Strain Anal Eng Des 2001;36:197–210. https://doi.org/10.1243/0309324011512748.

[4] Magness LS. High strain rate deformation behaviors of kinetic energy penetrator materials during ballistic impact. Mech Mater 1994;17:147–54. https://doi.org/10.1016/0167-6636(94)90055-8.

[5] Hecker SS, Stout MG, Staudhammer KP, Smith JL. Effects of Strain State and Strain Rate on Deformation-Induced Transformation in 304 Stainless Steel: Part I. Magnetic Measurements and Mechanical Behavior. Metall Trans A 1982;13:619–26. https://doi.org/10.1007/BF02644427.

[6] Bodner S. R., Partom Y. Constitutive Equations for Elastic-Viscoplastic Strain-Hardening Materials. J Appl Mech 1975;42:385–9. https://doi.org/10.1115/1.3423586.

[7] Zerilli Frank J., Armstrong Ronald W. Dislocation-mechanics-based constitutive relations for material dynamics calculations. J Appl Phys 1998;61:1816. https://doi.org/10.1063/1.338024.

[8] Molinari A., Ravichandran G. Constitutive modeling of high-strain-rate deformation in metals based on the evolution of an effective microstructural length. Mech Mater 2005;37:737–52. https://doi.org/10.1016/J.MECHMAT.2004.07.005.

[9] Nemat-Nasser S, Li YF, Isaacs JB. Experimental/ computational evaluation of flow stress at high strain rates with application to adiabatic shear banding. Mech Mater 1994;17:111–34. https://doi.org/10.1016/0167-6636(94)90053-1.

[10] Rusinek A, Zaera R, Klepaczko JR. Constitutive relations in 3-D for a wide range of strain rates and temperatures – Application to mild steels. Int J Solids Struct 2007;44:5611–34. https://doi.org/10.1016/J.IJSOLSTR.2007.01.015.

[11] Johnson GR, Cook WH. A Computational Constitutive Model and Data for Metals

Subjected to Large Strain, High Strain Rates and High Pressures. 1983.
[12] Zhao Han, Gary Gérard. The testing and behaviour modelling of sheet metals at strain rates from 10−4 to 104 s−1. Mater Sci Eng A 1996;207:46–50. https://doi.org/10.1016/0921-5093(95)10017-2.
[13] Zhao Han, Gary Gérard. On the use of SHPB techniques to determine the dynamic behavior of materials in the range of small strains. Int J Solids Struct 1996;33:3363–75. https://doi.org/10.1016/0020-7683(95)00186-7.
[14] Khan AS, Liang R. Behaviors of three BCC metal over a wide range of strain rates and temperatures: Experiments and modeling. Int J Plast 1999;15:1089–109. https://doi.org/10.1016/S0749-6419(99)00030-3.
[15] Khan AS, Suh YS, Kazmi R. Quasi-static and dynamic loading responses and constitutive modeling of titanium alloys. Int J Plast 2004;20:2233–48. https://doi.org/10.1016/j.ijplas.2003.06.005.
[16] Paul S, Dey P, Bhattacharjee S, Acharyya SK, Sahoo P, Chattopadhyay J. Phenomenological modelling of flow behaviour of 20MnMoNi55 reactor pressure vessel steel at cryogenic temperature with different strain rates. Def Technol 2019;15:326–37. https://doi.org/10.1016/j.dt.2018.08.007.
[17] Nemat-Nasser S, Li Y. Flow stress of f.c.c. polycrystals with application to OFHC Cu. Acta Mater 1998;46:565–77. https://doi.org/10.1016/S1359-6454(97)00230-9.
[18] Rusinek A, Klepaczko JR. Shear testing of a sheet steel at wide range of strain rates and a constitutive relation with strain-rate and temperature dependence of the flow stress. Int J Plast 2001;17:87–115. https://doi.org/10.1016/S0749-6419(00)00020-6.
[19] Zerilli FJ, Armstrong RW. Dislocation-mechanics-based constitutive relations for material dynamics calculations. J Appl Phys 1987;61:1816–25. https://doi.org/10.1063/1.338024.
[20] Peixinho N, Jones N, Pinho A. Experimental and numerical study in axial crushing of thin walled sections made of high-strength steels. J Phys IV JP 2003;110:717–22. https://doi.org/10.1051/jp4:20020778.
[21] Johnson GR, Cook WH. A Constitutive Model and Data for Metals Subjected to Large Strains, High Strain Rates, and High Temperature . Proceeding's 7th Int Symp Ballist 1983:541–7.
[22] Klepaczko J, Duffy J. Strain Rate History Effects in Body-Centered-Cubic Metals. Am Soc Test Mater 1982:251–68.
[23] Follansbee PS, Kocks UF. A constitutive description of the deformation of copper based on the use of the mechanical threshold stress as an internal state variable. Acta Metall

1988;36:81–93. https://doi.org/10.1016/0001-6160(88)90030-2.

[24] Tong Wei, Clifton Rodney J., Huang Shihui. Pressure-shear impact investigation of strain rate history effects in oxygen-free high-conductivity copper. J Mech Phys Solids 1992;40:1251–94. https://doi.org/10.1016/0022-5096(92)90015-T.

[25] Bodner S. R., Rubin M. B. Modeling of hardening at very high strain rates. J Appl Phys 1998;76:2742. https://doi.org/10.1063/1.357578.

[26] Frutschy K. J., Clifton R. J. High-temperature pressure-shear plate impact experiments on ofhc copper. J Mech Phys Solids 1998;46:1723–44. https://doi.org/10.1016/S0022-5096(98)00055-6.

[27] Frutschy K. J., Clifton R. J. High-temperature pressure-shear plate impact experiments using pure tungsten carbide impactors. Exp Mech 1998 382 1998;38:116–25. https://doi.org/10.1007/BF02321654.

[28] Kotkunde Nitin, Deole Aditya D., Gupta Amit Kumar, Singh Swadesh Kumar. Comparative study of constitutive modeling for Ti–6Al–4V alloy at low strain rates and elevated temperatures. Mater Des 2014;55:999–1005. https://doi.org/10.1016/J.MATDES.2013.10.089.

[29] TAO Zhi jun, FAN Xiao guang, YANG He, MA Jun, LI Heng. A modified Johnson–Cook model for NC warm bending of large diameter thin-walled Ti–6Al–4V tube in wide ranges of strain rates and temperatures. Trans Nonferrous Met Soc China 2018;28:298–308. https://doi.org/10.1016/S1003-6326(18)64663-1.

[30] Fields DS, Backofen WA. Determination of strain hardening characteristics by torsion testing. Proc. ASTM, vol. 57, 1957, p. 1259–72.

[31] Prakash G, Singh NK, Gupta NK. Flow behaviour of Ti-6Al-4V alloy in a wide range of strain rates and temperatures under tensile, compressive and flexural loads. Int J Impact Eng 2023;176:104549. https://doi.org/10.1016/j.ijimpeng.2023.104549.

[32] Rasaee Sajad, Mirzaei A. H., Almasi D. Constitutive modelling of Al7075 using the Johnson–Cook model. Bull Mater Sci 2020;43:1–8. https://doi.org/10.1007/S12034-019-1987-X/FIGURES/12.

[33] Hu F, Liu X, Wang B, Xiang Y. Investigations on the Johnson-Cook Constitutive and Damage-Fracture Model Parameters of a Q345C Steel. Metals (Basel) 2024;14. https://doi.org/10.3390/met14050509.

[34] Levadnyi I, Liu F, Gu Y. Identification of material parameters at high strain rates using ballistic impact tests and inverse finite element analysis. AIP Adv 2024;14. https://doi.org/10.1063/5.0197149.

[35] Geng Peihao, Qin Guoliang, Zhou Jun, Zou Zengda. Hot deformation behavior and constitutive model of GH4169 superalloy for linear friction welding process. J Manuf Process 2018;32:469–81. https://doi.org/10.1016/J.JMAPRO.2018.03.017.

[36] C.M. Sellars, W.J. McTegart. On the mechanism of hot deformation. Acta Metall 1966;14:1136–8.

[37] Zhang Hongming, Chen Gang, Chen Qiang, Han Fei, Zhao Zude. A physically-based constitutive modelling of a high strength aluminum alloy at hot working conditions. J Alloys Compd 2018;743:283–93. https://doi.org/10.1016/J.JALLCOM.2018.02.039.

[38] Shen J, Hu L, Sun Y, Wan Z, Feng X, Ning Y. A Comparative Study on Artificial Neural Network, Phenomenological-Based Constitutive and Modified Fields–Backofen Models to Predict Flow Stress in Ti-4Al-3V-2Mo-2Fe Alloy. J Mater Eng Perform 2019;28:4302–15. https://doi.org/10.1007/S11665-019-04174-0/FIGURES/12.

[39] Lin Y. C., Dong Wen Yong, Zhou Mi, Wen Dong Xu, Chen Dong Dong. A unified constitutive model based on dislocation density for an Al-Zn-Mg-Cu alloy at time-variant hot deformation conditions. Mater Sci Eng A 2018;718:165–72. https://doi.org/10.1016/J.MSEA.2018.01.109.

[40] Korkmaz ME, Verleysen P, Günay M. Identification of Constitutive Model Parameters for Nimonic 80A Superalloy. Trans Indian Inst Met 2018;71:2945–52. https://doi.org/10.1007/s12666-018-1394-9.

[41] Korkmaz ME, Günay M, Verleysen P. Investigation of tensile Johnson-Cook model parameters for Nimonic 80A superalloy. J Alloys Compd 2019;801:542–9. https://doi.org/10.1016/j.jallcom.2019.06.153.

[42] Korkmaz ME. Determination and Verification of Johnson–Cook Parameters for 430 Ferritic Steels via Different Gage Lengths. Trans Indian Inst Met 2019;72:2663–72. https://doi.org/10.1007/s12666-019-01734-9.

[43] Korkmaz ME. Verification of Johnson-Cook parameters of ferritic stainless steel by drilling process: Experimental and finite element simulations. J Mater Res Technol 2020;9:6322–30. https://doi.org/10.1016/j.jmrt.2020.03.045.

[44] Aktürk M, Boy M, Gupta MK, Waqar S, Krolczyk GM, Korkmaz ME. Numerical and experimental investigations of built orientation dependent Johnson–Cook model for selective laser melting manufactured AlSi10Mg. J Mater Res Technol 2021;15:6244–59. https://doi.org/10.1016/j.jmrt.2021.11.062.

[45] Teker E, Danish M, Gupta MK, Kuntoğlu M, Korkmaz ME. Hot Deformation Behavior and Strain Rate Sensitivity of 33MnCrB5 Boron Steel Using Material Constitutive Equations.

Trans Indian Inst Met 2022;75:717–26. https://doi.org/10.1007/s12666-021-02474-5.

[46] Wang J, Hu X, Yuan K, Meng W, Li P. Impact resistance prediction of superalloy honeycomb using modified Johnson–Cook constitutive model and fracture criterion. Int J Impact Eng 2019;131:66–77. https://doi.org/10.1016/j.ijimpeng.2019.05.001.

[47] Rajaraman D, Hertelé S, Fauconnier D. A novel calibration procedure of Johnson-Cook damage model parameters for simulation of scratch abrasion. Wear 2023;528–529. https://doi.org/10.1016/j.wear.2023.204977.

[48] Gerstgrasser M, Smolenicki D, Akbari M, Klippel H, Roelofs H, Cadoni E, et al. Analysis of two parameter identification methods for original and modified Johnson-Cook fracture strains, including numerical comparison and validation of a new blue-brittle dependent fracture model for free-cutting steel 50SiB8. Theor Appl Fract Mech 2021;112:102905. https://doi.org/10.1016/j.tafmec.2021.102905.

[49] Buchely MF, Wang X, Van Aken DC, O'Malley RJ, Lekakh S, Chandrashekhara K. The Use of Genetic Algorithms to Calibrate Johnson-Cook Strength and Failure Parameters of AISI/SAE 1018 Steel. J Eng Mater Technol Trans ASME 2019;141. https://doi.org/10.1115/1.4042382.

[50] Van der Giessen E, Needleman A. Discrete dislocation plasticity: A simple planar model. Model Simul Mater Sci Eng 1995;3:689–735. https://doi.org/10.1088/0965-0393/3/5/008.

[51] Ortiz M, Repetto EA, Si H. A continuum model of kinetic roughening and coarsening in thin films. J Mech Phys Solids 1999;47:697–730. https://doi.org/10.1016/S0022-5096(98)00102-1.

[52] Ashmawi WM, Zikry MA. Grain boundary effects and void porosity evolution. Mech Mater 2003;35:537–52. https://doi.org/10.1016/S0167-6636(02)00269-7.

[53] Borvik T, Hopperstad OS, Berstad T, Langseth M. Perforation of 12mm thick steel plates by 20mm diameter projectiles with flat, hemispherical and conical noses - Part II: Numerical simulations. Int J Impact Eng 2001;27:37–64. https://doi.org/10.1016/S0734-743X(01)00035-5.

[54] Banerjee A, Dhar S, Acharyya S, Datta D, Nayak N. Determination of Johnson cook material and failure model constants and numerical modelling of Charpy impact test of armour steel. Mater Sci Eng A 2015;640:200–9. https://doi.org/10.1016/j.msea.2015.05.073.

[55] Khare S, Kumar K, Choudhary S, Singh PK, Verma RK, Mahajan P. Determination of Johnson–Cook Material Parameters for Armour Plate Using DIC and FEM. Met Mater Int 2021;27:4984–95. https://doi.org/10.1007/s12540-020-00895-3.

[56] Tria DE, Trębiński R. Methodology for experimental verification of steel armour impact modelling. Int J Impact Eng 2017;100:102–16. https://doi.org/10.1016/j.ijimpeng.2016.10.011.

[57] Jia B, Zhang Y, Rusinek A, Xiao X, Chai R, Gu G. Thermo-viscoplastic behavior and constitutive relations for 304 austenitic stainless steel over a wide range of strain rates covering quasi-static, medium, high and very high regimes. Int J Impact Eng 2022;164:104208. https://doi.org/10.1016/j.ijimpeng.2022.104208.

[58] Banerjee A, Dhar S, Acharyya S, Datta D, Nayak N. Numerical Simulation of Ballistic Impact of Armour Steel Plate by Typical Armour Piercing Projectile. Procedia Eng 2017;173:347–54. https://doi.org/10.1016/j.proeng.2016.12.028.

[59] Gangwar V, Bhattacharjee S, Acharyya SK, Dhar S, Banerjee A, Chakraborty S. Effectiveness of thermoviscoplastic material models in predicting the thermomechanical behavior of rolled homogenous armor steel. Phys Scr 2024.

[60] Rusinek A, Zaera R, Klepaczko JR. Constitutive relations in 3-D for a wide range of strain rates and temperatures - Application to mild steels. Int J Solids Struct 2007;44:5611–34. https://doi.org/10.1016/j.ijsolstr.2007.01.015.

[61] Johnson GR, Cook WH. Fracture characteristics of three metals subjected to various strains, strain rates, temperatures and pressures. Eng Fract Mech 1985;21:31–48. https://doi.org/10.1016/0013-7944(85)90052-9.

[62] Jena PK, Manickam MAM, Venketachari S, Srivastava SC, Srivastava A, Chakrabarty S, et al. Microstructure, mechanical, ballistic property evaluation of RHA steel produced by continuous-casting route. J Appl Res Technol 2020;18:1–13. https://doi.org/10.22201/ICAT.24486736E.2020.18.1.927.

[63] Konca E. A comparison of the ballistic performances of various microstructures in mil-a-12560 armor steel. Metals (Basel) 2020;10. https://doi.org/10.3390/met10040446.

[64] Cabrilo A, Sedmak A, Burzic Z, Perkovic S. Fracture mechanics and fatigue crack propagation in armor steel welds. Eng Fail Anal 2019;106:104155. https://doi.org/10.1016/j.engfailanal.2019.104155.

[65] McDonald B, Bornstein H, Langdon G, Curry R, Orifici A. Deformation and Rupture of Armour Grade Steel under Localised Blast Loading. Procedia Eng 2017;197:13–22. https://doi.org/10.1016/j.proeng.2017.08.077.

[66] Gangwar V, Basu P, Acharyya SK, Dhar S, Chakraborty S, Banerjee A. Dynamic deformation and fracture surface investigation of rolled homogenous armor steel through Charpy impact testing. Theor Appl Fract Mech 2024;133:104592.

https://doi.org/10.1016/j.tafmec.2024.104592.
[67] Arias A, Rodríguez-Martínez JA, Rusinek A. Numerical simulations of impact behaviour of thin steel plates subjected to cylindrical, conical and hemispherical non-deformable projectiles. Eng Fract Mech 2008;75:1635–56. https://doi.org/10.1016/j.engfracmech.2007.06.005.
[68] Rusinek A, Rodríguez-Martínez JA, Zaera R, Klepaczko JR, Arias A, Sauvelet C. Experimental and numerical study on the perforation process of mild steel sheets subjected to perpendicular impact by hemispherical projectiles. Int J Impact Eng 2009;36:565–87. https://doi.org/10.1016/j.ijimpeng.2008.09.004.
[69] Gupta NK, Iqbal MA, Sekhon GS. Effect of projectile nose shape, impact velocity and target thickness on deformation behavior of aluminum plates. Int J Solids Struct 2007;44:3411–39. https://doi.org/10.1016/j.ijsolstr.2006.09.034.
[70] Lodygowski T, Rusinek A. Constitutive Relations under Impact Loadings. vol. 552. 2014.
[71] Ahn K, Huh H, Park L. Comparison of Dynamic Hardening Equations for Metallic Materials with the Variation of Crystalline Structures. Proc 5th Int Conf High Speed Form 2012:165–76.
[72] Abed F, Makarem F. Comparisons of constitutive models for steel over a wide range of temperatures and strain rates. J Eng Mater Technol 2012;134:1–10. https://doi.org/10.1115/1.4006171.
[73] Gupta AK, Krishnamurthy HN, Puranik P, Singh SK, Balu A. An exponential strain dependent Rusinek-Klepaczko model for flow stress prediction in austenitic stainless steel 304 at elevated temperatures. J Mater Res Technol 2014;3:370–7. https://doi.org/10.1016/j.jmrt.2014.08.001.
[74] Xu Z, Huang F. Comparison of physically based constitutive models characterizing armor steel over wide temperature and strain rate ranges. Model Simul Mater Sci Eng 2012;20. https://doi.org/10.1088/0965-0393/20/1/015005.
[75] Børvik T, Langseth M, Hopperstad OS, Malo KA. Ballistic penetration of steel plates. vol. 22. 1999. https://doi.org/10.1016/S0734-743X(99)00011-1.
[76] Wang J, Guo W, Guo J, Wang Z, Lu S. The Effects of Stress Triaxiality, Temperature and Strain Rate on the Fracture Characteristics of a Nickel-Base Superalloy. J Mater Eng Perform 2016;25:2043–52. https://doi.org/10.1007/s11665-016-2049-9.
[77] Wuertemberger L, Palazotto AN. Evaluation of Flow and Failure Properties of Treated 4130 Steel. J Dyn Behav Mater 2016;2:207–22. https://doi.org/10.1007/s40870-016-0059-1.
[78] Dassault Systèmes Simulia. Getting Started With ABAQUS 2016:1–621.

[79] Klepaczko JR, Rusinek A, Rodríguez-Martínez JA, Pecherski RB, Arias A. Modelling of thermo-viscoplastic behaviour of DH-36 and Weldox 460-E structural steels at wide ranges of strain rates and temperatures, comparison of constitutive relations for impact problems. Mech Mater 2009;41:599–621. https://doi.org/10.1016/j.mechmat.2008.11.004.

[80] Jankowiak T, Rusinek A, Wood P. A numerical analysis of the dynamic behaviour of sheet steel perforated by a conical projectile under ballistic conditions. Finite Elem Anal Des 2013;65:39–49. https://doi.org/10.1016/j.finel.2012.10.007.

[81] Xu Z, Huang F. Thermomechanical behavior and constitutive modeling of tungsten-based composite over wide temperature and strain rate ranges. Int J Plast 2013;40:163–84. https://doi.org/10.1016/j.ijplas.2012.08.004.

[82] Xu Z, Huang F. Comparison of constitutive models for FCC metals over wide temperature and strain rate ranges with application to pure copper. Int J Impact Eng 2015;79:65–74. https://doi.org/10.1016/J.IJIMPENG.2014.10.003.

[83] Pavlina EJ, Van Tyne CJ. Correlation of Yield strength and Tensile strength with hardness for steels. J Mater Eng Perform 2008;17:888–93. https://doi.org/10.1007/s11665-008-9225-5.

Chapter - 3

Experimental and Numerical study of Charpy V-notch Impact Test

Abstract

Dynamic loading conditions, especially at elevated temperatures, pose significant challenges for materials used in critical applications such as armour systems. This study investigated the dynamic response of RHA steel under elevated temperature through tensile and Charpy impact testing. Experimental tests are conducted on RHA steel specimens subjected to controlled tensile loading rates and Charpy impact testing at room and elevated *T*. The mechanical properties, including strength, ductility, and toughness, are systematically evaluated to understand the material behaviour under dynamic loading conditions at elevated temperatures. Finite element simulations are utilized to complement the experimental findings and provide insights into the underlying mechanism governing the material response to dynamic loading at high temperature. The J-C, R-K and suggested modifications in the J-C (MJ-C) material model are employed to simulate results validated against experimental data to enhance the predictive accuracy. When the resulting findings are compared to the experimental data, it is evident that the MJ-C model performs better in predicting energy absorption and force versus displacement.

3.1 Introduction

Armour steel is a low-alloy, high-strength, medium-carbon steel with a tempered martensitic microstructure that provides a high strength-to-ductility ratio. Armour material must have a high hardness and a high toughness to resist deformation caused by ballistic impact [1]. Dynamic characterization of this material [2] requires consideration of factors such as temperature and loading rate. Charpy impact testing is required to determine whether steels meet the minimum durability requirements for various armor applications [3].

To investigate the material $\dot{\varepsilon}$ sensitivity or for the dynamic characterization of materials, tension and compression tests at quasistatic, intermediate, and high $\dot{\varepsilon}$ are necessary for computational modelling. Quasistatic piercing tests, drop weight impact tests, and corresponding finite element simulations [4] were performed to analyse the behaviour of mild steel plates struck by a hemispherical indenter [5].

Impact testing helps to determine how tough a material is or how well it can absorb energy while undergoing plastic deformation under conditions of multiaxial stress [6]. The analysis also allows for the calculation of typical time, force, displacement, and absorbed energy values that correlate

with the cessation of unstable fracture. To establish the foundation for the formulation of toughness criteria for novel duplex classes, a series of fracture toughness and Charpy-V notch impact tests were methodically conducted on a variety of duplex stainless steels. [7,8] shows the effect of specimen size on the test results. Another useful study in the field of Charpy impact testing is the proposal of the numerical method [9] to simulate interacting ductile tearing and cleavage fracture. This approach is useful for the study of crack arrest following substantial cleavage fractures. In another paper [10] by the same authors, finite element modelling of ductile and cleavage fracture models was used to redefine the fracture energy. Zang et al. [11] studied the Ti-5Al-1V-1Sn-1Zr-0.8Mo alloy and found that, according to tensile tests, it exhibited an improvement in both yield strength and elongation at low temperatures, while its impact toughness decreased. This indicates that effective strengthening and toughening techniques for quasistatic tensile deformation could fail under impact deformation.

It has been already established [12–14] that in impact testing, the following points are important to consider in numerical simulations:

- The material model chosen to simulate impact events.
- Failure criterion of the material at different $\dot{\varepsilon}$.
- The geometry type, partition of geometry and mesh size.

To accurately analyse and assess the ballistic resistance of a material, it is crucial to understand how the material reacts within a short period of time when subjected to high loading. Xu and Huang [15] simulated the dynamic response of 603 armor steel using Johnson-Cook (J-C) and KHL material models [16] and compared the results with experimental results. It was found that thermal softening exerts a more pronounced influence than strain rate and work hardening. Whittington et al. [17] performed tension, compression and torsion tests at 20°C and 300°C to investigate the mechanical behaviour and damage progression of rolled homogeneous armour steel. The number and distribution of voids are also identified through fractography. A plasticity and damage model incorporating an internal state variable (ISV) was employed to capture the effect of the $\dot{\varepsilon}$, T, and stress state. The effect of the rate sensitivity on RHA steel was studied in a series of theoretical articles that did not include many experimental comparisons. A. Banerjee et al. [18] used the Johnson–Cook damage model for accurate failure prediction in RHA steel via finite element simulations of tensile and Charpy tests. A significant difference in accuracy was observed between the experimental and computational findings. Such comparisons were also carried out for other steels [14,19,20].

This Chapter presents a comprehensive study on room and high-temperature Charpy impact testing of armor steel. Through meticulous experimentation and detailed analysis, the aim was to clarify

the intricate relationship between temperature and mechanical properties in armor steel. By subjecting the material to a range of temperatures representative of operational environments, the aim is to gain insights into its performance across varying thermal conditions. This study conducts a simulation of the Charpy impact test using two material models: the phenomenological J-C model and the semi-physical R-K model. Simulations are carried out at impact velocities of 3, 4, 5, 6, 8 and 9 m/s, considering both room and elevated temperatures of 100°C and 150°C. A newly developed material model, termed the modified Johnson-Cook (MJ-C) model, is introduced in Chapter 2 also used. The accuracy of the models is assessed by comparing simulation results for force versus displacement and energy versus time with experimental data.

3.2 Charpy Impact experiment

Charpy impact tests were conducted at various impact velocities for both RHA and projectile steel. Material model coefficients derived from tensile tests were used to simulate these impact tests. For RHA steel, experiments were performed at room temperature for impact velocities of 3, 4, 5, 6, and 8 m/s, as well as at elevated temperatures of 100°C and 150°C for impact velocities of 8 m/s and 9 m/s, respectively. In the case of projectile steel, experiments were carried out at impact velocities of 8, 9, 10, and 11 m/s.

The tests were conducted using the INSTRON CEAST 9350 setup, as shown in Fig. 3.1, with specimens fabricated according to ASTM designation E23-18. For projectile steel, the specimen thickness was reduced to 5 mm to accommodate its higher strength, which exceeded the load-sensing capability of the machine. The anvils were positioned 40 mm apart, and an impactor weighing 6.12 kg, supplemented with additional weights, was used to provide the energy required to fracture the specimens.

Energy absorption is calculated excluding frictional losses. Fig. 3.2, 3.3 & 3.7a shows the force - displacement plots, while Fig. 3.6 displays the energy-initial impact velocity v_o curves.

The fracture energy of the Charpy V-notch (CVN) specimen decreases with increasing impact velocity v_0, as illustrated in Fig. 3.4, 3.5 & 3.7b. The energy from the impactor is absorbed for elastic work, localized plastic deformation, and overall deformation of the specimen. Generally, energy absorption decreases with higher impact velocities, leading to rapid deformation localization and early specimen failure. Contrary to this the energy necessary for the specimen to fracture increased when the initial impact velocity v_o increased, for high temperature as depicted in Fig. 3.5. For projectile steel, energy absorption decreases as impact velocity increases, while the peak force rises with increasing velocity as shown in Fig. 3.7a & b.

The nomenclature of broken specimen with load vs displacement curve is shown in Fig. 3.8.

Fig. 3.1 Instron CEAST 9350 impact testing system

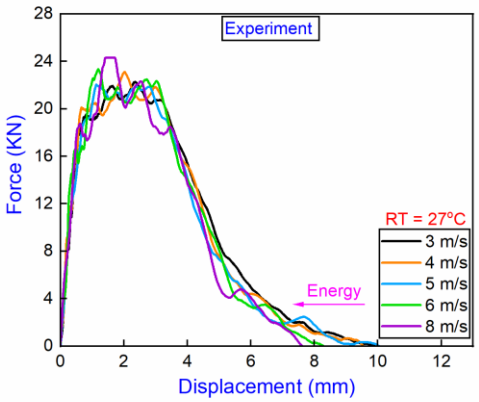

Fig. 3.2 Force *vs* displacement curve of Charpy V-notch armour steel sample.

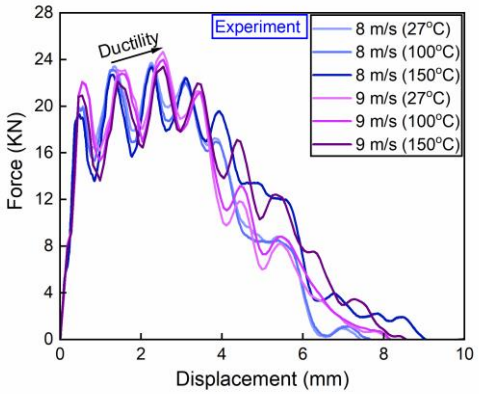

Fig. 3.3 Force *vs* displacement curve of Charpy V-notch sample at high temperature for armour steel.

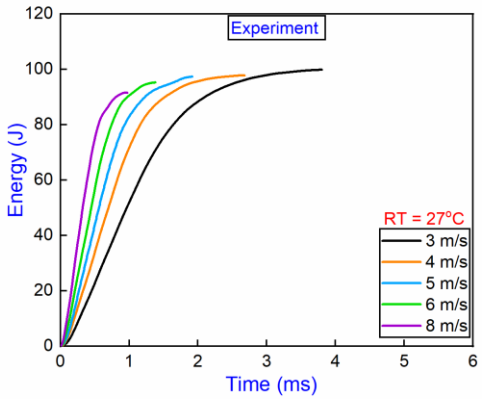

Fig. 3.4 Energy *vs* initial impact velocity curve of Charpy V-notch armour steel sample at room temperature.

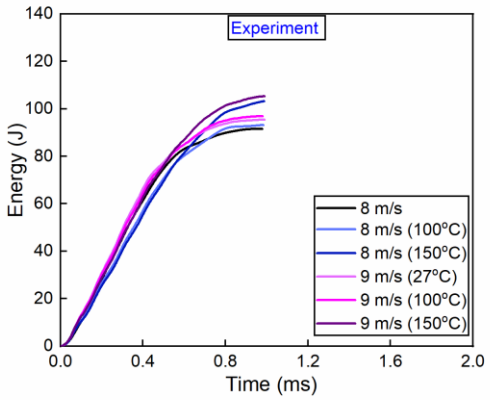

Fig. 3.5 Energy *vs* initial impact velocity curve of Charpy V-notch for armour steel sample at high temperature.

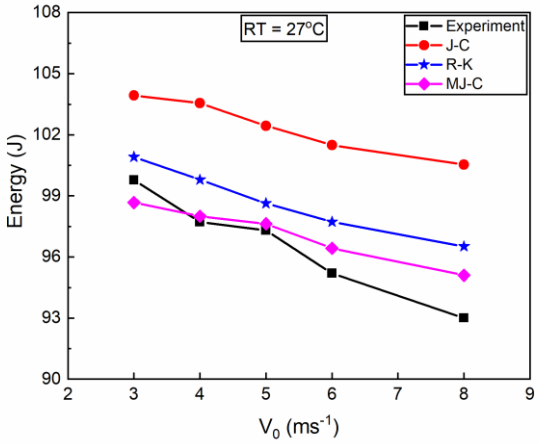

Fig. 3.6 Comparison of experimental and simulated initial impact velocities v_0 vs energy absorbed by the armour steel CVN specimen.

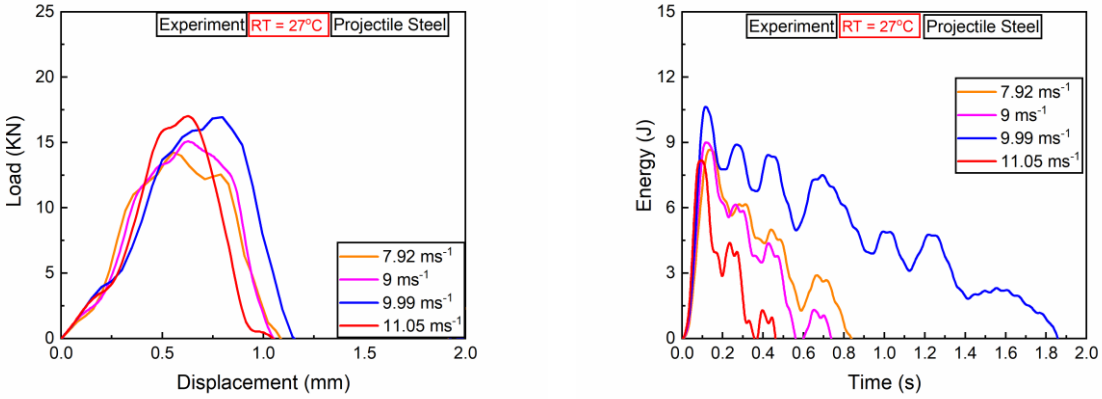

Fig. 3.7 Projectile steel (a) load vs displacement (b) energy vs time curve

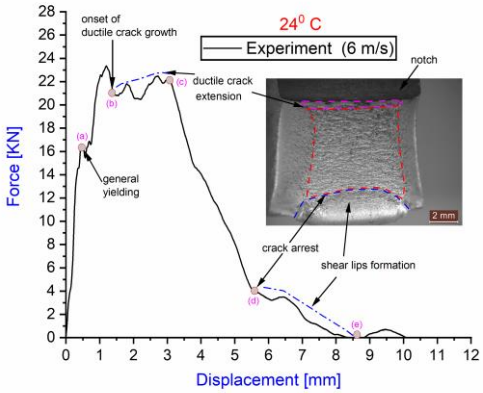

Fig. 3.8 Nomenclature of broken specimen

3.3 FEA simulation of numerical model for Charpy impact

Two types of discretizing geometries are compared for modelling: curvature-type partitions (CTPs) and straight-cut partitions (SCPs). The force-displacement and energy absorption predictions are investigated with J-C, MJ-C, and R-K material models together with the J-C failure model.

As shown in Fig. 3.9, the impactor is modelled as a discrete non-deformable rigid body with a reference point for boundary conditions. The Charpy V-notch (CVN) specimen is modelled as a 3D deformable body, as shown in Fig. 3.9. General contact with the penalty friction formulation is used to simulate the interaction between the impactor and the specimen. Based on an analytical approximation and an experimental study by A. Rusinek et al.[23], a constant coefficient of friction

of 0.25 is used for steel. Considering the element type, mesh density, and computation time, the specimen geometry is splitted into two portions: a middle portion, and an external portion. The middle portion have a curvature-type partition starting from the tip of the V-notch, as shown in Fig. 3.9. This curvature replicates the shape of the localized deformation at the notch tip, initiating the crack propagation process as observed in the experiment. The middle portion of the specimen is meshed using C3D8R elements from the ABAQUS library (8-node linear brick, reduced integration with enhanced hourglass control mode, and distortion control with element deletion). This kind of hexahedral element has been successfully used for nonlinear plasticity analysis [22,24,29,30,41]. As suggested by Zukas and Scheffler [42], an effort is made to retain the aspect ratio of the elements as close to unity as possible. Sensitivity to mesh size is previously studied because the mesh size and density affect the damage process [43]. The middle portion of the model have 32325 elements with an element size of $\Delta x = \Delta y = \Delta z = 0.4$ mm. The external part is discretized using C3D8R hexahedral elements. The total number of elements in the external part is 7500 with an element size of $\Delta x = 1.4$ mm and $\Delta y = \Delta z = 0.4$ mm. The impactor is modelled with 11676 type R3D4 linear quadrilateral elements. In a straight-cut partition, a small strip is considered where fine meshing of element size $\Delta x = 0.07$ mm in $\Delta y = \Delta z = 0.1$ mm is employed, as shown in Fig. 3.9. This is observed by simulating several model geometries. The total number of elements in the small strip was 48,000 linear hexahedral elements of type C3D8R, and in the rest of the body, there were 4,89,800 elements. All the boundary conditions employed are the same as those in the curvature-type partition. The thermoviscoplastic material models and failure model are incorporated through the VUMAT subroutine in ABAQUS Explicit. The sensitivity to the mesh size has already been investigated, as shown in Fig. 3.10, since the mesh size and density influence the damage process [62]. Simulations are performed at impact velocities of 3, 4, 5, 6, and 8 ms^{-1}. The simulated crack initiation and propagation in the Charpy V-notch specimen are depicted in Fig. 3.11. Comparisons between the experimental and simulated force versus displacement (Fig. 3.12 & 3.13), maximum force versus initial impact velocity v_o (Fig. 3.14), energy versus initial impact velocity v_o (Fig. 3.6), and energy versus time curve is depicted in Figs. 3.13b, 3.15, 3.16 & 3.17. The CTP geometry predicts a lesser force than SCP in the force versus displacement curve. The SCP geometry exhibited a higher peak force and shorter ductile fracture extension. As shown in Fig. 3.16, the experimental curve indicates the unstable crack extension occurs at the maximum load point and continues up to the displacement of 3.03 mm. This result matches the prediction by the CTP geometry, whereas, in the SCP, the failure initiates at an extremely early displacement of 0.97 mm as depicted in Fig. 3.12 force versus displacement curve. Finally, the displacement at failure and energy absorbed for failure predicted by the SCP geometry match better with the experimental results than those predicted by the CTP. Compared with the SCP geometry, the CTP exhibits a superior match in terms of energy absorption until ductile

fracture initiation. As observed in the experimental curve, the peaks exhibit a nearly identical pattern in the CTP geometry.

From the force vs. initial impact velocity v_o curves at different velocities, it is apparent that although qualitative matching between the simulated and experimental results occurs for all the material models, the error in the prediction of the peak load is lower for the MJ-C and J-C models. The R-K model overpredicts the peak load. The value of the error decreases with increasing striking velocity. However, the R-K model predictions for the post-peak failure process are close to those of the experiments followed by the MJ-C model and then the J-C model.

The stress vs. strain in the x-direction at the mid-plane middle section is plotted in Fig. 3.19 for a velocity of 6 ms^{-1}. There is not much variation in the J-C and MJ-C models, but the R-K model shows higher values.

To estimate the plastic strain rate ($\dot{\varepsilon}_p$) variation, three positions on the specimen are selected for the CTP geometry, as shown in Fig. 3.18. These locations correspond to the tip of the notch, middle height and the top surface of the specimen. Table 3.1 shows the average strain rate values upto a displacement of 1 mm. There is a variation in the strain rate values. Material parameters in this investigation are calibrated from test data upto 36.439 s^{-1}. Further improvement in simulation can be achieved using test data at higher strain rates.

The J-C model average error is 5.48 % high among three material models in terms of energy absorbed by the specimen while, the MJ-C average error is 2.03 %, and the R-K model average error is 3.42 %. However, the errors for all the three material models are below 10%.

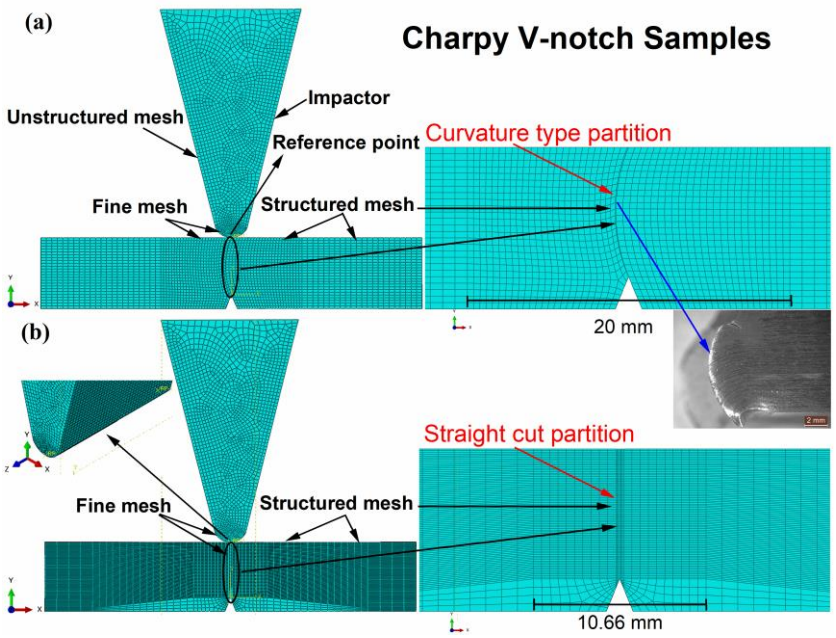

Fig. 3.9 FE model of the Charpy V-notch specimen for (a) curvature type partition (CTP) and (b) straight cut partition (SCP); both geometries are meshed via the structural meshing technique to maintain the aspect ratio at almost unity.

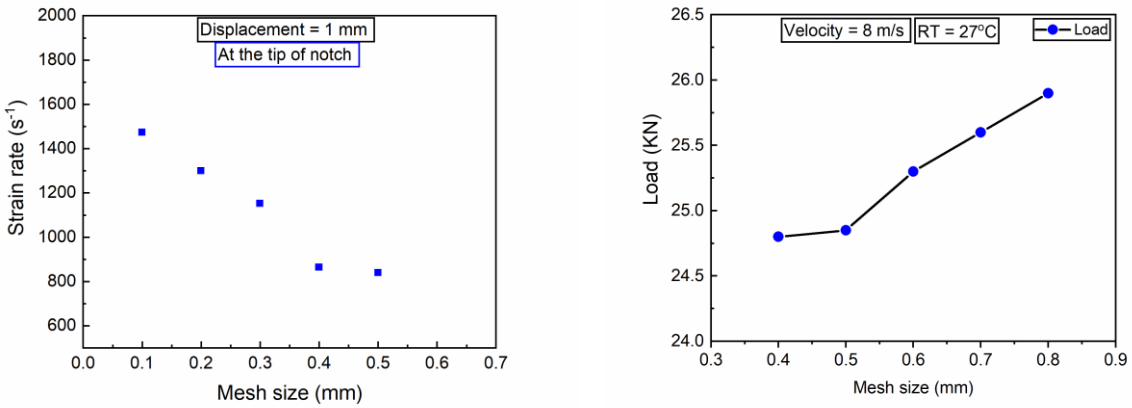

Fig. 3.10 Variation in the strain rate and load with different mesh sizes.

(a) J-C

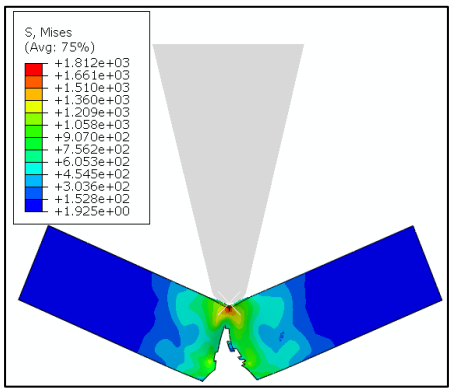

(a) MJ-C

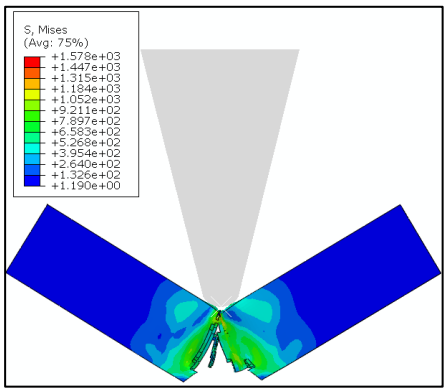

(c) MJ-C

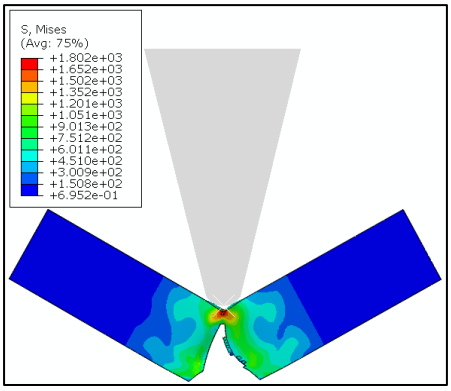

(d) R-K

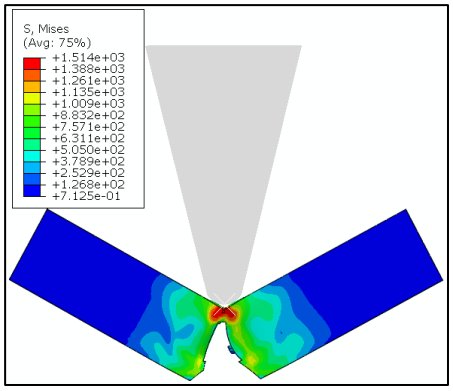

Fig. 3.11 FE simulation of crack initiation and propagation in the Charpy V-notch specimen by the MJ-C model at a velocity of 9 ms^{-1}: (a), (c), and (d) for the CTP geometry and (b) for the SCP geometry, at 150°C, for armour steel.

(a)

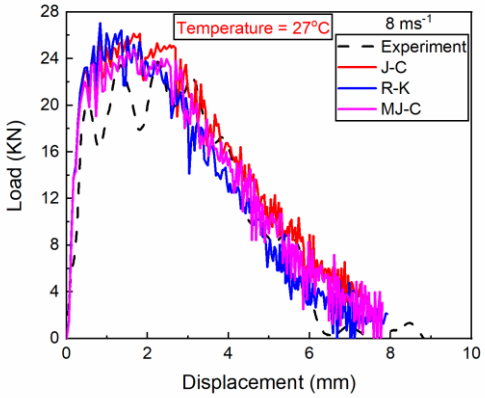
Temperature = 27°C
8 ms-1
Experiment
J-C
R-K
MJ-C
Load (KN)
Displacement (mm)

(b)

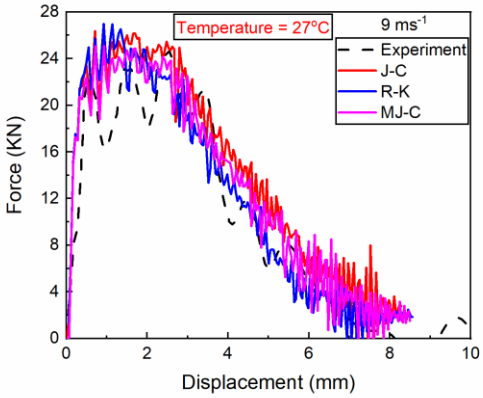
Temperature = 27°C
9 ms-1
Experiment
J-C
R-K
MJ-C
Force (KN)
Displacement (mm)

(c)

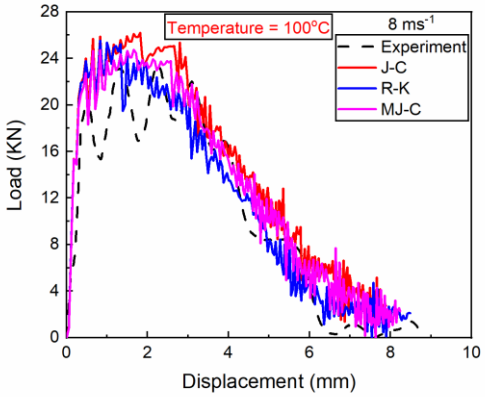
Temperature = 100°C
8 ms-1
Experiment
J-C
R-K
MJ-C
Load (KN)
Displacement (mm)

(d)

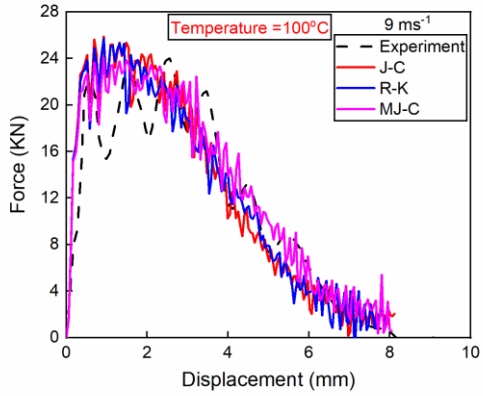
Temperature =100°C
9 ms-1
Experiment
J-C
R-K
MJ-C
Force (KN)
Displacement (mm)

(e) (f)

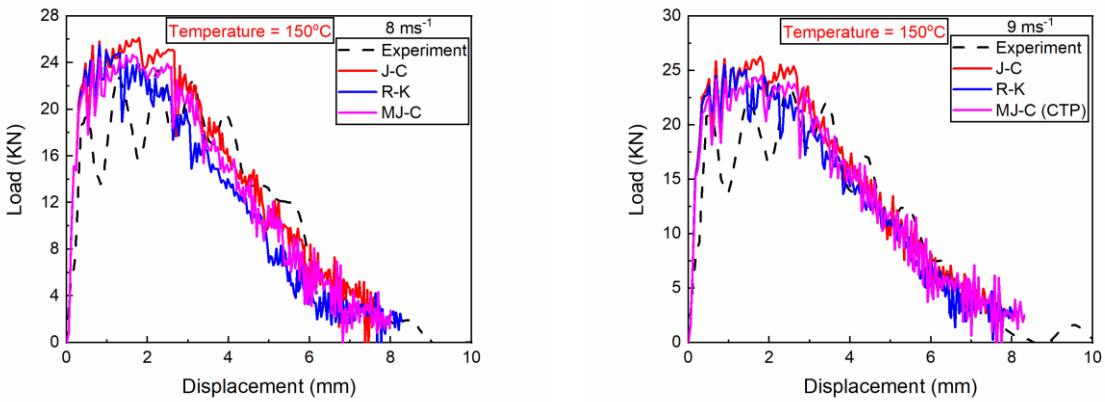

Fig. 3.12 Comparison of the simulated and experimental forces vs. displacement of the Charpy V-notch specimen for the CTP geometry impacted at (a) 8 and (b) 9 ms^{-1} at 27°C, (c) 8 and (d) 9 ms^{-1} at 100°C, (e) 8 and (f) 9 ms^{-1} at 150°C, for armour steel.

(a) (b)

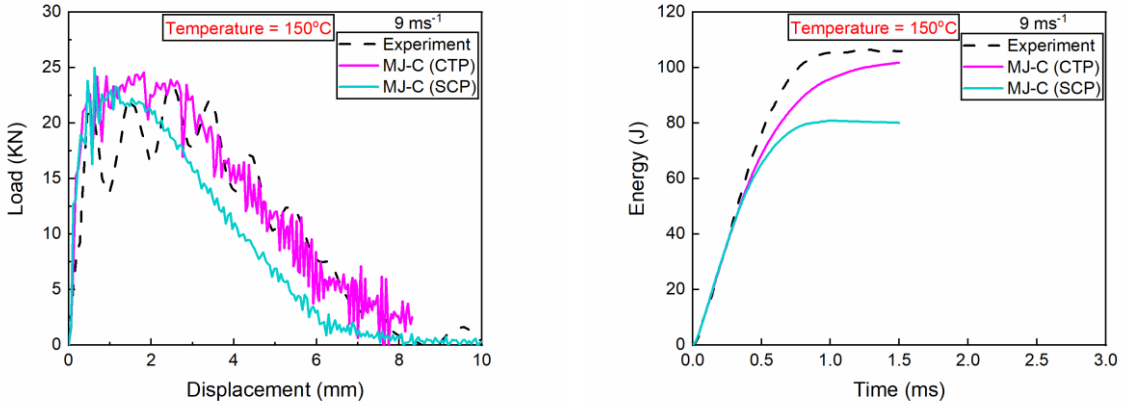

Fig. 3.13 The (a) force vs. displacement and (b) energy vs. time, curves for the SCP geometry and comparison with those for the CTP geometry.

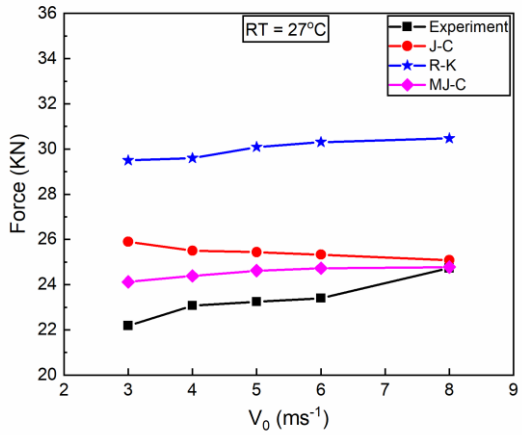

Fig. 3.14 Comparison of the simulated and experimental forces vs. initial impact velocities (v_o) for CTP geometry for armour steel.

(a) (b)

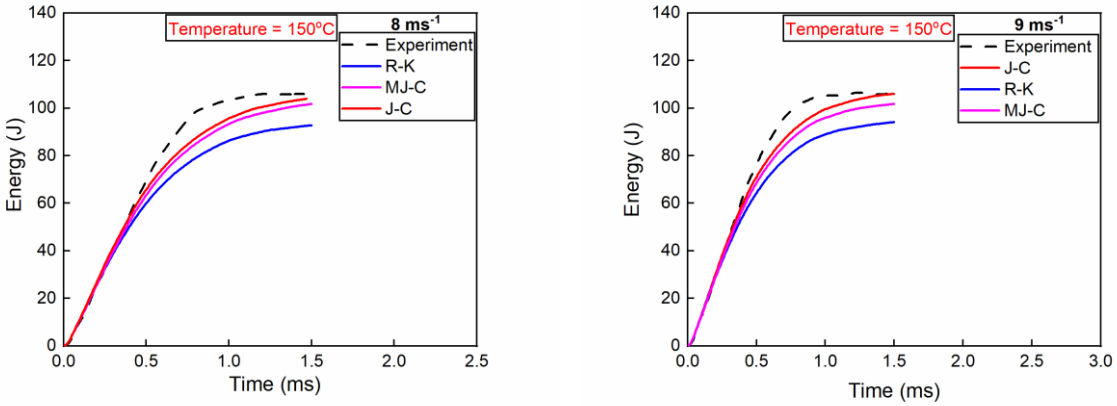

Fig. 3.15 Comparison of the simulated and experimental temporal variations in the energy absorbed by the Charpy V-notch specimen impacted at 150°C: (a) 8 and (b) 9, ms^{-1}.

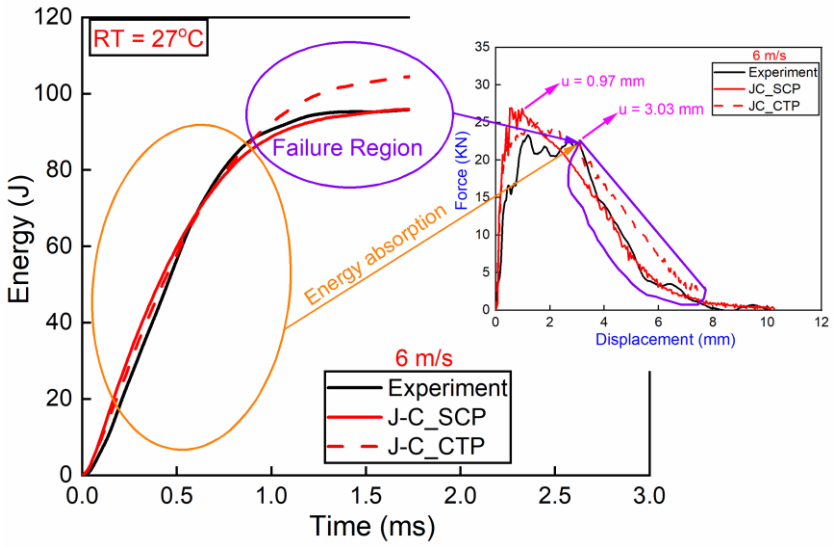

Fig. 3.16 The energy and force vs. displacement curve for the SCP geometry and comparison with those for the CTP geometry. The orange colour indicates the region in which energy is absorbed by the material, and the violet colour indicates the failure and crack arrest region. The point where the orange and violet elliptical regions touch is the point where failure starts.

(a) 3 ms^{-1} (b) 4 ms^{-1}

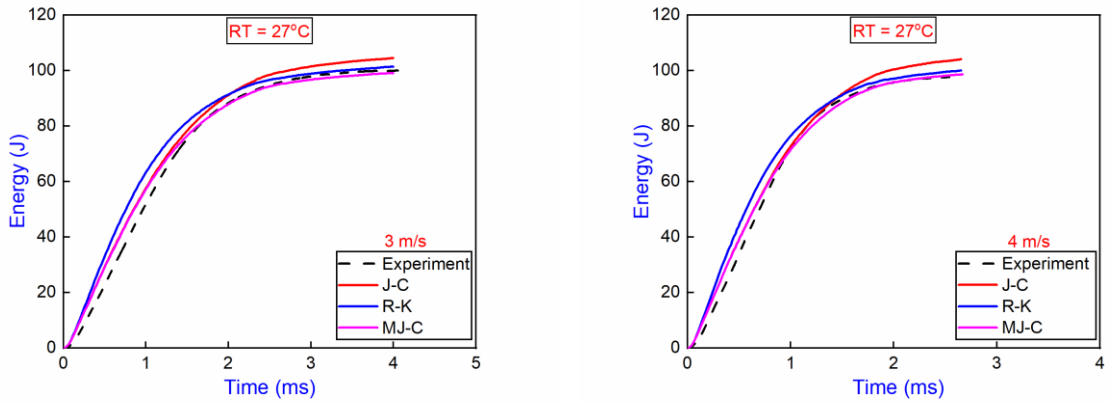

Fig. 3.17 Comparison of simulated and experimental temporal variation of energy absorbed by Charpy V-notch specimen impacted at (a) 3 ms^{-1}, (b) 4 ms^{-1}.

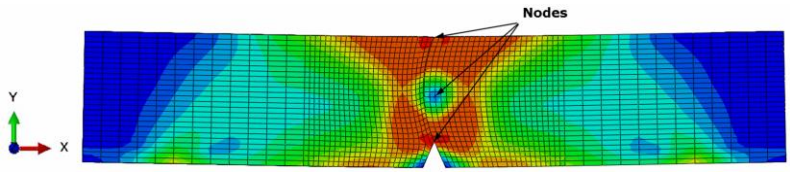

Fig. 3.18 Selection of nodes for estimation of the strain rate

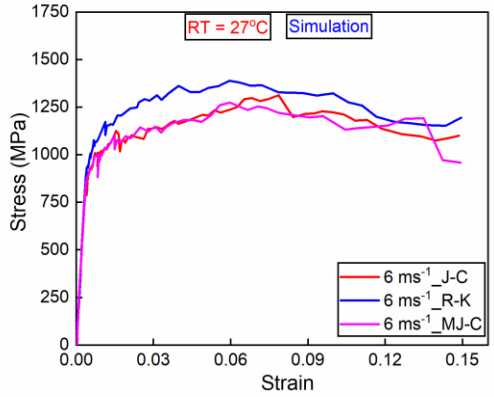

Fig. 3.19 Stress vs. strain at the mid-surface element of the fractured Charpy specimen; in the R-K model, the $\dot{\varepsilon}$ hardening is greater than that in the J-C and MJ-C models.

Table 3.1 Average strain rate achieved at three positions upto a displacement of 1 mm

Velocity (ms^{-1})	**Achieved Strain rate (s^{-1})**			
	Material model	**Tip of Notch**	**Middle**	**Top surface**
3	J-C	300	54	160
	MJ-C	355	53	164
	R-K	410	55	169
4	J-C	445	69	321
	MJ-C	559	76	338
	R-K	669	88	348
5	J-C	543	111	358
	MJ-C	452	137	409
	R-K	553	156	454
6	J-C	731	154	446
	MJ-C	709	185	449
	R-K	766	210	464
8	J-C	968	183	576
	MJ-C	941	204	617
	R-K	988	236	730

3.4 Prediction capability of the material models

From Fig. 3.12 it is evident that at room temperature, the R-K model shows the highest overprediction among all three material models. Conversely, at high temperature, the J-C model exhibits the highest overprediction. The MJ-C model predictions are closest to the experimental results across all temperature ranges. A decrease in the maximum load prediction is observed in all three material models, as listed in Table 3.2.

Table 3.2 Comparison of the experimental results and simulation prediction trends in decreasing order for the peak load

Order	**1**	**2**	**3**	**4**	**5**	**6**
Experiment	9	8	9	8	9	8
Velocity (ms^{-1})	(RT)	(RT)	(100°C)	(100°C)	(150°C)	(150°C)
Simulation	9	9	8	8	9	8
Velocity (ms^{-1})	(RT)	(100°C)	(RT)	(100°C)	(150°C)	(150°C)

To determine the accuracy of the material models in the prediction of the peak load experienced by the specimen at given velocities. The prediction error is calculated. The average error of the J-C model is 10.35% higher than that of the other three material models in terms of peak load prediction. In comparison, the MJ-C average error is 3.94%, and the R-K model average error is 9.64%. Fig. 3.20 shows the average error in prediction by three material models. The error of the R-K and MJ-C material models are less than 10%.

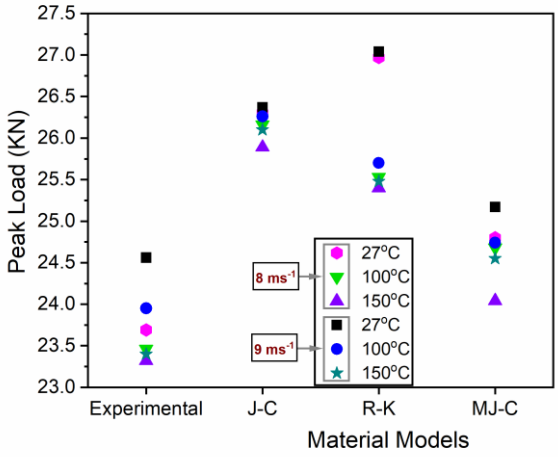

Fig. 3.20 Peak load prediction by all the material models

3.5 Characterization of the fractured surface of the Charpy specimen

The characterization of the fractured surfaces began with macroscopic observations followed by microscopic ones. All the specimens fractured in mode I, i.e., opening of the V-notch of the Charpy specimen. The fracture surfaces of post-mortem samples from the Charpy test are inspected for three striking velocities: 3, 6, and 8 ms^{-1}. The surface at 4 ms^{-1} is not observed due to corrosion on the fractured surface. Fig. 3.21 shows that the failure process involves both plane strain and plane stress conditions, i.e., mixed stress state conditions. The cross-sectional area of a flat fracture surface signifies failure under plane strain conditions, while the sides of the specimen show a reduction in the area and formation of shear lips, indicating failure under plane stress conditions. The reduction in energy absorption at a higher strain rate may be due to failure under plane strain conditions, which involves less ductility and lower failure strain, and the localization of plastic deformation increased void nucleation rate at higher strain rates. The variation in the flat fracture area against impact velocity is shown in Table 3.3. An increase in the flat fracture area means that the plane strain condition dominates the fracture process.

Table 3.3 Flat surface area vs impact velocity

Impact Velocity (ms^{-1})	Flat area (mm^2)
3	41.184
6	42.665
8	46.432

The microstructure of the fracture surface is observed microscopically through SEM imaging at high magnification. The optical microstructure of the 'as-received' material shows a typical tempered martensitic structure, including a ferritic matrix with large number of dispersed precipitates at the ferrite laths. These precipitates are mainly cementite and second-phase precipitates due to tempering. The SEM microstructure showed that equiaxed dimples and microvoids are present on all the fractured surfaces, indicating that the crack began and spread from there. The presence of dimple-like features on the fracture surface indicates ductile failure, which is desirable for armor steel as it enhances the impact energy absorption [44]. The damage progression follows void nucleation, growth, and coalescence processes [45]. In all Figs. 3.22(a-d), dimple formation was observed. Significant variations in the fractured surfaces is observed from velocities of 3 ms^{-1} to 8 ms^{-1}, as shown in Fig. 3.22(a,b,c). The variations in the void parameters of the fracture surface with respect to the striking velocity are listed in Table 3.4. Large number of fine and shallow dimples are visible at a striking velocity of 8 m/s. More number of fine and shallow dimples represents the good yield strength of the material but limited deformation. On the other hand, extensive large dimples represent somewhat lower yield strength and greater

ductility before fracture [17,46]. Percentage elongation and fracture strain would be more when the dimples are large and the depth is more.

No cracks are observed in the shear lip region, but there are noticeable large dimples that are shallow, along with a number of small dimples, as shown in Fig. 3.22(d). It is observed that for low strain rate fractures, the number of voids is less, but the average void area is greater. However, for high-strain-rate fractures, the number of voids increases, and the average void area decreases. The voids are small in size for high strain rate fractures, which restricts plastic deformation, causing more hardening and less ductility. The void nucleation rate increases for fast fracture under high strain rate loading.

Table 3.4 Variation in the fracture surface parameters with the velocity

	Velocity ms^{-1}		
	3	**6**	**8**
No. of voids	49825	58923	59527
Dimple diameter (μm)	15.34	14.11	11.66
	11.40	6.81	7.68
	7.36	12.11	12.12
	6.11	8.734	9.41
	9.90	7.16	10.59
Average Void area (μm)	1.846	1.732	0.743

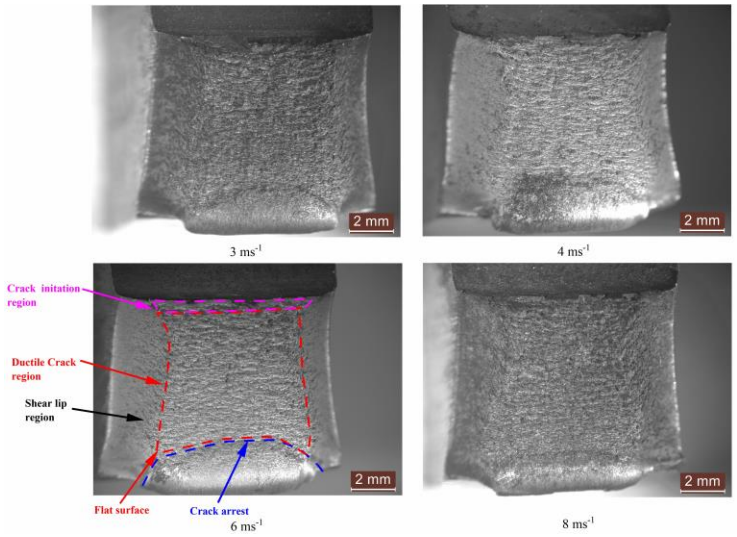

Fig. 3.21 Fractured surfaces of the Charpy test specimen

(a) 3 ms^{-1} (b) 6 ms^{-1}

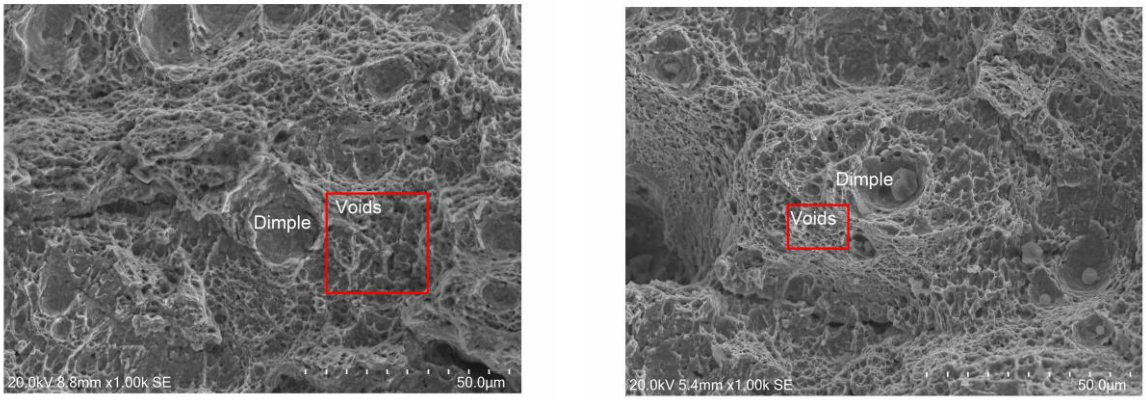

(c) 8 ms^{-1} (d) 3 ms^{-1}

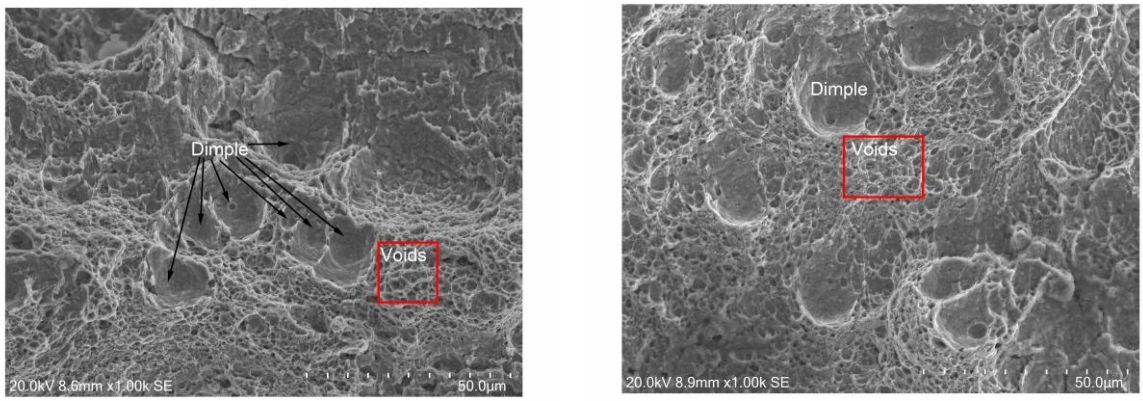

Fig. 3.22 Post-fracture SEM images at (a,b,c) middle zone and, (d) shear lip of Charpy specimen.

3.6 Conclusion

- The Charpy impact test was performed at room temperature with striking velocities of 3, 4, 5, 6, and 8 m/s. The results indicate that with increasing striking velocity, the peak force increases while the displacement decreases. Additionally, energy absorption decreases as the striking velocity increases. At higher velocities (corresponding to higher strain rates), plastic deformation at the notch tip is restricted, and global plastic deformation is limited, resulting in reduced energy absorption. Further tests were conducted at elevated temperatures ($100^{o}C$ and $150^{o}C$) using striking velocities of 8 m/s and 9 m/s, respectively. The results show that at higher velocities, the peak force and displacement increase, and energy absorption also increases with higher striking velocities and elevated temperatures.

- The Charpy impact test was simulated using the straight-cut partition (SCP) geometry with the J-C material model for comparison with the curvature-type partition (CTP) geometry. The CTP geometry accurately predicts the failure initiation point, aligning with the experimental curve, whereas the SCP geometry predicts failure at a much earlier stage. Simulations of the SCP geometry were also performed using the MJ-C material model for further comparison with the CTP geometry. Overall, the CTP geometry provides better predictions for the load-displacement response and energy absorption. Additionally, the peak patterns in the CTP geometry closely resemble those observed experimentally.
- The simulation results of the Charpy tests show a very high strain rate at the notch tip (988 s^{-1} for a striking velocity of 8 ms^{-1}). The simulated peak force closely matches the experimental results (within 10%) for the J-C and MJ-C models. The R-K model overpredicts the peak force. However, the R-K model predictions for the post-peak failure process are close to those of the experiments followed by the MJ-C model and then the J-C model.
- The energy absorbed in the Charpy tests is calculated via simulation. The simulation results agree with the experimental results. The energy absorption rates (slope of energy-time curves) also show a good match with the experimental results.
- The increase in peak load is influenced by a combination of strain rate hardening and strain hardening overcoming thermal softening due to adiabatic heating. At 27°C and a loading rate of 8-9 ms^{-1}, the increase in the peak load is primarily attributed to higher loading rate sensitivity and a higher dynamic strain hardening rate. In contrast, at 150°C and the same loading rate of 8-9 ms^{-1}, thermal softening becomes more dominant which decreases the amount of hardening.
- The increase in ductility of the armor steel with increasing loading rate in the studied temperature range may be due to two reasons. First, because the drop weight impact test was completed very quickly, the heat generated by deformation did not have enough time to dissipate into the surroundings. As a result, the entire process can be considered adiabatic. Due to adiabatic heating, the material softened, which facilitated dislocation nucleation and movement during high loading rate deformation under triaxial stress state yielding a higher failure strain [43]. Consequently, the softened armor steel demonstrated improved ductility under triaxial stress. Second, strain hardening increased at a temperature of 200°C.
- Due to the combined effect of the arguments stated in (iii and iv). The overall energy absorption capability of the armor steel increases.
- The predicted peak loads in the simulations differ for all three material models at different temperatures. At 27°C, the R-K model tends to overpredict, while the J-C model begins to overpredict at 100°C and 150°C. Conversely, the MJ-C model closely aligns with

experimental results across all temperatures. Additionally, the postpeak failure behavior varies: at 27^{o}C, the MJ-C model closely matches experimental results at a striking velocity of 8 ms^{-1}, whereas the R-K model performs well at 9 ms^{-1}. At 100^{o}C, the MJ-C model demonstrates the best postpeak failure prediction, and at 150^{o}C, the J-C model is effective at 8 ms^{-1} while the MJ-C model performs well at 9 ms^{-1}.

- The energy absorbed in the Charpy tests is calculated via simulation. The simulation results agree with the experimental results. The energy absorption rates (slope of energy-time curves) also show a good match with the experimental results.

3.7 Summary

The experimental and numerical study of a typical RHA armor steel material through tensile and Charpy impact testing yields the following conclusions:

a) Tensile tests conducted from quasistatic to dynamic strain rates at room temperature were sufficient for the extraction of the material parameters (constants) of three material models, viz. for the J-C, R-K, and MJ-C material models.

b) Compared with the experimental data, MJ-C material model most accurately predicts the force vs. displacement and the energy absorbed by the specimen.

c) Putting an index 'r' in $\ln(\dot{\varepsilon}/\dot{\varepsilon}_R)$ in the $\dot{\varepsilon}$-dependent term in the standard J-C model increases the accuracy in predicting the strength to failure of the material under study. Using a temperature-dependent strain hardening exponent 'n' yields a better temperature softening effect at high temperatures. Putting an index 'r' in $\ln(\dot{\varepsilon}/\dot{\varepsilon}_R)$ in the $\dot{\varepsilon}$-dependent term in the standard J-C model increases the accuracy in predicting the strength to failure of the material under study, especially at higher strain rates. Using a temperature-dependent strain hardening exponent 'n' yields a better temperature softening effect at high temperatures which is also observed in actual situations.

d) High strain rate loading promotes plane strain fracture restricts plastic deformation (shear lips thickness will be less), and absorbs less energy.

e) The fractography images show that the number of void formations increases and the void area decreases with increasing strain rate. This explains the higher void nucleation rate, fast fracture, and restricted plastic deformation for high strain rate loading.

f) The material ductility was enhanced as a result of the interaction between the high strain rate, stress state, and temperature, which was achieved through intensive adiabatic heating and in situ high-temperature testing.

g) For high strain rate loading, the energy absorption rate is greater for RHA steel in the studied loading range.

h) The CTP geometry demonstrates superior predictive accuracy compared to the SCP geometry in terms of load versus displacement and the energy absorption characteristics of the material. This suggests that the CTP configuration provides a more reliable representation of the material response under stress, thereby offering enhanced predictive capabilities for engineering applications requiring precise load and energy absorption measurements.

References

[1] I.G. Crouch, S.J. Cimpoeru, H. Li, D. Shanmugam, Armour steels, 2017. https://doi.org/10.1016/b978-0-08-100704-4.00002-5.

[2] H. Nahme, E. Lach, H. Nahme, E.L. Dynamic, H. Strength, A. Steels, J. De Physique, Dynamic Behavior of High Strength Armor Steels To cite this version : HAL Id : jpa-00255522, 07 (1997).

[3] A. Cabrilo, M. Cvetinov, Fatigue crack propagation and charpy impact properties in armor steel welds, Mater. Plast. 54 (2017) 694–699. https://doi.org/10.37358/mp.17.4.4927.

[4] B. Liu, C. Guedes Soares, Effect of strain rate on dynamic responses of laterally impacted steel plates, Int. J. Mech. Sci. 160 (2019) 307–317. https://doi.org/10.1016/j.ijmecsci.2019.06.034.

[5] B. Jia, A. Rusinek, R. Pesci, S. Bahi, R. Bernier, Thermo-viscoplastic behavior of 304 austenitic stainless steel at various strain rates and temperatures: Testing, modeling and validation, Int. J. Mech. Sci. 170 (2020) 105356. https://doi.org/10.1016/j.ijmecsci.2019.105356.

[6] T.F. Kiefer, R.D. Keys, F.R. Schwartzberg, Charpy Impact Testing at 20°K, Adv. Cryog. Eng. (1965) 56–62. https://doi.org/10.1007/978-1-4684-3108-7_7.

[7] H. Kurishita, H. Kayano, M. Narui, M. Yamazaki, Current status of small specimen technology in Charpy impact testing, J. Nucl. Mater. 212–215 (1994) 1682–1687. https://doi.org/10.1016/0022-3115(94)91113-4.

[8] H. Kurishita, T. Yamamoto, M. Narui, H. Suwarno, T. Yoshitake, Y. Yano, M. Yamazaki, H. Matsui, Specimen size effects on ductile-brittle transition temperature in Charpy impact testing, J. Nucl. Mater. 329–333 (2004) 1107–1112. https://doi.org/10.1016/j.jnucmat.2004.04.307.

[9] J.S. Kim, Y.J. Kim, M.W. Lee, K.S. Kim, K. Shibanuma, Fracture simulation model for API X80 Charpy test in Ductile-Brittle transition temperatures, Int. J. Mech. Sci. 182 (2020) 105771. https://doi.org/10.1016/j.ijmecsci.2020.105771.

[10] J.S. Kim, Y.J. Kim, M.W. Lee, K.S. Kim, K. Shibanuma, Finite element simulation of drop-weight tear test of API X80 at ductile-brittle transition temperatures, Int. J. Mech. Sci. 191 (2021) 106103. https://doi.org/10.1016/j.ijmecsci.2020.106103.

[11] L. Zhang, Q. Wang, J.Q. Ren, C. Xin, D.J. Chen, X.F. Lu, Comparative study on the effect of test temperature on tensile and charpy impact properties of Ti–5Al–1V–1Sn–1Zr-0.8Mo

alloy, Mater. Sci. Eng. A 879 (2023). https://doi.org/10.1016/j.msea.2023.145231.
[12] H. Kim, J. Park, M. Kang, S. Lee, Interpretation of Charpy impact energy characteristics by microstructural evolution of dynamically compressed specimens in three tempered martensitic steels, Mater. Sci. Eng. A 649 (2016) 57–67. https://doi.org/10.1016/j.msea.2015.09.099.
[13] H. Kosuge, T. Kawabata, T. Okawa, Microstructural design strategy to maintain the brittle fracture toughness of hard-soft dual phase steel after cyclic plastic strain, Mater. Des. 203 (2021) 109603. https://doi.org/10.1016/j.matdes.2021.109603.
[14] B. Tanguy, J. Besson, R. Piques, A. Pineau, Ductile to brittle transition of an A508 steel characterized by Charpy impact test. Part II: Modeling of the Charpy transition curve, Eng. Fract. Mech. 72 (2005) 413–434. https://doi.org/10.1016/j.engfracmech.2004.03.011.
[15] Z. Xu, F. Huang, Comparison of physically based constitutive models characterizing armor steel over wide temperature and strain rate ranges, Model. Simul. Mater. Sci. Eng. 20 (2012). https://doi.org/10.1088/0965-0393/20/1/015005.
[16] A.S. Khan, R. Liang, Behaviors of three BCC metal over a wide range of strain rates and temperatures: Experiments and modeling, Int. J. Plast. 15 (1999) 1089–1109. https://doi.org/10.1016/S0749-6419(99)00030-3.
[17] W.R. Whittington, A.L. Oppedal, S. Turnage, Y. Hammi, H. Rhee, P.G. Allison, C.K. Crane, M.F. Horstemeyer, Capturing the effect of temperature, strain rate, and stress state on the plasticity and fracture of rolled homogeneous armor (RHA) steel, Mater. Sci. Eng. A 594 (2014) 82–88. https://doi.org/10.1016/j.msea.2013.11.018.
[18] A. Banerjee, S. Dhar, S. Acharyya, D. Datta, N. Nayak, Determination of Johnson cook material and failure model constants and numerical modelling of Charpy impact test of armour steel, Mater. Sci. Eng. A 640 (2015) 200–209. https://doi.org/10.1016/j.msea.2015.05.073.
[19] Y. Cao, Y. Zhen, M. Song, H. Yi, F. Li, X. Li, Determination of Johnson–Cook parameters and evaluation of Charpy impact test performance for X80 pipeline steel, Int. J. Mech. Sci. 179 (2020). https://doi.org/10.1016/j.ijmecsci.2020.105627.
[20] C. Wang, Z. Tong, W. Zhong, H. Lin, G. Ning, C. Zhang, B. Yu, S. Xu, W. Yang, A method for directly measuring fracture toughness and determining reference temperature for RPV steels by Charpy impact test, Eng. Fract. Mech. 243 (2021) 107526. https://doi.org/10.1016/j.engfracmech.2021.107526.
[21] Ş. Karagöz, Ş.H. Atapek, A. Yilmaz, Microstructural and fractographical studies on quenched and tempered armor steels, Mater. Test. 52 (2010) 316–322. https://doi.org/10.3139/120.110134.
[22] A. Arias, J.A. Rodríguez-Martínez, A. Rusinek, Numerical simulations of impact behaviour of thin steel plates subjected to cylindrical, conical and hemispherical non-deformable projectiles, Eng. Fract. Mech. 75 (2008) 1635–1656. https://doi.org/10.1016/j.engfracmech.2007.06.005.
[23] A. Rusinek, J.A. Rodríguez-Martínez, R. Zaera, J.R. Klepaczko, A. Arias, C. Sauvelet, Experimental and numerical study on the perforation process of mild steel sheets subjected

to perpendicular impact by hemispherical projectiles, Int. J. Impact Eng. 36 (2009) 565–587. https://doi.org/10.1016/j.ijimpeng.2008.09.004.
[24] T. Jankowiak, A. Rusinek, P. Wood, A numerical analysis of the dynamic behaviour of sheet steel perforated by a conical projectile under ballistic conditions, Finite Elem. Anal. Des. 65 (2013) 39–49. https://doi.org/10.1016/j.finel.2012.10.007.
[25] M. Storchak, P. Rupp, H. Möhring, T. Stehle, Storchak, M., Rupp, P., Möhring, H. C., & Stehle, T. (2019). Determination of Johnson–Cook constitutive parameters for cutting simulations. Metals, 9(4), 473., (2019).
[26] T. Lodygowski, A. Rusinek, Constitutive Relations under Impact Loadings, 2014.
[27] B.J. Tuazon, K.O. Bae, S.H. Lee, H.S. Shin, Integration of a new data acquisition/processing scheme in SHPB test and characterization of the dynamic material properties of high-strength steels using the optional form of Johnson-Cook model, J. Mech. Sci. Technol. 28 (2014) 3561–3568. https://doi.org/10.1007/s12206-014-0817-8.
[28] A. Rusinek, J.R. Klepaczko, Shear testing of a sheet steel at wide range of strain rates and a constitutive relation with strain-rate and temperature dependence of the flow stress, Int. J. Plast. 17 (2001) 87–115. https://doi.org/10.1016/S0749-6419(00)00020-6.
[29] J.R. Klepaczko, A. Rusinek, J.A. Rodríguez-Martínez, R.B. Pecherski, A. Arias, Modelling of thermo-viscoplastic behaviour of DH-36 and Weldox 460-E structural steels at wide ranges of strain rates and temperatures, comparison of constitutive relations for impact problems, Mech. Mater. 41 (2009) 599–621. https://doi.org/10.1016/j.mechmat.2008.11.004.
[30] A. Rusinek, J.A. Rodríguez-Martínez, R. Zaera, J.R. Klepaczko, A. Arias, C. Sauvelet, Experimental and numerical study on the perforation process of mild steel sheets subjected to perpendicular impact by hemispherical projectiles, Int. J. Impact Eng. 36 (2009) 565–587. https://doi.org/10.1016/j.ijimpeng.2008.09.004.
[31] G.R. Johnson, W.H. Cook, Fracture characteristics of three metals subjected to various strains, strain rates, temperatures and pressures, Eng. Fract. Mech. 21 (1985) 31–48. https://doi.org/10.1016/0013-7944(85)90052-9.
[32] A. Rusinek, J.A. Rodríguez-Martínez, A. Arias, J.R. Klepaczko, J. López-Puente, Influence of conical projectile diameter on perpendicular impact of thin steel plate, Eng. Fract. Mech. 75 (2008) 2946–2967. https://doi.org/10.1016/j.engfracmech.2008.01.011.
[33] N.K. Gupta, M.A. Iqbal, G.S. Sekhon, Effect of projectile nose shape, impact velocity and target thickness on deformation behavior of aluminum plates, Int. J. Solids Struct. 44 (2007) 3411–3439. https://doi.org/10.1016/j.ijsolstr.2006.09.034.
[34] B.S. Henry, A.R. Luxmoore, The stress triaxiality constraint and the Q-value as a ductile fracture parameter, Eng. Fract. Mech. 57 (1997) 375–390. https://doi.org/10.1016/s0013-7944(97)00031-3.
[35] J. Peng, Y. Wang, Q. Dai, X. Liu, L. Liu, Z. Zhang, Effect of stress triaxiality on plastic damage evolution and failure mode for 316L notched specimen, Metals (Basel). 9 (2019). https://doi.org/10.3390/met9101067.
[36] Z. Zhang, Y. Wu, F. Huang, Effect of stress triaxiality cut-off value in the fracture criterion

on predicting the ballistic behavior of Al2024-T351 plate impacted by blunt- hemisphere- and ogival-nosed projectiles, J. Mater. Res. Technol. 25 (2023) 138–165. https://doi.org/10.1016/j.jmrt.2023.05.186.
[37] Y. Zhang, B. Guo, Q. Li, X. Li, J. Jian, Y. Jin, J. Ao, Damage and Cracking Prediction of AISI 410 Martensitic Stainless Steel at Elevated Temperatures, Steel Res. Int. 92 (2021) 1–12. https://doi.org/10.1002/srin.202100030.
[38] G. Testa, N. Bonora, A. Ruggiero, G. Iannitti, D. Gentile, Stress triaxiality effect on void nucleation in ductile metals, Fatigue Fract. Eng. Mater. Struct. 43 (2020) 1473–1486. https://doi.org/10.1111/ffe.13212.
[39] M. Murugesan, D.W. Jung, Johnson cook material and failure model parameters estimation of AISI-1045 medium carbon steel for metal forming applications, Materials (Basel). 12 (2019). https://doi.org/10.3390/ma12040609.
[40] J. Wang, W. Guo, J. Guo, Z. Wang, S. Lu, The Effects of Stress Triaxiality, Temperature and Strain Rate on the Fracture Characteristics of a Nickel-Base Superalloy, J. Mater. Eng. Perform. 25 (2016) 2043–2052. https://doi.org/10.1007/s11665-016-2049-9.
[41] K.M. Kpenyigba, T. Jankowiak, A. Rusinek, R. Pesci, B. Wang, Effect of projectile nose shape on ballistic resistance of interstitial-free steel sheets, Int. J. Impact Eng. 79 (2015) 83–94. https://doi.org/10.1016/j.ijimpeng.2014.10.007.
[42] J.A. Zukas, D.R. Scheffler, Practical aspects of numerical simulations of dynamic events: Effects of meshing, Int. J. Impact Eng. 24 (2000) 925–945. https://doi.org/10.1016/S0734-743X(00)00012-9.
[43] L.Y. Qian, G. Fang, P. Zeng, Q. Wang, Experimental and numerical investigations into the ductile fracture during the forming of flat-rolled 5083-O aluminum alloy sheet, J. Mater. Process. Technol. 220 (2015) 264–275. https://doi.org/10.1016/j.jmatprotec.2015.01.031.
[44] P.K. Jena, M.A.M. Manickam, S. Venketachari, S.C. Srivastava, A. Srivastava, S. Chakrabarty, K. Siva Kumar, Microstructure, mechanical, ballistic property evaluation of RHA steel produced by continuous-casting route, J. Appl. Res. Technol. 18 (2020) 1–13. https://doi.org/10.22201/ICAT.24486736E.2020.18.1.927.
[45] P.K. Jena, B. Mishra, M. RameshBabu, A. Babu, A.K. Singh, K. SivaKumar, T.B. Bhat, Effect of heat treatment on mechanical and ballistic properties of a high strength armour steel, Int. J. Impact Eng. 37 (2010) 242–249. https://doi.org/10.1016/j.ijimpeng.2009.09.003.
[46] W.M. Garrison, N.R. Moody, Ductile fracture, J. Phys. Chem. Solids 48 (1987) 1035–1074. https://doi.org/10.1016/0022-3697(87)90118-1.

Chapter - 4

Calibration of tensile tests in drop-weight impact machine and implementation in simulation of Charpy impact tests

Abstract

Material modeling and simulation of deformation under very high loading rates in the dynamic/impact range are applied in crash resistance, ballistic impact analysis, and other high-strain-rate phenomena. For material models applicable for high loading rate needs tensile test data at high and very high strain rates. Servo-hydraulic VHS tensile test data from Intermediate to higher strain-rate > ($500\ s^{-1}$) is reliable but expensive, and there are also complexities in experiment. Tensile testing at high $\dot{\varepsilon}$ (up to $1500\ s^{-1}$) can be conducted using a drop-weight impact testing machine with a specialized fixture, where the impactor velocity controls the strain-rate. In INSTRON CEAST 9350 drop weight impact testing machine tensile tests are conducted at four velocities for amour steel. A 5MHz data acquisition system (DAQ) measures strain in specimen gauge length mounted with high-elongation strain gauge. An extensometer is used to calibrate the strain gauge in a quasi-static $10^{-4}\ s^{-1}$ tensile test. Tensile test data from impact machine is compared with stress-strain data from the INSTRON servo-hydraulic testing machine with DIC for different $\dot{\varepsilon}$. Close matching in elastic modulus, yield strength, tensile strength, and elongation are observed. Material parameters for a strain rate-dependent material model (MJ-C model) are extracted from drop-weight impact testing data combined with other tensile test data. These parameters are then used in FE simulations of high strain-rate tensile tests and validated against experimental results. Later, the same material model parameters are used to simulate Charpy impact tests at various velocities and compared with experimental results that also show close matching.

4.1 Introduction

Characterization of armor steel from intermediate to high strain rate is necessary because it has to undergo large plastic deformation during its service. The strain rate hardening of armor steel offers significant advantage in energy absorption during ballistic impact or crash event. Therefore, rigorous testing of the material is required for efficient design application, but it is of great challenge especially at high strain rates. According to a survey report presented by [1–3], it is typically 50 times more expensive to produce high strain-rate tensile data than quasi-static tensile data in accordance with Euronorms [4]. The testing technology of steels at high strain rates is still under development phase. Generally, two types of test setup commonly used for high $\dot{\varepsilon}$ testing are

servo-hydraulic and Split Hopkinson setup. The servo-hydraulic test setup will work in open loop for strain rate (>10 s^{-1}) [1,5]. The limitation in traditional test setup like INSTRON 5582 or INSTRON 8801 was the extensometer used lost its structural integrity above strain rate 1 s^{-1} and when testing at extremely high speeds, the extensometer response would not be quick enough because of inertia effect also the inertia of the system. Non-contact types of extensometers are available nowadays like Electro-optical, Doppler, and laser extensometers. Material elongation is measured by capturing the image by high-speed cameras and processing in DIC. Although the method is quite reliable but the cost of conducting a single experiment is very high. The most accurate way to measure strain is to attach a strain gauge to the specimen gauge section.

This study aims to explore the acceptability of tensile test results at a high strain-rate conducted in INSTRON CEAST 9350 drop weight impact testing machine. The data is compared with the results of equivalent strain-rate obtained from servo-hydraulic test setup employed with DIC. The material parameters for material models J-C, R-K and MJ-C are extracted from new test data. Then numerical simulation is performed by using J-C, R-K and MJ-C material model for tensile test and for Charpy impact test simulation is only performed by MJ-C material model. The validity of the parameters is verified by numerical simulation of Charpy impact test.

4.2 Tensile test in Drop Weight Impact testing machine

High strain rate stress-strain data is a crucial component of the material inputs for precise computer prediction. The tensile tests at four velocities in INSTRON CEAST 9350 Impact test set up are conducted at room temperature by employing strain gage to measure sample displacement. Before this calibration of strain gauge is necessary.

4.2.1 Procedure for strain gauge calibration

For testing at higher $\dot{\varepsilon}$, the selection of strain gauge is based on material elongation at lower strain rate (10^{-1} s^{-1}) which is usually less than 20%. The specimen drawing for high $\dot{\varepsilon}$ is shown in Fig. 4.1. Test results for this data is already presented in Chapter 2. Therefore, high elongation strain gauges are used (to measure more than 20% strain) along with the high elongation adhesive. The load was captured by the load sensor of the testing machine. The strain gauge is pasted directly over the gauge length of specimen. The wire of the strain gauge is connected to the data acquisition system. The raw data are generated in the form of voltage. This voltage signal is converted into strain by suitable calibration of the strain gauge with the material under study. This require the calibration of the strain gauge using an extensometer at a quasi-static strain-rate to verify the relationship exist between voltage output and extensometer displacement [6]. For a given test speed, different metals & alloys will introduce different levels of steady strain rate into

the specimen gauge length. Although it is desirable to minimize such strain rate variations as a function of specimen resistance, there are practical limitations to what can be achieved. Since the displacement rate evolving stain rate can be calculated for each test using the specimen gauge length, it is crucial to calibrate both strain measuring devices (strain gauges and data acquisition system) [3]. The tensile specimen is first calibrated with strain gauges and data acquisition system up to the yield point at a quasi-static strain rate for this the strain gauge and extensometer are attached in the sample gauge length, as shown in Fig. 4.2. The DAQ gives signal in form of voltage vs time Fig. 4.3a displays the filtered voltage vs. time curve while the extensometer displacement *vs.* time plot is presented in Fig.4.3b. To determine the exact straining in the gauge section of specimen the signal is filtered without altering its original characteristics. The filtered voltage vs. extensometer displacement is then plotted, and a calibration constant 0.087 is obtained from the curve fitting shown in Fig. 4.4. As the fitting is linear because the data obtained appears to be linear at both ends and also for convenience the potential difference versus extensometer data are fitted as linear.

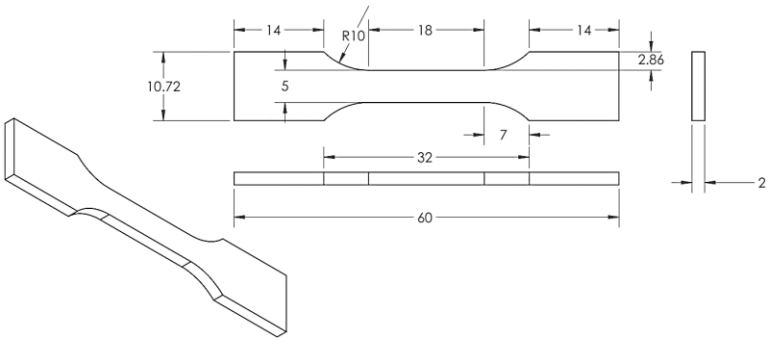

Fig. 4.1 High strain-rate tensile test specimen drawing

Fig. 4.2 Armour material tensile sample with strain gauge and extensometer for calibration of strain gauge

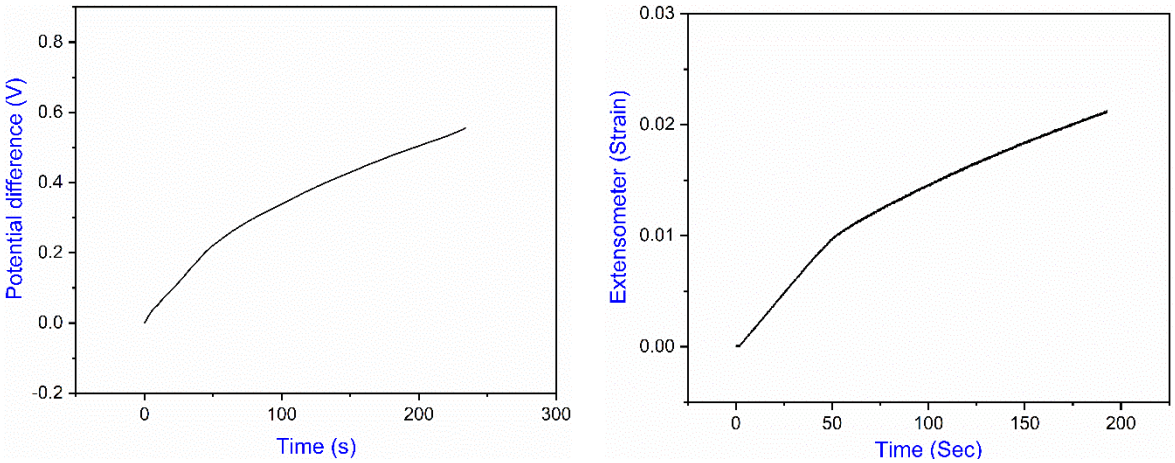

(a) **(b)**

Fig. 4.3 (a) Potential difference (Voltage) from strain gauge vs. time (b) Extensometer (strain) vs. time curve from INSTRON 5582

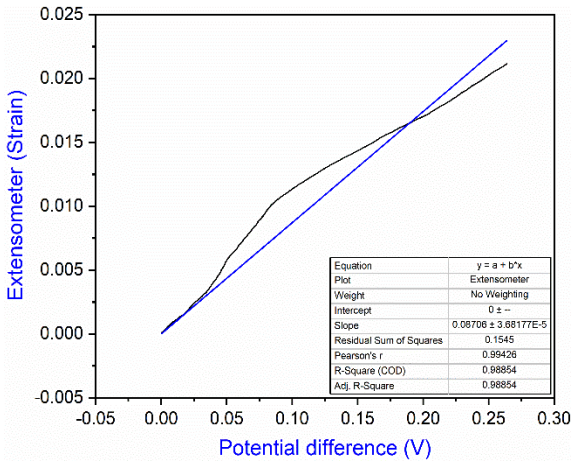

Fig. 4.4 Extraction of calibration constant

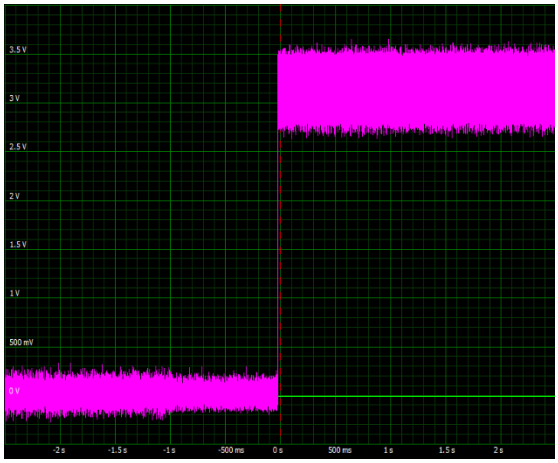

Fig. 4.5 High strain rate test voltage signal (voltage *vs*. time)

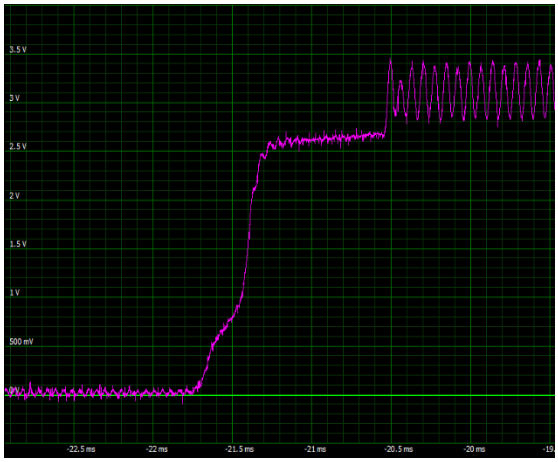

Fig. 4.6 Zoom view of voltage *vs*. time signal

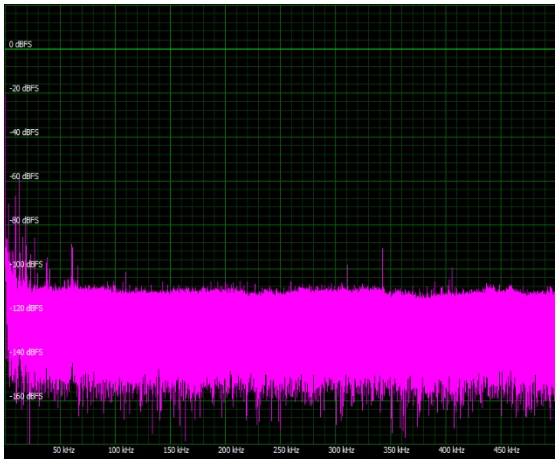

Fig. 4.7 FFT of voltage *vs*. time signal

Fig. 4.8 Voltage *vs*. time signal after noise reduction (red)

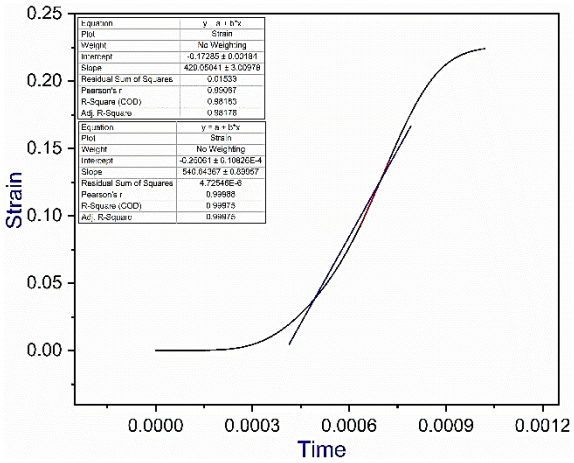

Fig. 4.9 Plot of strain rate reached with strain gauge

4.2.2 High strain-rate tensile test

The high strain rate tensile test is then performed in INSTRON CEAST 9350 test setup using another sample with strain gauge. Strain signal in form of voltage as shown in Fig. 4.5 depicts the voltage *vs*. time signal for this at a velocity of 3 m/s. The signal obtained is too much noisy and hence the signal is properly filtered to reduce noise. As the maximum noise frequency must be known for filtering, the FFT (Fast Fourier transform) is done to convert it into frequency domain. After determining the maximum noise level, a low-pass filter is applied to cut off the upper frequency. The signal left after filtering is shown in Fig. 4.8; this is the actual voltage that comes out due to strain gauge displacement. The voltage signal is then multiplied by calibration constant (0.087) to obtain the strain signal. The engineering strain vs. time plot is shown in Fig. 4.9. The force vs. time is shown in Fig. 4.10. The engineering stress-strain diagram is then plotted as seen in Fig. 4.11. The true-stress vs. true plastic strain curve obtained from engineering stress-strain diagram. True-stress vs. true plastic strain curves for different velocities are determined from experiment in a drop-weight impact machine and are smoothened by curve fitting and shown in Fig. 4.12.

The true stress vs. plastic strain curves obtained from both the servo-hydraulic machine (tested elsewhere) and drop weight impact machine at almost similar $\dot{\varepsilon}$ are shown in Fig. 4.13. The matching in the response is continued upto ultimate stress. The J-C, R-K and MJ-C material parameters are then extracted from experimental results of tensile tests at different $\dot{\varepsilon}$ including the tensile test data from drop weight impact machine. The material models parameters are extracted from intermediate to high strain-rate test data obtained from drop-weight machine and are listed in Table. 4.1. The tensile test data from drop weight machine are available upto $\dot{\varepsilon}$

997.95 s^{-1}. The accuracy in FE simulation of tensile tests depends on the accuracy of material parameters, which depends on the pool of test data. In this case, FE simulation of tensile tests at high $\dot{\varepsilon}$ are performed with material parameters as listed in Table. 4.1 and compared with experimental results to assess the accuracy of the material parameters.

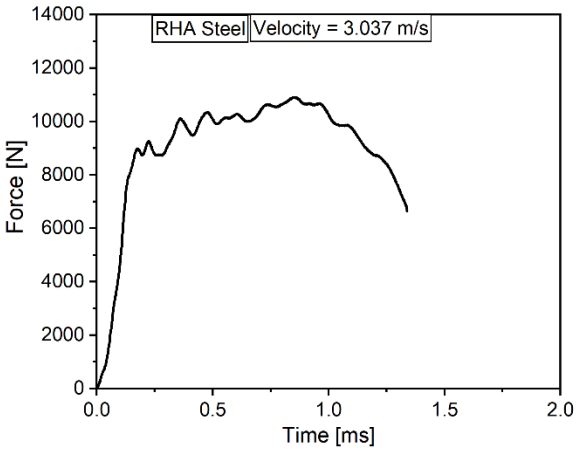

Fig. 4.10 Force vs. time curve at 3 m/s velocity

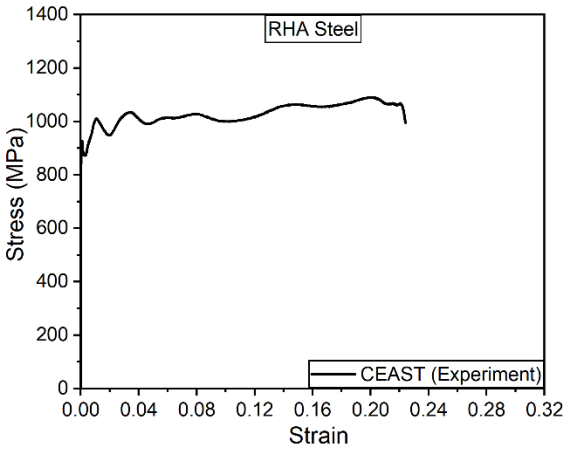

Fig. 4.11 Raw data of CEAST with strain gauge implemented

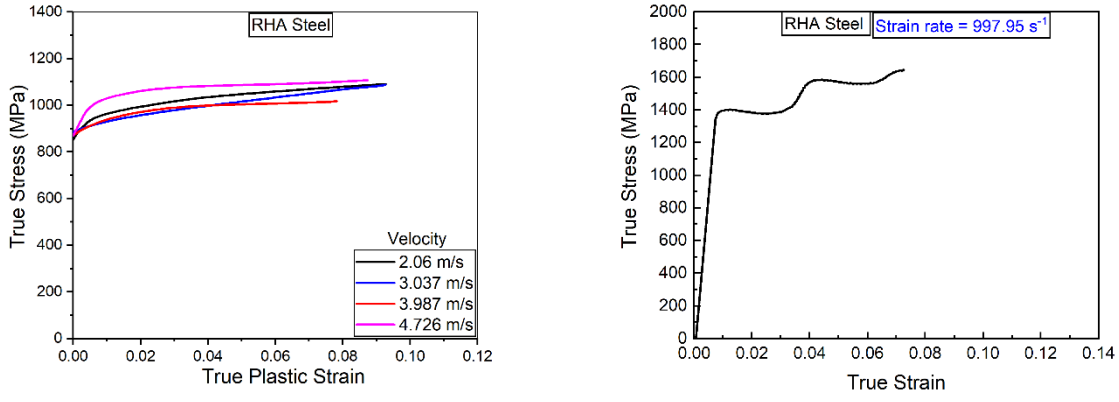

(a) (b)

Fig. 4.12 True stress vs. plastic strain curves at four velocities (a) Intermediate strain-rate (b) high strain-rate (997.95 s^{-1}) at velocity 16 m/s.

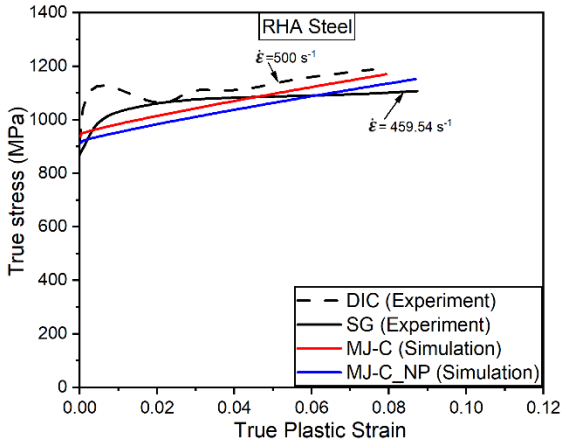

Fig. 4.13 True stress vs. true plastic strain experimental data comparison of servo-hydraulic with DIC and Impact testing machine with strain gauge

Table 4.1 Viscoplastic material models and failure model coefficient values

J-C model parameters	Value	MJ-C model parameters	Value	R-K model parameters	Value	J-C failure model parameters	Value
A	854.34 MPa	A	854.34 MPa	B_0	1467.72 MPa	D_1	0.015
B	1789.69 MPa	B	1789.69 MPa	n_0	0.078	D_2	0.70
C	0.006	G_1	0.007	ε_0	0.0041	D_3	-7.79
n	0.86	G_2	0.87	D_1	0.65	D_4	0.174
m	1.50	r	0.93	v	0.247	D_5	1.22
		G_3	0.707	σ_0^*	656.12 MPa		
		m	1.30	m	2.94		
				D_2	0.02		
				θ^*	0.61		
				T_m	1773 K		
				$\dot{\varepsilon}_{max}$	10^4		
				$\dot{\varepsilon}_{min}$	10^{-5}		

4.3 Numerical model

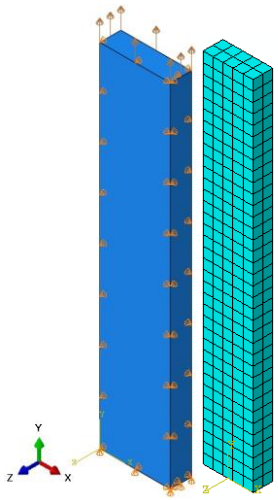

Fig. 4.14 Quarter tensile specimen model

High strain rate tensile tests are simulated in ABAQUS standard CAE software for all material models at velocity 4.726 m/s. Fig. 4.14 shows a typical quarter tensile sample with boundary

conditions. The specimens are modeled with C3D8 elements with a total number of 360 elements and 666 nodes. The material model is implemented through a user-defined material code VUMAT into ABAQUS software. To differentiate between MJ-C material model parameters here the new parameters is denoted as MJC_NP. The results from both sets for different strain rates (velocities) are obtained and compared with experimental results as shown in Fig. 4.15(a-d). At all the given strain rates (velocities) the material parameters extracted from experimental data of INSTRON CEAST 9350 test system show better matching with experiments. It suggests that the inclusion of test data from drop-weight machine enhances the quality of material parameters. For further verification of the validity of test results Chapy impact test simulation has been performed by using the parameters extracted from both the experimental results and compared with experimental results.

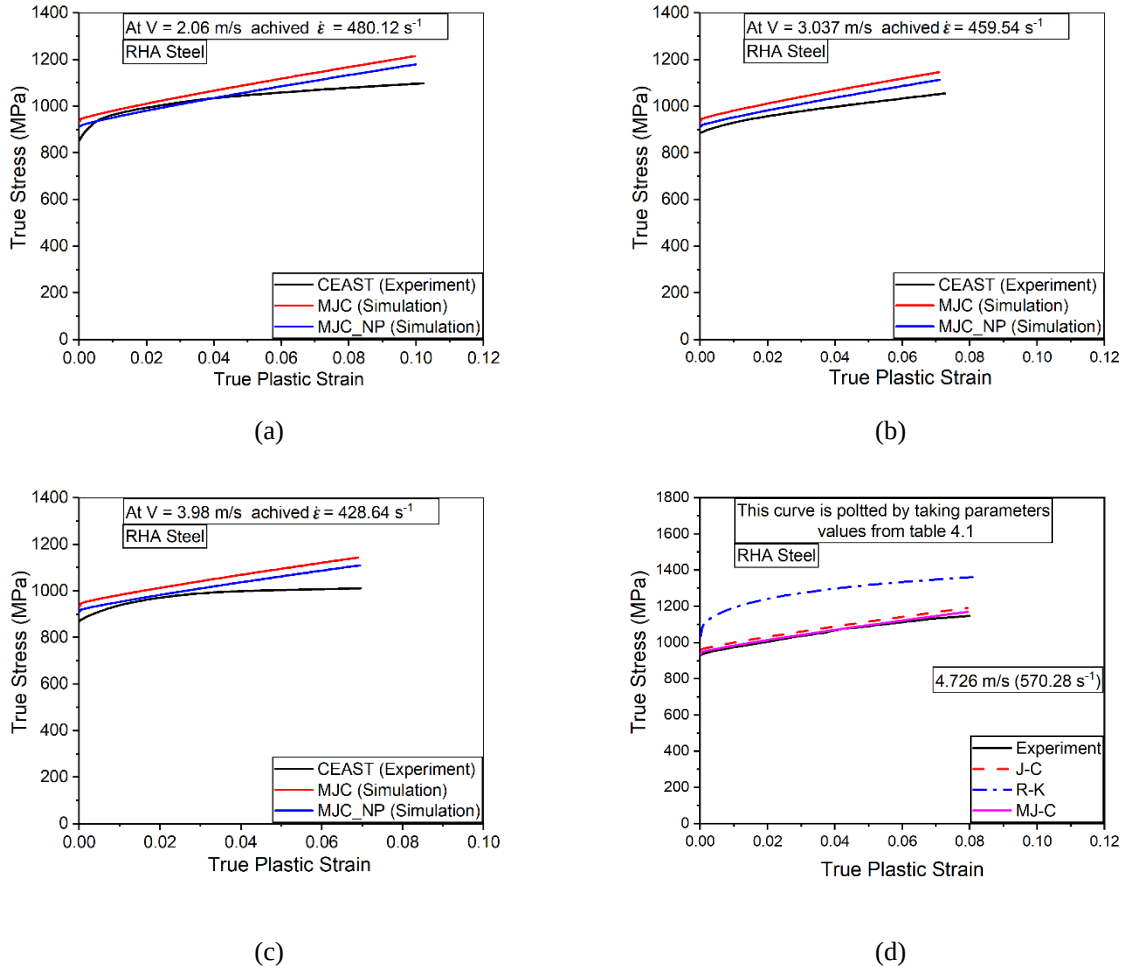

Fig. 4.15 Comparison of true stress vs. true plastic strain experimental data and simulation by material models by the

parameters extracted from servohyraulic with DIC and Impact testing machine CEAST 9350 with strain gauge.

4.4 Charpy test Simulation by employing parameters extracted results of tensile test done in CEAST drop weight test setup and parameters derived from servo-hydraulic test set-up with DIC results

Impact of Charpy V-notch specimen at velocities 3 m/s and 4 m/s is simulated in ABAQUS Explicit FEA software. The material parameters are implemented through VUMAT code and plugged with software. The specimen was modelled according to the ASTM standard E23-18. The anvil or striker is made discrete rigid and sample is made deformable. The velocity boundary condition is given to anvil and specimen is fixed in x-z direction with restricted rotation in y-direction. The simulation is done by parameters extracted from both the experimental results. From Fig. 4.16 it is clear that MJ-C_NP simulation results are very near to the experimental results for both the velocities. The peak force in the experiment is 23.11 kN, whereas MJ-C model predicted 25.02 kN, while MJ-C_NP predicted 24.3 kN which is very nearer to the experimental value. The error was 5.14% in case of MJ-C_NP where as in case of MJ-C the error is 8.26% in prediction of peak force.

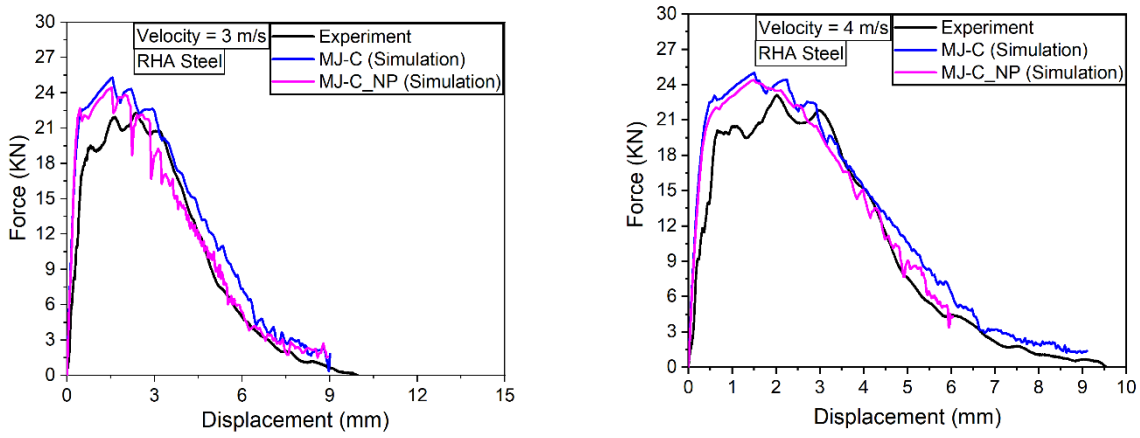

(a) (b)

Fig. 4.16 Experimental and simulated Charpy V-notch impact results at impact velocities (a) 3 m/s and (b) 4 m/s

4.5 Comparison among experimental methods of three type of test system

The four main components of the high strain-rate test system include—input techniques (parameters like data capturing frequency), specimen geometry (whether using short or long specimen because if the specimen mass is large then inertia will be more), clamping techniques

(gripping), and measurement tools (data acquisition system, pre and post processing of data)—are essential for accuracy of the test results. The detailed operational method of servo-hydraulic VHS [6–9] and split Hopkinson are given in the literature [10,11] here only INSTRON CEAST 9350 system described in detail. All three-machine comparison are listed in Table 3. According to the specifications outlined in the standards, the CEAST 9350 is a drop tower impact tester used to perform instrumented tests on plates, film specimens, and tridimensional parts. It is manufactured and designed with the modularity concept. The detailed dimension and function of the parts are mentioned in the manual [12,13]. The strain gauge force sensor is used to capture the force. The specimen is attached in the two grips by four screws. The static grip is close to the force sensor and it is fixed as shown in Fig. 4.17. The dynamic grip, move with a certain velocity when the striker hit it. The global displacement is measured by the photocells. The energy required for fracture specimen is calculated by the Eq. 4.7. The equivalent impact height is calculated by Eq. 4.8. The grip section of the tensile sample must stay in the elastic deformation regime all over the tensile test because the strain gauge force sensors collect load data from the grip. In order to prevent the grip section from yielding during testing, the material of the grip and the width section of the testing sample were chosen carefully. The design of sample for servo-hydraulic VHS is like one grip section end is longer than the other to allow uniform loading in the segment whereas for split Hopkinson and CEAST 9350 the geometry is like the traditional dog bone specimen but the sample size is small [11,14].

The impact energy is calculated by the machine automatically according to the formula:

$$E_{impact} = ½\ m_{total}\ v_{impact}^2 \tag{4.7}$$

where, E_{impact} = *Impact energy*, v_{impact} = *Impact velocity*, m_{total} = *Total mass*

$$m_{total} = m_{striker} + m_{carriage} + m_{weights} + m_{extension}$$

where, $m_{striker}$ = Tup mass (bring from tup database), $m_{carriage}$ = Carriage mass, $m_{weights}$ = Mass of additional weights, $m_{extension}$ = Extension mass

By fixing the falling mass, the impact height values can be adjusted to produce a particular impact energy. Impact energy can also be set, but it will only be roughly calculated when the text is executed. The impact velocity is the only parameter that the instrument can control, and it can be controlled with two decimal places of accuracy. Therefore, the value obtained for the Impact velocity will be approximated with a precision of two decimal digits as the system recalculates the energy formula to position the tup at the proper height. As a result, the Impact energy will also be approximated. Enter the desired impact velocity or a number that complies with global

standards.

Using the following formula, this value is used to determine the equivalent impact height:

$h_{impact} = v_{impact}^2 / 2g$ (4.8)

where, h_{impact} = Equivalent impact height, g = acceleration due to gravity

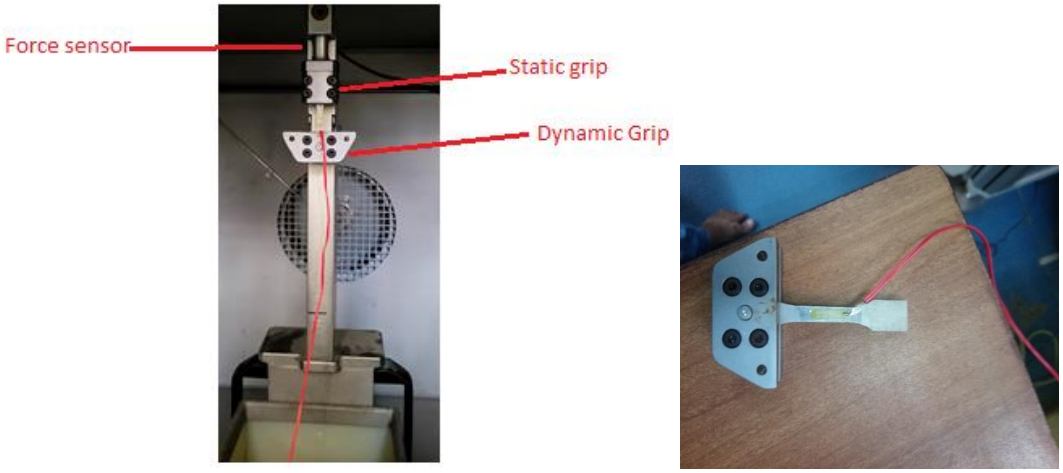

Fig. 4.17 Griping system in CEAST 9350

Table. 4.2 Comparison between three types of test systems

Parameters	Servo-hydraulic VHS	Split Hopkinson	CEAST 9350
Operating temperature	-100ºC to 250ºC or induction of heating system upto 1000ºC (if DIC is integrated with the system)	-150ºC to 650ºC (with additional chamber)	-70ºC to 150ºC (with dedicated environmental chamber)
Operational velocity	25 ms^{-1}	50 ms^{-1}	0.8 ms^{-1} to 25 ms^{-1} (with additional accessories)
Purpose	Automotive crash event	Impact and blast	Impact and blast
Maximum impact load Sensing	40 KN to 100 KN	100 KN	15 KN
Type of force sensor	Piezoelectric load cell	Force is sensed by strain gauge mounted on bar	Strain gauge type
Operating pressure	280 bar (hydraulic oil)	16 bar (air gas gun)	6 to 10 bar (compressed air)
Strain rate achieved without additional accessories	500 s^{-1}	10^4 s^{-1}	1500 s^{-1}
Strain rate achieved with additional accessories	10^3 s^{-1}	$>10^5$ s^{-1}	10^4 s^{-1}
Cost of performing single experiment [15]	High	Low in comparison to VHS system	Low in comparison to VHS system

4.6 Conclusion

- In computer simulations of both the tensile test and the Charpy impact test, the material parameters of the MJ-C_NP material model that were derived from tests performed in the INSTRON CEAST 9350 test system along with strain gauge provide a better prediction. It demonstrates that the material's properties from tests done with a drop-weight impact testing device are closer to the values needed for accurate numerical prediction.
- The maximum velocity of drop-weight impact testing machine and servo-hydraulic test system is almost similar. Despite of this there is a constraint in the requirement of high-speed camera of DIC system in terms of frame speed. High FPS (frame per second) camera can be used but it will ultimate increase the cost of setup which have an impact on overall cost of testing per sample.
- The acquisition of accurate high-strain-rate data is critically dependent on mitigating dynamic oscillations, or 'ringing,' in the measured load signal. This phenomenon is a function of the entire testing system's natural frequency, including the specimen geometry, fixtures, and load cell type.

  The servo-hydraulic system utilized a piezoelectric load cell. While these sensors offer a very high natural frequency and are excellent for capturing rapid force transitions, their high stiffness can make the recorded signal more susceptible to excitation by high-frequency stress waves, manifesting as significant ringing. Conversely, the Instron CEAST 9350 drop-weight system employed a strain gauge-based load cell. The characteristics of this specific setup, potentially including a different mechanical filtering effect or a lower natural frequency damped by the system's structure, resulted in a measured load signal with a different noise profile, which was empirically observed to require less aggressive filtering for the given test conditions.

  Crucially, for both systems, the validity of the final stress-strain data was not reliant on the raw load signal alone. The primary strain measurement was obtained using optical Digital Image Correlation (DIC), which is immune to mechanical ringing. Furthermore, the raw load data from both systems was processed using validated filtering techniques (e.g., low-pass Butterworth filters) as recommended by standards like ISO 26203-2. This post-processing step ensures that the final data represents the material's response by removing system-specific oscillations, thereby allowing for a fair comparison of results derived from both experimental setups.
- The test sample size required for tensile testing in CEAST 9350 very small compared to that

required in servo-hydraulic test system especially for high $\dot{\varepsilon}$ testing, therefore the material requirement is less. It is estimated that from one tensile test sample of servo-hydraulic set-up, at least fifteen sample can be prepared to conduct similar test in CEAST 9350. Therefore, the cost of testing per sample is very low in the latter.

- Investigations are still in progress on the intermediate to high strain rate test results. Because of this, only tests for intermediate $\dot{\varepsilon}$ are presented in this study. It can fill the gap between the results of the intermediate to high $\dot{\varepsilon}$ test.

References

[1] P.K.C. Wood, C.A. Schley, M. Buckley, J. Smith, An improved test procedure for measurement of dynamic tensile mechanical properties of automotive sheet steels, SAE Tech. Pap. (2007). https://doi.org/10.4271/2007-01-0987.

[2] P.K.C. Wood, C. a Schley, R. Beaumont, M. a Williams, M. a Buckley, A new strain rate dependent spot weld model for automotive crash applications, (2009) 1–14. http://strathprints.strath.ac.uk/30723/.

[3] P.K.C. Wood, C.A. Schley, Strain Rate Testing of Metallic Materials and Their Modelling for Use in CAE Based Automotive Crash Simulation Tools (Recommendations and Procedures), 2009. http://scholar.google.com/scholar?hl=en&btnG=Search&q=intitle:Strain+Rate+Testing+of+Metallic+Materials+and+their+Modelling+for+use+in+CAE+based+Automotive+Crash+Simulation+Tools+(Recommendations+and+procedures)#0.

[4] B. Standard, Metallic materials—tensile testing—part 1: method of test at ambient temperature, Bs En (2001).

[5] P.K.C. Wood, C.A. Schley, R. Beaumont, M.A. Williams, M.A. Buckley, Improved efficiency and quality control in the manufacture and preparation metallic specimens for high rate tensile testing, (2014) 5–10.

[6] P.K.C. Wood, C.A. Schley, M. Buckley, J. Smith, An improved test procedure for measurement of dynamic tensile mechanical properties of automotive sheet steels, SAE Tech. Pap. 116 (2007) 302–312. https://doi.org/10.4271/2007-01-0987.

[7] D.M. Bruce, D.K. Matlock, J.G. Speer, A.K. De, Assessment of the strain-rate dependent tensile properties of automotive sheet steels, SAE Tech. Pap. (2004). https://doi.org/10.4271/2004-01-0507.

[8] P.K.C. Wood, C.A. Schley, I. McGregor, T. Dutton, M. Bloomfield, R. Bardenheier, Characterising performance of automotive materials at high strain rate for improved crash design, J. Phys. IV JP 134 (2006) 1167–1174. https://doi.org/10.1051/jp4:2006134178.

[9] H. Huh, J.H. Lim, S.H. Park, High speed tensile test of steel sheets for the stress-strain curve at the intermediate strain rate, Int. J. Automot. Technol. 10 (2009) 195–204. https://doi.org/10.1007/s12239-009-0023-3.

[10] B. Yan, Y. Kuriyama, A. Uenishi, D. Cornette, M. Borsutzki, C. Wong, Recommended practice for dynamic testing for sheet steels - Development and round robin tests, SAE Tech. Pap. 115 (2006) 147–157. https://doi.org/10.4271/2006-01-0120.
[11] N. Ledford, H. Paul, G. Ganzenmüller, M. May, M. Höfemann, M. Otto, N. Petrinic, Investigations on specimen design and mounting for Split Hopkinson Tension Bar (SHTB) experiments, EPJ Web Conf. 94 (2015) 1–6. https://doi.org/10.1051/epjconf/20159401049.
[12] C. Impact, Accessories for CEAST Impact Systems, (n.d.). http://www.instron.us/en-us/products/testing-systems/impact-systems/drop-weight-testers/9340-drop-tower.
[13] Instron, CEAST 9300 Series, CEAST 9300 Ser. Droptower Impact Syst. (2009).
[14] Q. Wang, F. Xu, L. Xing, D. Huang, B. Wu, Intelligent optimization design of specimen on sheet materials for Split Hopkinson Tensile Bar tests, IOP Conf. Ser. Mater. Sci. Eng. 563 (2019). https://doi.org/10.1088/1757-899X/563/2/022016.
[15] B. Standard, Metallic materials—tensile testing—part 1: method of test at ambient temperature, Bs En (2001). http://scholar.google.com/scholar?hl=en&btnG=Search&q=intitle:Metallic+Materials+-+Tensile+Testing+-+Part+1:+Method+of+test+at+ambient+temperature#9.

Chapter - 5

Effect of Projectile strength on ballistic impact properties of RHA steel

Abstract

Ballistic impact is a highly complex phenomenon involving extremely high loading rates—up to several thousand per millisecond—along with changes in material properties and boundary conditions. In this work, a 40 mm thick rolled homogeneous armor (RHA) plate was impacted at ordnance velocities and the analysis was conducted both experimentally and numerically. The plate was impacted by a deformable projectile having cylindrical body, stepped shape and blunt nose. High-speed imaging techniques were used to capture the impact event and measure various parameters. Different failure modes of the plates were observed at various striking velocities. The impact test was then numerically simulated using thermoviscoplastic material models the: Johnson-Cook, Rusinek-Klepaczko, and Modified Johnson-Cook (MJ-C).

5.1 Introduction

In the ballistic impact phenomenon, a complex stress state develops, rapidly varying with position and time. Time-dependent dynamic fractures also occur. The study of ballistic impact on rolled homogenous armor steel (RHA) steel involves integrating experimental observations and computational modelling to understand penetration mechanics under high strain rates. Borvik et al. [1] pioneered this field by using Johnson-Cook viscoplastic and damage models [2] within the LS-DYNA finite element frame works to simulate ballistic penetration, laying the groundwork for advanced material models. Building on this, Camacho and Ortiz [3] developed a Lagrangian finite element model for ductile penetration, emphasizing the importance of adaptive meshing in mitigating element distortions and accurately capturing high-velocity field variations. Zukas and Scheffler [4] highlighted the critical role of computational mesh quality, demonstrating discrepancies between experimental results and numerical predictions in high-velocity impact scenarios due to mesh inadequacies, and exploring the effects of boundary reflections and length-to-diameter ratios on numerical accuracy.

Borvik et al. [5,6] further investigated the effects of projectile nose shape on the deformation and penetration of Weldox 460E steel plates. Their experiments showed that blunt projectiles were more efficient at lower velocities, while conical projectiles required less energy at higher velocities, influencing energy absorption and failure modes. Adaptive meshing was employed in their simulations to address conventional meshing issues. Understanding of the correct viscoplastic

constitutive relation for a material requires knowledge of its atomic structure, such as whether it is FCC or BCC. Chia-Jung Hu et al. [7] evaluated the ballistic performance of modified rolled homogenous armor (MRHA) steel, comparing it with AerMe 100, AISI 1045 and 4130 steels. Their tests revealed the formation of "white"-etched adiabatic shear bands on the front surface of target plates made from AerMet 100, 4130, and MRHA steels, indicating transformed bands due to crystallographic phase transitions.

Bruce and David [8] found that the energy absorption between different materials was highly dependent upon the strain limit chosen for the calculation. Large plastic deformation take place during dynamic events not only in case of impact and penetration events but also in high speed machining operations.

For ballistic impact phenomenon, dynamic behaviour of high strength armor steel material should be analysed carefully. Nahme and Lach [9] worked on dynamic properties of Mars 190, Mars 240 and Mars 300 armor steel from strain rate 10^{-3} s^{-1} to 10^{6} s^{-1} where they also showed the influence of the loading process on the microstructure and the fracture mechanism. Kasonde and Waldo [10] carried out systematic analysis of the microstructure and the fracture surfaces of 13 laboratory melted tempered martensitic armour steels to understand the improved ballistic performance of these steels. In an observation they found that the detrimental effect of inclusion on ballistic performance depends on the tempering T and on the $\dot{\varepsilon}$.

In 2013 Jankowiak et al. [11] explored the dynamic response of sheet steel under perforation by a conical projectile. The investigation took into account factors such as the target's thickness, its constitutive material model, the mass of the projectile, the friction at the interface, and the projectile's shape. To properly analyse the actual material failure pattern and deformation patterns suitable material model is necessary. In 2014 Whittington et al. [12] studied the behaviour of RHA (Rolled Homogenous armour) steel at 25^{o}C and 300^{o}C and at $\dot{\varepsilon}$ of 10^{-3} s^{-1} and 1000 s^{-1} to evaluate the effect of stress state on plasticity and fracture. In 2015 Tria et al. [13] studied the effectiveness of four ductile fracture models: Modified Johnson-cook (MJC), the Cockcroft-Latham (CL), the maximum shear stress and the constant failure strain model. These models are used to capture material fracture properties and shear plugging failure in 30PM steel plates. In 2015 Trajkovski et al. [14] study the flow and fracture properties of high-strength armour steel PROTAC 500. The J-C strength and fracture model are used for numerical simulation.

In 2015 Kpenyigba et al. [15] examined how the projectile's nose geometry affects the ballistic resistance of IF steel. Their study covered impact velocities ranging from 35 to 180 m/s and utilized the Rusinek-Klepaczko (RK) thermoviscoplastic material model for numerical simulations. The

results demonstrated that this model effectively captures the physical mechanisms involved in the perforation process.

In 2017 Tria and Trebinski [16] presented a novel methodology for experimental verification of constitutive models and numerical algorithms used in terminal ballistics of small arms ammunitions. The methodology comprises of the following elements: identification of material models in a set of independent tests, terminal ballistics testing of conditions covering the most important cases of bullet-target interactions, while providing enough data to assess the scatter of parameters measured in the experiments and the deviation of modelling results from the experiments. In 2017 Banerjee et al. [17] investigated the ballistic resistance of typical armour steel plate of medium thickness by ogive-nosed projectile striking at ordinance velocity. The J-C material model was used for numerical simulation. In 2017 McDonald et al. [18] evaluated two steels, a high hardness steel (HHA) and a Rolled homogenous armour steel (RHA). A series of 30 blast experiments are carried out. In terms of deformation resistance and rupture threshold the HHA steel outperform a more ductile RHA steel.

In 2019 T.Fras et al. [19] investigated armour steel of high hardness 600-640 HB plate failure by striking the deformable projectile at velocity 300 ms^{-1}. In 2020 E.Konca [20] studied the ballistic performance of various microstructures in MIL-A-12560 armour steel. The steel was subjected to isothermal heat treatments at three different temperatures, 360^{o}C, 320^{o}C and 270^{o}C. The promising nature of the bainite microstructure was confirmed as the sample isothermally treated at 360^{o}C provided approximately 10% higher ballistic protection as compared to the regular RHA sample of tempered martensite microstructure.

In 2020 P.K.Jena et al. [21] studied the impact resistance of rolled homogenous steel of five different thickness i.e. 20, 30, 40, 50, and 80 mm through continuous casting route. The microstructure, mechanical and ballistic properties of the continuous cast steel is compared with the steel produced by conventional ingot cast route. In 2020 S.Choudhary et al. [22] conducted experimental and numerical research on a newly developed high-strength armor steel plate. Their numerical simulations incorporated four ductile fracture criteria: Modified Johnson-Cook (MJC), Cockcroft-Latham (CL), Constant Failure Strain (CFS), and Maximum Shear (MS) stress failure criteria. The study compared these simulation results with impact test data from a 1000 × 1000 × 6 mm steel plate subjected to 7.62 × 51 mm NATO ball ammunition, meeting National Institute of Justice Level 3 protection standards. The MJC, CL, and CFS criteria closely matched the experimental findings, whereas the Maximum Shear stress failure criterion did not accurately predict the observed behavior.

In 2021 et al. [23] studies showed that high-nitrogen steel (HNS) with austenitic microstructures outperformed traditional medium-carbon, low-alloy steels with tempered martensitic microstructures in structural armor applications. Ballistic tests compared HNS and rolled homogeneous armor (RHA) steel plates against tungsten heavy alloy penetrators at 1630 ± 20 m/s. HNS exhibited higher ballistic performance and lower normalized depth of penetration due to its higher dynamic flow stress. Post-ballistic hardness measurements indicated greater energy dissipation in HNS targets, and microstructural analysis revealed that adiabatic shear band-induced cracking significantly influenced the failure of both steel targets.

In 2023 Zhao Zhang et al. [24] utilized finite element analysis to determine appropriate stress triaxiality cut-off values in fracture criteria affecting the ballistic performance of 9.94 mm thick Al2024-T351 plates when impacted by blunt, hemispherical, and ogival-nosed projectiles. The investigation, carried out in ABAQUS/Explicit, employed a (MJC) model alongside the DF2021 criterion, systematically varying the stress triaxiality cut-off parameter between 0.0 and 0.5. The ballistic limit velocity increased with higher cut-off values for blunt projectiles and showed varying effects for hemisphere and ogival-nosed projectiles. Different projectile shapes resulted in varied shear plug or fragment profiles. DF2021 with a 0.1 cut-off parameter aligned best with experiments. The study highlights the importance of considering stress triaxiality cut-off values in predicting ballistic behavior.

The analysis presented by Timothy [25,26] indicates that it is important to consider both the critical strain for ASB formation and the thermal diffusivity to analyze the propensity to ASB formation. Based on earlier studies [23,27], it can be expected that HNS will have more resistance to ASB formation due to its very high critical strain for ASB (in comparison to RHA steel), resulting from higher values of strain hardening and strain rate sensitivity and lower thermal softening.

From the literature review it is clear that very few studies are available dealing with **thick plate penetration resistance and failure patterns** at ordinance velocity. In this work, ballistic impact on typical rolled homogenous armour plate tests were analyzed both experimentally and numerically using thermo-viscoplastic material models: Johnson-Cook, Rusinek-Klepaczko, and a newely developed material model namely, Modified Johnson-Cook (MJ-C). The projectile, made of high-strength steel, was considered deformable. The results from the simulations were compared with the experimental data.

5.2 Overview of study

Ballistic impact experiments are initially performed at various impact velocities on a 40 mm thick RHA steel plate. Subsequently, ballistic impact simulations are conducted using three different material models, along with the failure model discussed in Chapter 2.

The projectile used for the study had a stepped shape, with a diameter of 30 mm and a length of 100 mm. The configuration of the projectile and the plate in the simulations was identical to that used in the experiments. All scenarios were analyzed using constant coefficients of friction.

Simulations were carried out considering both rigid and deformable projectiles. This approach was adopted because experimental observations revealed that the projectile deformed at higher striking velocities. Consequently, simulations were performed with a deformable projectile, incorporating a failure criterion for both the plate and the projectile.

5.3 Experiments

Ballistic impact tests are conducted to validate the numerical models. To perform the experiment, the design of a suitable test fixture is crucial. Most important that the target armor plate must be held firmly during the impact, while on the other hand, there must be clearance on all sides for the high-speed cameras and artificial illumination system to have an unobstructed view of the impact event. In this experiment, a suitable holder made of mild steel I-section beams was used to hold the plate in a firm vertical position. The entire setup is depicted in Fig. 5.1.

This study focuses on the ballistic resistance of a 40 mm thick RHA steel plate. The dimensions of the plates are 500 x 500 x 40 mm. The plates are impacted by stepped shape cylindrical projectiles with a maximum diameter of 30 mm (caliber), referred to as 30 mm armor-piercing (AP) shots (Projectile). The projectile are made of high-strength steel (PHS 1500), featuring a high strength and hardness. The projectile has a 1 mm diameter pointed nose shape. Each projectile weighs approximately 300 grams. The geometry of plate and projectile are shown in Fig. 5.2.

The projectile is fired from a typical gun and is propelled by the combustion of the specified propellant. The striking velocities on the target plate are varied by appropriately changing the propellant mass. The striking velocity is measured by typical foil and counter method [17]. Additionally, high-speed video camera is used to capture the impact phenomenon and also estimate the striking velocity & post-perforation residual velocity by frame-by-frame analysis. Provision is also made for artificial illumination on the target keeping in view the high-speed impact event. During the experiment, multiple projectiles were impacted on the target plate at different striking velocities. Above a certain threshold velocity, complete perforation occurred. As the projectile is

deformable, deformation and breakage of the projectile after impact could be seen. The residual velocity of the projectile was difficult to estimate due to the disintegration of the projectile and the debris cloud formed during the impact. As a result, the residual velocity of larger debris fragments was considered instead. Table 5.1 shows the experimental results and the same are plotted in Fig. 5.3 and Rechet-Ipson [25,26] constants are determined listed in Table 5.2.

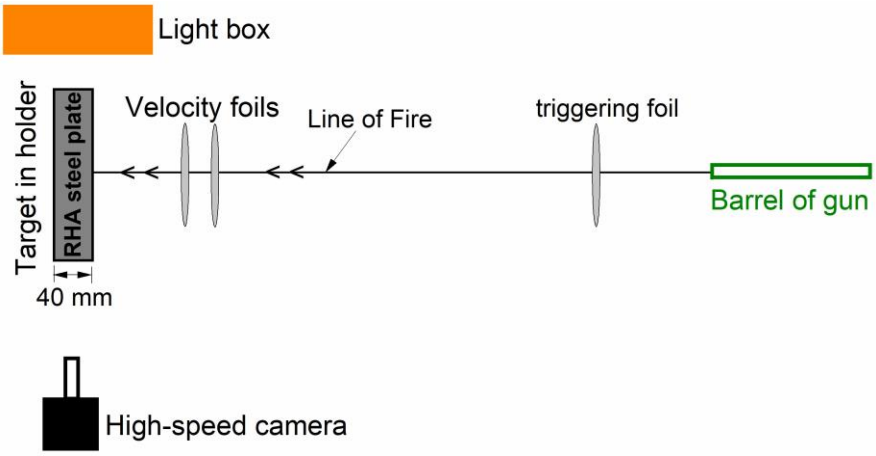

Fig. 5.1 Schematic of the full experimental setup of the ballistic impact test

The **Recht-Ipson equation** provides an empirical relationship to estimate the residual velocity of a projectile after penetrating a target plate. For thick target plates, the dynamics of penetration involve complex interactions, including energy dissipation, material deformation, and potential projectile disintegration. The projectile residual velocity is primarily function of the balance of its initial kinetic energy and the energy required for penetration. The equation assumes that the target material is homogeneous and isotropic. Secondary effects such as temperature rise, projectile erosion, and spalling are not explicitly accounted for.

T/L = is the ratio of plate thickness to projectile length.

The T/L ratio for both rigid and deformable projectile is 0.4. The T/d ratio for rigid and deformable projectile is same i.e 1.33.

T/d = is the ratio of plate thickness to projectile diameter, if ($T/d < 0.5$) the plate is considered thin otherwise thick.

A target is considered "thick" when its thickness exceeds the diameter of the projectile and can cause significant deceleration or deformation of the projectile. A thick target absorbs a substantial

portion of the projectile kinetic energy through plastic deformation, fracture, and material flow. Projectile disintegration or fragmentation often occurs.

Since the mass of the plug ejected from target plate was not known accurately and also the projectile gets fragment therefore the mass of plug is not taken into consideration. Therefore, the Eq. (5.2) is used to calculate the post-perforation velocity. The original equation for thick plate is

$$v_r = \left\{ \frac{v^2 - v_{bl}^2}{\left[1+\frac{M_{epm}}{M_P}\right]\left[1+\omega\left(\frac{D^2}{d^2}\right)\frac{T}{L}\right]} \right\}^{1/2} \tag{5.1}$$

The equation is modified to

$$v_r = \left[\left(\frac{v^2 - v_{bl}^2}{b}\right)\right]^a \tag{5.2}$$

The equation is further validated with the simulated results in the later section.

Where v_r is the residual velocity, v is the striking velocity, v_{bl} is the ballistic limit velocity, T is the thickness of the plate, L is the length of the projectile, ω is the ratio of plate to projectile material density, D is the plug diameter, d is the projectile diameter, M_{epm} is the ejected plug mass, M_P is the impact plug mass, a and b are the parameters to be determined. With the help of Eq. (5.2) the residual velocity at any given striking velocity can be determined.

(a)

(b)

Fig. 5.2 (a) RHA steel plate fixed with the help of fixtures, (b) Projectile or armor piercing shot (AP shot)

Table 5.1 Experimental results of ballistic impact by deformable projectile

Round No.	v (m/s)	v_r (m/s)	Entry hole Dia. (mm)		Exit hole Dia. (mm)		Remarks
			H	V	H	V	
1	850	NR	50	51	48	46	Through-hole
2	806.5	NR	50	52	49	45	Through-hole
3	757.6	0	51	53	NA		Incomplete penetration
4	803.4	166	52	53	45	45	Through-hole
5	757.2	0	50	54	NA		Incomplete penetration
6	775	0	50	50	NA		-do-
7	795	137	53	43	40	35	Through-hole
8	793	128	50	50	45	32	Through-hole

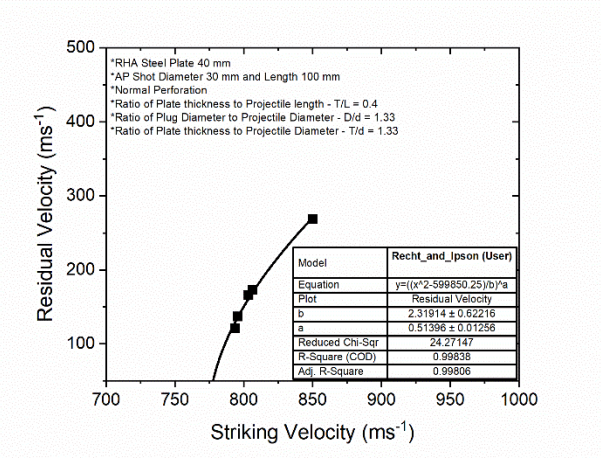

Fig. 5.3 Recht-Ipson parameters

Table 5.2 Recht and Ipson parameters from experimental results

v_{bl} (ms^{-1})	a	b
785	0.51	2.3

The minimum velocity at which the plate begins to resist penetration is 775 ms^{-1}. At this velocity, the projectile becomes embedded in the plate, and a bulge forms on the rear side. At a slightly higher velocity of 795 ms^{-1}, the projectile exits the plate with a residual velocity of 137 ms^{-1}. Hence, the ballistic limit of the plate is determined approximately to be 785 ms^{-1}.

5.4 Effect of Coefficient of friction on velocity

Friction significantly influences both the failure process and the resulting residual velocity, as detailed in the subsequent section. Consequently, the analysis accounts for the variation of the friction coefficient with velocity. When a friction force **F** acts over a displacement ***x***, it performs work equal to **F** multiplied by ***x***. The rate of energy transfer is governed by the sliding distance per unit time—namely, the velocity ***v***. Therefore, the product **F***v* is a key factor in determining outcomes such as the temperature increase due to sliding. The variation of the coefficient of friction with velocity is shown in Fig. 5.4. It is apprarant from the curve that tendency of the friction tries to reduce the velocity. This curve is taken from [27]. The values are shown in the actual curve upto 500 ms^{-1} here the curve is extrapolated upto a velocity of 1000 ms^{-1}. The exponential equation Eq. (5.3) is fitted and the parameters are detemined.

$$\mu = h + k\, e^{sv} \tag{5.3}$$

Where, h, k and s are the constants detrmined from curve fitting.

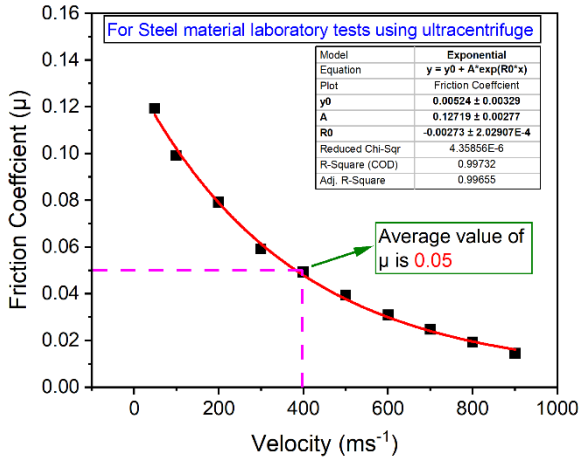

Fig. 5.4 Data for high-speed laboratory friction tests using an ultracentrifuge [27].

5.5 FE modelling

The RHA armor steel plate impact was numerically simulated using the ABAQUS CAE software. The rate-dependent behavior and failure of the armor material have been modelled using the J-C, MJ-C and R-K constitutive relations and failure models, respectively. The material models parameters used in simulation are from Table 4.1 in Chapter 4. The simulation results have been analyzed and the post-impact behavior of the plate has also been studied.

5.5.1 Modelling of target and projectile

The assembled model, which was created in Abaqus Explicit, consists of two parts: i) projectile, and ii) the plate. First, simulation is done by assuming the projectile as rigid and then the simulation for deformable projectile is performed. The projectile is considered deformable because the deformation is observed in the experiment as depicted in Fig. 5.5, which has a stepped shape.

A 3D model of an armor plate with a cross-section of 500 x 500 mm and a thickness of 40 mm was built. All the geometries were meshed with quadrilateral C3D8R brick elements, as shown in Fig. 5.6-5.8. Two portions are created at the center of the plate, first a 50 mm diameter circle was sectioned at the center of the plate to provide fine meshing with an element length of 0.01 x 2 mm and second partition circle was constructed of radius 86 mm meshed using a 1.62 x 2 mm element size, while the rest of the plate was meshed more coarsely. For modeling the plate, two meshing techniques were used: structured and unstructured. The partition radius upto 86 mm unstructured meshing technique was used and rest of the plate meshed with structural mesh. The material properties for three different material models were assigned according to the models discussed in previous chapter. In the computational methods, incremental plasticity theory was used. The Johnson-Cook, Modified Johnson-Cook (MJ-C), and R-K plasticity material models were implemented in ABAQUS CAE using vectorized user-defined material code (VUMAT). An 86 mm circular domain was used as the input for a damage model derived from the Johnson-Cook failure model, a method frequently applied in high-velocity impact simulations [31, 33]. Damage evolution was tracked through cumulative plastic strain with an incorporated linear softening behavior. To capture the highly dynamic nature of the problem, the model was implemented as a nonlinear dynamic explicit analysis with linear interpolation, a common practice in high-velocity impact studies (e.g., [40,43]). The simulation employed automatic time stepping, and convergence was ensured through distortion control, element deletion, and default hourglass control. An initial temperature of 300 K (approximately 27°C) was set, and the material was assumed to behave in a linear elastic manner until the equivalent stress surpassed the yield stress. Additionally, the J-C failure model was integrated using VUMAT FORTRAN code.

The armor plate displacement was fixed in all the directions. The projectile displacement in the x and y directions and rotation about the x, y, and z axes were fixed, with velocity applied in the z-direction, as shown in Fig. 5.9.

The distortion control and element deletion were given only up to the diameter of 86 mm. The fine mesh of element size 0.1 x 1 mm^2 was given in all simulations with structured and unstructured meshing. In unstructured meshing the mesh is distributed randomly upto the radius of 86 mm. To reduce the computational time, the mesh was coarsened outside the 86 mm radius

circle. The target is assigned identical geometrical properties as in the experiment. For contact interactions, a node-to-surface contact algorithm was used, with the armor plate nodes as slave nodes and the projectile surface as master nodes. For a deformable projectile, the penalty contact method was employed for mechanical constraints. For the sake of computational efficiency, friction was defined as temperature independent, a tangential behavior penalty contact with a friction coefficient of 0.05 (see Fig. 5.4) was selected, along with normal behavior hard contact allowing separation after contact. A mesh sensitivity analysis was performed to evaluate the impact of mesh size on the residual velocity and plastic deformation of the target plate. The mesh size in the thickness direction was refined progressively, from 4 mm to 1 mm as shown in Fig. 5.10. Refining the mesh further below 1 mm resulted in challenges with mesh convergence, a reduction in plug size, and a significant increase in computational time.

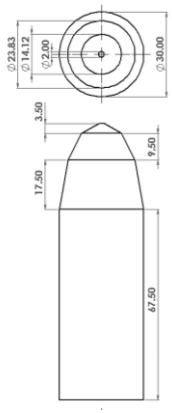

Fig. 5.5 Geometry of projectile

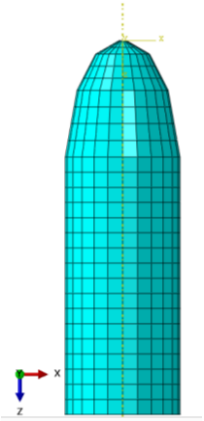

Fig. 5.6 Projectile meshing

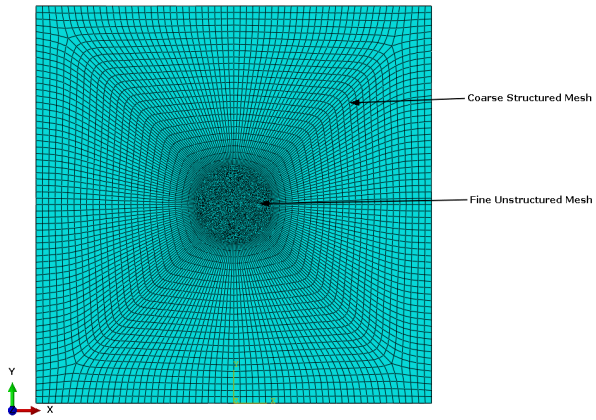

Fig. 5.7 Armour Plate 500 x 500 mm and 40 mm thickness Meshing

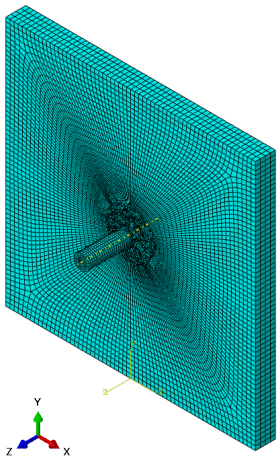

Fig. 5.8 Assembly of Projectile and Armour Plate

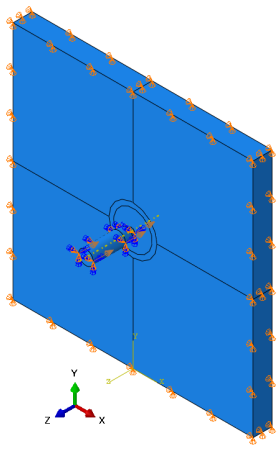

Fig. 5.9 Boundary conditions in armor plate and projectile

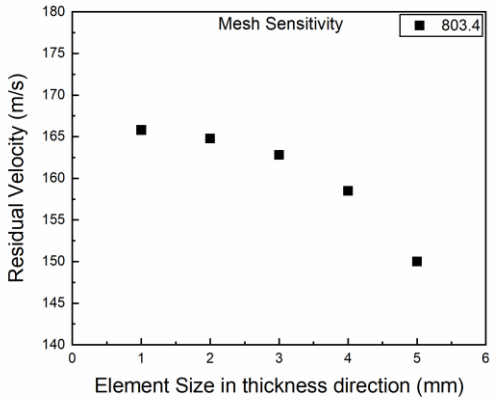

Fig. 5.10 Mesh size dependence in FE simulation

5.6 Results and discussions

5.6.1 Experimental post-impact observations

Fig. 5.11 shows the armour plate after impact in experiment, highlighting a complete perforation hole and a partially embedded projectile. The embedded projectile caused a bulge and a circumferential crack. The front of the plate displays both a complete perforation and an embedded projectile, with different material deformation patterns.

It is important to note that ballistic impact experiments with gun-fired projectiles moving at ordinance velocities yield very limited measurable parameters. Consequently, the quantitative validation of simulation results is primarily based on comparing the post-impact residual velocity of the projectile, the ballistic limit curve, and the damage pattern on the armour plate.

The ballistic limit of the plate was determined using experimentally measured striking velocity (v) and residual velocity (v_r) data, and a ballistic limit curve was generated (Fig. 5.3). The striking and residual velocities are listed in Table 5.1. These experimental results were compared with simulation results to validate the numerical model.

During impact, projectile generates an extensive zone of plastic deformation in the target plate. Simultaneously, the area of projectile nose that contacts the plate increases as perforation occurs, thereby enhancing the plate resistance to penetration. Front surface of the target plate is shown in Fig. 5.11a while rear surface with bulge and perforation is shown in Fig. 5.11b. It is apparent from the Fig. 5b that bulge is created. The projectile nose shape causes failure by plugging of the target plate. This failure mode is dominated by shear banding found generally when blunt projectile penetrates 10-12 mm thick plate [6,28,29]. After severe localized bulging, cup-shaped plug is ejected from the target by stepped shape projectile. Generally, for conical projectile petals can be seen [7,30]. In this case, the petals are not formed smoothly. Instead, a circumferential crack develops, leading to localized yielding that weakens the material, causing it to eject from the plate. From Fig. 5.11b significant differences in the penetration behavior during penetration are apparent. The interface force between the projectile and target contact point, the stress generated and the plastic strain reached can be know from simulation as discussed later. On the rear side of the plate, localized tanning around the perforated hole suggests varying temperature rises at seven distinct locations shown in Fig. 5.11b.

(a) (b)

Fig. 5.11 Post impact features of RHA plate

5.6.2 FE simulation and post impact observations

The validated material models parameters are used to simulate ballistic impact tests. The friction model discussed in Section 5.4 is implemented. Simulations were performed by using constant friction coefficients 0.05. Initially, the material model parameters are applied for simulating impacts with a rigid projectile having an ogive nose shape, diameter of 40 mm and length of 100 mm, and a mass of approximately 1 kg. The target plate thickness is set to 50 mm, and the simulation results are compared with the published data from Banerjee et al. [17]. The simulated results are shown in Fig. 5.12 and results are listed in Table 5.3. The simulated results closely matching with the experiment.

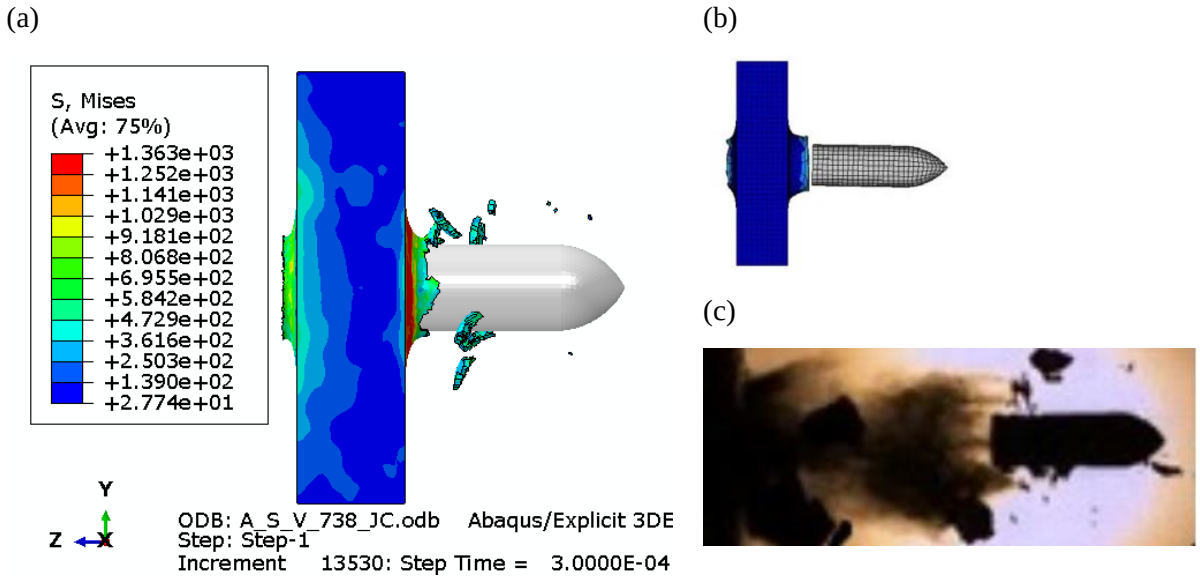

Fig. 5.12 Validation of rigid projectile [17] (a) simulation result validated with (b) A. Banerjee simulation result (c) experimental result

Table 5.3 Comparison with A. Banerjee et al. simulation results in ms^{-1}

Striking Velocity (V) (m/s)	**Experimental [17] v_r**	**Simulated v_r [17]**	**Simulated v_r**
738	413	450	425

The FE modelling for rigid projectile is validated and then additional simulations are performed using a stepped-shaped rigid projectile with a mass of 300 grams, a diameter of 30 mm, and a length of 100 mm. For these simulations, the target plate thickness is reduced to 40 mm as used in experiment. Finally, simulations are conducted by taking the projectile as deformable. The numerical results from simulations are presented in Tables 5.4 for rigid projectile and in Tables 5.5 for deformable projectile. The topography of the deformed plate is shown in Fig. 5.13. The first step involves comparing the ballistic limit velocity (v_{bl}) predicted by numerical simulations with experimental results. A direct comparison of experimental and simulated ballistic test results is shown in Fig. 5.14 & 5.15, where the performance curves for three material models—the Johnson-Cook (J-C), Modified Johnson-Cook (MJ-C), and R-K— are presented.

The deformed shape of plate when struck by rigid projectile is shown in Fig. 5.16, while that when struck by deformed projectile is shown in Fig. 5.17. The deformed plate configurations (see Fig. 5.17) qualitatively and quantitatively align with the physical behaviour of the target plate during

penetration and perforation. The figures also demonstrate material failure patterns that closely matches with the experimental observations.

The von-Mises stress profile for rigid projectile at different velocities are shown in Fig. 5.16 & 5.17. All simulation results were fitted with Recht-Ipson equation. The computed residual velocities were inserted into the Recht-Ipson model and the parameters are derived for each material model and are listed in Table 5.6 & 5.7. The Recht-Ipson parameters shows large variations.

Table 5.4 Ballistic test experimental and simulation results for J-C, R-K, and MJ-C material models (Rigid Projectile)

Experimental Striking Velocity (v) ms^{-1}	Experiment v_r (ms^{-1})	J-C v_r (ms^{-1})	MJ-C v_r (ms^{-1})	R-K v_r (ms^{-1})
706	0	0	0	77.05
757.6	0	75.31	146.74	250.11
803.4	166	253	291.12	353.78
850	NA	356.78	387.32	439.18

Table 5.5 Ballistic test experimental and simulation results for J-C, R-K and MJ-C material models (deformable Projectile)

Experimental Striking Velocity (V) ms^{-1}	Experiment V_r (ms^{-1})	J-C V_r (ms^{-1})	MJ-C V_r (ms^{-1})	R-K V_r (ms^{-1})
740*	0	0	0	30.07
757.6	0	0	0	102.18
793.7	100	0	120.54	234.14
795.6	137	0	129.51	235.38
803.4	166	43.22	164.54	253.84
806.5	NA	63.85	173.19	257.08
850	NA	232.60	287.33	342.27

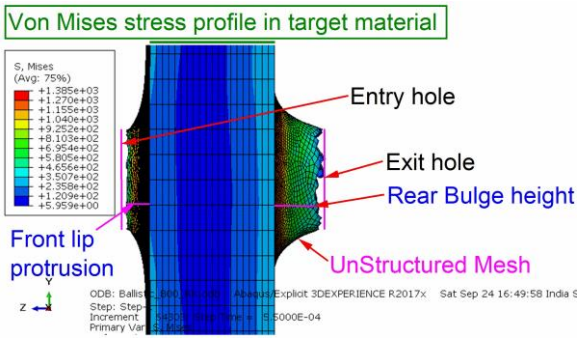

Fig. 5.13 Topography of armor plate after impact

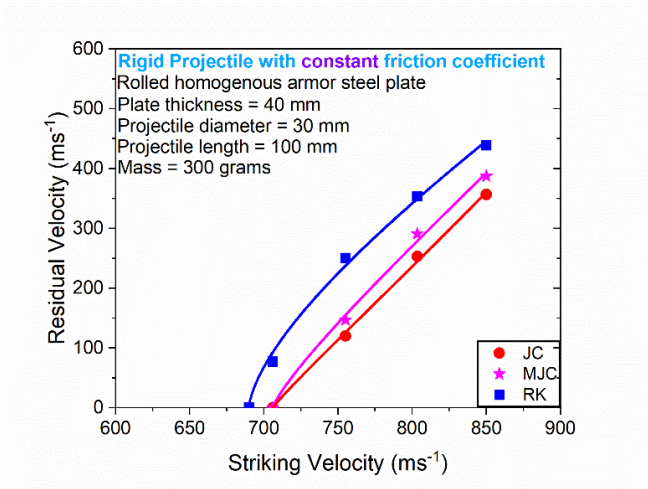

Fig. 5.14 Simulated RV *vs* SV for rigid projectile of 100 mm in length and 30 mm diameter

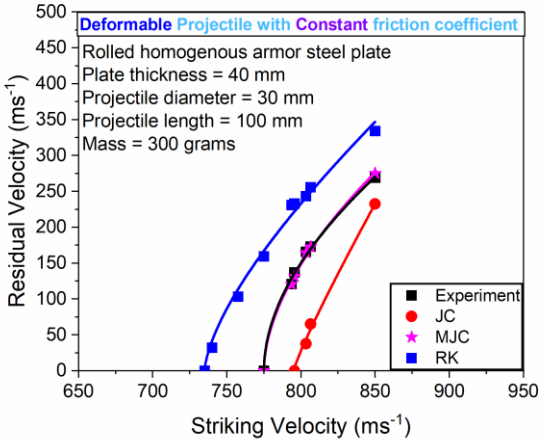

Fig. 5.15 Simulated RV *vs* SV for deformable projectile of 100 mm in length and 30 mm diameter

Table. 5.6 Comparison of the Recht-Ipson fitted parameters for J-C, MJ-C and R-K material models (Rigid Projectile).

Experiment (Defromable)		**J-C**		**MJ-C**		**R-K**	
a	**b**	**a**	**b**	**a**	**b**	**a**	**b**
0.51	2.3	0.92	373.96	0.81	147.06	0.65	21.92

Table. 5.7 Comparison of the Recht-Ipson fitted parameters for J-C, MJ-C and R-K material models (Deformable projectile).

Experiment		**J-C**		**MJ-C**		**R-K**	
a	**b**	**a**	**b**	**a**	**b**	**a**	**b**
0.51	2.3	0.87	173	0.54	4.38	0.66	25.96

J-C Material Model

$v = 803.4\ ms^{-1}$	$v_r = 253\ ms^{-1}$	$v = 706\ ms^{-1}$	$v_r = 0\ ms^{-1}$

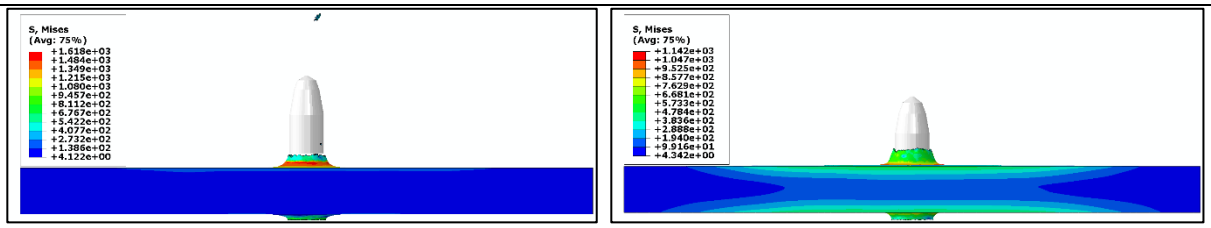

MJ-C Material Model

$v = 803.4\ ms^{-1}$	$v_r = 291.12\ ms^{-1}$	$v = 706\ ms^{-1}$	$v_r = 0\ ms^{-1}$

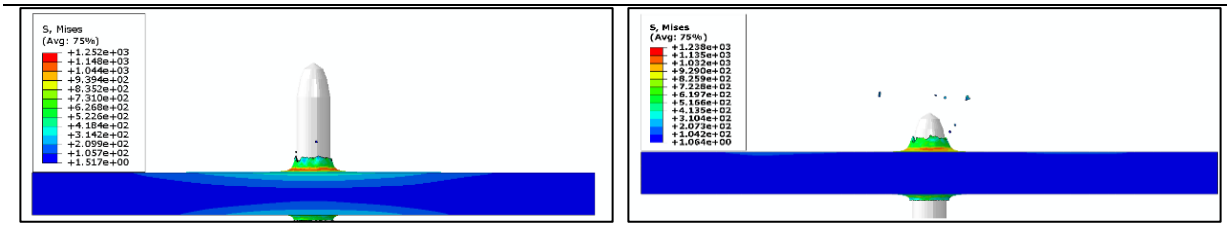

R-K Material Model			
$v = 803.4\ ms^{-1}$	$v_r = 353\ ms^{-1}$	$v = 706\ ms^{-1}$	$v_r = 77.05\ ms^{-1}$

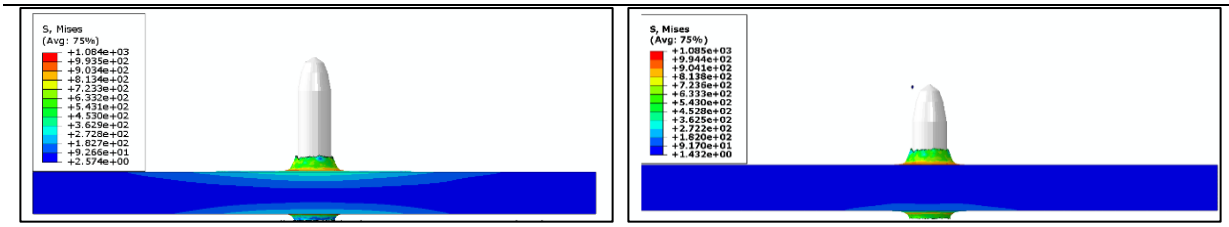

Fig. 5.16 Von-mises stress profile by target plate striking with rigid projectile

J-C Material Model			
$v = 803.4\ ms^{-1}$	$v_r = 40.68\ ms^{-1}$	$v = 757\ ms^{-1}$	$v_r = 0\ ms^{-1}$

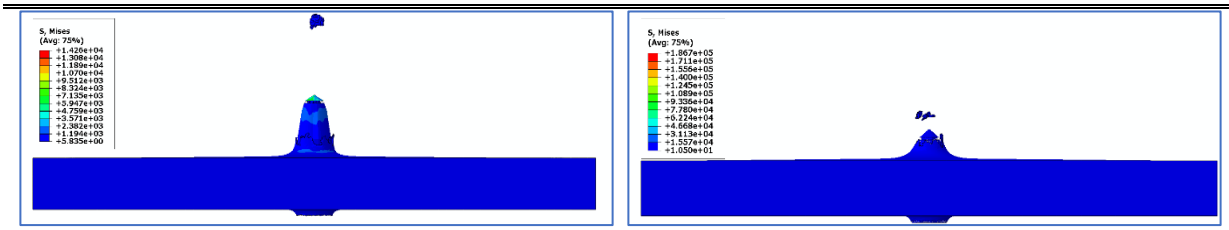

MJ-C Material Model			
$v = 803.4\ ms^{-1}$	$v_r = 164.75\ ms^{-1}$	$v = 757\ ms^{-1}$	$v_r = 0\ ms^{-1}$

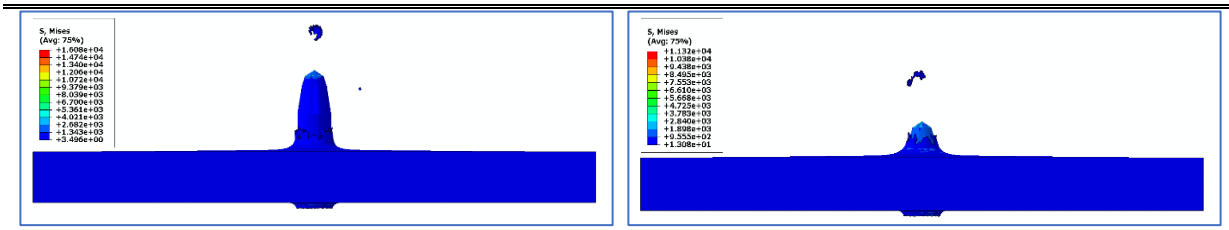

R-K Material Model			
v = 803.4 ms^{-1}	v_r =254.93 ms^{-1}	v = 757 ms^{-1}	v_r = 101.2 ms^{-1}
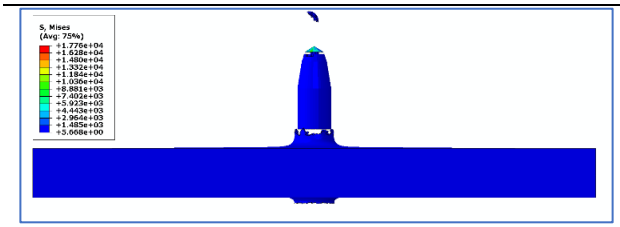		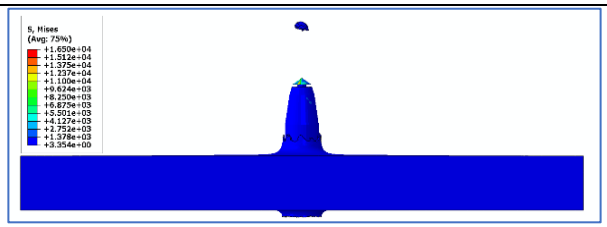	

Fig. 5.17 Comparison of Von-Mises stress profile by using different material models and friction coefficient

Figs. 5.16 & 5.17 show the von Mises stress distribution from the finite element (FE) simulations. Upon impact, the target plate exhibits circular bulging around the impact zone. The projectile is embedded in the plate in case of J-C and MJ-C material models simulation at velocity 757 m/s, in MJ-C model simulation a small size debris also forms. In a ballistic impact involving a deformable projectile, momentum is transferred to the target and surrounding material, generating debris upon impact. Unlike a rigid projectile, a deformable one undergoes plastic deformation, dissipating a significant portion of its kinetic energy within itself and the target, reducing the energy available for debris ejection. The debris disperses outward but eventually stops due to external resistive forces such as surface friction and aerodynamic drag. The stopping distance depends on these resistive effects rather than just the initial momentum transfer. In high-velocity impacts, the projectile may fragment, leading to a wider and more energetic debris spread, whereas in low-velocity impacts, deformation dominates, limiting debris movement and favoring localized material displacement. In the numerical model using R-K material model, a plug is seen to be formed and moving in front of projectile nose. The maximum interface forces experienced by the deformable projectile at 806 and 775 ms^{-1} velocities are shown in Fig. 5.18. Fig. 5.18a illustrates the relationship between force (kN) and displacement (mm) under conditions where the friction coefficient remains constant at a velocity of 806 m/s. The force starts at zero and increases progressively with displacement, indicating the presence of material deformation, contact resistance, or impact-induced forces. Since the friction coefficient is constant, any variations in force are primarily due to the material response rather than frictional fluctuations. The force buildup suggests that as displacement progresses, resistance increases, possibly due to strain hardening, energy dissipation, or other dynamic effects. At high velocities, such as 806 m/s, the force evolution can be significantly influenced by strain rate sensitivity, material failure

mechanisms, or material responses under impact conditions. The peak force value and its post-peak behavior may provide insights into material yielding, fracture onset, or stability under applied loading. Fig. 5.18b demonstrates the force evolution over time under a constant friction coefficient at a velocity of 775 m/s. The force initially increases, reflecting the interaction between the contacting surfaces and material response. The controlled friction condition ensures a more stable force profile, with variations likely caused by material deformation or wave propagation effects. At high impact speeds, the force-time relationship suggests that friction and inertia significantly influence the system dynamic response, making it crucial to optimize these factors for improved performance and reduced instability. The deformable projectile exerts a lower maximum force resulting in a lesser residual velocity compared to rigid projectile. The average interface force exerted by R-K model is more compared to J-C and MJ-C models therefore the exit velocity is more, but the difference between three material models is less at 806 m/s.

The total absorbed energy and kinetic energy, by the system is shown in Fig. 5.19-5.21. Although the difference in force exerted among the three materials is minimal when a constant friction coefficient is used, the total energy predicted for the entire system is higher when the R-K model is applied. The J-C model predicts the lowest energy among them. The hourglass control was set to its default value. Additionally, significant losses in energy and mass may occur due to element erosion, particularly at impact velocities close to the ballistic limit.

To account for these losses, the target plate was modelled with a local partitioned structure (50 mm and 86 mm) and a global section encompassing the remaining plate, using previously discussed material properties.

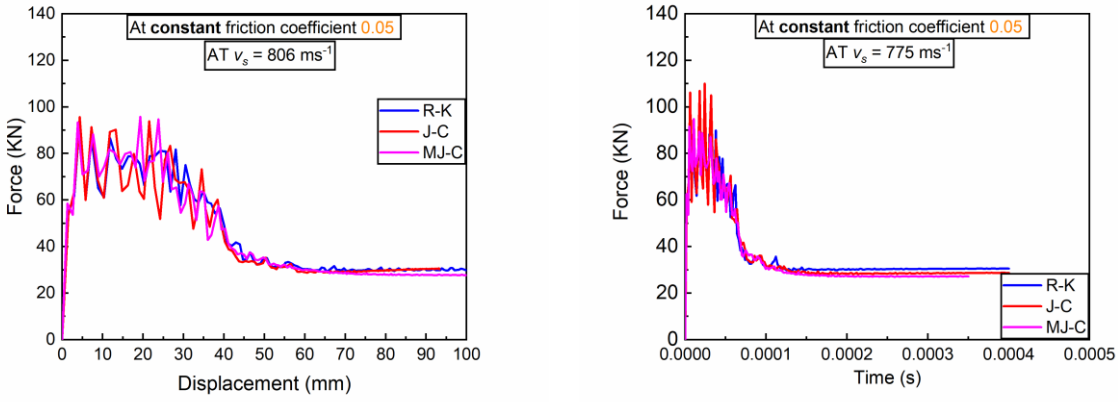

(a) (b)

Fig. 5.18 Force exerted by deformable projectile on the target plate

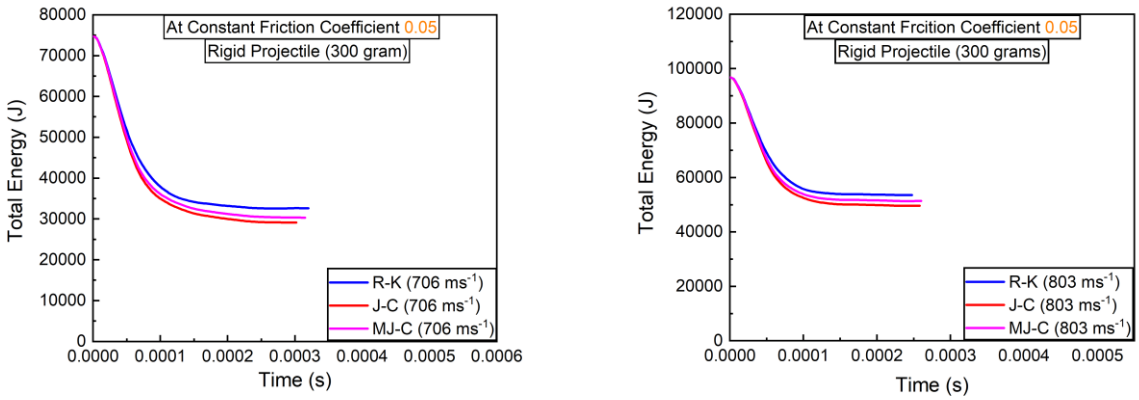

(a) (b)

Fig. 5.19 Total energy imparted by the rigid projectile vs time

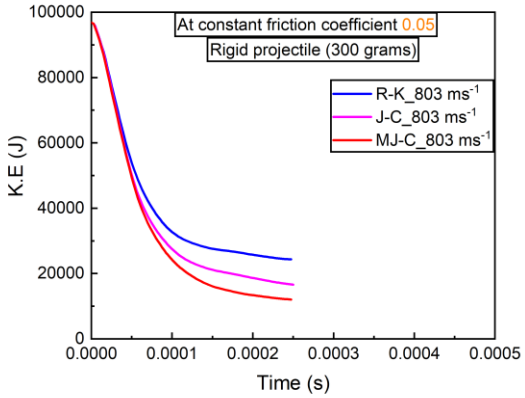

Fig. 5.20 Kinetic energy imparted by the rigid projectile vs time

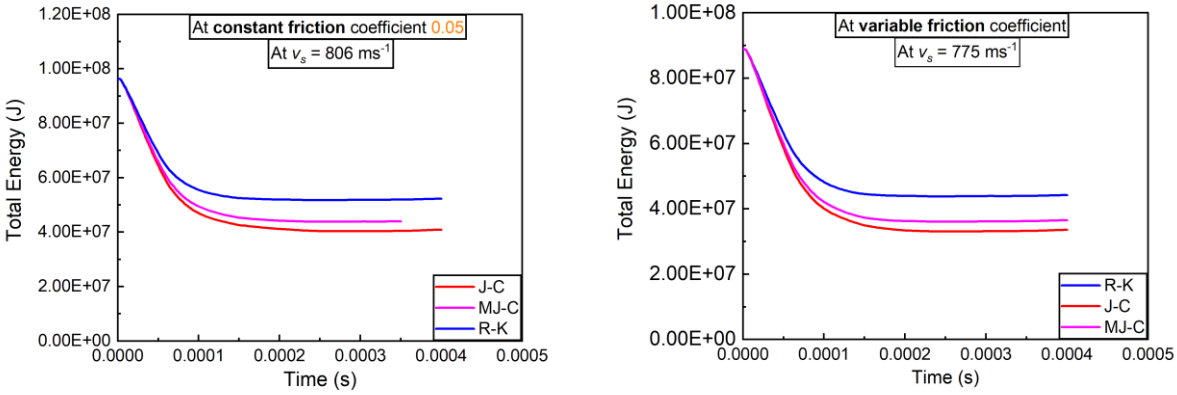

Fig. 5.21 Total energy plots at v_s 806 and 775 ms^{-1} (deformable projectile)

The FE simulation highlights the propagation of stress waves radiating outward in a circular pattern from the impact point, as observed in Figs. 5.22 and 5.23. In ductile materials, these stress waves induce plastic deformation rather than immediate fracture. However, as the waves propagate, they generate hoop stress (circumferential tensile stress), which can contribute to the formation of circumferential cracks (Fig. 5.24a &b) if the accumulated strain leads to localized necking and eventual failure. Unlike brittle materials, where cracks form abruptly, ductile materials exhibit gradual void nucleation, growth, and coalescence before crack initiation. The simulation results closely resemble experimental observations, as both show signs of circumferential deformation and crack development due to prolonged plastic flow and stress concentration. This agreement confirms that the numerical model effectively captures the fracture behavior of ductile materials under impact loading. Examination of the simulated plate cross-section at specific time intervals (e.g., t = 5.0e-04, 1.1e-04 and 2.92e-04) see Fig. 5.25 & 5.26 reveals a compressive stress front propagating into the plate near the plastically penetrating projectile.

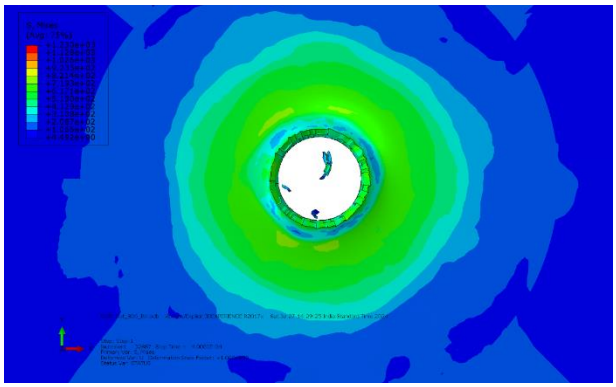

(a) Front of deformed target plate (R-K model)

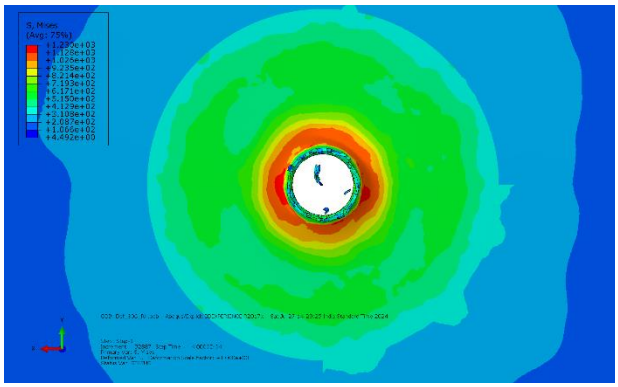

(b) Rear of deformed target plate (R-K model)

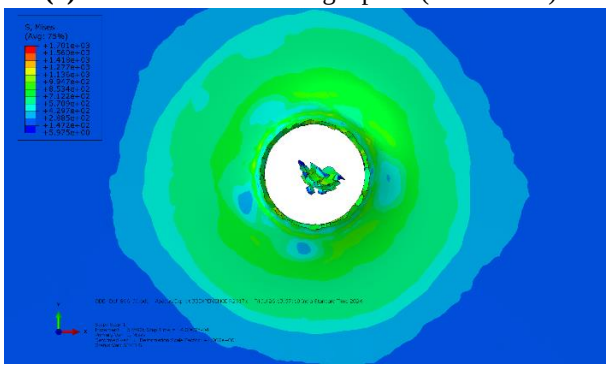

(c) Front of deformed target plate (J-C model)

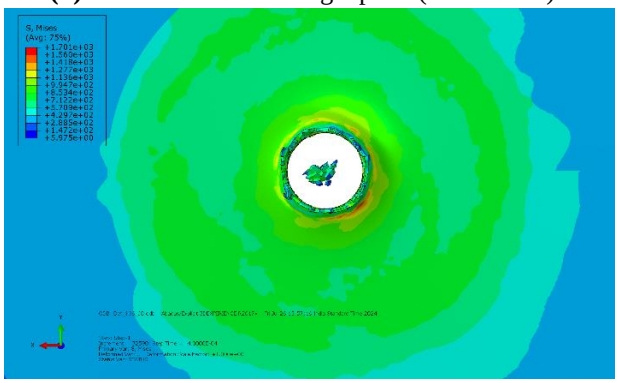

(d) Rear of deformed target plate (J-C model)

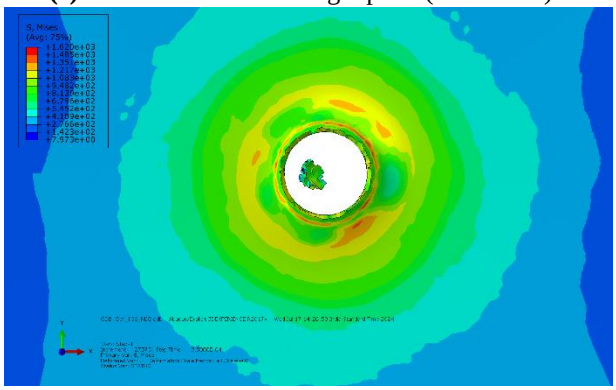

(e) Front of deformed target plate (MJ-C model)

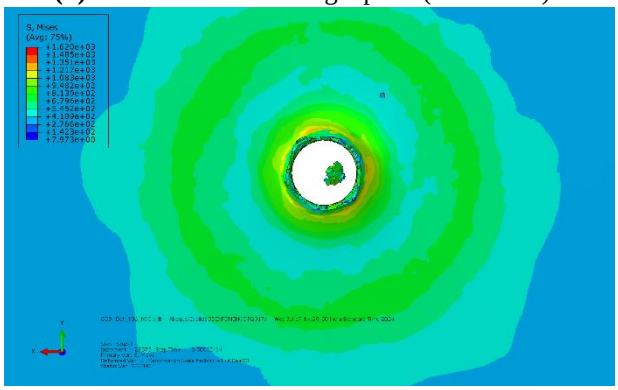

(f) Rear of deformed target plate (MJ-C model)

Fig. 5.22 Target plate front and rear stress waves pattern at 806 ms^{-1} velocity

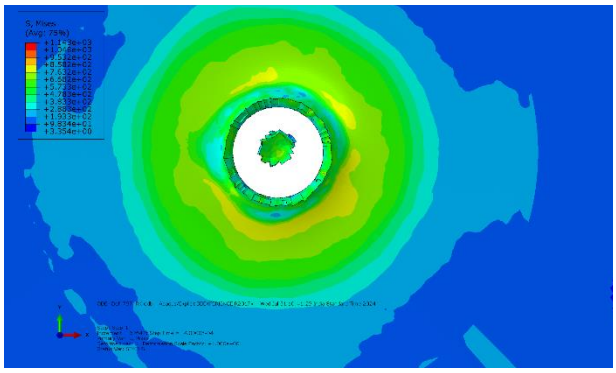

(a) Front of deformed target plate (R-K model)

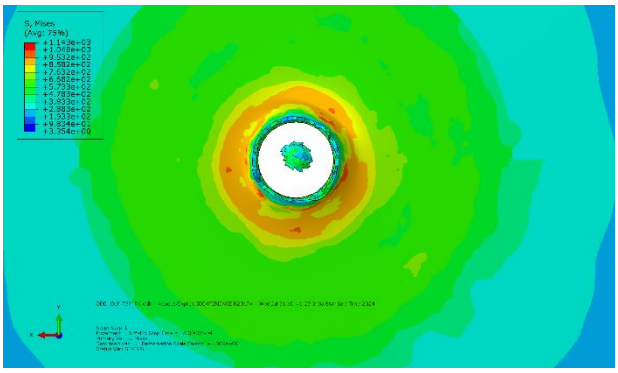

(b) Rear of deformed target plate (R-K model)

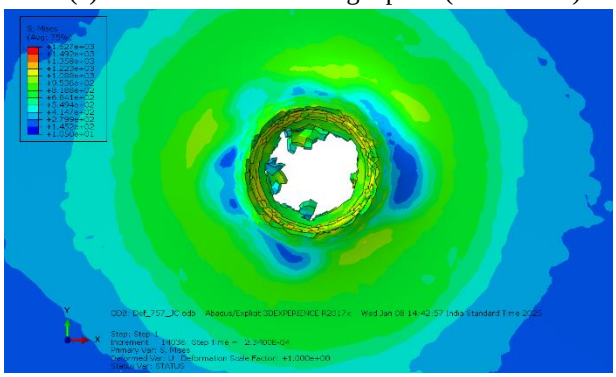

(c) Front of deformed target plate (J-C model)

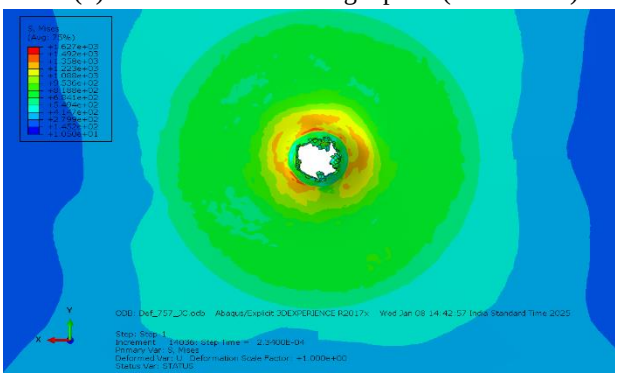

(d) Rear of deformed target plate (J-C model)

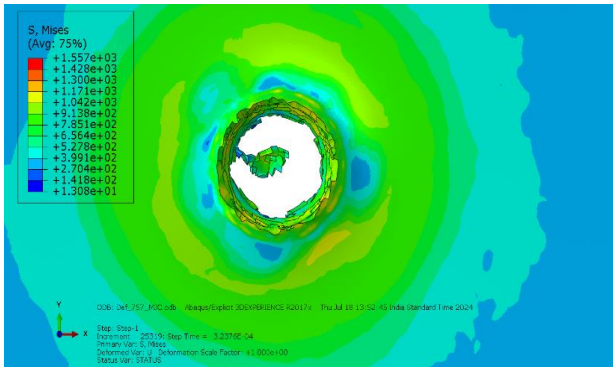

(e) Front of deformed target plate (MJ-C model)

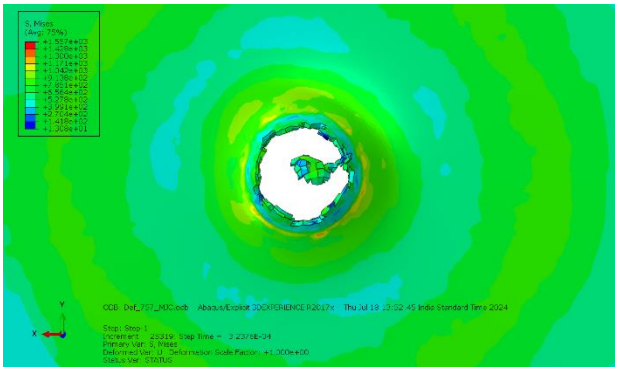

(f) Rear of deformed target plate (MJ-C model)

Fig. 5.23 Target plate front and rear stress waves pattern at 757 ms^{-1} velocity

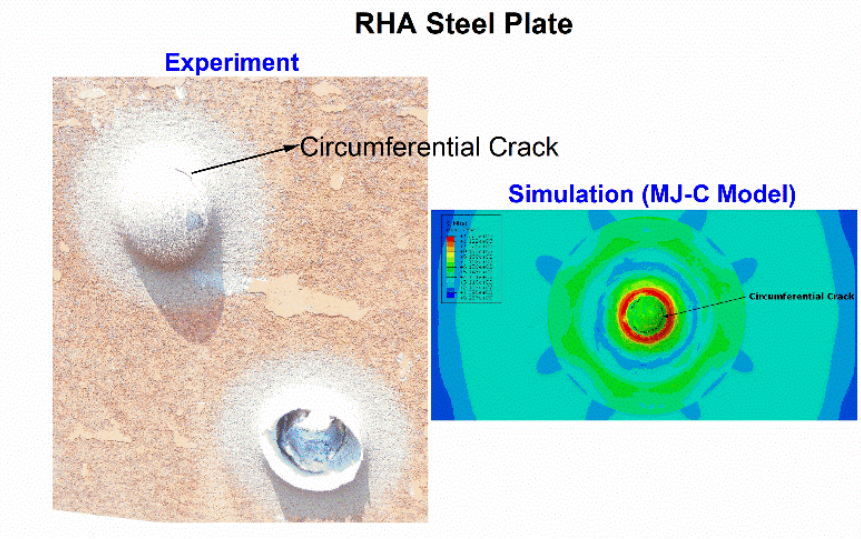

Fig. 5.24 Circumferential crack develop in target plate (a) experiement (b) simulation (MJ-C)

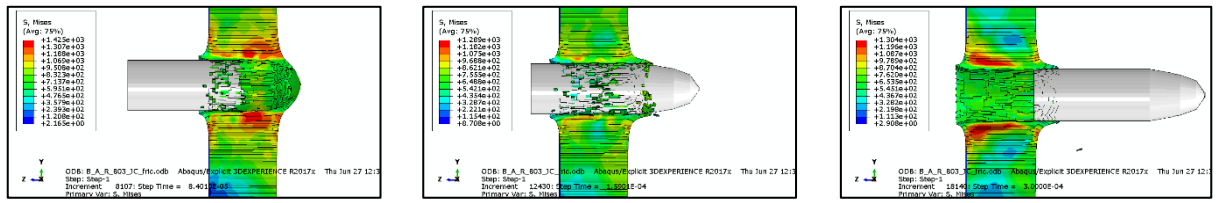

J-C

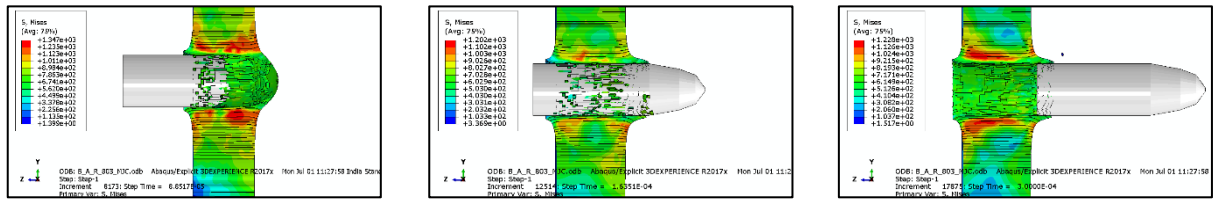

MJ-C

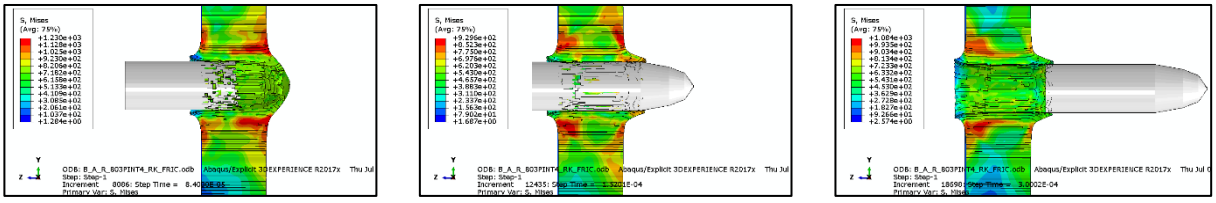

R-K

Fig. 5.25 von-Mises stress distribution profile of target plate by rigid projectile

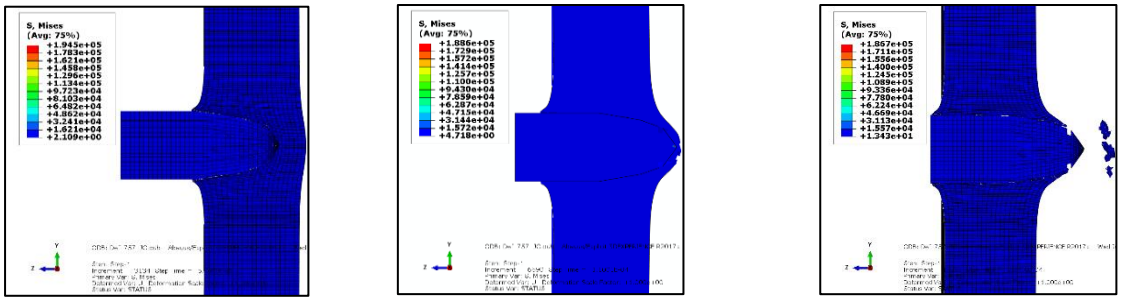

J-C

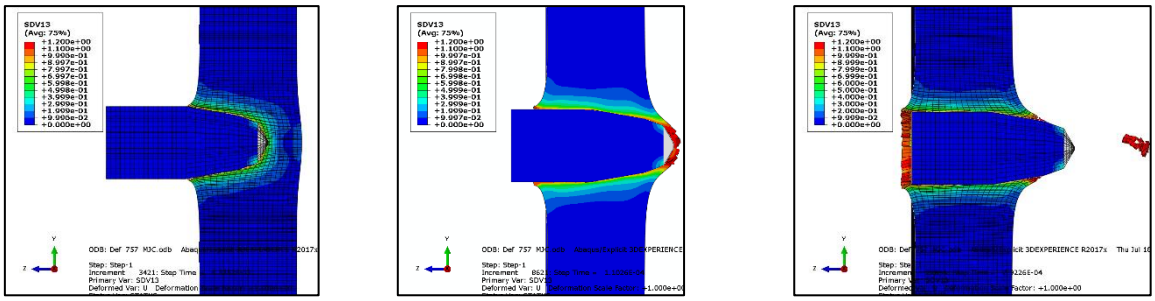

MJ-C

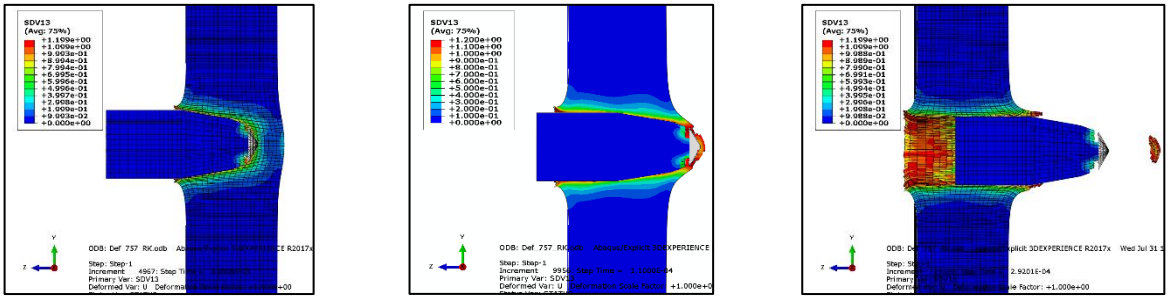

R-K

Fig. 5.26 von-Mises stress distribution profile of target plate by deformable projectile at 757 m/s

According to the FE simulation, localized compressive stresses reach values of up to 1410.81 MPa for R-K, 1709 MPa for J-C and 1600.36 MPa for MJ-C exceeding the experimentally measured maximum tensile stresses during impact testing. On the reverse side of the plate, a tensile stress field develops due to wave reflections at the free surface. The maximum tensile stress of approximately 1385.41 MPa for R-K, 1662.82 MPa for J-C and 1586.72 MPa for MJ-C occurs just before the projectile perforates the plate, near its rear surface.

The correlation coefficients between the experimental data and the models are as follows:

- Experimental and J-C: **0.803**
- Experimental and R-K: **0.986**
- Experimental and MJ-C: **0.999**

These values suggest a very strong correlation between the experimental data and the MJ-C model, followed by the R-K model, with the J-C model having a moderate correlation.

The simulations indicate overestimate of the ballistic performance for R-K material model under estimate for J-C material model and good matching for MJ-C material model. The overestimation in ballistic performance observed in the R-K material model may be attributed to the inherent strain rate sensitivity formulation within the model. This overestimation has already been evident in tensile and Charpy V-notch simulations through load -displacement response. The ballistic limit range follows the order: $v_{bl(r\text{-}k)} < v_{bl(MJ\text{-}C)} \leq v_{ble} < v_{bl(J\text{-}C)}$. Numerical simulations employing all the considered constitutive models precisely captured the relationship between the projectile residual velocity and its ballistic limit. If considering safe armor design, the R-K model provides the most conservative predictions among all three material models.

High-temperature experiments, conducted up to 500°C, were used to determine material parameters. However, ballistic impact experiments can result in peak temperatures of approximately 2500°C, as reported in [31]. Due to insufficient data, the thermal softening behaviour at higher temperatures could not be thoroughly modelled. Fig. 5.26 illustrates that most elements are removed from the front of the projectile during the simulation. The maximum plastic strain is reached in the early stages of impact due to the high loading conditions, leading to instantaneous erosion of these elements.

In simulation the projectile tip upto 2 mm in length is given elastic properties and rest of the projectile is deformable because if the projectile is fully deformable, numerical simulations for some impact velocities are prematurely terminated due to numerical instability, which prevents the completion of the calculation as shown in Fig. 5.27. This instability arises from crack formation in the target plate, leading to an inability to continue the simulation. It is also important to note that the fracture time in the numerical simulations cannot be validated due to the lack of experimental data for comparison. The failure time evolution as a function of impact velocity for all constitutive models follows a typical parabolic profile, as shown in Fig. 5.28. The velocity *vs.* displacement profile shown in Fig. 5.29 indicates that the residual velocity predicted by the R-K model becomes constant after 90 mm of displacement. Similarly, the MJ-C model predicts a constant residual velocity after 90 mm, whereas the J-C model shows a continuously decreasing

velocity, approaching zero. It is important to note that all displacements are measured from the tip (front) of the projectile. These variations in predicted residual velocity likely result from differences in energy absorption by the target plate for each material model. The distinct material behavior predicted by each constitutive model significantly influences the plate response during perforation, thereby affecting the energy absorption mechanism throughout the perforation process.

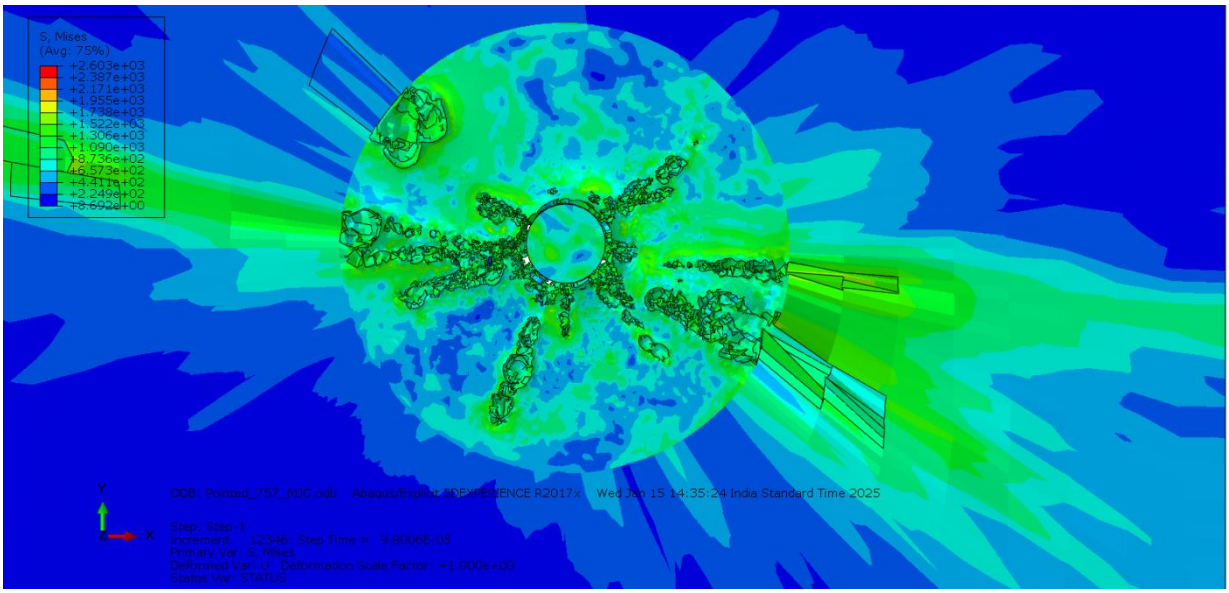

Fig. 5.27 Cracks formed in the RHA plate

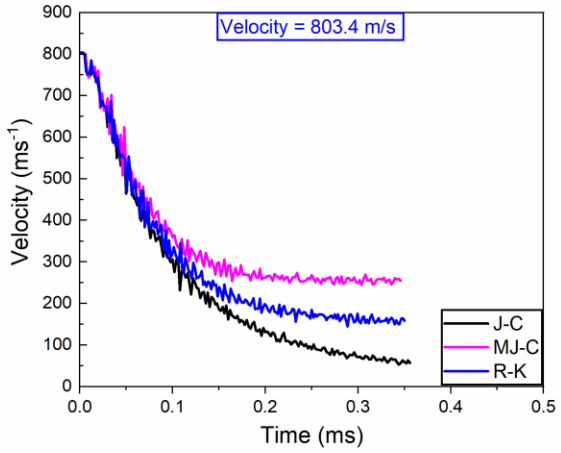

Fig. 5.28 Velocity *vs* time plot at 803.4 ms^{-1} velocity

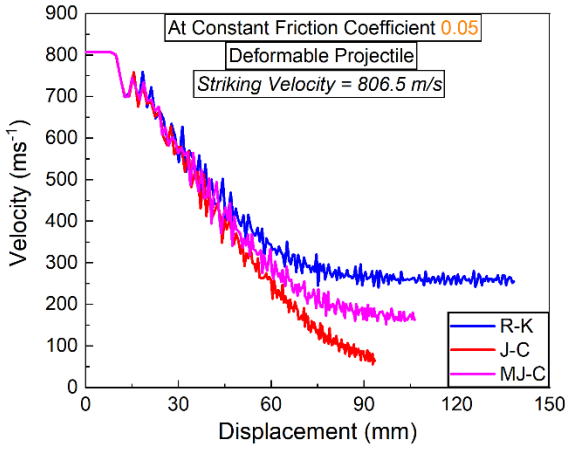

Fig. 5.29 Velocity *vs* displacement plot at 806.5 ms^{-1} velocity

During projectile impact, the material in the immediate vicinity of the contact zone experiences significant deformation, with strains reaching up to approximately 2 and strain rates spanning from 1 s^{-1} to 10^5 s^{-1}. A numerical study demonstrated that when a 30 mm diameter projectile traveling at 803 m/s strikes a 40 mm thick RHA steel plate, the average strain rate reaches around 10^4 s^{-1} with an average plastic strain of about 0.32. This finding highlights the importance of examining the dynamic flow behavior of target materials to fully understand their ballistic performance. Observations indicate that both projectile and armor steels exhibit considerably higher dynamic flow stresses. At higher strain rates, the limited time available for thermal energy to assist

dislocation movement over short-range barriers necessitates greater applied stress [32]. Moreover, projectile steel shows higher quasi-static and dynamic flow stress values compared to RHA steel. Overall, the dynamic flow stress at any given strain is influenced by the combined effects of strain rate hardening, strain hardening, and thermal softening—with the elevated stress in projectile steel mainly attributable to its higher strain rate sensitivity and increased dynamic strain hardening rate.

The front and rear lip protrusion is shown in Fig. 5.30 for three materials models when target plate is impacted by deformable projectile. The front and rear hole enlargement values are listed in Tables 5.8 & 5.9. It means only the target plate deformation changes with change in impact force. Numerical simulations indicate higher maximum deformations compared to experimental results at identical impact velocities see Fig. 5.30. This discrepancy arises because numerical values are recorded immediately after fracture, while experimental values account for the effects of elastic rebound. The front lip protrusion and rear bulge length comparison is listed from Tables 5.10 & 5.11 for variable and constant friction value. It is also important to note that only for R-K model failure pattern of the target plate matching with the experimental pattern of front and rear ends. The failure pattern at the front end predicted by the J-C and MJ-C models matches the experimental observations. However, at the rear end, a discrepancy arises, as cracks are predicted by the models but are not observed in the experiment. Since side-view data of the plate is unavailable, this discrepancy cannot be fully justified or analyzed, as the absence of side-view information limits the ability to verify whether the cracks formed due to numerical inaccuracies, secondary failure mechanisms, or material behavior variations. The failure predicted by J-C and MJ-C model have crack formation which is there in the actual profile. Similar observation is for 757 ms^{-1} velocity. Regardless, every constitutive model predicts a similar failure mechanism, culminating in the ejection of a plug as the final stage of the perforation process.

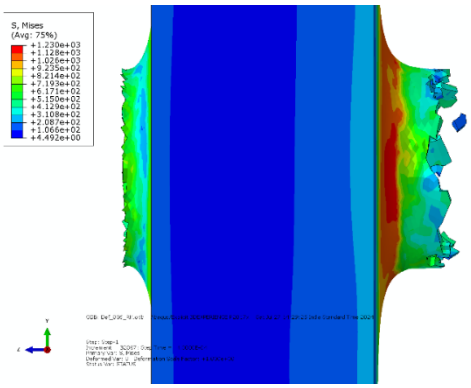

(a) Front lip protrusion and rear bulge formation (R-K model at 806.5 ms^{-1})

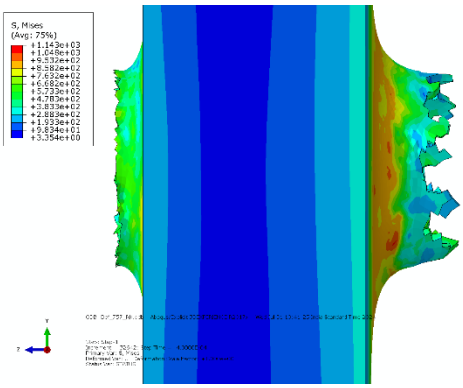

(b) Front lip protrusion and rear bulge formation (R-K model at 757 ms^{-1})

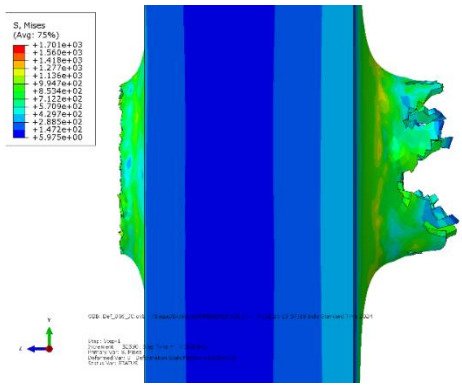

(c) Front lip protrusion and rear bulge formation (J-C model at 806.5 ms^{-1})

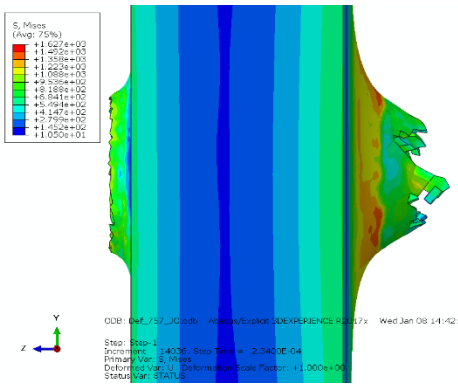

(d) Front lip protrusion and rear bulge formation (J-C model at 757 ms^{-1})

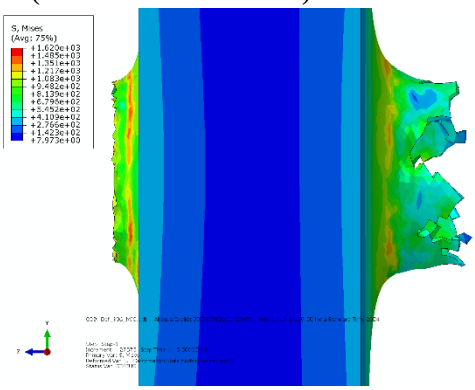

(e) Front lip protrusion and rear bulge formation (MJ-C model at 806.5 ms^{-1})

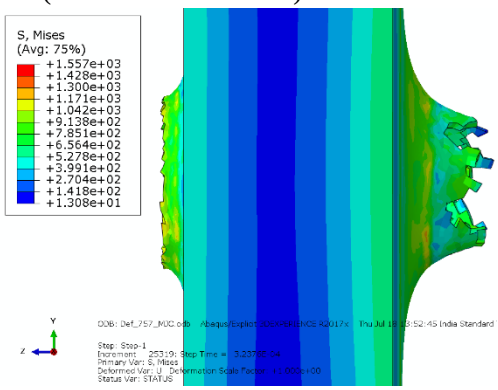

(f) Front lip protrusion and rear bulge formation (MJ-C model at 757 ms^{-1})

Fig. 5.30 Target plate front lip protrusion and rear bulge/cracks formation

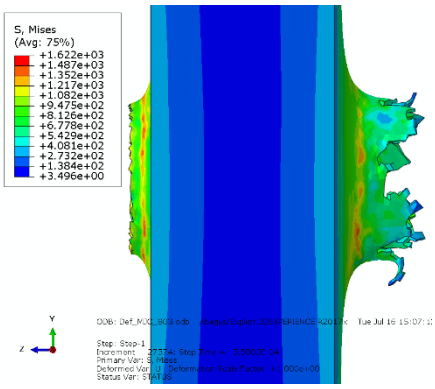

(a) Front lip protrusion and rear bulge formation by only tip elastic (MJ-C model at 803 ms^{-1})

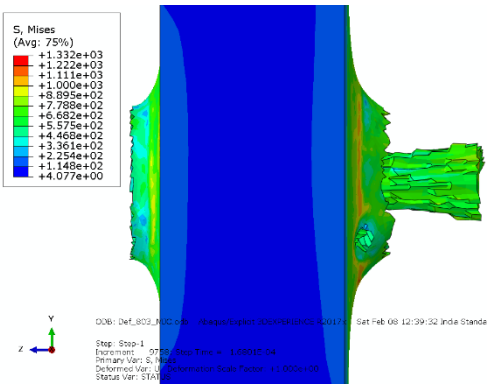

(b) Front lip protrusion and rear bulge formation by fully deformable projectile (MJ-C model at 803 ms^{-1})

Fig. 5.31 Target plate front lip protrusion and rear bulge/cracks formation

From the above observations it is concluded that the formation of petal and plug depends upon the material model, the interaction properties chosen and the value of striking velocity. The plug size and shape depend upon the mesh size. In the present study it is observed that if the mesh size is coarse the size of the plug is more. And for fine mesh size the hole is generated but the plug size is very small.

As shown in Fig. 5.31 the material failure pattern in case when the projectile is having elastic tip only is different from that when the whole projectile is deformable. In Fig. 5.31a petals formation is observed and rear lip size is more than in Fig. 5.31b when projectile is fully deformable. This means that the failure pattern whether it is petal formation or clear edge formation by removal of material in form of plug not only depends upon the thickness of the plate, projectile shape type but also on the characteristics the projectile possess i.e. it is rigid, elastic or deformable or mixture these.

Table. 5.8 Front and rear hole diameter in mm (at 806 ms^{-1})

	Experiment	J-C	MJ-C	R-K
Front	50	30.66	32.61	39.15

	Experiment	J-C	MJ-C	R-K
Rear	45-49	32.91	33.61	35.70

Table. 5.9 Front and rear hole diameter in mm (at 757 ms^{-1})

	Experiment	J-C	MJ-C	R-K
Front	51	31.16	31.47	34.99

	Experiment	J-C	MJ-C	R-K
Rear	NA	14.5	26.5	33.91

Table. 5.10 Front lip and rear bulge length in mm (at 806 ms^{-1})

	Experiment	J-C	MJ-C	R-K
Front Lip	NA	4.4	4.4	5.06

	Experiment	J-C	MJ-C	R-K
Rear Bulge	NA	17.45	18.36	12.06

Table. 5.11 Front lip and rear bulge length in mm (at 757 ms^{-1})

	Experiment	J-C	MJ-C	R-K
Front Lip	NA	4.05	3.6	4.8

	Experiment	J-C	MJ-C	R-K
Rear Bulge	NA	17.5	14.05	10.33

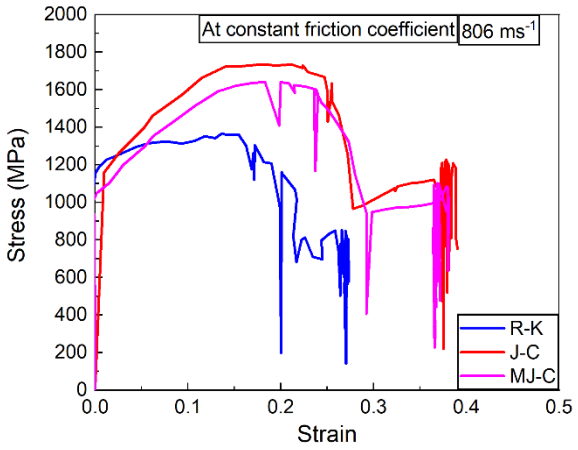

Fig. 5.32 Stress vs strain curves at 806 ms^{-1}

The Von-Mises maximum stress predicted by J-C material model is more at 806 ms^{-1}. Whereas, the R-K model prediction is lowest and MJ-C is slightly below J-C and also shows more work hardening see Fig. 5.32.

5.7 Ballistic performance index by each material model

The Ballistic Performance Index (BPI) involves integrating target material strength and projectile characteristics. The widely used Modified Bernoulli's Equation for Ballistic Impact can serve as a strong foundation. This approach accounts for the projectile mass, velocity, and the yield strength of the target.

$$BPI = \frac{v_s^2 - v_r^2}{t\,\sigma_y} \tag{5.4}$$

Where:

- v_s = striking velocity ($803.4\ \mathrm{m/s}$)
- v_r = residual velocity ($166\ \mathrm{m/s}$)
- t = target plate thickness ($40\ \mathrm{mm}$)
- σ_y = yield strength of RHA steel ($1270\ \mathrm{MPa} = 1270 \times 10^6\ \mathrm{Pa}$)

Table 5.12 Ballistic performance index (m^2/s^2/Pa-m) by different material models

v	Experiment	J-C	R-K	MJ-C
793.7	0.0121	0.01242	0.01136	0.01212
803.4	0.01215	0.01266	0.01141	0.01216

This value reflects the material and projectile interaction during ballistic impact. It is normalized by the yield strength of the material, offering a comparison for different materials or configurations. A higher **BPI** indicates better ballistic resistance under the same conditions.

5.7.1 Ballistic limit, Energy and ballistic efficiency calculations

The **Lambert-Jonas equation** [33] is widely used to model projectile penetration into armor plates. It describes the relationship between the residual velocity, striking velocity, and the ballistic limit velocity. The equation is:

$$v_r = \left[v_s^p - v_b^p\right]^{1/p} \tag{5.5}$$

Where:
v_r = residual velocity ($166\ \mathrm{m/s}$)
v_s = striking velocity ($803\ \mathrm{m/s}$)
v_b = ballistic limit velocity (to be determined)
p = velocity exponent, typically $p = 2$ for RHA steel

The ballistic limit velocity (v_b) is approximately $785.6\,\mathrm{m/s}$ which means the plate can resist projectiles traveling below this velocity without full perforation.

The penetration depth can be expressed using the following Eq. (5.6), which refines penetration prediction based on v_s, v_b, and the plate thickness:

$$P = t\left(\frac{v_s}{v_b}\right)^q \tag{5.6}$$

Where P is the penetration depth, q is the empirical constant, q = 1.8 for high strength materials like RHA steel. The penetration depth is 41.6 mm. The effect of plate thickness on residual velocity curve is shown in Fig. 5.32.

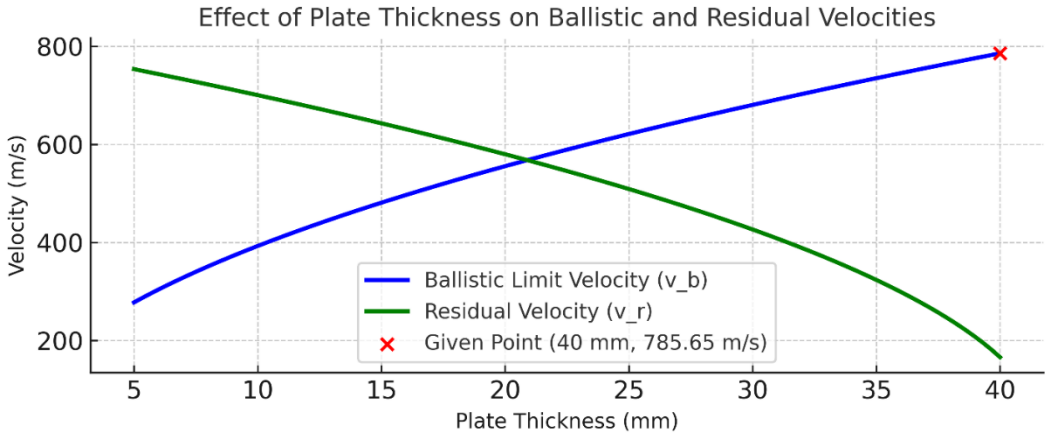

Fig. 5.33 Effect of plate thickness on ballistic and residual velocities

Since P > t, the projectile fully perforated the plate with some energy remaining.

When a projectile strikes a plate like RHA steel, part of the kinetic energy is dissipated through:

1. **Projectile deformation**: Energy lost to plastic deformation and fragmentation of the projectile.
2. **Plate deformation**: Energy absorbed by the target in bending, fracture, and shear.
3. **Energy lost to heat and sound**: Minor in most cases but can be factored into dissipation.

The total energy of the projectile before it strikes the target is the kinetic energy:

$$\mathrm{E_{total}} = \frac{1}{2}\, m\, v_s^2 = 96721\ \mathrm{J} \tag{5.7}$$

Kinetic energy loss in penetration is:

$$E_{loss} = \frac{1}{2}\, m\, [v_s^2 - v_r^2] \quad (5.8)$$

So, the **energy loss during penetration** is 92588 J.

Kinetic energy absorbed by the plate (E_{plate}) is related to the yield strength, thickness, and volume of the plate directly affected by the projectile.

$$E_{plate} = \sigma_y\, V_{plate} \quad (5.9)$$

Where $V_{plate} = A_{projectile}\,.\,t = 2.827 \times 10^{-5}$ m^3, E_{plate} is equal to 35100 J.

Now, **energy remaining in projectile** is

$E_{res} = ½\ m\ v_r^2 = 4134$ J

Energy distribution summary

Initial energy (E_{total}) 96721 J
Energy absorbed by plate deformation: 35100 J
Energy retained by the projectile: 4134 J
Energy dissipated (e.g., heat, sound, and projectile deformation):

$E_{dissipated} = E_{total} - (E_{plate} + E_{res}) = 57487$ J

The energy pie charts are shown in Figs. 5.33 & 5.34. The resistance of the RHA plate to penetration is given by:

$$R_{plate} = \sigma_y.V.t \quad (5.10)$$

The volume of the projectile is 4.94×10^{-5} m^3, from above relation R_{plate} is 2509 J. Now by comparing the E_{loss} and R_{plate} it is clear that the energy loss is significantly higher than the resistance of the RHA steel plate, indicating that the projectile will penetrate the target easily.

The ballistic efficiency (BE) should thus be:

$$BE = E_{loss} / E_{total} = 95.8\ \% \quad (5.11)$$

The Ballistic Efficiency (BE) of the projectile is approximately 95.8%. This means that about 95.8% of the projectile total energy is effectively used in penetrating the target.

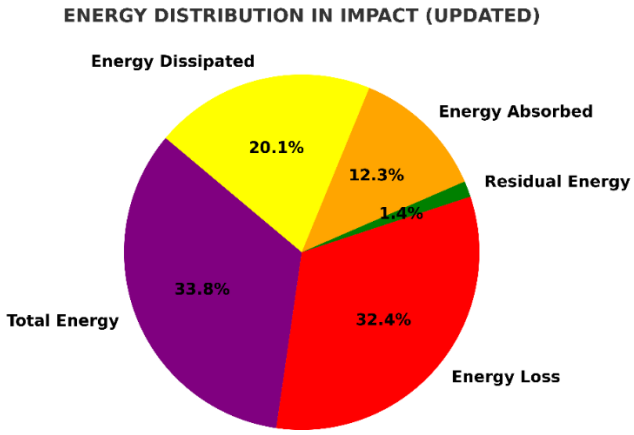

Fig. 5.34 Energy distribution in impact

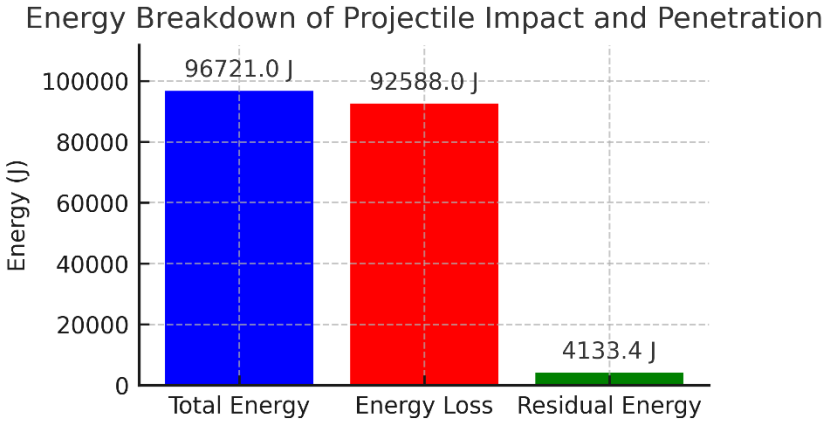

Fig. 5.35 Energy breakdown of projectile impact and penetration

5.8 Micro-mechanism of energy absorption by RHA steel and Kinetic energy impacted by the Projectile Steel

Finite element simulations show that the stress wave propagation from the impact zone spreads out in a circular pattern. To evaluate the ballistic performance against armor-piercing projectiles, it is crucial to understand the various energy absorption mechanisms and failure processes occurring during the projectile-target interaction. Depending on the projectile characteristics (such as size, shape, velocity, and density), the target properties (including strength, ductility, toughness, and thickness), and the specific test conditions [34], several energy dissipation mechanisms and

failure modes may act simultaneously. For instance, when armor-piercing projectiles strike soft, ductile targets—particularly when the plate thickness exceeds the projectile diameter—the failure is primarily governed by a ductile-hole growth process and petalling [34]. . During impact, the hard steel core of the projectile typically maintains its shape, except when striking high-strength targets, while the surrounding target material is displaced mainly through plastic deformation [35]. Consequently, materials that exhibit higher dynamic flow stress tend to offer greater resistance to penetration, which is a key factor contributing to the superior ballistic performance of RHA steel [21,36,37].

Several analytical models have been developed in the literature [38,39] to calculate the resisting stress imposed by a target plate on rigid-sharp projectiles. Equally, studying deformable projectiles is essential since their ballistic behavior can vary significantly with changes in projectile thickness and diameter. In this study, the same model is applied to both deformable and rigid projectiles, with the computed resisting stress subsequently used to determine the ballistic limit velocity. While some approaches estimate resisting forces using cavity expansion analysis [40] obtained the resisting stress through numerical simulations. According to their work [41,42], the ballistic limit velocity is calculated by

$$v_{bl}^2 = \frac{2H\sigma_r}{\rho_p L_{eff}} \tag{5.12}$$

Here v_{bl} denotes the ballistic limit velocity, H represnts the target thickness, σ_r is the resisting stress, ρ_p is the projectile density. The effective length, L_{eff}, is determined by the relation, $\pi r^2 \rho_p L_{eff} = m$. Where, m is the mass of the projectile and r is its radius. For cases where the ratio H (target thickness)/ D (Projectile diameter) exceeds 1), the resisting stress is defined as follows:

$$\sigma_r = Y[2 + 0.8 \ln\left(\frac{H}{D}\right)] \tag{5.13}$$

According to Eq. (5.12), the critical thickness (H) for perforation can be determined by setting the ballistic limit velocity v_{bl} equal to the initial impact velocity (v_o). In this case, the computed resisting stress is 2859.74 MPa, which represents the average stress around the crater.

In this study, high strain rate tensile tests were performed up to a maximum rate of 1000 s^{-1}. Consequently, the flow stress (Y) was determined using the data obtained at a strain rate of 1000 s^{-1} and a plastic strain of 0.2. This approach is justified, as both RHA and projectile steels exhibit minimal strain rate sensitivity within the investigated strain rate range, as discussed in Chapter 2. Here, Y is set at 1.68 GPa for projectile steel and 1.27 GPa for RHA steel, with the ballistic limit velocity, v_{bl} taken as 775 m/s, corresponding to the initial impact velocity.

The analysis indicates that the dynamic flow stress at high strains—often referred to as effective strength according to Rosenberg et al. [41,42] —is critical in determining the ballistic performance of soft targets against rigid armor-piercing projectiles. Their model also provides a means to predict the critical thickness for perforation. Differences in the ballistic behavior of RHA steel can largely be attributed to variations in its dynamic flow stress.

Moreover, projectile steel exhibits a higher strain hardening rate than RHA steel, as discussed in Chapter 2. This increased strain hardening facilitates a broader distribution of plastic deformation, since the plastic wave velocity is directly linked to the slope of the stress-strain curve in the plastic region. A faster plastic wave ensures that a greater volume of material participates in energy absorption, which enhances ballistic resistance. Additionally, studies [21,43] have shown that normalized hardness measurements near the impact craters increase toward the crater edge compared to the base material. In RHA steel, this hardness rise extends over a larger area, which is attributed to its higher strain hardening rate due to the activation of deformation twins during impact. This behavior suggests that more material is involved in energy dissipation during the perforation process.

It is clear that the amount of bulging also increases with velocity for MJ-C and R-K models as shown in simulation Table 5.19-5.22.

When a deformable projectile strikes a target, much of its kinetic energy is expended through the plastic deformation of the target, the development of adiabatic shear bands (ASBs), and the cracks that form along these bands [44,45]. The energy absorbed by plastic deformation increases when the material exhibits a higher flow stress and when a larger volume of material is involved in dissipating the projectile energy. Additionally, some energy is consumed by the deformation of the projectile itself. Notably, projectile blunting is more significant when impacting high-strength targets compared to lower-strength ones [34], which reduces the projectile penetration capability and thereby enhances the target's defensive performance. However, high-strength targets are not immune to failure; they may shatter or perforate due to low-energy failure mechanisms such as brittle cracking, spalling, or fragmentation [46]. Thus high strength targets may not exhibit higher ballistic performance in all cases. . In this study, RHA steels are used because their toughness and ductility prevent brittle cracking. Moreover, when the target thickness to projectile diameter ratio (t/d) is around one—as is the case here—the predominant failure mode against deformable projectiles is ASB-induced plug ejection [44]. Since adiabatic shear band formation is a key feature during high-velocity impacts, resistance to ASB development, along with high dynamic flow stress and material toughness, plays a critical role in determining ballistic performance. Studies on ASB formation [21–25] have indicated that materials with a low strain hardening coefficient, minimal

strain rate sensitivity, a high thermal softening parameter, low density, and low specific heat capacity tend to form ASBs more readily, thus influencing their overall failure behavior.

Adiabatic shear bands (ASBs) during ballistic impacts occur due to thermo-mechanical instabilities at high strain rates. At these rates, there is insufficient time for heat to dissipate, causing localized temperature increases that lead to severe deformation in confined regions [47]. Research on ASB formation [48,49] shows that materials with high density, elevated specific heat capacity, greater strain hardening coefficients, and enhanced strain rate sensitivity, coupled with a low thermal softening parameter, are more susceptible to ASB-induced plug formation. Since projectile steel exhibits both higher strain hardening and greater strain rate sensitivity compared to RHA steel, it is expected to better resist ASB formation. In this study, we quantitatively evaluate the adiabatic shear sensitivity of both projectile and RHA steel using an analytical equation derived by Wright et al. [48,49].

According to Wright et al. [48,49], the susceptibility to ASB formation is given by Eq.

$$\frac{X_{SB}}{\alpha/m} = \min\left\{1,\ \frac{1}{\left(\frac{n}{m}\right)+\sqrt{\frac{n}{m}}}\right\} \tag{5.14}$$

Based on the determined values for *n*, *m* and thermal softening parameter, the adiabatic shear band sensitivity parameters X_{SB} for 40 mm thick RHA steel plate is calculated to be 10.5. This relatively high value indicates that RHA steel is considerably prone to adiabatic shear localization. In contrast, projectile steel exhibits a much lower sensitivity to ASB formation, with an X_{SB} value is 2.5, implying better resistance against shear localization.

Various parameters obtained from tension stress–strain curves of the two steels are summarized in Table (Chapter 2). It can be observed from that projectile steel has a higher strain rate sensitivity, higher strain hardening coefficient and lower thermal softening than RHA steel. Hence, projectile steel exhibits a substantially higher resistance to ASB formation (higher critical strain for ASB formation) than RHA steel. In addition to strain hardening, strain rate hardening and thermal softening effects, thermal diffusivity has also been suggested to have a considerable influence on shear band formation [22, 28–31]. This is because thermal diffusivity determines the actual temperature profile developed inside the shear band. Generally, materials with lower thermal diffusivity will have higher temperatures inside the shear band [28]. Earlier works have shown that a material with lower thermal diffusivity will more easily undergo adiabatic shear band formation [29–31]. The RHA steel composition used in the present study is close to the class of low-alloy steels, whereas projectile steel belongs to the high strength steel category. Generally, high strength steels have lower thermal diffusivities than low-alloy steels [28].

The penetration of projectiles in a monolithic target has been mainly found to occur in four phases: transient, quasi-steady state primary penetration, secondary penetration and recovery phases [33]. The contributions coming from the transient and recovery phases to the total penetration depth will be less substantial, and they can be ignored for projectiles with high L/D ratios. Hence, the total penetration can be primarily attributed to quasi-steady state penetration and, to a lesser extent, to secondary penetration [34, 35].

During a projectile impact, the target material near the projectile-target interface undergoes large strain deformation under high strain rates and high temperatures and then erodes after reaching a critical strain [44, 45]. Hence, it is important to understand the failure behavior of the material under the conditions prevailing at the projectile-target interface. This study shows that ASB-induced fragmentation is an important mechanism to study for target erosion during penetration in high-hardness armor steels. However, the post ballistic analysis of the steels not carried because of the confidentiality agreement.

Thus the next step is to examine the permanent deflection of the impacted plates. It has to be noted that, for the boundary value problem studied, plastic deformation in form of bending acts as a main mechanism for energy absorption by the target. The RHA sheets show much reduced permanent bending for the whole range of impact velocities investigated. The amount of kinetic energy of the striker converted into plastic work is strongly dependent on the metal considered.

The strain hardening rate of RHA steel increases from quasi-static to dynamic range and decreases at high temperature. During compressive deformation, the strain is concentrated at a relatively soft phase contributes to the strain hardening. The RHA consist of retained austenite with tempered martensite. Thus the internal stress caused by various kinds of phases in steel affects significantly the strain-hardening rate. According to Sugimoto et al. [50], the retained austenite in the bainitic matrix leads to a long-range compressive internal stress, this contributes to a high strain hardening both in an early stage of strain and at high strains. As well as the role of retained austenite in the strain partitioning, the deformation-induced transformation enables the austenite to enhance the strain-hardening rate. The RHA contain a little initial retained austenite 12%, and the martensitic transformation hardly occurred even in the dynamic compressive deformation. On the other hand, all the retained austenite transformed into the marteniste during the dynamic deformation. According to the previous research results of Garcia-Mateo et al. [51], the deformation-induced transformation of retained austenite in bainitic steels leads to transformation-induced plasticity (TRIP), which significantly increases the strain-hardening rate and thus favorable contributes to tensile properties. This increase of strain hardening is attributed to a volume expansion of the transforming region, which results in additional plastic deformation of the surrounding area [51]. Therefore, the RHA steel exhibited the higher strain-hardening rate than the projectile steel due to

the internal stress occurring during the deformation among various constituents and due to the TRIP effect by retained austenite.

5.9 Conclusion

A systematic investigation of the ballistic impact behavior of typical rolled homogeneous armor steel was conducted through a series of sequential impact tests. Complementary numerical simulations—employing three distinct material models—were performed to validate both the calibrated constitutive parameters and the algorithm capability to replicate the impact process and the dynamic response of the RHA steel plate. Based on this analysis, several conclusions have been drawn.

- The armour plate can stop the projectile completely if it hits at 775 m/s. However, if the projectile speed increases to 793 m/s, it passes through the plate, coming out the other side at 128 m/s. This means the ballistic limit, at which the plate is just about to let the projectile break through is around 785 m/s. This value helps determine how much protection the armour provides before it fails to stop the projectile.
- The analysis is highly dependent on mesh of both projectile and armour plate. The impacted area must be fine mesh with unstructured meshing.
- The force increases with displacement due to material deformation and contact resistance under a constant friction coefficient at 806 m/s. Since friction remains unchanged, force variations are primarily influenced by strain-rate effects and material behaviour. At high velocity, factors like energy dissipation, yielding, or failure mechanisms contribute to force evolution, with peak force indicating possible material response under impact loading.
- The force evolution over time at a constant friction coefficient and 775 m/s velocity. The force initially rises due to surface interaction and material response, while the controlled friction condition maintains a stable profile. Variations in force are likely due to material deformation and wave propagation. At high impact speeds, friction and inertia significantly influence the system dynamic response.
- The correlation coefficient of 0.99 predicted by the MJ-C model indicates a strong positive correlation between the model predictions and actual data, signifying high accuracy and reliability.
- To ensure numerical stability in simulations, the projectile tip (up to 2 mm) is assigned elastic properties, while the rest of the projectile remains deformable. If the projectile is fully deformable, numerical instability occurs at certain impact velocities, leading to premature termination of simulations, as shown in Fig. 5.27. This instability arises due to crack formation in the target plate, which disrupts the simulation process and prevents the

completion of calculations. Applying elastic properties to the tip helps mitigate these issues, ensuring a stable and successful simulation.

- The impact of a projectile induces high strain deformation (up to ~2) over a wide strain rate range (1 s^{-1} to 10^5 s^{-1}). A 30 mm diameter projectile travelling at 803 m/s impacting a 40 mm thick armour steel plate generates an average $\dot{\varepsilon}$ of 10^4 s^{-1} and plastic strain of 0.32. These results emphasize the importance of studying dynamic flow behavior to enhance ballistic performance under high strain rate conditions.
- Fig. 5.31 shows that material failure patterns differ based on projectile characteristics. With an elastic tip, petal formation occurs, while a fully deformable projectile results in a smaller rear lip and potential plug formation. This indicates that failure modes depend not only on plate thickness and projectile shape but also on whether the projectile is rigid, elastic, or deformable, influencing the impact response and material removal mechanism.
- The plug removal from armour plate travels at low speed when fully deformable projectile considered (Fig. 5.31b). In these analysis element deletion upon reaching a certain value of plastic strain was given. Since, the stiffness in that element will be zero in which that value of plastic strain has reached and element no longer participate in calculations. But the elements remain attached to the other elements as shown in Fig. 5.36.

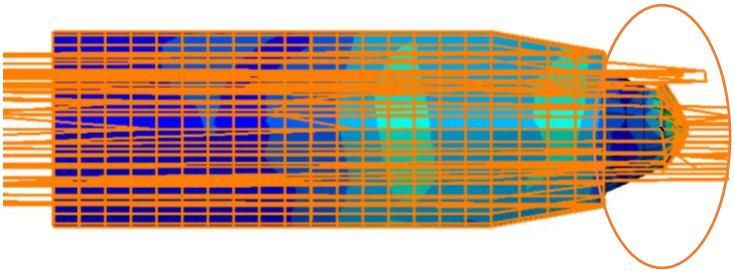

Fig. 5.36 Deformed projectile shows deleted element attached with the other elements

- For MJ-C material models, the ballistic limit is very close to experimental values. The R-K material model predicts slightly lower ballistic limit.
- The projectile length does not have any effect in case of deformable projectile but for rigid projectile length of the projectile influence the residual velocity.
- For all three materials, the entry and exit hole diameters are roughly the same but significantly different from experimental values.

References

[1] Børvik T, Langseth M, Hopperstad OS, Malo KA. Ballistic penetration of steel plates. vol. 22. 1999. https://doi.org/10.1016/S0734-743X(99)00011-1.

[2] Johnson GR, Cook WH. Fracture characteristics of three metals subjected to various strains, strain rates, temperatures and pressures. Eng Fract Mech 1985;21:31–48. https://doi.org/10.1016/0013-7944(85)90052-9.

[3] Camacho GT, Ortiz M. Adaptive Lagrangian modelling of ballistic penetration of metallic targets. Comput Methods Appl Mech Eng 1997;142:269–301. https://doi.org/10.1016/S0045-7825(96)01134-6.

[4] Zukas JA, Scheffler DR. Practical aspects of numerical simulations of dynamic events: Effects of meshing. Int J Impact Eng 2000;24:925–45. https://doi.org/10.1016/S0734-743X(00)00012-9.

[5] Borvik T, Hopperstad OS, Berstad T, Langseth M. Perforation of 12mm thick steel plates by 20mm diameter projectiles with flat, hemispherical and conical noses - Part II: Numerical simulations. Int J Impact Eng 2001;27:37–64. https://doi.org/10.1016/S0734-743X(01)00035-5.

[6] Borvik T, Hopperstad OS, Berstad T, Langseth M. Perforation of 12mm thick steel plates by 20mm diameter projectiles with flat, hemispherical and conical noses Part I: Experimental study. Int J Impact Eng 2002;27:19–35. https://doi.org/https://doi.org/10.1016/S0734-743X(01)00034-3.

[7] Hu CJ, Lee PY, Chen JS. Ballistic performance and microstructure of modified rolled homogeneous armor steel. J Chinese Inst Eng Trans Chinese Inst Eng Ser A/Chung-Kuo K Ch'eng Hsuch K'an 2002;25:99–107. https://doi.org/10.1080/02533839.2002.9670684.

[8] Bruce DM, Matlock DK, Speer JG, De AK. Assessment of the strain-rate dependent tensile properties of automotive sheet steels. SAE Tech Pap 2004. https://doi.org/10.4271/2004-01-0507.

[9] Nahme H, Lach E, Nahme H, Dynamic EL, Strength H, Steels A, et al. Dynamic Behavior of High Strength Armor Steels To cite this version : HAL Id : jpa-00255522 1997;07.

[10] Maweja K, Stumpf W. The design of advanced performance high strength low-carbon martensitic armour steels. Part 1. Mechanical property considerations. Mater Sci Eng A 2008;485:140–53. https://doi.org/10.1016/j.msea.2007.08.048.

[11] Jankowiak T, Rusinek A, Wood P. A numerical analysis of the dynamic behaviour of sheet steel perforated by a conical projectile under ballistic conditions. Finite Elem Anal Des 2013;65:39–49. https://doi.org/10.1016/j.finel.2012.10.007.

[12] Whittington WR, Oppedal AL, Turnage S, Hammi Y, Rhee H, Allison PG, et al. Capturing the effect of temperature, strain rate, and stress state on the plasticity and fracture of rolled homogeneous armor (RHA) steel. Mater Sci Eng A 2014;594:82–8. https://doi.org/10.1016/j.msea.2013.11.018.

[13] Tria DE, Trebinski R. On the influence of fracture criterion on perforation of high-strength steel plates subjected to armour piercing projectile. Arch Mech Eng 2015;62:157–79.

https://doi.org/10.1515/meceng-2015-0010.
[14] Trajkovski J, Kunc R, Pepel V, Prebil I. Flow and fracture behavior of high-strength armor steel PROTAC 500. Mater Des 2015;66:37–45. https://doi.org/10.1016/j.matdes.2014.10.030.
[15] Kpenyigba KM, Jankowiak T, Rusinek A, Pesci R, Wang B. Effect of projectile nose shape on ballistic resistance of interstitial-free steel sheets. Int J Impact Eng 2015;79:83–94. https://doi.org/10.1016/j.ijimpeng.2014.10.007.
[16] Tria DE, Trębiński R. Methodology for experimental verification of steel armour impact modelling. Int J Impact Eng 2017;100:102–16. https://doi.org/10.1016/j.ijimpeng.2016.10.011.
[17] Banerjee A, Dhar S, Acharyya S, Datta D, Nayak N. Numerical Simulation of Ballistic Impact of Armour Steel Plate by Typical Armour Piercing Projectile. Procedia Eng 2017;173:347–54. https://doi.org/10.1016/j.proeng.2016.12.028.
[18] McDonald B, Bornstein H, Langdon G, Curry R, Orifici A. Deformation and Rupture of Armour Grade Steel under Localised Blast Loading. Procedia Eng 2017;197:13–22. https://doi.org/10.1016/j.proeng.2017.08.077.
[19] Fras T, Faderl N, Roth CC, Mohr D. Strikers with different nose shape impacting an armour steel - numerical modelling. 12th Eur LS-DYNA Conf 2019.
[20] Konca E. A comparison of the ballistic performances of various microstructures in mil-a-12560 armor steel. Metals (Basel) 2020;10. https://doi.org/10.3390/met10040446.
[21] Jena PK, Manickam MAM, Venketachari S, Srivastava SC, Srivastava A, Chakrabarty S, et al. Microstructure, mechanical, ballistic property evaluation of RHA steel produced by continuous-casting route. J Appl Res Technol 2020;18:1–13. https://doi.org/10.22201/ICAT.24486736E.2020.18.1.927.
[22] Choudhary S, Singh PK, Khare S, Kumar K, Mahajan P, Verma RK. Ballistic impact behaviour of newly developed armour grade steel: An experimental and numerical study. Int J Impact Eng 2020;140:103557. https://doi.org/10.1016/j.ijimpeng.2020.103557.
[23] Singh BB, Sukumar G, Paman A, Balaji G, Siva Kumar K, Madhu V, et al. A Comparative Study on the Ballistic Performance and Failure Mechanisms of High-Nitrogen Steel and RHA Steel Against Tungsten Heavy Alloy Penetrators. J Dyn Behav Mater 2021;7:60–80. https://doi.org/10.1007/s40870-020-00270-8.
[24] Zhang Z, Wu Y, Huang F. Effect of stress triaxiality cut-off value in the fracture criterion on predicting the ballistic behavior of Al2024-T351 plate impacted by blunt- hemisphere- and ogival-nosed projectiles. J Mater Res Technol 2023;25:138–65. https://doi.org/10.1016/j.jmrt.2023.05.186.
[25] Limmer KR, Lloyd JT, Field DM, Magagnosc DJ, Hornbuckle C, Walter TR, et al. Designing Steels to Mitigate Failure during Ballistic Deformation (Summary Technical Report, Oct 2018-Sept 2021). 2022.
[26] Anderson CE, Holmquist TJ, Sharron TR. Quantification of the effect of using the Johnson-Cook damage model in numerical simulations of penetration and perforation. Proc - 22nd Int Symp Ballist 2005:963–70.

[27] Bhav Singh B, Sukumar G, Prakasa Rao P, Siva Kumar K, Madhu V, Arockia Kumar R. Superior ballistic performance of high-nitrogen steels against deformable and non-deformable projectiles. Mater Sci Eng A 2019;751:115–27. https://doi.org/10.1016/j.msea.2019.02.044.
[28] Ipson RFR and TW. Ballistic Perforation Dynamics. J Appl Mech 1963;30:384–91.
[29] Ipson TW, Recht RF. Ballistic-penetration resistance and its measurement. Exp Mech 1975;15:249–57. https://doi.org/10.1007/bf02318057.
[30] Balu PJ. Friction Science and Technology. 2016.
[31] Armstrong RW, Walley SM. High strain rate properties of metals and alloys. Int Mater Rev 2008;53:105–28. https://doi.org/10.1179/174328008X277795.
[32] Jena PK, Mishra B, RameshBabu M, Babu A, Singh AK, SivaKumar K, et al. Effect of heat treatment on mechanical and ballistic properties of a high strength armour steel. Int J Impact Eng 2010;37:242–9. https://doi.org/10.1016/j.ijimpeng.2009.09.003.
[33] Arias A, Rodríguez-Martínez JA, Rusinek A. Numerical simulations of impact behaviour of thin steel plates subjected to cylindrical, conical and hemispherical non-deformable projectiles. Eng Fract Mech 2008;75:1635–56. https://doi.org/10.1016/j.engfracmech.2007.06.005.
[34] Woodruff C, Dean SW, Cagle C, Luke Croessmann C, Pantoya ML. Comparing pyrometry and thermography in ballistic impact experiments. Meas J Int Meas Confed 2022;189:110488. https://doi.org/10.1016/j.measurement.2021.110488.
[35] Mechanical metallurgy - Dieter_ George Ellwood.pdf n.d.
[36] Ben-Dor G, Dubinsky A, Elperin T. A class of models implying the Lambent- Jonas relation. Int J Solids Struct 2001;38:7113–9. https://doi.org/10.1016/S0020-7683(00)00425-X.
[37] Chen J, Li S, Ma S, Chen Y, Liu Y, Tian Q, et al. The Anti-Penetration Performance and Mechanism of Metal Materials: A Review. Engineering 2024;40:131–57. https://doi.org/10.1016/j.eng.2024.03.023.
[38] Dodd B, Coghe F. Damage caused to metals by kinetic and chemical energy projectiles. Secur Use Innov Technol Against Terror 2009:33–46. https://doi.org/10.13140/RG.2.1.1667.0881.
[39] McDonald B, Bornstein H, Ameri A, Daliri A, Orifici AC. Plasticity and ductile fracture behaviour of four armour steels. Int J Solids Struct 2019;176–177:135–49. https://doi.org/10.1016/j.ijsolstr.2019.05.013.
[40] McDonald B, Bornstein H, Ameri A, Escobedo-Diaz JP, Orifici AC. High strain rate and high temperature response of two armour steels: Experimental testing and constitutive modelling. EPJ Web Conf 2018;183:3–8. https://doi.org/10.1051/epjconf/201818301022.
[41] Saxena A, Dwivedi SP, Kumaraswamy A, Srivastava AK, Maurya NK. Influence of SD effect on Johnson–Cook hardening constitutive material model: Numerical and experimental investigation for armor steel. Mech Adv Mater Struct 2022;29:285–302. https://doi.org/10.1080/15376494.2020.1765266.
[42] Chocron S, Anderson CE, Grosch DJ, Popelar CH. Impact of the 7.62-mm APM2 projectile

against the edge of a metallic target. Int J Impact Eng 2001;25:423–37. https://doi.org/10.1016/S0734-743X(00)00063-4.
[43] Holmen JK, Johnsen J, Jupp S, Hopperstad OS, Børvik T. Effects of heat treatment on the ballistic properties of AA6070 aluminium alloy. Int J Impact Eng 2013;57:119–33. https://doi.org/10.1016/j.ijimpeng.2013.02.002.
[44] Rosenberg Z, Dekel E. On the deep penetration and plate perforation by rigid projectiles. Int J Solids Struct 2009;46:4169–80. https://doi.org/10.1016/j.ijsolstr.2009.07.027.
[45] Rosenberg Z, Dekel E. Revisiting the perforation of ductile plates by sharp-nosed rigid projectiles. Int J Solids Struct 2010;47:3022–33. https://doi.org/10.1016/j.ijsolstr.2010.07.003.
[46] Jena PK, Ponguru Senthil P, Siva Kumar K. Effect of tempering time on the ballistic performance of a high strength armour steel. J Appl Res Technol 2016;14:47–53. https://doi.org/10.1016/j.jart.2016.02.002.
[47] Sukumar G, Patra AK, Kumar A, Thakur RK, Singh BB, Bhattacharjee A, et al. A comparative study on dynamic deformation and ballistic impact response of Ti–4Al–2.5V–1.5Fe–0.25O and Ti–6Al–4V alloys. Mater Sci Eng A 2024;889:145727. https://doi.org/10.1016/j.msea.2023.145727.
[48] Bassim MN, Odeshi AG, Bolduc M. Deformation and failure of a rolled homogeneous armour steel under dynamic mechanical loading in compression. 12th Int Conf Fract 2009, ICF-12 2009;5:3464–73.
[49] Dey S, Børvik T, Hopperstad OS, Leinum JR, Langseth M. The effect of target strength on the perforation of steel plates using three different projectile nose shapes. Int J Impact Eng 2004;30:1005–38. https://doi.org/10.1016/j.ijimpeng.2004.06.004.
[50] Woodward RL. The penetration of metal targets which fail by adiabatic shear plugging. Int J Mech Sci 1978;20:599–607. https://doi.org/10.1016/0020-7403(78)90018-8.
[51] Wright TW. The physics and mathematics of adiabatic shear bands 2002:241.
[52] Wright TW. Approximate analysis for the formation of adiabatic shear bands. J Mech Phys Solids 1990;38:515–30. https://doi.org/10.1016/0022-5096(90)90012-S.
[53] Sugimoto K ichi, Srivastava AK. Microstructure and Mechanical Properties of a TRIP-Aided Martensitic Steel. Metallogr Microstruct Anal 2015;4:344–54. https://doi.org/10.1007/s13632-015-0221-5.
[54] Garcia-Mateo C, Caballero FG, Chao J, Capdevila C, Garcia De Andres C. Mechanical stability of retained austenite during plastic deformation of super high strength carbide free bainitic steels. J Mater Sci 2009;44:4617–24. https://doi.org/10.1007/s10853-009-3704-4.

Chapter – 6

Effect of projectile nose shape and armour microstructure on ballistic performance

Abstract

This study explores the ballistic resistance of typical rolled homogeneous armour (RHA) plates against projectiles with varying nose shapes—blunt, conical, and hemispherical—through a detailed finite element simulation approach. The research emphasizes the influence of projectile nose geometry on penetration mechanics, energy absorption, and failure characteristics of the target plate and hence on the ballistic performance of the armour plate. Simulation techniques were employed to model high-velocity impacts, accurately capturing material deformation, stress distribution, and damage evolution. Key metrics such as residual velocity, depth of penetration, and plate failure modes were analyzed to assess the effect of nose shape variations. The findings provide critical insights into the behaviour of armour plates under impact, contributing to the development of optimized armour solutions in defense engineering. Additionally, different heat treatment protocol also employed to change the microstructure of armour steel to improve its strength and toughness. Simulations is also carried out by changing the values of parameters A, B, and n of J-C strength model equation.

6.1 Introduction

The failure mode due to notably influenced by the projectile nose shape, which directly affects the energy absorbed by the target plate. Extensive research has aimed to determine the minimum impact velocity required for complete perforation across various projectile-plate configurations—a threshold known as the ballistic limit [1]. For example, cylindrical projectiles with flat faces tend to perforate the plate through adiabatic shear band propagation, ultimately leading to plug ejection and a reduced ballistic limit [2-3]. In contrast, when ovate, conical, or hemispherical projectiles are used, the plate is typically perforated via ductile hole enlargement and petalling [4].

Borvik et al. [1,2] further investigated projectile nose shape effects on the deformation and penetration of Weldox 460E steel plates. Their experiments showed that blunt projectiles were more efficient at lower velocities, while conical projectiles required less energy at higher velocities, influencing energy absorption and failure modes. Adaptive meshing was employed in their simulations to address conventional meshing issues. Understanding of the correct viscoplastic constitutive relation for a material requires knowledge of its atomic structure, such as whether it is FCC or BCC. Chia-Jung Hu et al. [3] evaluated the ballistic performance of modified rolled

homogenous armor (MRHA) steel, comparing it with AerMe 100, AISI 1045 and 4130 steels. Their tests revealed the formation of "white"-etched adiabatic shear bands on the front surface of target plates made from AerMet 100, 4130, and MRHA steels, indicating transformed bands due to crystallographic phase transitions.

The shape of the front area of projectile greatly affect the deformation mechanism of the target plates. The thickness of the target plate also has an effect on the ballistic resistance. Sometimes the same nose shape result in different ballistic resistance for thin plate and thick plate and the deformation pattern also [4,5]. The L/D ratio also determine ballistic performance. Three prime factors to influence ballistic performance are as L/D ratio, nose shape and thickness of the plate. If the nose radius of projectile changes, the critical impact energy changes and maximum energy observed at nose radius where mode of failure changes from shear plugging to tensile stretching. Several researchers [5,6] found that the blunt shape penetrators penetrate the target more efficiently than ogive and hemispherical projectiles while others [7] found that the conical projectiles are more efficient penetrators and as the nose angle decrease the perforation resistance of the target tends to drop for thick carbon steel plates. N.K Gupta et al. [8] tested plates of various thicknesses (0.5 to 3 mm) with projectiles of different nose shapes (hemispherical, ogive, blunt), all with the same diameter (19 mm) and length (50.8 mm). Hemispherical projectiles caused the highest deformation. Ogive projectiles were most efficient for plates up to 1.5 mm thick, while blunt projectiles required the least energy for thicker plates (2-3 mm). Hemispherical projectiles had the highest ballistic limit velocity. The Johnson-Cook material model was used for simulations in most of the studies.

In 2008 Arias et al. [9] published a study on the numerical analysis of thin steel plates perforated by different projectile shapes using adaptive meshing for impact velocities ranging from 190 to 600 m/s. The study examined the effects of adiabatic shear bands, plastic work, and temperature gradients. Blunt projectiles caused failure through shear band propagation and plug ejection, conical projectiles induced radial compression and hole enlargement, while hemispherical projectiles exhibited a combination of these failure modes depending on the impact velocity. In 2009 Rusinek et al. [10] examine the normal impact of hemispherical projectile. The tests were conducted covering a wide range of impact velocities. Three material model are chosen for numerical analysis J-C, P-L, and R-K. In 2010 P.K Jena et al. [11] studied the effect of heat treatment on the mechanical and ballistic properties of a high strength armour steel. The ballistic behaviour of the heat-treated plates was evaluated by impacting against non-deformable hard-core projectiles at 840±15 m/s at normal angle of attack.

In 2013 Jankowiak et al. [12] investigated the dynamic response of sheet steel perforated by a conical projectile. Their study considered several factors, including the target thickness and constitutive model, the projectile mass, the friction between the projectile and the target, and the projectile shape. In 2014 Whittington et al. [13] studies the behaviour of RHA (Rolled Homogenous armour) steel at 25^{o}C and 300^{o}C and at $\dot{\varepsilon}$ of 10^{-3} s^{-1} and 1000 s^{-1} the stress state on plasticity and fracture. In 2015 Tria et al. [14] study the effectiveness of four ductile fracture models: MJC, the CL, the maximum shear stress and the constant failure strain model. These models are used to capture material fracture properties and shear plugging failure in 30PM steel plates. In 2015 Trajkovski et al. [15] study the flow and fracture properties of high-strength armour steel PROTAC 500. The JC material and failure model are used for numerical simulation.

For both hemispherical and conical nose shapes, the ballistic velocities are of a similar magnitude, which is consistent with experimental observations [1]. It is also noted that in the conical configuration, the residual velocity v_r nearly equals the initial impact velocity (v) when v exceeds 500 m/s. Various formulations have been proposed to express the ballistic limit as a function of the initial impact velocity [6]. The most commonly used approach is the relation presented in [31] which defines the residual velocity in terms of specific parameters associated with both the plug and the projectile. In 2016 Jena et al. [24] described and analysed the effect of tempering time on the ballistic and mechanical properties of a high strength armour steel. The marginal variation is observed in strength and hardness with increasing tempering time at 2, 24 and 48 h. The Charpy impact values are found to be decreasing. Ballistic performance also decreased with increasing tempering time.

This chapter presents numerical simulations that investigate the perforation of a 40 mm thick armor steel plate by projectiles with various nose shapes. The primary objective is to understand how different projectile geometries influence the ballistic resistance of the target material. The analysis covers impact velocities ranging from 750 to 950 m/s. In all cases, the projectiles have a 30 mm diameter and are deformable, while the targets are 40 mm thick. The thermo-viscoplastic behavior of the target is modeled using modified Johnson-Cook constitutive models, whereas the standard Johnson-Cook model is applied to the projectile material. These simulations are conducted using the non-linear finite element software ABAQUS/Explicit. Additionally, the chapter examines how different heat treatment protocols affect the microstructure, strength, and toughness of armor steel, and explores the impact of varying the JC parameters A, B, and n on the material's ballistic resistance.

6.2 Modelling of Different nose shape

The nose shape of a projectile significantly influences its penetration mechanics and interaction with target materials. In simulation studies, accurately modelling of different nose geometries is essential to capture the distinct behaviour of each shape during high-velocity impacts. The primary nose shapes considered in ballistic studies are blunt, conical, and hemispherical as shown in Fig. 6.1.

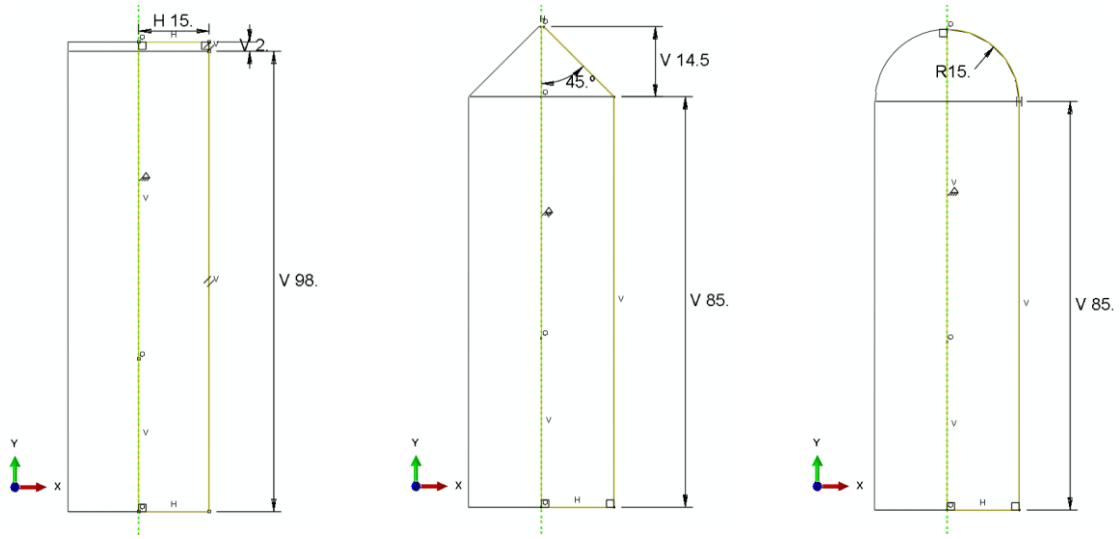

(a) (b) (c)

Fig. 6.1 (a) Blunt nose projectile (b) Conical nose projectile (c) Hemispherical nose projectile

6.2.1 Modelling Approach

Finite element modelling of these nose shapes involves:

- **Geometric Definition**: Precise 3D geometric profiles are created for each nose shape. The hemispherical nose is defined as a half-sphere, while conical and blunt shapes are straightforward to model.
- **Mesh Design**: The projectile and target are discretized into fine meshes, ensuring adequate resolution near the nose region to capture stress concentrations and deformation accurately.
- **Material Properties**: The projectile is typically modelled with high-strength materials, while the armour steel target incorporates strain-rate-dependent material models to simulate realistic behaviour.
- **Boundary and Initial Conditions**: Impact velocity, angle, and constraints are applied to replicate experimental conditions.

Governing Parameters

The study of nose shapes involves evaluating parameters such as:

- **Contact Pressure Distribution**: Determining how forces are applied across the contact surface.
- **Stress Wave Propagation**: Understanding how shock waves travel through the target material.
- **Failure Mechanisms**: Identifying modes like plugging, spalling, or shear failure.

6.2.2 Finite element analysis

6.2.2.1 Conical Nose Shape:

A conical-nosed projectile features a pointed geometry with a fixed half-angle. The sharp tip enhances penetration by concentrating the impact forces over a smaller area, thereby reducing the initial resistance of the target. However, the conical shape can also generate higher localized stresses within the target material, potentially leading to shear-driven failure. Due to the continuously varying diameter of the conical nose, the projectile remains in contact with the target surface throughout penetration, increasing resistance. This geometric characteristic can lead to the projectile being arrested within the target. Additionally, the effect of friction is influenced by the projectile geometry.

The residual velocity as a function of time is shown in Fig. 6.2. The force exerted by the projectile, considering different material models, is presented in Fig. 6.3. The von-Mises stress profile at different time interval is shown in Fig. 6.4. Fig. 6.4a shows that a very high stress are generated when the projectile is in the middle of the plate. The stress surrounds the nose of the projectile.

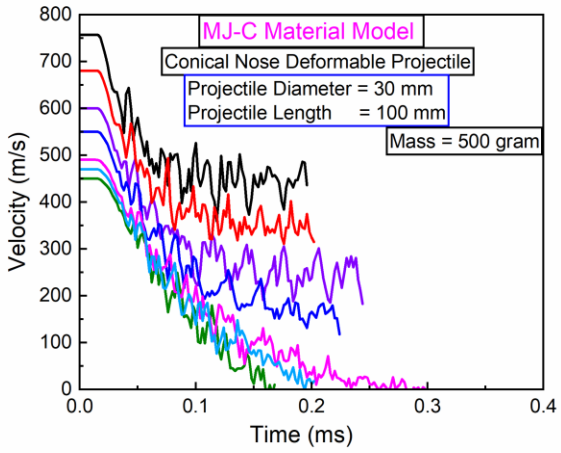

Fig. 6.2 Conical nose deformable projectile velocity vs time graph via MJ-C material model

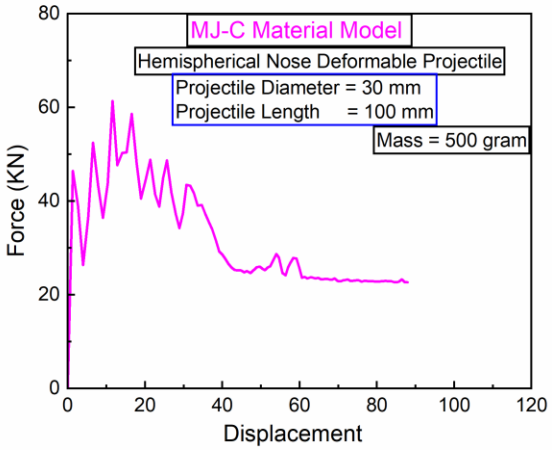

Fig. 6.3 Conical nose deformable projectile force vs displacement graph via MJ-C material model

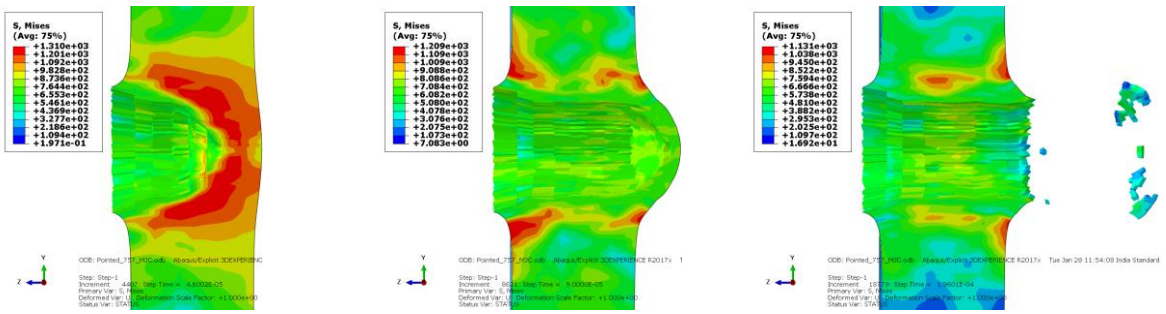

(a) **(b)** **(c)**

Fig. 6.4 Von-Mises stress profile in target plate impacted by conical projectile

6.2.2.2 Hemispherical Nose Shape:

A hemispherical nose features a smooth, rounded surface, providing a balance between penetration efficiency and target material damage. This shape minimizes drag forces while maintaining effective penetration depth. The curved geometry ensures more uniform stress distribution upon impact, delaying the onset of target failure compared to blunt or conical shapes. The velocity vs time profile is shown in Fig. 6.5, whereas the von-Mises stress distribution inside the plate is shown in Fig. 6.6. The load vs displacement curve is not plotted for this because it is difficult to identify how many nodes are in contact with the plate on striking because of the curved surface. In the hemispherical scenario, the combined compressive and tensile stresses cause a small plug with minimal thickness to be ejected.

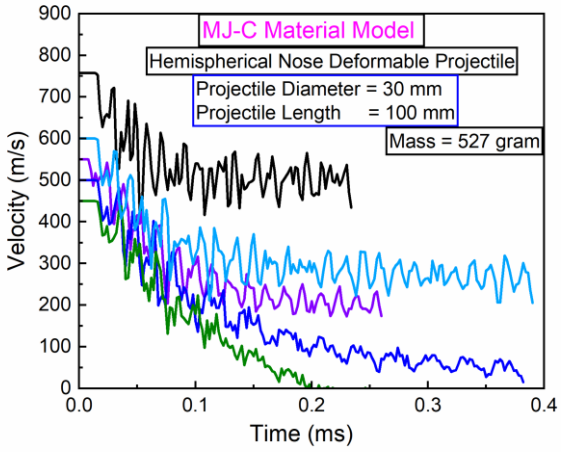

Fig. 6.5 Hemispherical nose deformable projectile velocity vs time graph via MJ-C material model

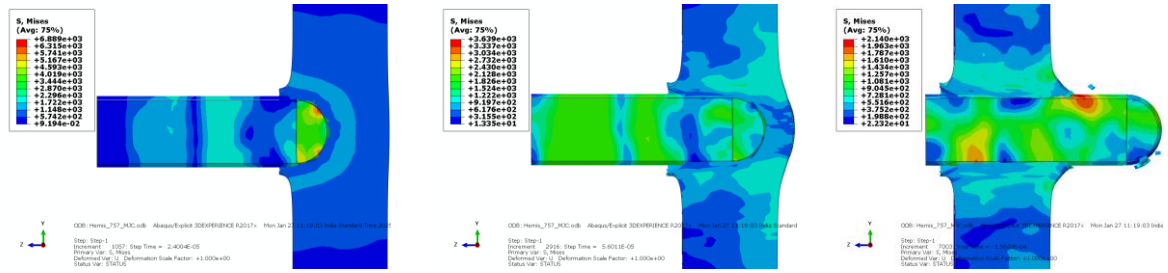

Fig. 6.6 Von-Mises stress profile in target plate impacted by hemispherical projectile

In the hemispherical configuration, failure originates from necking near the projectile-plate contact zone. However, at an impact velocity of 757 m/s, necking is observed at the upper part of the contact area, accompanied by hole enlargement caused by uniform plastic flow on the impacted side. At higher velocities, the confinement of plastic deformation on the impact face reduces overall plastic flow, leading to the development of circumferential necking.

6.2.2.3 Blunt nose projectile:

A blunt nose projectile features a flat or nearly flat front surface, resulting in a larger contact area upon impact. This geometry facilitates greater energy dissipation through plastic deformation of the target material. While blunt projectiles typically induce localized damage, their penetration efficiency may be lower at sub-ordinance velocities due to increased drag forces during penetration [1,16,17].

However, the present analysis indicates that at ordinance velocity, the blunt-nose projectile demonstrates higher impact effectiveness compared to the other projectile configurations. The shear failure observed in the target material is more pronounced around the projectile nose region, leading to significant localized deformation and formation of plug.

The velocity-time profile at different impact velocities is presented in Fig. 6.7. The force exerted by the projectile on the target surface, as illustrated in Fig. 6.8, shows that the force levels is quite high. Additionally, the stress wave propagation generated around the penetration region is visualized in Fig. 6.9, highlighting the dynamic response of the target material to ballistic loading.

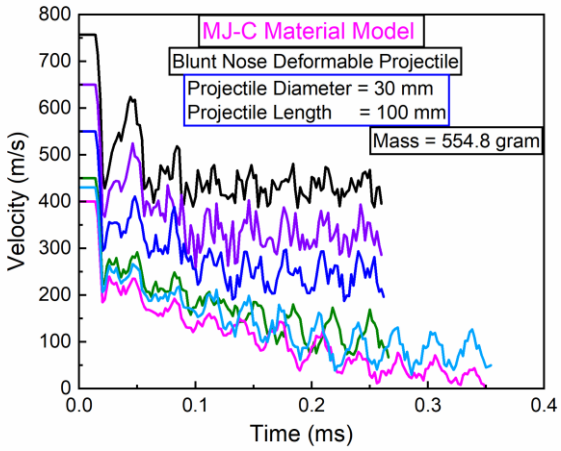

Fig. 6.7 Blunt nose deformable projectile velocity vs time graph via MJ-C material model

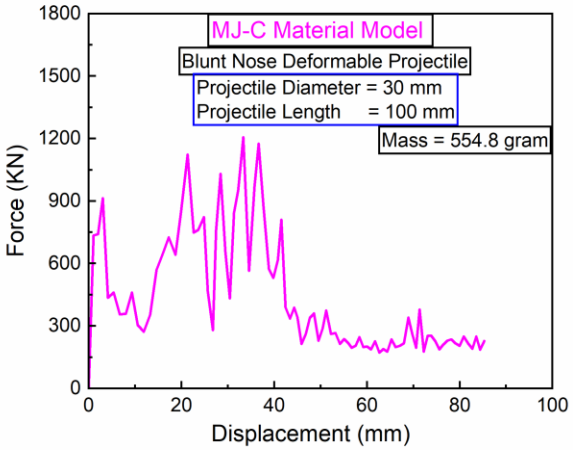

Fig. 6.8 Blunt nose deformable projectile force vs displacement graph via MJ-C material model

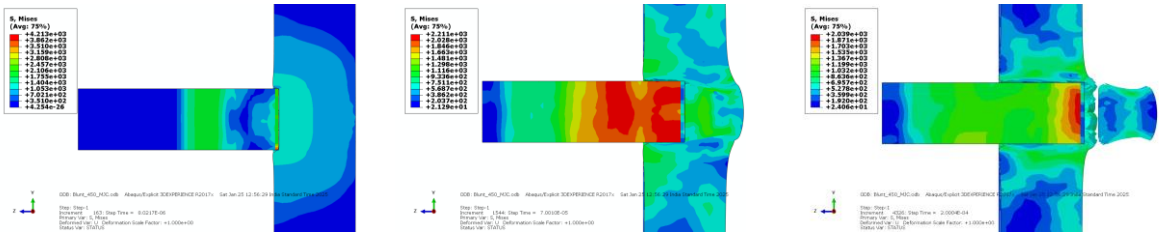

(a) **(b)** **(c)**

Fig. 6.9 Von-Mises stress profile at different time period at 450 m/s striking velocity and plug removal at final stage.

Upon impact with the target plate, the projectile experiences a sudden reduction in velocity, as illustrated in Fig. 6.9a(at time t = 4.96e – 06 s). During the initial penetration phase, significant velocity fluctuations are observed. These fluctuations gradually diminish as the projectile moves deeper into the target plate.

The observed fluctuations can be attributed to the element erosion mechanism. When the projectile strikes the target, elements at the contact interface undergo plastic deformation. If the plastic strain in an element exceeds the predefined failure criterion, the element is eroded and removed from the simulation. However, some elements that have not yet reached the failure threshold remain in contact with the projectile, causing variations in the velocity profile.

At higher impact velocities, the fluctuations are more pronounced due to rapid and successive element erosion events. As the velocity decreases, the fluctuations become less significant. Additionally, at lower velocities, the target plate exhibits increased resistance to penetration, leading to a distinct change in the velocity profile.

6.2.3 Comparison of results of three nose shapes

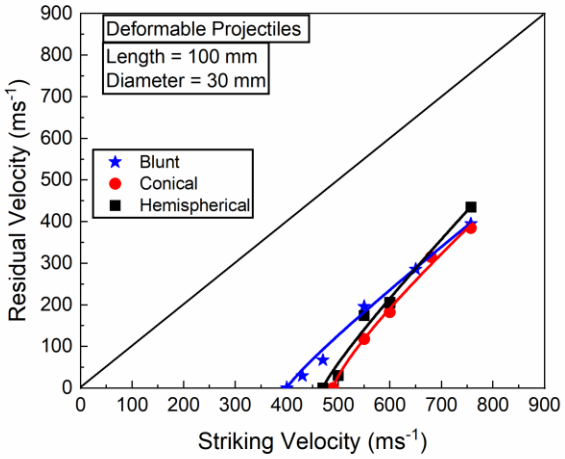

Fig. 6.10 Lambert-Jonas equation fitting for different nose shapes projectiles

Table 6.1 Lambert's-Jonas equation parameters comparison

Nose Shapes	a	p
Blunt	0.87	1.13
Conical	0.77	1.28
Hemispherical	0.86	1.19

The relationship between striking and residual velocity for different nose shapes is shown in Fig. 6.10. Among the three nose shapes, the blunt-nosed projectile experiences the least ballistic resistance from the plate. However, it exerts the highest force on the plate compared to the other two projectile configurations. At a striking velocity of 757 m/s, the hemispherical-nosed projectile exhibits the highest residual velocity, as observed in Fig. 6.10. Table 6.1 presents a comparison of the Lambert-Jonas equations for different nose shapes. Initially, only in the case of the blunt-nosed projectile does the plate offer maximum resistance, leading to a sudden decrease in velocity, as illustrated in Fig. 6.11.

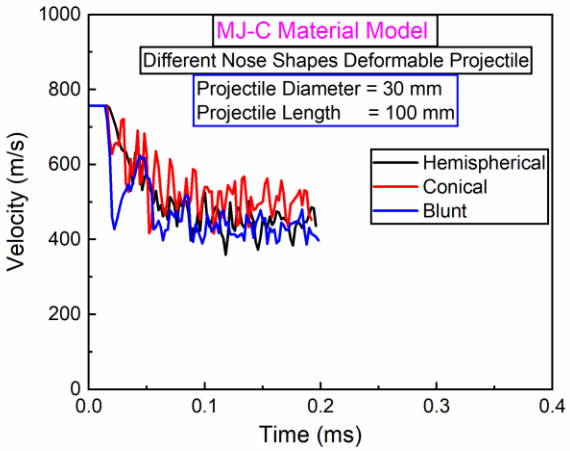

Fig. 6.11 Different nose shape velocity vs time profile comparison at 757 m/s velocity

The inlet and exit hole configurations vary across the three projectile types, as shown in Fig. 6.12. In the case of the blunt-nosed projectile, no neck formation occurs on the inlet side, whereas the other two configurations exhibit neck formation. On the exit side of the plate, the blunt-nosed projectile causes minimal plastic deformation, while the conical and hemispherical projectiles induce greater plastic deformation. The blunt-nosed projectile produces a large and heavy plug, whereas the hemispherical-nosed projectile generates a much smaller plug. The plug formed by the conical-nosed projectile splits into two parts.

The significance of these observations lies in understanding the perforation mechanics of different projectile nose shapes and their impact on target plates, which is crucial for applications in ballistics, impact engineering, and protective structures. Here's why this study matters:

a. Ballistic Resistance & Plate Performance

The blunt-nosed projectile experiences the least ballistic resistance from the plate, meaning it penetrates more easily than the other two shapes. The hemispherical-nosed projectile achieves the highest residual velocity, indicating it retains more energy after perforation. The blunt-nosed projectile exhibits an intermediate behavior between the hemispherical and conical shapes.

b. Force Transmission & Structural Damage

The blunt-nosed projectile exerts higher force, leading to significant stress concentration and higher initial resistance from the plate. The absence of neck formation in the blunt-nosed projectile suggests a different failure mechanism compared to conical and hemispherical projectiles.

c. Material Deformation & Plug Formation

The blunt-nosed projectile produces a larger, heavier plug, indicating that shear-dominated failure occurs in the plate. This is crucial for applications involving controlled perforation (e.g., industrial punching, armor design). The conical-nosed projectile plug splits into two, showing a mixed failure mode involving both shear and ductile fracture. The hemispherical-nosed projectile produces the smallest plug, suggesting gradual material displacement rather than abrupt shearing, which could influence protective armor design by distributing impact energy over a larger area.

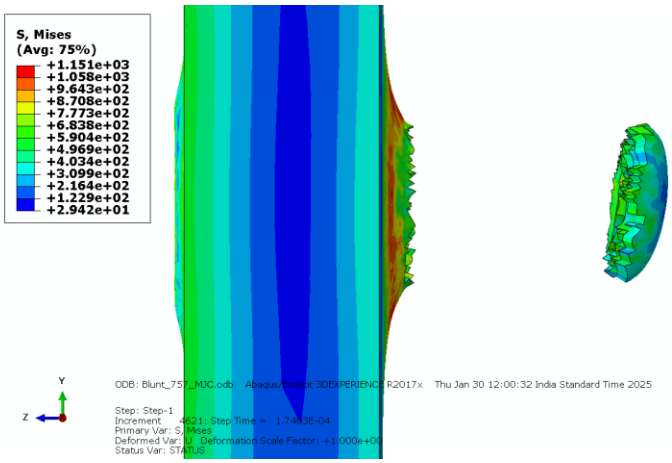

(a)

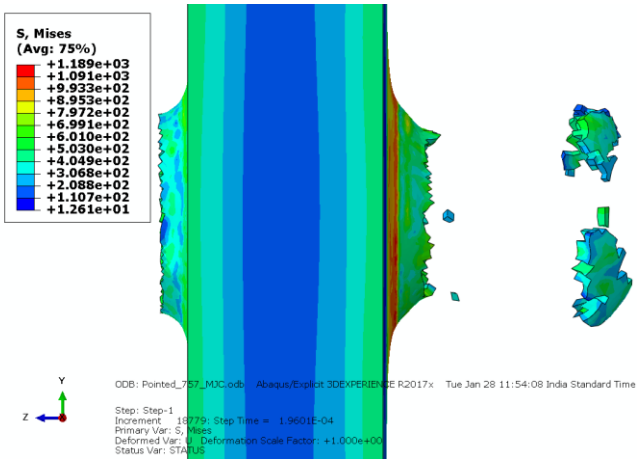

(b)

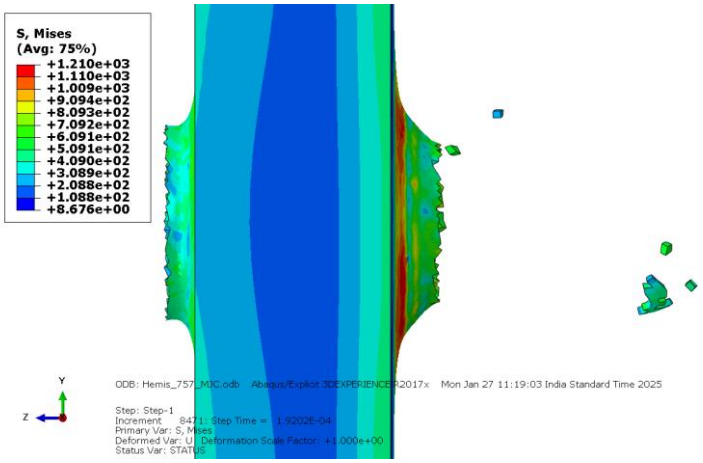

(c)

Fig. 6.12 Inlet and exit hole profile by (a) Blunt (b) Conical (c) Hemispherical nose shapes projectile

6.3 Effect of microstructure on ballistic performance

6.3.1 Heat Treatment of Armour Steel

The ballistic resistance of the armour steel as received is estimated by FE simulation using appropriate material model and compared with experimental results. The ballistic resistance of the material depends upon the elasto-plastic properties of the material. The elasto-plastic properties of the material can be changed by heat treatment in various ways. Identification of suitable heat treatment protocol to enhance the ballistic resistance is one of the area of interest for practical application. Considering such a need the as received material is heat treated with various

austenitizing temperature to achieve varied elasto-plastic properties. Tensile testing for each heat treated steel have been done to measure elasto plastic properties. FE simulation for estimating ballistic resistance for each heat treated steel is also performed to identify optimum heat treatment of the given steel for highest ballistic resistance. Armour steel heat-treated at 4 different temperature ranging from 800°C to 950°C, two different quenching medium was used i.e oil quenching and ice quenching followed by tempering with a tempering temperature of 350°C and hold time of 150 mins.

Table 6.2 Heat Treatment table for armour material

S.No.	Operation	Equipment	Temperature of Heating (°C)	Time of soaking (mins)	Quenching/cooling
1.	Hardening	Furnace	800 850 900 950	60	Oil (Servo quench)
2.	Oil Quenching	Oil bath	≤ 40 (oil)	10-15	-do-
3.	Ice Quenching	Ice in a bucket	-	15-20	-do-
4.	Tempering	Furnace	350,360	150	Air

The Johnson-Cook material model equation are as follows.

$$\sigma\ (\varepsilon^{p}, \dot{\varepsilon^{p}},\ T) = [A+B(\varepsilon^{p})^{n}]\ [1+C\ln(\frac{\dot{\varepsilon^{p}}}{\dot{\varepsilon_{0}}})][1-(T^{*})^{m}]$$

J-C model is described by five material parameters of which A, B and n are fundamental elasto plastic properties which are highly influenced by microstructure [18,19] of the material. Rate sensitivity parameter C and temperature sensitivity m are also influenced by the microstructure but not significantly [18,20]. Considering the degree of influence and burden of experiment A, B and n are determined for different microstructure in this study. The elasto-plastic material properties (A, B, n) in J-C material model are extracted from the experimental tensile tests for different heat treated material. The value of A is determined from the yield stress for the test at reference strain rate (10^{-4} s^{-1}) and reference temperature. B & n are extracted from the fitted equation between (σ - A) vs plastic strain of tensile test results at at reference strain rate (10^{-4} s^{-1}) and reference temperature.

6.3.2 Experimental Results

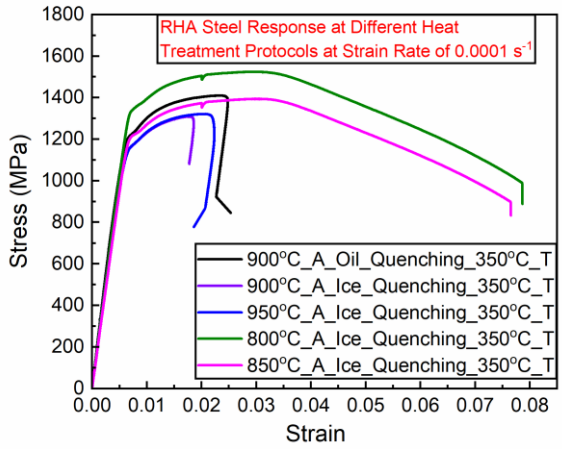

Fig. 6.13 RHA steel response under different heat treatments schedules

Table 6.3 Mechanical properties at RT for armour steel Austenitizing temperature: 900°C, Oil Quenched and Tempering temperature: 350°C, hold time 150 mins

Strain Rate s^{-1}	Specimen No.	Specimen Specification		Elastic Modulus	Yield Strength at 0.2% offset	Ultimate strength
		Diameter	Gauge Length	GPa	MPa	MPa
10^{-4}	3	5.75	37.68	207	1227.14	1406.37

Table 6.4 Mechanical properties at RT for armour steel, Austenitizing temperature: 900°C, Ice Quenched and Tempering temperature: 350°C, hold time 150 mins

Strain Rate s^{-1}	Specimen No.	Specimen Specification		Elastic Modulus	Yield Strength at 0.2% offset	Ultimate strength
		Dia.	Gauge Length	GPa	MPa	MPa
10^{-4}	1	5.94	38.21	211	1190.18	1309.06

Table 6.5 Mechanical properties at RT for armour steel Austenitizing temperature: 800°C, oil quenched and tempering temperature: 350°C, hold time 150 mins

Strain rate s^{-1}	Specimen No.	Specimen Specification		Elastic Modulus	Yield Strength at 0.2% offset	Ultimate strength
		Dia.	Gauge Length	GPa	MPa	MPa
10^{-4}	1	5.94	38.70	209.2	1366.022	1517.71

Table 6.6 Mechanical properties at RT for armour steel Austenitizing temperature: 950°C, oil quenched and tempering temperature: 350°C, hold time 150 mins

Strain Rate s^{-1}	Specimen No.	Specimen Specification		Elastic Modulus	Yield Strength at 0.2% offset	Ultimate strength
		Diameter (mm)	Gauge Length (mm)	GPa	MPa	MPa
10^{-4}	1	5.94	37.98	204.8	1194.977	1320.99

Table 6.7 Mechanical properties at RT for armour steel Austenitizing temperature: 850°C, Oil Quenched and Tempering temperature: 350°C, hold time 150 mins

Strain Rate (s^{-1})	Specimen No.	Specimen Specification		Elastic Modulus	Yield Strength at 0.2% offset	Ultimate strength
		Diameter (mm)	Gauge Length (mm)	GPa	MPa	MPa
10^{-4}	1	5.94	39.79	197.78	1251.081	1385.59

Table 6.8 Variation of the J-C material model parameters with austenitizing temperature, quenching medium and tempering temperature

Austenitizing Temperature (°C)	Quenching Medium	Tempering Temperature (°C)	A	B	n
800	Oil Quenching	350	1366.247	1780.11	0.588
850	Oil Quenching	350	1251.081	1963.203	0.613
900	Oil Quenching	350	1245.89	2136.14	0.56
900	Ice Quenching	360	1190.18	3419.77	0.69
950	Oil Quenching	350	1194.947	2338.591	0.63106

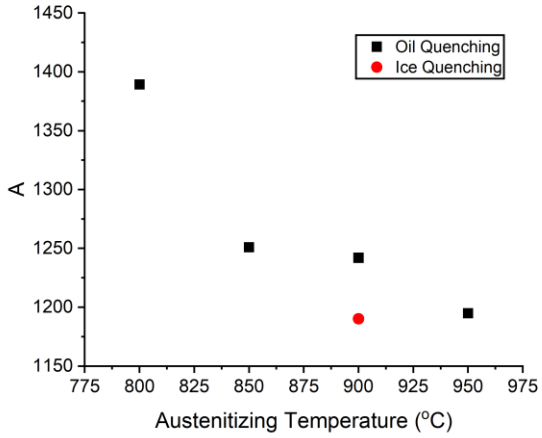

Fig. 6.14 Variation of parameter A with austenitizing temperature

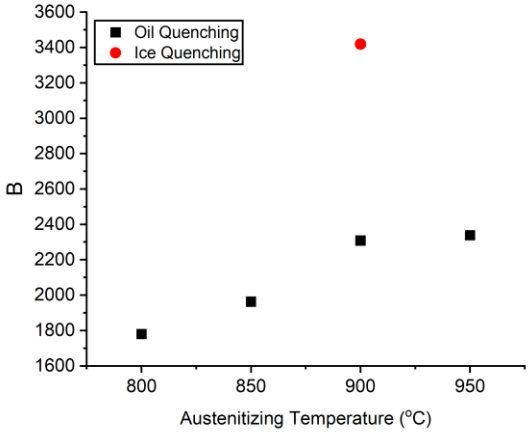

Fig. 6.15 Variation of parameter B with austenitizing temperature

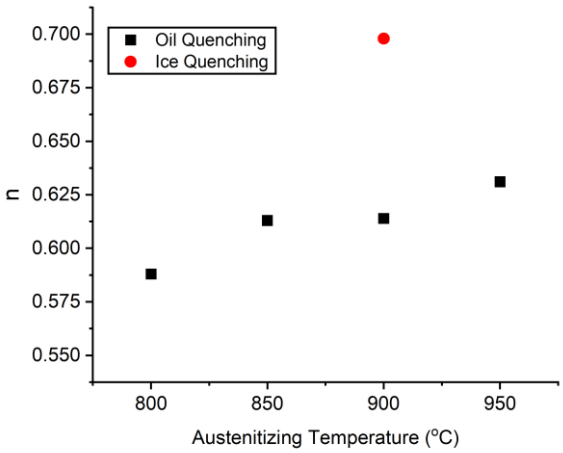

Fig. 6.16 Variation of parameter n with austenitizing temperature

6.4 Observations

- The Fig. 6.13 presents the stress-strain response of armour steel under different heat treatment protocols at a $\dot{\varepsilon}$ of $0.0001\ s^{-1}$. The graph compares five different heat treatment conditions, including variations in austenitizing temperatures (800 °C to 950 °C) and quenching media (oil and ice), followed by tempering at 350 °C. The stress-strain curves reveal distinct mechanical behaviors influenced by these thermal treatments. Typically, higher austenitizing temperatures and ice quenching result in higher peak stress, indicating increased strength due to refined microstructures. However, variations in ductility suggest a trade-off between strength and toughness. The ultimate tensile strength, yield point, and fracture point vary among the treatments, emphasizing the role of heat treatment in tailoring mechanical properties. This analysis provides valuable insights into optimizing the heat treatment process for enhanced structural performance of armour steel in protective applications.
- The stress vs strain curve at different strain rates is shown in Fig. 6.13. The elongation or ductility of the steel gets reduced but the strength is increased as compared to the as received armour steel. For as received armour steel the ultimate stress comes at strain 0.06 but for heat treated steel it remains at 0.03. The J-C material model parameters are listed in Table. 4. Further comparison on ballistic performance by heat treatment of armour steel discussed in next section.
- The value of yield stress A is decreasing exponentially with the increase of austenitizing temperature as shown in Fig. 6.14.

- The value of parameter B goes on increasing with the increase of austenitizing temperature as shown in Fig. 6.15.
- The value of parameter n increases with rising austenitizing temperature as shown in Fig. 6.16.
- The value of parameter B and n for ice quenching medium is greater than oil quenching medium with same austenitizing temperature 900 °C. However, the value of A is less compared to oil quenched cooling.

The effect of heat treatment on tensile properties are apparent from the tensile test results and the variation of material properties A, B, n also presented in the plot. The ballistic resistance of armour plate depends on the values of A, B, n in a combined manner. The combined effect on ballistic resistance can be assessed by FE simulation of ballistic impact of armour plates with varied input of A, B, n. Initially FE simulations have been done assuming projectile as rigid to characterise the armour resistance against different A, B, n and also verified with deformable projectiles. By analysing the FE simulation results best option of heat treatment is identified based on highest ballistic resistance and then ballistic limit is identified for that heat treatment process.

6.5 FE simulation for ballistic resistance of armour of different heat treated (oil quenched) steel with rigid projectile

FE simulations are done for the following four type of heat treatment schedule. The rigid projectile of stepped shape as discussed in previous Chapter 5 of length 100 mm and diameter 30 mm has taken into consideration. The plate thickness is 40 mm. The mesh size, boundary conditions and value of friction coefficient are same as discussed in previous Chapter 5.

Table. 6.9 Heat treatment schedule of RHA steel

Austenitizing Temperature (°C)	Quenching Medium	Tempering Temperature (°C)	A	B	n
800	Oil Quenching	350	1389.247	1780.11	0.588
850			1251.081	1963.203	0.613
900			1245.89	2136.14	0.56
950			1194.947	2338.591	0.63106

a. Inlet velocity: 1300 m/s

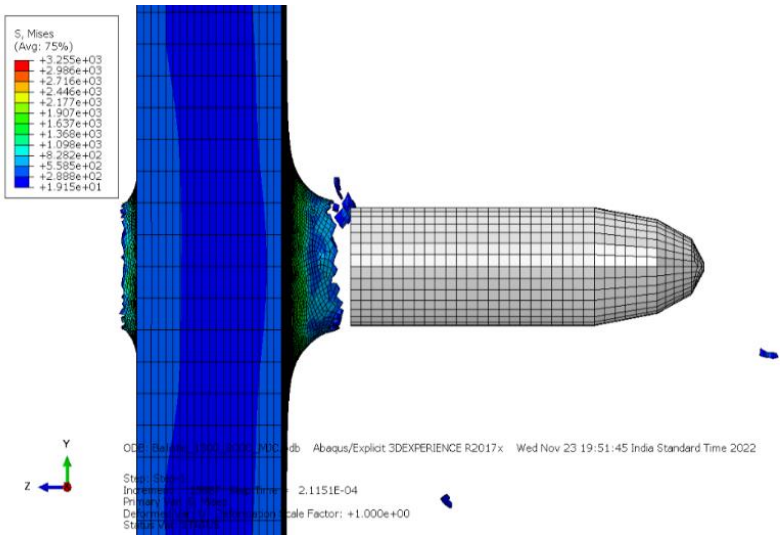

Fig. 6.17 Deformed shape of armour plate with rigid projectile at 1300 m/s (800°C austenitizing) (thickness of plate = 40 mm)

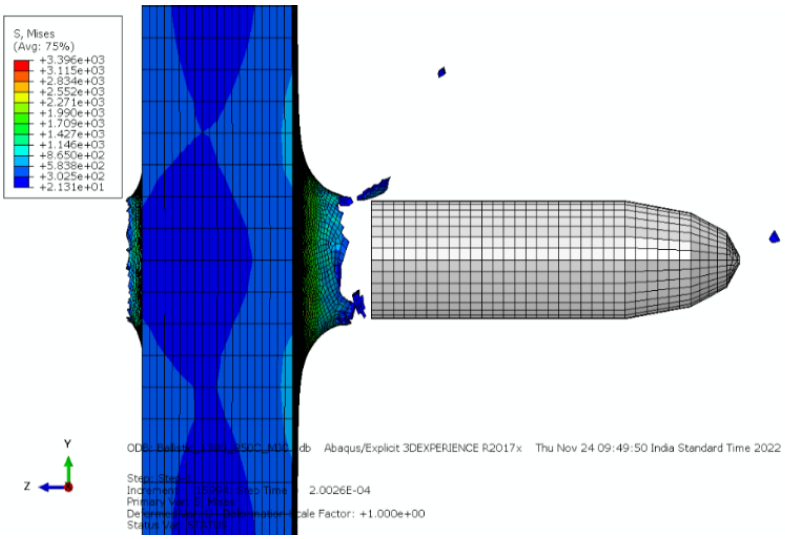

Fig. 6.18 Deformed shape of armour plate with rigid projectile at 1300 m/s (850°C austenitizing) (thickness of plate = 40 mm)

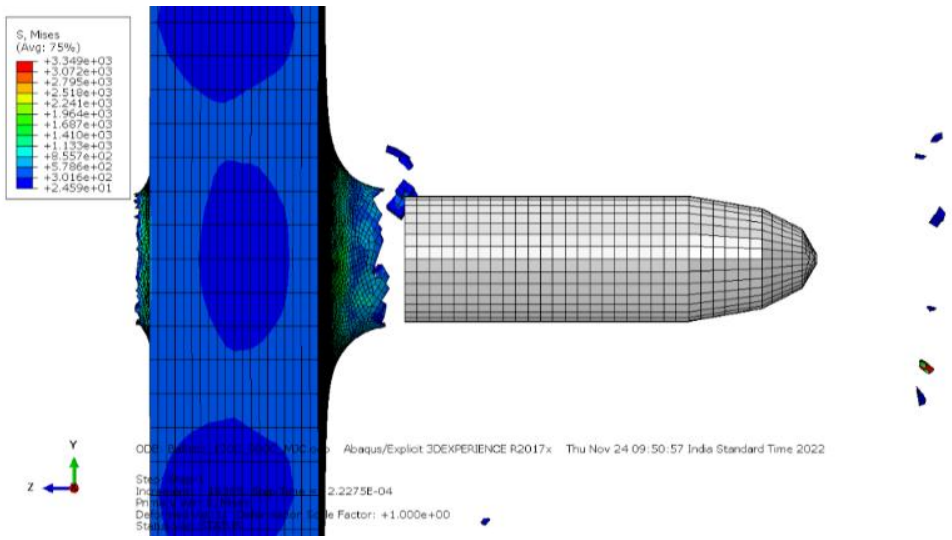

Fig. 6.19 Deformed shape of armour plate with rigid projectile at 1300 m/s (900^{o}C austenitizing) (thickness of plate = 40 mm)

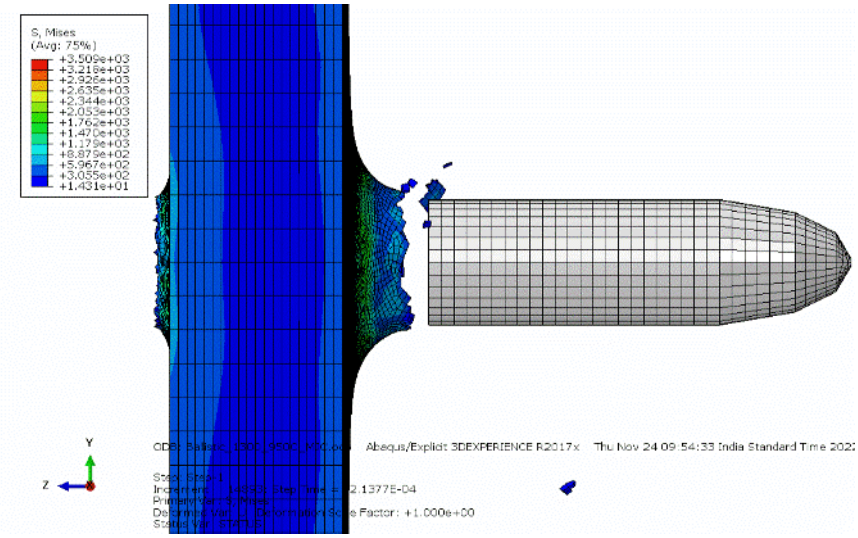

Fig. 6.20 Deformed shape of armour plate with rigid projectile at 1300 m/s (950^{o}C austenitizing) (thickness of plate = 40 mm)

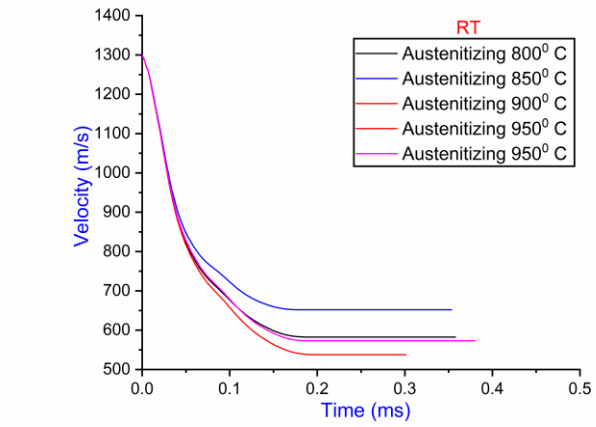

Fig. 6.21 Velocity vs time plot for as received geometry rigid projectile at 1300 m/s

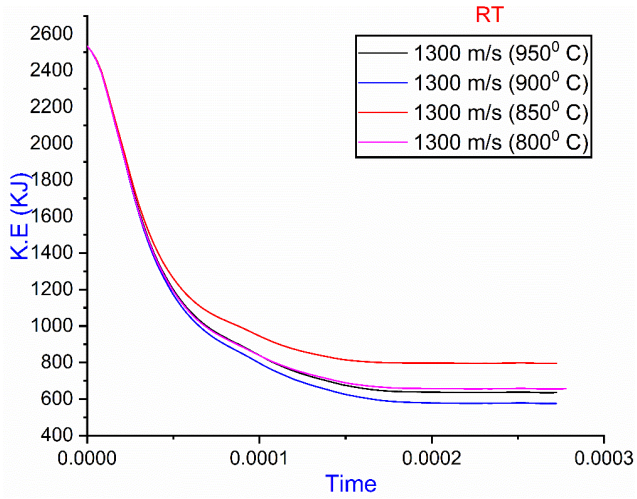

Fig. 6.22 Kinetic energy vs time plot for as received geometry of rigid projectile at 1300 m/s and at different austenitizing temperature

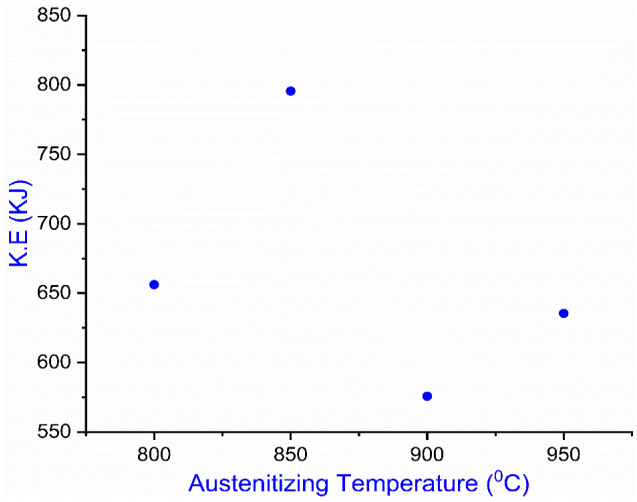

Fig. 6.23 Residual kinetic energy vs austenitizing temperature plot

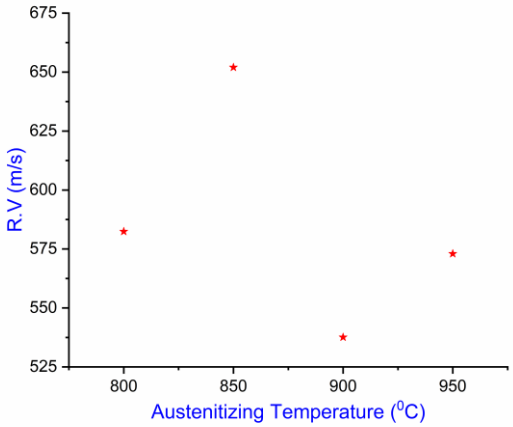

Fig. 6.24 Residual velocity vs austenitizing temperature plot

Ballistic performance index (B.P.I.) = $\frac{Change\ in\ kinetic\ energy}{Initial\ kinetic\ energy}$

$$= \frac{\frac{1}{2}mV_i^2 - \frac{1}{2}mV_r^2}{\frac{1}{2}mV_i^2}$$

$$= 1 - \left(\frac{V_r}{V_i}\right)^2$$

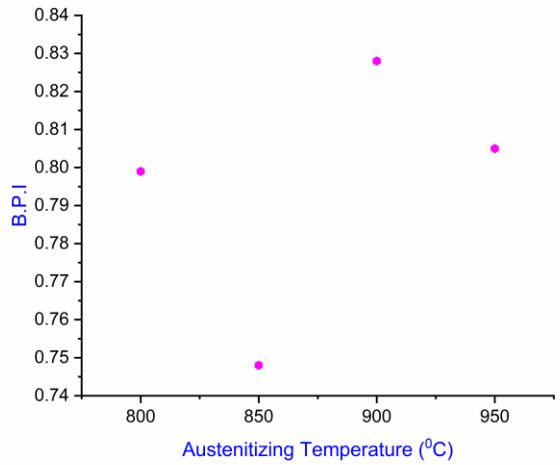

Fig. 6.25 Ballistic performance index (B.P.I) vs austenitizing temperature plot for rigid projectile

From the above results comparing the exit velocity of the projectile entering with the same striking velocity of 1300 m/s it is clear that material heat treated with austenising temperature as 900°C shows maximum ballistic resistance. Hence Several FE simulations for assessing ballistic resistance for this material with different striking velocity is done and the velocity at which the exit velocity approaches to zero is identified.

6.5.1 Comparison of ballistic resistance between as received and heat treated steel at 900°C

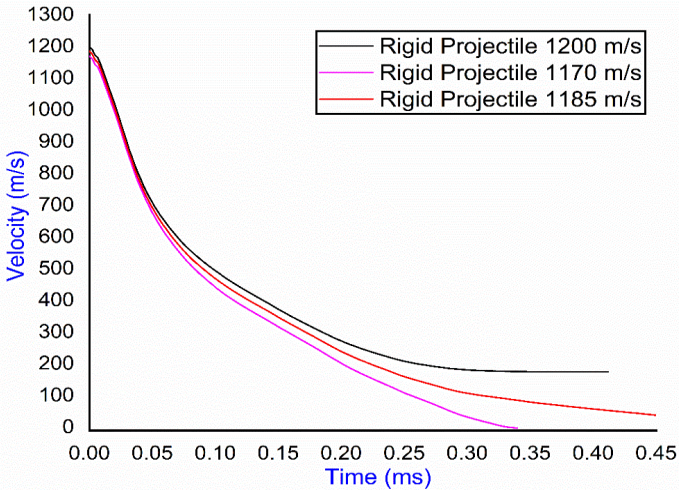

Fig. 6.26 Velocity vs time plot for as received geometry rigid projectile of 900 °C austenitizing temperature.

6.5.2 FE simulation for ballistic resistance assuming projectile as rigid for as received armour material

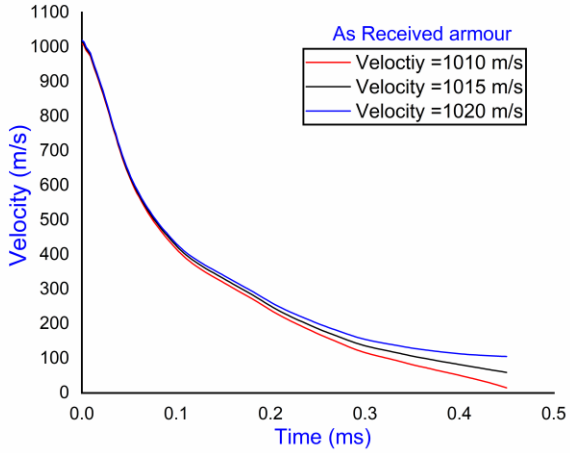

Fig. 6.27 Ballistic limit for as received armour material with rigid projectile by MJ-C material model

6.5.3 S.V vs R.V for rigid projectile and as received armour material by MJ-C model

Table. 6.10 Striking vs residual velocity for rigid projectile

S.V m/s	R.V m/s
1010	0
1015	60
1020	105.47

FE simulations with different striking velocities for the armor plate of 40 mm thick heat treated with austenitizing temperature 900^{o}C and tempering temperature 350^{o}C and hold time 150 min have been done to find the striking velocity for zero residual velocity. Thus, the ballistic limit is found to 1185 m/ sec. In previous simulation, the ballistic limit of 40 mm armor plate of 'as received' material was found to be 1015 m/sec. Therefore, the heat treatment process of autenitizing temperature 900^{o}C with tempering at 350^{o}C for a hold time of 150 min increases the ballistic limit by 14%.

6.5.4 FE simulation for ballistic resistance or armour of different heat-treated steel with deformable projectile:

Inlet velocity: 1000 m/s

Material: FE simulations are done using ABAQUS for following four heat treated steel.

Table. 6.11 Heat treatment schedule of RHA steel

Austenitizing Temperature (°C)	Quenching Medium	Tempering Temperature (°C)	A	B	n
800	Oil Quenching	350	1389.247	1780.11	0.588
850	Oil Quenching	350	1251.081	1963.203	0.613
900	Oil Quenching	300	1245.89	2136.14	0.56
950	Oil Quenching	350	1194.947	2338.591	0.63106

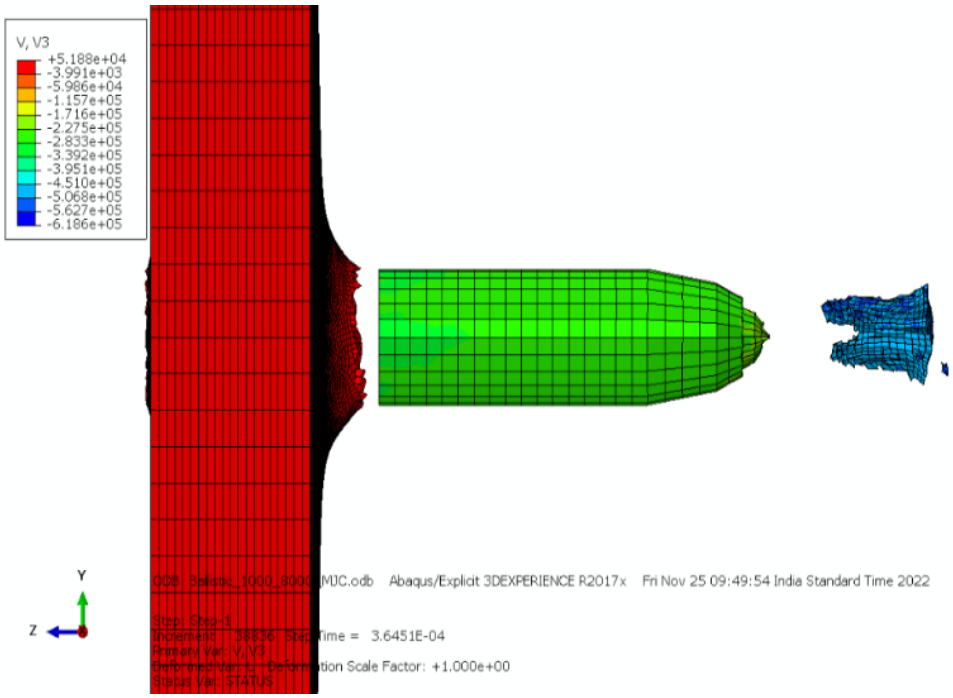

Fig. 6.28 Deformed shape of Armor plate and projectile at 1000 m/s (800°C austenitizing)

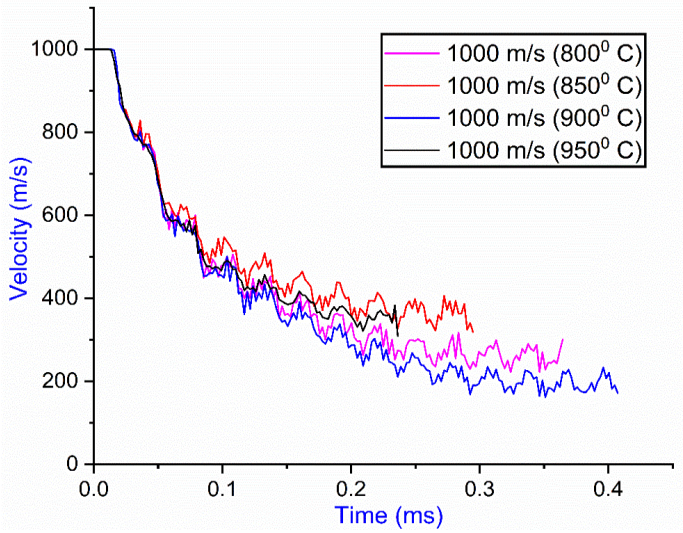

Fig. 6.29 Velocity vs time plot for as received geometry deformable projectile at 1000 m/s

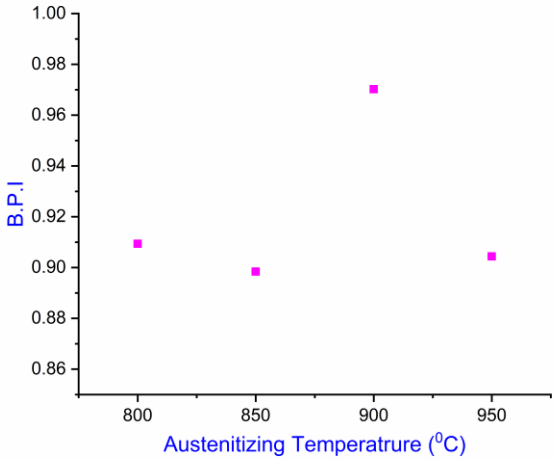

Fig. 6.30 Ballistic performance index (B.P.I) vs austenitizing temperature plot for deformable projectile

6.6 Conclusion

- From these above observations it is apparent that not only the nose shape of the projectile but also the projectile type (rigid or deformable) is responsible for the type of failure pattern (eg. petalling, plug etc.).
- As received armour plate can stop completely pointed tip projectile at 800 m/s but other type of projectile easily penetrates the plate.
- Since, experiments are not conducted for the different projectile nose shape, simulated results for the residual velocity, the type and amount of plug ejection and ductile hole enlargement could not be compared with experimental results. But from simulation results several significant observations are possible which are important for application.
- The conical projectile penetrates the target in a less efficient way than blunt and hemispherical projectile when the target thickness is 40 mm.
- There is much difference in modes of failure for all projectile configurations. The blunt projectile produces heavy plug mass, the hemispherical projectile have plug mass less than produces by blunt projectile whereas conical projectile shattered the plug into pieces.
- Projectile nose shape blunt shape have lowest ballistic limit. The conical nose shape have higher ballistic limit and hemispherical nose shape have slightly lower than conical nose shape.
- At a velocity of 757 m/s, the hemispherical projectile exits the plate with a greater residual velocity than both the blunt and conical projectiles.
- After multiple simulations, it is concluding that one sort of mesh size for a certain type of material model does not appear to be acceptable for other types of material models. As a result, different mesh sizes are employed in our investigation for three types of material models in both armour plate and projectile.
- Proper heat treatment of armour steel can improve the ballistic properties and therefore improve the ballistic limit also.
- Fig. 6.30 depicts the ballistic performance index is also highest with deformable projectile in case of heat treated steel austenized at temperature of 900^{o}C.
- The MJ-C material model is used to execute the improved parametric studies on armour plate simulation for verifying ballistic limits.

References

[1] T. Borvik, O.S. Hopperstad, T. Berstad, M. Langseth, Perforation of 12mm thick steel plates by 20mm diameter projectiles with flat, hemispherical and conical noses - Part II: Numerical simulations, Int. J. Impact Eng. 27 (2001) 37–64. https://doi.org/10.1016/S0734-743X(01)00035-5.

[2] T. Borvik, O.S. Hopperstad, T. Berstad, M. Langseth, Perforation of 12mm thick steel plates by 20mm diameter projectiles with flat, hemispherical and conical noses Part I: Experimental study, Int. J. Impact Eng. 27 (2002) 19–35. https://doi.org/https://doi.org/10.1016/S0734-743X(01)00034-3.

[3] C.J. Hu, P.Y. Lee, J.S. Chen, Ballistic performance and microstructure of modified rolled homogeneous armor steel, J. Chinese Inst. Eng. Trans. Chinese Inst. Eng. Ser. A/Chung-Kuo K. Ch'eng Hsuch K'an 25 (2002) 99–107. https://doi.org/10.1080/02533839.2002.9670684.

[4] R.F.R. and T.W. Ipson, Ballistic Perforation Dynamics, J. Appl. Mech. 30 (1963) 384–391.

[5] T.W. Ipson, R.F. Recht, Ballistic-penetration resistance and its measurement, Exp. Mech. 15 (1975) 249–257. https://doi.org/10.1007/bf02318057.

[6] A.L. Wingrove, The influence of projectile geometry on adiabatic shear and target failure, Metall. Trans. 4 (1973) 1829–1833. https://doi.org/10.1007/BF02665409.

[7] S.S. Santoshi OHTE, Hiroyasu YOSHIZAWA, Norimasa CHIBA, Impact strength of steel plates struck by projectiles, Bull. JSME 25 (1982) 2278–2281.

[8] N.K. Gupta, M.A. Iqbal, G.S. Sekhon, Effect of projectile nose shape, impact velocity and target thickness on deformation behavior of aluminum plates, Int. J. Solids Struct. 44 (2007) 3411–3439. https://doi.org/10.1016/j.ijsolstr.2006.09.034.

[9] A. Arias, J.A. Rodríguez-Martínez, A. Rusinek, Numerical simulations of impact behaviour of thin steel plates subjected to cylindrical, conical and hemispherical non-deformable projectiles, Eng. Fract. Mech. 75 (2008) 1635–1656. https://doi.org/10.1016/j.engfracmech.2007.06.005.

[10] A. Rusinek, J.A. Rodríguez-Martínez, R. Zaera, J.R. Klepaczko, A. Arias, C. Sauvelet, Experimental and numerical study on the perforation process of mild steel sheets subjected to perpendicular impact by hemispherical projectiles, Int. J. Impact Eng. 36 (2009) 565–587. https://doi.org/10.1016/j.ijimpeng.2008.09.004.

[11] P.K. Jena, B. Mishra, M. RameshBabu, A. Babu, A.K. Singh, K. SivaKumar, T.B. Bhat, Effect of heat treatment on mechanical and ballistic properties of a high strength armour steel, Int. J. Impact Eng. 37 (2010) 242–249. https://doi.org/10.1016/j.ijimpeng.2009.09.003.

[12] T. Jankowiak, A. Rusinek, P. Wood, A numerical analysis of the dynamic behaviour of sheet steel perforated by a conical projectile under ballistic conditions, Finite Elem. Anal. Des. 65 (2013) 39–49. https://doi.org/10.1016/j.finel.2012.10.007.

[13] W.R. Whittington, A.L. Oppedal, S. Turnage, Y. Hammi, H. Rhee, P.G. Allison, C.K. Crane, M.F. Horstemeyer, Capturing the effect of temperature, strain rate, and stress state

on the plasticity and fracture of rolled homogeneous armor (RHA) steel, Mater. Sci. Eng. A 594 (2014) 82–88. https://doi.org/10.1016/j.msea.2013.11.018.
[14] D.E. Tria, R. Trebinski, On the influence of fracture criterion on perforation of high-strength steel plates subjected to armour piercing projectile, Arch. Mech. Eng. 62 (2015) 157–179. https://doi.org/10.1515/meceng-2015-0010.
[15] J. Trajkovski, R. Kunc, V. Pepel, I. Prebil, Flow and fracture behavior of high-strength armor steel PROTAC 500, Mater. Des. 66 (2015) 37–45. https://doi.org/10.1016/j.matdes.2014.10.030.
[16] S. Dey, T. Børvik, O.S. Hopperstad, J.R. Leinum, M. Langseth, The effect of target strength on the perforation of steel plates using three different projectile nose shapes, Int. J. Impact Eng. 30 (2004) 1005–1038. https://doi.org/10.1016/j.ijimpeng.2004.06.004.
[17] Z. Zhang, Y. Wu, F. Huang, Effect of stress triaxiality cut-off value in the fracture criterion on predicting the ballistic behavior of Al2024-T351 plate impacted by blunt- hemisphere- and ogival-nosed projectiles, J. Mater. Res. Technol. 25 (2023) 138–165. https://doi.org/10.1016/j.jmrt.2023.05.186.
[18] P.K. Jena, P. Ponguru Senthil, K. Siva Kumar, Effect of tempering time on the ballistic performance of a high strength armour steel, J. Appl. Res. Technol. 14 (2016) 47–53. https://doi.org/10.1016/j.jart.2016.02.002.
[19] P.K. Jena, M.A.M. Manickam, S. Venketachari, S.C. Srivastava, A. Srivastava, S. Chakrabarty, K. Siva Kumar, Microstructure, mechanical, ballistic property evaluation of RHA steel produced by continuous-casting route, J. Appl. Res. Technol. 18 (2020) 1–13. https://doi.org/10.22201/ICAT.24486736E.2020.18.1.927.
[20] B. McDonald, H. Bornstein, A. Ameri, J.P. Escobedo-Diaz, A.C. Orifici, High strain rate and high temperature response of two armour steels: Experimental testing and constitutive modelling, EPJ Web Conf. 183 (2018) 3–8. https://doi.org/10.1051/epjconf/201818301022.

Chapter -7

Application of a fracture based failure model to simulate the failure of armour plates subjected to ballistic impact

Abstract

Characterisation of material for armour resistance against ballistic impact by simulation is highly effective to reduce experimental cost and also to search for a new material or to identify optimum microstructure of some existing material. Material models suitable for simulation of ballistic impact of a typical RHA steel plate has been explained in the previous chapters and was coupled with the Johnson-Cook damage model to assess the armour resistance. The results regarding exit velocity at exit and ballistic limit show good matching with experimental results. But exact failure pattern was not attempted to be modelled in the simulation. In this chapter, fracture toughness based failure model has been implemented in couple with the existing material model for high strain rates to simulate the failure pattern in ballistic impact. The dominant failure patterns of plate are bulging and petalling. While bulging can be simulated by plastic strain based failure model petalling requires crack growth simulation using fracture mechanics. Thus, developing reliable numerical models for ballistic impact of armour plates in the practical scenario are the motivation of this work. Such a comprehensive simulation tool will help in reduction in testing, designing and identification of appropriate material to be used as armour plate.

7.1 Introduction

In ballistic field, armour hardness is prime characteristic to resist against kinetic energy of projectiles. But this increase in strength is usually accompanied by a decrease in ductility. Therefore, the knowledge of their fracture behaviour of the armour material is very important to understand their ballistic performance. Gailly and Petit [1] performed plate impact experiment in a spalling configuration. They showed that the spall stress is not a good criterion to characterize the fracture mechanism involved during ballistic impact. However, it was shown that it gives valuable information on crack nucleation. Moreover, in this study it was observed that the fracture mode remained ductile even at very high velocities. Further, Gailly and Pineau [2] investigated crack propagation and crack arrest in a very high strength armour steel. They made ring shaped specimen geometry in which the variation of fracture toughness K with crack length follows a bell shape curve. This is useful to investigate both crack initiation, rapid crack propagation and crack arrest. The ring specimen was initially devised for brittle cleavage fracture. A special emphasis is led on the effect of crack velocity on crack arrest fracture toughness. The mechanics of dynamic

fracture based on elasto-dynamic analysis of mathematically sharp plane cracks and the observed terminal velocities or the phenomenon of crack branching are satisfactorily explained by K. Ravi [3–5] in 1982. The issue was looked into from both macroscopic and microscopic perspectives. He wrote a number of articles [6,7] on these issues. J.F. Kalthoff [8] conducted research on high rate fracture-toughness data that were acquired under impact loading circumstances by assessing the local crack-tip reaction immediately at the crack instability moment. Kobayashi et al. [9] used Server's equation to calculate tensile properties from Charpy tests. Fengchun et al. [10] presented a novel method for measuring the dynamic fracture toughness K_{ID} utilizing HPS bar loaded instrumented Charpy impact test. Nikita Kazarinov et al. [5,11,12] used the finite element method with embedded incubation time fracture criterion to simulate dynamic crack growth under quasi-static loading. The results of the simulation allow one to draw the conclusion that the incubation time approach is a useful tool for predicting the onset and propagation of fractures at different loading rates. J. Bleyer [13] employed the variational phase-field model in 2016 to study the dynamic propagation of cracks. The dynamics of simulated crack propagation interacting with heterogeneities reveal the intricate relationship between branching mechanisms and heterogeneity patterns. D.T. Ngo [14] concentrated on the quasi-static loading conditions and dynamic crack propagation in brittle materials in laboratory experiments. The cohesive zone model, which has been implemented in ABAQUS software, was used in conjunction with the extended finite element method. It was discovered that this method permits consideration of the damage process zone preceding the crack tip, and the crack path can be arbitrarily chosen without regard to mesh dependencies. Their simulations demonstrated both dynamic crack growth and the propagation of stress waves caused by fracturing. In 2021, Sha Li and colleagues [15] used the quasi-static material point method to model the propagation of cracks. To simulate the opening of cracks, they used the theory of multiple displacement fields in the vicinity of the cracks. The maximum circumferential stress criterion is used to predict the growth of the crack after the interaction integral method has computed the stress intensity factors (SIFs) based on the realisation of crack opening. Using the incubation time of brittle fracture concept introduced by Petrov and Morozov, V. Bratov [16] worked on numerical simulations of dynamic crack propagation and fracture of initially intact media in the same year. He also presents examples of simulations using the finite element method with embedded dynamic fracture criterion. Examples include the evolution of fracture zones in initially intact media, propagation arrest, and dynamic fracture initiation. It was shown that this method could provide a precise explanation for every type of phenomenon related to dynamic fracture. One salient characteristic of the method that sets it apart from most other dynamic fracture criteria is the requirement to include an extra material parameter, namely the experimentally assessed ease of fracture in order to forecast fracture dynamics.

The reviewed literature does not explicitly address the impact of cracks on the ballistic resistance of armour plates, particularly for typical Rolled Homogeneous Armour (RHA) steel. This chapter presents a numerical investigation into the influence of dynamic fracture toughness on the ballistic resistance of armour steel. Experimental studies were conducted to determine the relevant fracture toughness parameters.

This study evaluates the ballistic resistance of armour plates by analysing the effects of crack presence, number, size, and orientation. The impact resistance of the plate is assessed for different crack configurations through simulations. The results show how these factors influence structural integrity and residual strength. However, due to the complexity of crack morphology, it is challenging to replicate these conditions experimentally, making direct validation difficult. Despite this limitation, the simulation results provide valuable insights into how cracks affect the plate durability. If cracks or defects caused by initial impacts can be detected using Non-Destructive Testing (NDT) methods, these findings can help estimate the remaining strength of the armour plate after multiple uses.

7.2 FE modelling of internal Crack in armour plate using damage model

7.2.1 Viscoplastic material model and Failure model

The Johnson-cook [17] viscoplastic material model is used for expressing the equivalent stress as a function of strain, strain rate and temperature and the J-C failure model is used to capture the failure criterion in RHA steel plate. These material models are already discussed in detail in Chapter 2. This model is widely used by several researchers [18–20] for simulation of dynamic behaviour of steel over wide range of $\dot{\varepsilon}$ and T.

7.2.2 Crack growth Modelling in armour plate under ballistic impact

In a thick armour plate without a preexisting long crack, crack nucleation will occur in defect spots. The defects are of microstructural or geometrical in nature. Therefore, a homogeneous plate with uniform initial defects can be deformed as bulging and there after ductile holing in a ballistic impact. The cracks along with non-uniform plastic deformation will occur when there is a heterogeneity in the in the initial defect distribution. The cracks nucleate in maximum defect sites. Micro cracks joins to form a long crack which propagates according to the principles of fracture mechanics. This process alters the stress distribution (stress shielding etc) of the plate. A real life defect distribution should be statistical in nature. However, in order to study the stress and plastic strain distribution with cracks and non-uniform plastic deformation (like petalling) few cases with known defect distributions are studied in this Chapter.

7.2.3 Geometric modelling of damage for FE analysis in ABAQUS Explicit solver

7.2.3.1 Modelling of Petals

i. *Plate thickness* - 20 mm
ii. *Projectile type* - 30 mm rigid ogive KE projectile

For simulating the petal formation in armour plate during ballistic impact the heterogeneity in the damage distribution in the armour plate is to be introduced. Geometric modelling of damage distribution is done by introducing four patches as shown in Fig. 7.1. Four radial patches with 90^{o} apart are incorporated with larger initial damage to ensure faster damage evolution along these patches. The crack should generate and propagate along the weaker sections of the plate. Four radial strips of sectional area *A* are drawn on the plate cross section. The depth of the strip is throughout the thickness of the plate. These strips are considered to be the weaker sections of the plate. The material points falling in the strips are marked as type 1 whereas the material points out side strips are marked as type 0.

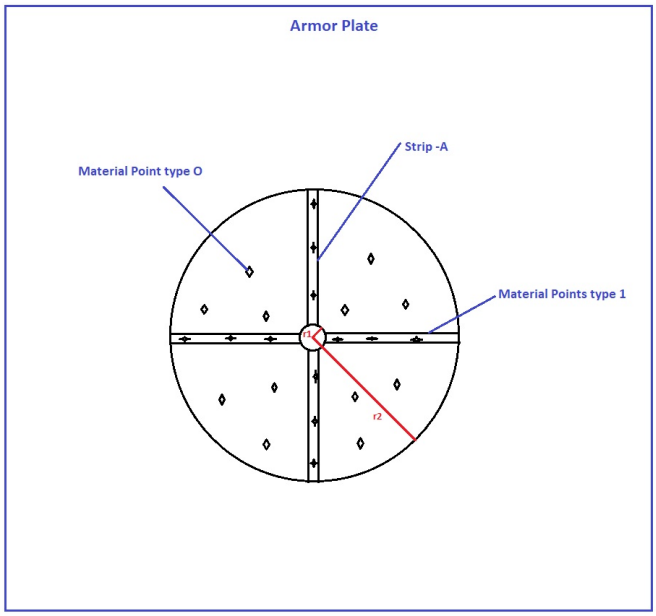

Fig. 7.1 Armour Plate with radial strips

The nonlinear damage growth law used in the simulation is:

$$\dot{D} = \frac{1-\exp(-mD_0)}{(1-\mathrm{D})(\varepsilon_f - \varepsilon_{p,d})}\dot{\varepsilon}_{pl} \qquad (7.1)$$

Where, D_0 = initial damage

m= material constant

D= current damage

ε_f= fracture strain

$\varepsilon_{p,d}$ = threshold strain taken as strain at ultimate stress

It is evident from damage growth law that damage growth rate depends on initial damage D_0. Type 1 material points (material points within the strips) are assigned with higher initial damage ($D_0 = 0.05$) and the rest of the material points are assigned with $D_0 = 0.001$. The element deletion criterion is either that the damage value reaches the critical damage $D_{cr} = 0.5$ or the equivalent plastic strain reaches the critical value of fracture strain which is 1.2 obtained from experiment [21–24], whichever occurs earlier. The critical plastic strain criterion is kept along with the critical damage criterion to limit the excessive distortion of the element during plastic deformation. The crack generated in the strip is shown in Fig. 7.2.

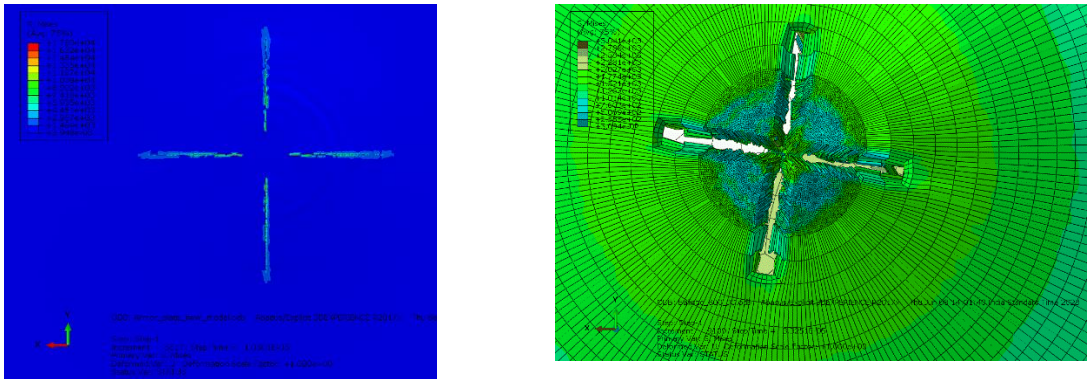

Fig. 7.2 (a) Radial crack generated in armor plate (b) Crack generated in 20mm thick armour plate before petalling

The radial lengths of the strips are limited between r_1=1 mm to r_2=10 mm in radial direction (Fig. 7.1). Thus, four symmetrical radial cracks of size 10mm are generated. Further deformation bends the slices between the radial cracks giving the shape of 4 petals. Fig. 7.3 shows the petals formed in 20 mm thick armour plate by a 30 mm K.E ogive nosed projectile. The plot of velocity vs time shows that residual velocity is quite high when crack of sufficient size is present as shown in Fig. 7.4.

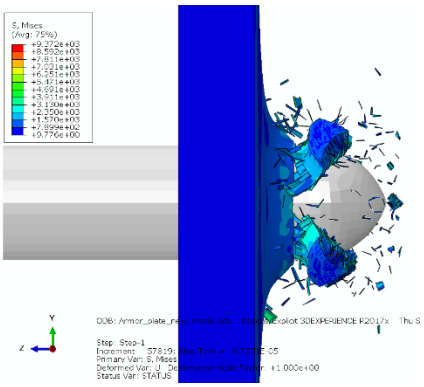

Fig. 7.3 Petals form in armour plate

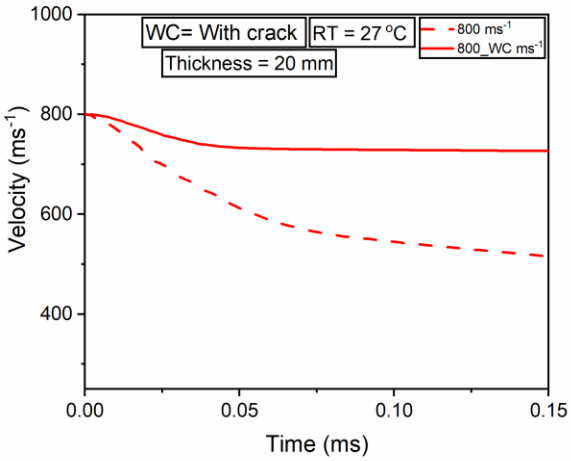

Fig. 7.4 Velocity vs time graph at 800 m/s

7.2.3.2 Modelling of radial cracks as brittle inserts in armour plate

i. *Plate thickness* - 20 mm
ii. *Projectile type* - 30 mm rigid ogive KE projectile

In this model the strips are considered as brittle inserts. Only modification is that the depths of the inserts are not throughout the thickness of the plate. It is restricted to 10 mm from the rear side of the plate. The material points on the inserts are marked as type 1 where the rest of the material points are marked as type 0. Since the inserts are brittle in nature, the type 1 material points are stressed elastically and type 0 material points are deformed elastic-plastically as predicted by Johnson-Cook material model. The element deletion criterion for brittle inserts are critical stress

criterion, $\sigma \geq \sigma_{cr.}$ here, σ_{cr} is the critical stress for failure as determined from fracture tougness as follows

$$K_{IC} = \sigma_{cr}\sqrt{\pi a} \tag{7.2}$$

Where σ_{cr} = critical stress and a = crack length.

K_{IC} = Critical stress intensity factor or fracture toughness determined from fracture tests. In the above equation, crack length 'a' is considered as the minimum size of element in FE mesh. Knowing K_{IC} and 'a', the critical stress σ_{cr} can be determined from above equation. The value of Maximum positive principal stress is compared with the value of critical stress to control failure of the element. For type 0 material points (material points other than inserts) ductile failure criterion (critical plastic strain criterion) is used. In this simulation the value of the critical plastic strain is taken as 1.2 (120%).

7.3 Fracture toughness testing for armour material (RHA) at different loading rates

The event of ballistic impact is highly dependent on loading rate and hence the fracture toughness of the armour to be used in simulation is considered as loading rate dependent. The nature of the fracture behaviour may be brittle or ductile depending on the loading rate. Hence both the types of fracture toughness tests (*J-R* and K_{IC}) are explored for the armour material. Test matrix for fracture (*J-R* and K_{IC}) was planned according to the requirement. Due to the constraint of availability of material, one-quarter of CT specimens were designed for testing. One-quarter compact tension (CT) specimens extracted from armour plate are fabricated in accordance with ASTM E-1820 [25]. The dimensions of the above-mentioned one-quarter CT specimens are as shown in Fig. 7.5. All the fracture (*J-R* and K_{IC}) tests were conducted in INSTRON servo-hydraulic machine.

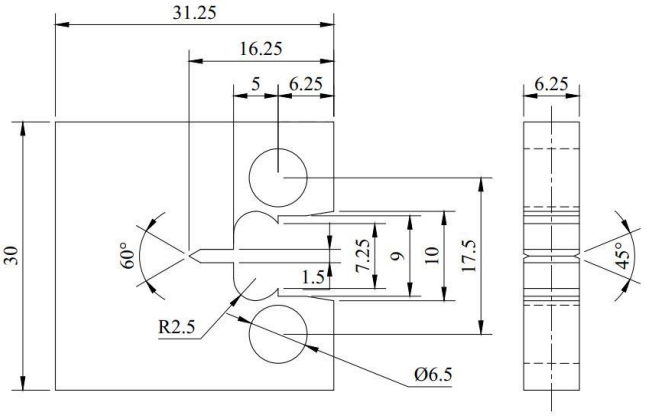

Fig. 7.5 Geometry of CT specimen used for Fracture Testing.

7.3.1 Crack Size Measurement with Unloading Compliance Method

Crack size can be measured during experiment with elastic compliance technique on compact specimen through crack opening displacement measured along the unloading line. The load line displacement (Δ) is composed of two components, i.e. Δ_{nc} and Δ_c as shown in the following equation.

$$\Delta = \Delta_{nc} + \Delta_c \tag{7.3}$$

Where Δ_{nc} is load line displacement in absence of crack and Δ_c is the additional displacement due to crack. For compact specimen, $\Delta_{nc} = 0$ because it is measured at the crack mouth. Now, to measure the crack length a fifth order polynomial was established as per ASTM E1820 between normalized crack length (a/W) and unloading compliance as shown in the following equations:

$$\frac{a}{W} = 1.00196 - 4.06319U_{LL} + 11.242U_{LL}^2 - 106.043U_{LL}^3 + 464.335U_{LL}^4 - 650.677U_{LL}^5 \tag{7.4}$$

where,

$U_{LL} = \frac{1}{1+\sqrt{Z_{LL}}}$ and $Z_{LL} = \frac{BE\Delta}{P}$

$B =$ Specimen thickness (For side grooved specimen, $B_e = B - \frac{(B-B_N)^2}{B}$)

B_N = Net thickness, E = Young's Modulus and Δ/P = Compliance.

7.3.2 Fatigue Pre-cracking

Before fracture testing a fatigue pre-cracking is necessary to obtain a sharpened crack of desired size and straightness which eliminates the effect of a machined starter notch in specimen *K*-calibration.

- Before fatigue pre-cracking the notch length was measured as 11.25 mm ($a/W = 0.45$).
- The length of the fatigue pre-crack should not be less than 5% of the initial notch length (a_0) as per ASTM E1820.
- As per ASTM E1820 the fatigue pre-crack length should be such that the a/W ratio is restricted within the range of 0.45 to 0.70 for J and δ determination. So the pre-crack length was maintained at 1.25 mm for all the specimens so that the a/W ratio could be fixed with 0.5. Therefore, after pre-cracking the total crack length was obtained as 12.5 mm.
- Fatigue pre-cracking was conducted in load control mode.

- During the ΔK decreasing test, the stress intensity factor range (ΔK) for a given crack length is determined using the following equation provided by the test system.

$$\Delta K = \frac{\Delta P}{B\sqrt{W}} \frac{(2+\propto)}{(1-\propto)^{1.5}} (0.886 + 4.64 \propto -13.32 \propto^2 + 14.72 \propto^3 - 5.64 \propto^4) \quad (7.5)$$

Where, $\propto = \frac{a}{W}$

- To avoid increase in K_{max} and ΔK with crack length, as observed in constant load cycle fatigue pre-cracking, the load range was gradually reduced during pre-cracking using the following equation:

$$\Delta K = \Delta K_0 \exp[C(a - a_0)] \quad (7.6)$$

Where, $C = \frac{1}{\Delta K} \frac{d\Delta K}{da} > -0.08\,\text{mm}^{-1}$, ΔK_0 and a_0 are the initial ΔK and crack size respectively.

- The initial value of maximum fatigue load was adopted as 30% of P_f with a force ratio of 0.1 according to ASTM E1820.

$$P_f = \frac{0.4Bb_0^2\sigma_{FS}}{(2W+a_0)} \quad (7.7)$$

Where, $\sigma_{FS} = \frac{(\sigma_{YS}+\sigma_{TS})}{2}$

7.3.3 Fracture Testing (*J-R* curve)

ASTM E1820 describes the standard procedure for fracture testing and thereby evaluation of fracture toughness (J_{IC}) of metal. Fracture toughness is measured at the onset of ductile crack growth following the *J-R* resistance curve obtained from monotonically loading the specimen up to failure. Crack growth has been measured with the help of unloading compliance method as described earlier. The test specimens were made side-grooved to 20% net depth to restrain the crack growth along the plane of symmetry for the minimization of short crack growth and to avoid shear lips or crack tunnelling as per ASTM E1820. At first the fatigue pre-cracking has been done on the above mentioned side-grooved specimen following the same procedure as mentioned before but in this case the pre-crack length was maintained at 1.25 mm for all the specimens so that the a/W ratio could be fixed with 0.5. Therefore, after pre-cracking the total crack length was obtained as 12.5 mm. The objective of this test procedure is to develop a load displacement dataset

to evaluate *J-R* curve from which the fracture toughness (J_{Ic}) of a material is computed following ASTM E1820 standard procedure.

- The fracture toughness resistance curve procedure has been used to evaluate fracture toughness using COD gauge as crack growth measuring equipment.
- This process requires an elastic unloading procedure throughout the crack extension for measuring crack growth using unloading compliance method.
- The J-R fracture tests have been conducted in displacement control mode with a loading rate of 0.01 mm/s, 0.05 mm/s, 0.075 mm/s and 0.1 mm/s.
- With the help of unloading compliance method, the initial crack length (a_0) was measured within a load range from 0.5 to 1.0 times the maximum pre-cracking load which is about 2.5 kN and thereby a provisional initial crack size was determined by averaging with ten unloading-reloading sequences.
- The data acquisition software collects information related to load (P), load line displacement (LLD), and crack length (a) during the testing process.
- For high-temperature fracture testing, a ceramic-lined furnace is integrated with the machine, allowing the test to reach the required temperature. A 30-minute soaking period is then applied to ensure uniform temperature distribution across the test samples.

7.3.4 J_{IC} Computation

In addition to measuring load (P), load line displacement (LLD) and crack length (a), the value of J was computed through the following procedure and thereby the J -Δa curve was obtained from which the fracture toughness (J_{IC}) was determined. For computation of J with respect to crack growth (Δa), the most convenient way is to divide J into its elastic and plastic components as shown in the following equations.

$$J = J_{el} + J_{pl} \tag{7.8}$$

Where elastic component of J (J_{el}) is computed from elastic stress intensity factor K as shown in the following equation.

$$J_{el} = \frac{K^2\,(1-\nu^2)}{E} \tag{7.9}$$

For side grooved specimen the stress intensity factor is computed from the following equation, where 'B' is the gross thickness (B = 6.25 mm) and 'B_N' is the net thickness (B_N = 5 mm).

$$K = \frac{P}{\sqrt{BB_N W}} f(a/W) \tag{7.10}$$

According to ASTM E1820, the plastic component of J (J_{pl}) is computed from the plastic area (A_{pl}) under the load–displacement curve as shown in the following equation. Where 'η' is a dimensionless constant, 'B_N' is the net thickness and 'b_0' is the initial uncrack ligament length.

$$J_{pl} = \frac{\eta A_{pl}}{B_N b_0} \tag{7.11}$$

After obtaining the *J-Δa* curve, two exclusion lines were drawn with a slope of $M\sigma_F$ at different crack extensions of 0.15 mm and 1.5 mm respectively. Where σ_F is the flow stress defined by averaging a material yield and ultimate strength. The value of $'M'$ here is taken as 2 according to ASTM E-1820 standard. All those data points that fall within the exclusion lines were fitted to a power law regression. The regression is a power law in the form of

$$J = C_1(\Delta a)^{C_2} \tag{7.12}$$

Where, C_1 and C_2 are constants coefficient and exponent respectively for regressions and are not based on measurements. After regression analysis, considering a crack extension of 0.2 mm, an offset line is drawn taking the same slope of $M\sigma_F$. The point at which this offset line will intersect the power law fitting curve, that intersecting points define as J_Q and Δa_Q as shown in the following Fig. 7.6. Qualification of J_Q as J_{IC}, a size independent value of elastic-plastic fracture toughness (J_{IC}) has been considered, if:

i. Thickness , $B > 25\frac{J_Q}{\sigma_Y}$,

ii. Initial uncrack ligament length , $b_0 > 25\frac{J_Q}{\sigma_Y}$,

iii. The slope of the power law regression line, $\frac{dJ}{da}$, evaluated at $\Delta a_Q$is less than σ_Y.

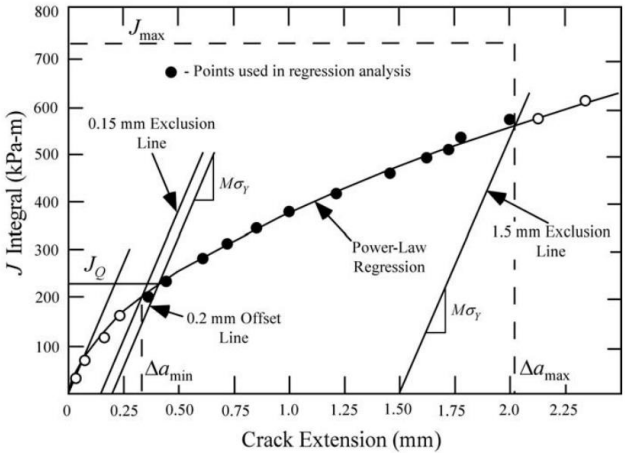

Fig. 7.6 Procedure for determination of J_{IC} from J - Δa curve [26].

7.3.5 Fracture Toughness (J_{IC}) Results (Load-Displacement Curve)

Loading Rate (mm/s)	Test Temperature (°C)	Load-Displacement Curve	Fracture Toughness (J_{IC}) (MPamm$^{0.5}$)
0.01	27	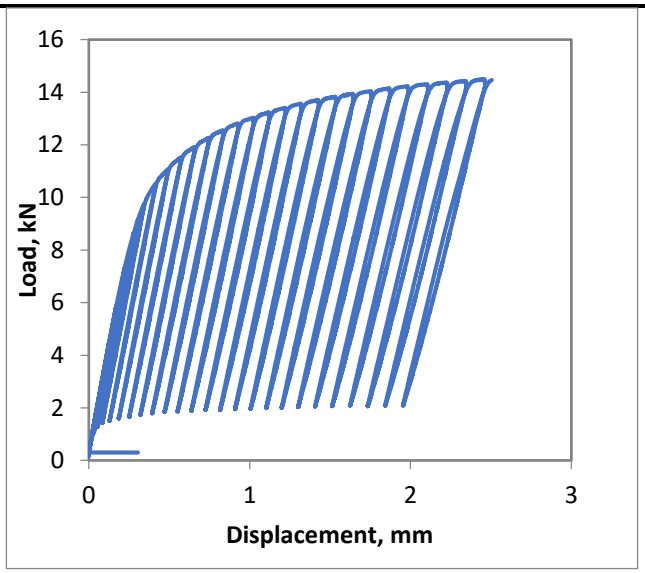	30.46
0.05	27	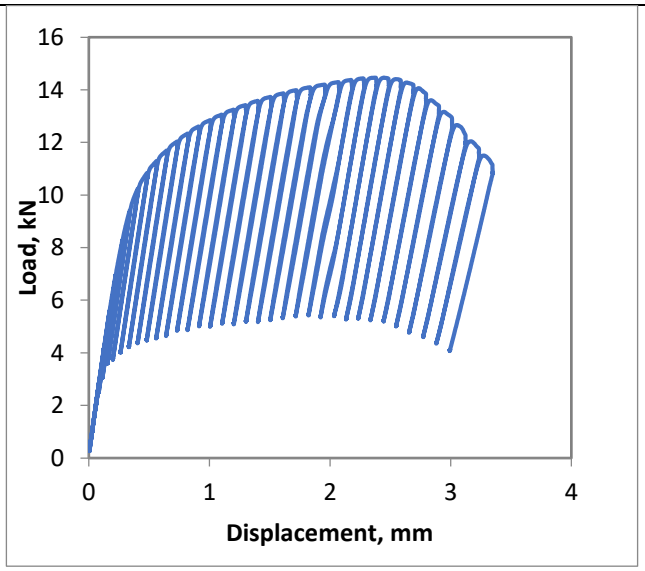	45

0.075	27	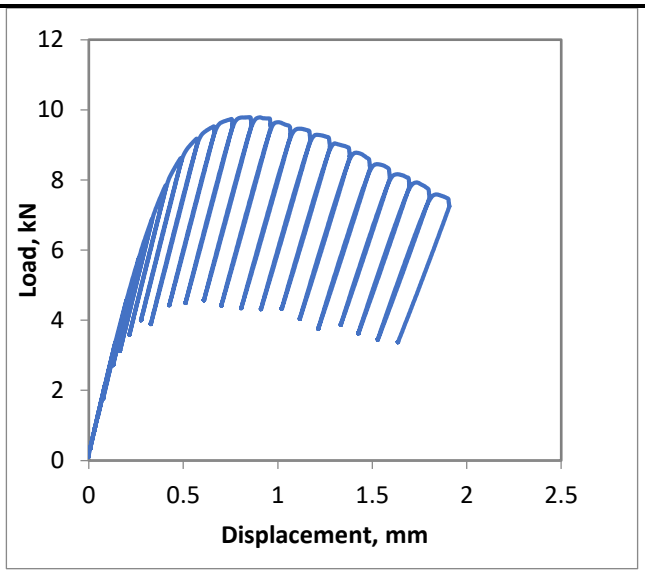	32.12
0.1	27	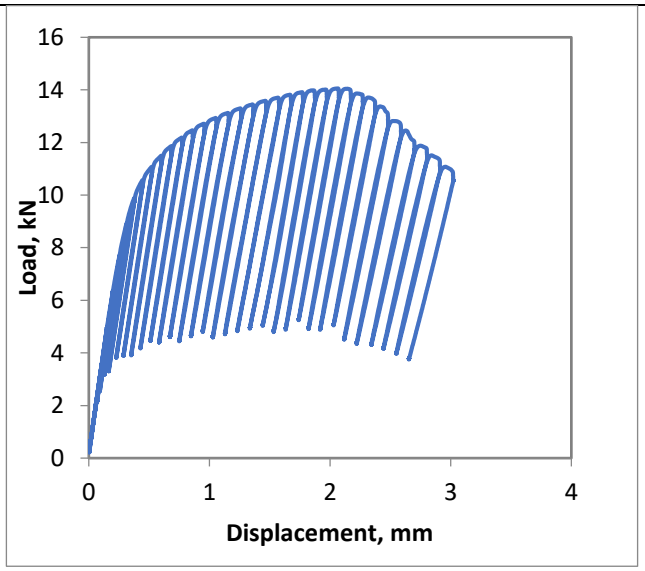	48.96

0.01	200	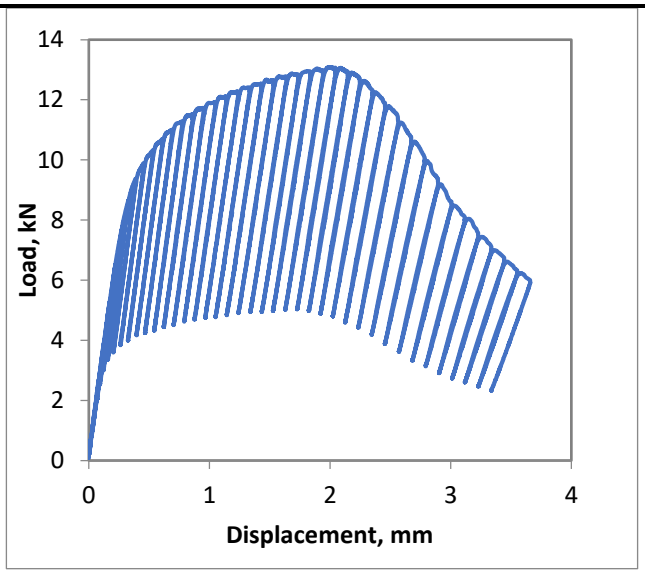	240.19
0.01	400	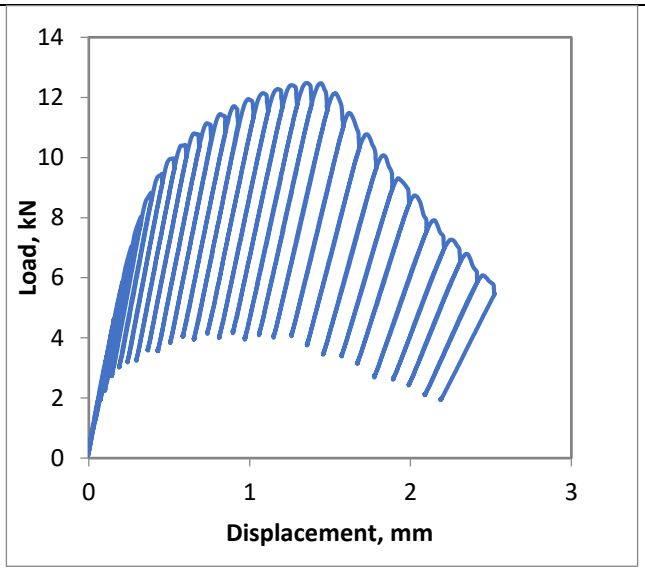	205.86

7.3.6 Fracture Toughness (J_{IC}) Results (J-R Curve)

Loading Rate (mm/s)	Test Temperature (ºC)	J-R Curve	Fracture Toughness (J_{IC}) (MPa.mm)
0.01	400	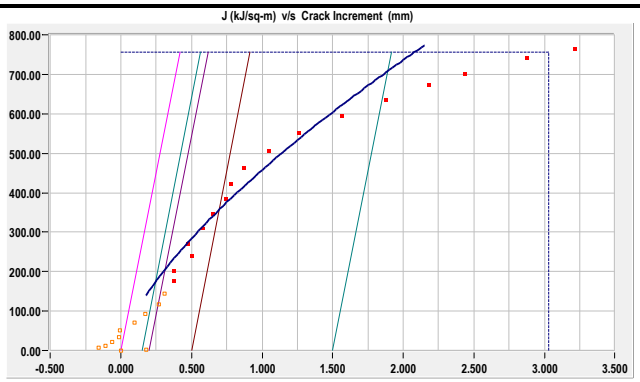	205.86

7.3.7 K_{IC} Fracture test

Material deformation behaviour can be classified as linear elastic, nonlinear elastic, or elastic-plastic**.** The choice of fracture parameter and test method depends on how the material deforms. In brittle fracture, a linear elastic zone forms around the crack tip, where initiation toughness primarily influences fracture resistance, with minimal additional resistance to crack propagation. In such cases, the energy required for crack extension beyond initiation is relatively small compared to the energy stored in the test system, leading to unstable failure without the possibility of measuring fracture resistance beyond crack initiation. As a result, fracture toughness is typically assessed as a point value and represented by the stress intensity factor (K) at crack initiation. The ASTM E399 standard is used to determine plane strain fracture toughness (K_{IC}), measuring toughness at or near the onset of crack growth.

7.3.8 K_{IC} Computation

According to ASTM E1820, plane strain fracture toughness (K_{IC}), is defined as the crack-extension resistance under mode I loading in conditions where the crack tip experiences plane strain with minimal plastic-zone adjustment. This toughness measurement is taken at the onset of crack extension (2% or less) under predominantly linear-elastic conditions. The ASTM E399 standard outlines the procedure for conducting K_{IC} testing, which requires fatigue pre-cracking to

generate a sharp crack in the specimen. The initial crack size which includes both the crack starter notch and fatigue crack, must be within 0.45 W to 0.55 W as per ASTM E399.

During testing, load and crack opening displacement are recorded. Fig. 7.7 presents three distinct load–displacement curves, each associated with a critical load P_Q. To determine P_Q and ultimately $K_{IC,}$ the 5% secant method is employed, where a secant line with a slope equal to 95% of the initial elastic loading slope is used to find P_5.

- In Type I curves, where the load–displacement graph remains smooth with minimal deviation from linearity before reaching the maximum load (P_{max}), $P_Q = P_5$.
- In Type II curves, where unstable crack growth (i.e., a pop-in) occurs before reaching P_5 and extend beyond the 5% secant line, P_Q is taken at the pop-in initiation. If the pop-in is minor and does not cross the secant line, it is disregarded.
- In Type III curves, where complete specimen failure occurs before reaching 5% nonlinearity, $P_Q = P_{max}$.

Using the $P_Q$value and the measured crack length, the conditional fracture toughness K_Q is determined through a specified equation:

$$K_Q = \frac{P_Q}{\sqrt{BB_N W}} f(a/W) \tag{7.13}$$

where, $f(a/W)$ is a geometry function that depends on the crack size to specimen width ratio a/W only. For CT specimens,

$$f(a/W) = \frac{(2+\propto)}{(1-\propto)^{1.5}} (0.886 + 4.64 \propto -13.32 \propto^2 + 14.72 \propto^3 - 5.64 \propto^4) \tag{7.14}$$

where, $\propto = \frac{a}{W}$

Since apparent toughness K_Q reduces as specimen size increases until reaching a stable lower bound, ASTM E399 imposes specimen size requirements to ensure that K_{IC} represents a valid plane strain toughness measurement. In addition to the initial crack size constraint ($0.45 \leq a/W \leq 0.55$), two validity conditions proposed by Brown and Srawley must be satisfied for K_Q to qualify as a valid K_{IC} result:

i. Thickness , $B, a > 2.5 \left(\frac{K_Q}{\sigma_Y}\right)^2$,

ii. $P_{max} \geq 1.1\, P_Q$,

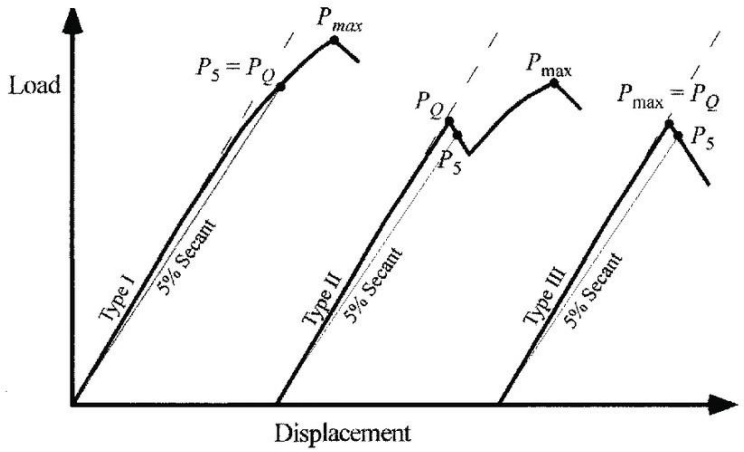

Fig. 7.7 Three typical types of load-displacement curves with the critical load P_Q defined for each type [25].

7.3.9 Fracture Toughness (K_{IC}) Results

Loading Rate (mm/s)	Test Temperature (ºC)	Load vs. Load Line Displacement (LLD) Curve	Fracture Toughness (K_{IC}) ($MPa\sqrt{m}$)
0.05	27	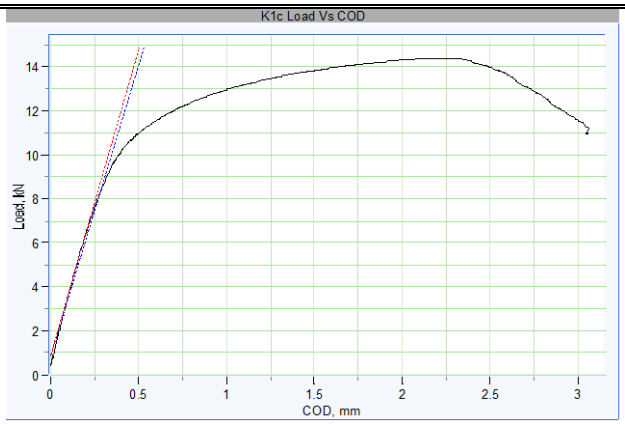	91

0.5	27	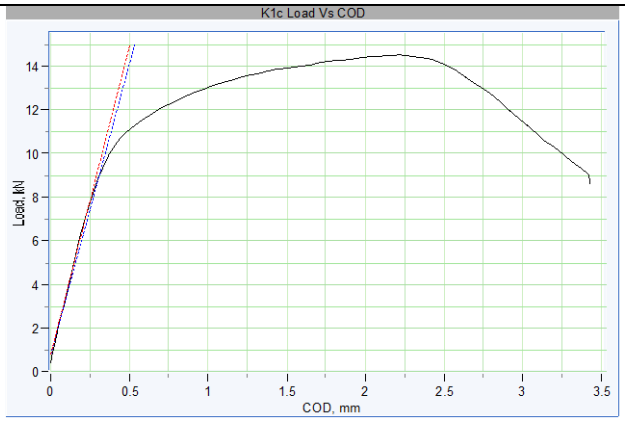	99
1.0	27	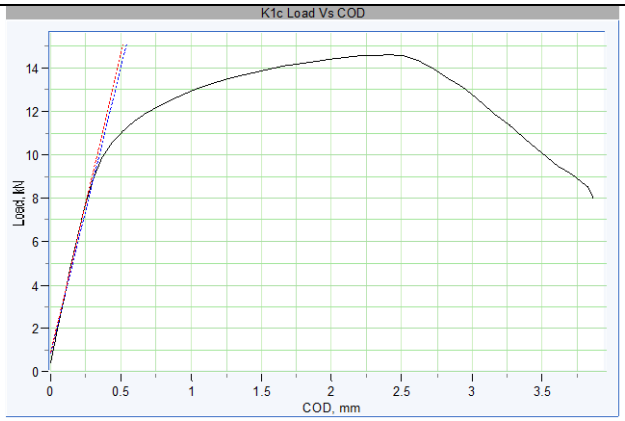	97
1.5	27	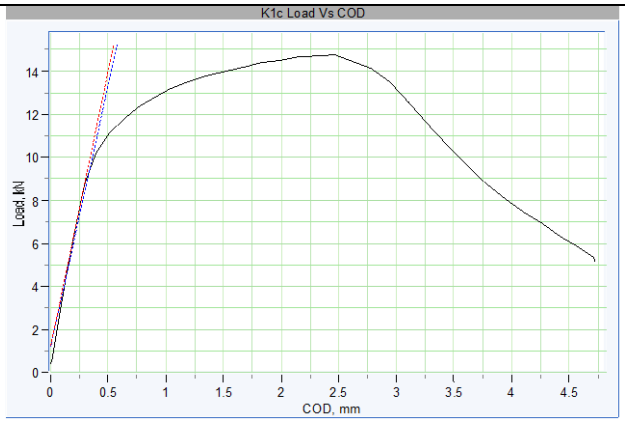	114

7.4 Crack initiation fracture toughness

In ductile–brittle transition fracture, toughness exhibits significant variability due to the ‘‘weakest link’’ failure mechanism, which initiates cleavage in these materials. In some cases, cleavage initiation toughness can be expressed using a critical elastic K_C, while in others, an elastic–plastic J-integral is necessary for an accurate assessment. For each specimen, the J-integral at cleavage onset (J_C) is (the critical value of J where brittle cleavage fracture starts in the specimen. It indicates the fracture driving force required for cleavage initiation) first determined and then converted to K_{JC}. From a J–R curve, key elastic–plastic fracture mechanics (EPFM) parameters can be extracted, including plane strain initiation toughness (J_{IC}), which qnatify crack growth resistance near the onset of stable crack growth for mode-I loading.

Since, defining crack initiation in ductile metals is challenging, different test standards adopt varied definition of initiation toughness, as discussed by Roos and Eisele. ASTM E1820 define J_{IC} at the intersection of a 0.2-mm offset line and the J–R curve, represents as J_Q in Fig. 7.7. Which illustrates the standard procedure for evaluating J_{IC}. Experiments show that J_{IC} is essentially independent of specimen size within the range of compact tension (CT) specimens specified in ASTM E1820.

Since the J– integral concept is applicable to both elastic and fully-plastic conditions, K_{JC} is related to J_{IC} through:

$$K_{JC} = \sqrt{J_{IC}E} \tag{7.15}$$

Begley and Landes [27] recognized that linear elastic fracture mechanics (LEFM) is a special case of nonlinear elastic fracture mechanics, leading to the relationship between related J_{IC} to K_{IC} in Eq. (7.15). However, since J_{IC} and K_{IC} are defined by different ASTM standards (E1820 and E399, respectively), they cannot be directly correlated. Therefore, in accordance with ASTM E1820, K_{JC} is used when fracture toughness is measured using J_{IC} from E1820 method, while K_{IC} is applied when toughness is determined using E399 methodology. The value of loading rates vs toughness parameters is listed in Table 7.1.

K_{IC} tests is done at $0.05\ \mathrm{mm/s}$ and the result is compared with K_{JC} value obtained from J_{IC} test at the same loading rate and found to be matching within 10%. To measure the dynamic toughness at fast loading rates K_{ID} test are performed. For this Charpy V-notch pre-cracked specimen is widely used. The detailed procedure is discussed in the next section.

Table 7.1 Loading rates vs the fracture toughness parameters

Loading Rate (mm/s)	Test Temperature (ºC)	Test Type	Fracture Toughness (J_{IC}) (J/m^2)	Fracture Toughness (K_{IC}) ($MPa\sqrt{m}$)	Fracture Toughness (K_{JC}) ($MPa\sqrt{m}$)
0.01	27	J-R	30.46	.....	79.59
0.05	27	J-R and K_{IC}	45	90.56	96.75
0.075	27	J-R	32.12	.....	81.74
0.1	27	J-R	48.96	.....	100.91
0.5	27	K_{IC}	.....	98.64	
1.0	27	K_{IC}	.....	96.99	
1.5	27	K_{IC}	.....	113.67	
0.01	200	J-R	240.1	.....	223.47
0.01	400	J-R	205.6	.....	206.79

7.5 Fracture toughness K_{ID} test of pre-cracked Charpy V-notch specimen in drop weight impact testing machine

Dynamic fracture toughness (K_{ID} or K_{IC} (t)) can be evaluated from the following Eq. (7.16). This equation is used when fracture occurs before general yielding. It is linear elastic fracture toughness.

$$K_{Id} = \frac{P_f S}{BW^{3/2}} f\left(\frac{a}{W}\right) \tag{7.16}$$

Where, P_f = fracture load and a is the initial crack length

$$f\left(\frac{a}{W}\right) = \frac{\sqrt[3]{\frac{a}{W}}}{2\left(1+2\frac{a}{W}\right)} \frac{1.99-\left(\frac{a}{W}\right)\left(1-\frac{a}{W}\right)\left[2.15-3.93\left(\frac{a}{W}\right)+2.7\left(\frac{a}{W}\right)^2\right]}{\left(1-\frac{a}{W}\right)^{3/2}}$$

The value of K_{Id} is listed in Table 7.2.

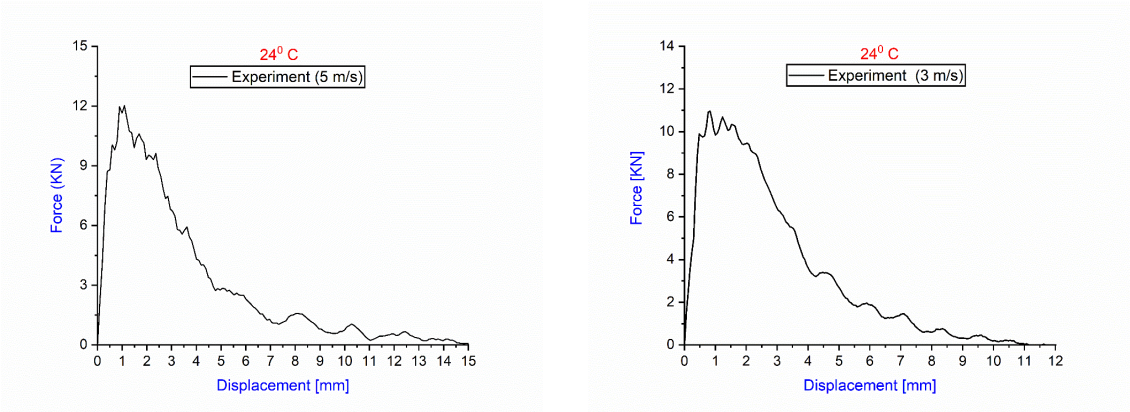

Fig. 7.8 Load vs displacement curves of Charpy V-notch impact testing at 3 m/s and 5 m/s

Table 7.2 Dynamic fracture toughness

Velocity mm/s	P_F (KN)	Fracture Toughness (K_{Id}) MPa-$m^{0.5}$
3000	11	117.27
5000	12	127.96

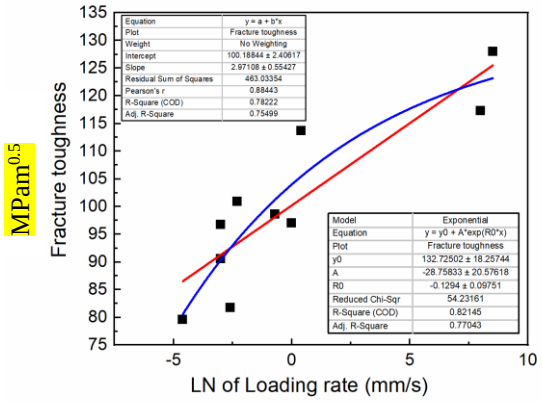

Fig. 7.9 Fracture toughness vs loading rate curve (all values of fracture toughness are plotted and fitted with the equation to find the relationship).

7.6 Ballistic impact analysis through fracture mechanics

7.6.1 Finte element modelling

Armor plate of cross section 500 x 500 mm and 40 mm thickness is modelled in ABAQUS CAE software. A rigid projectile is considered of diameter 30 mm and length 100 mm. Fine meshing was employed along the centre of the plate where the projectile strikes. In the rest of the plate coarse meshing was employed. The finite element model of armour plate in ABAQUS pre-processor includes the following steps.

1. Building the part geometry.
    - Armour plate size 500 x 500 mm in cross-section and 40 mm thickness.
2. Assigning the properties.
    - The J-C thermoviscoplastic material model with damage initiation and evolution criterion for plate.
3. Coefficient of friction between projectile and armour plate assumed to be 0.05.
4. Defining boundary conditions.
    - The sides of the plate were fixed in x,y, and z directions.
    - The projectile motion was constrained in x and y direction along with fixed rotation in all directions.
    - A predefined velocity field was provided over the entire projectile in z-direction.
5. Meshing with explicit quadrilateral C3D8R Brick element as shown in Fig. 7.10 to Fig. 7.11.

7.6.2 Assignment of Material Model and Failure model

In computational methods, the incremental plasticity theory is commonly used. The Johnson-Cook plasticity material model were implemented in ABAQUS CAE software using vectorised user defined material code (VUMAT). When the equivalent stress is less than the yield stress of the material, the material behaves linearly elastically, according to these models the Johnson-cook failure model also plugged in VUMAT FORTRAN language code.

7.6.3 Modelling the contact-impact

In ABAQUS CAE software, surface to surface contact (Explicit) was considered, with whole armour plate nodes acting as slave nodes and the entire projectile surface acting as master. In the case of a rigid projectile, the kinematic contact method is used in mechanical constraint formulation. Tangential behaviour penalty contact with coefficient of friction 0.01 was selected in the contact property option. Normal behaviour was also considered with hard contact, and separation was permitted following contact.

7.6.4 Boundary and Initial conditions

Armour plate displacement was fixed in x and y direction. In projectile displacement in x and y and rotation about x, y and z are fixed and velocity applied in z-direction as shown in Fig. 7.13.

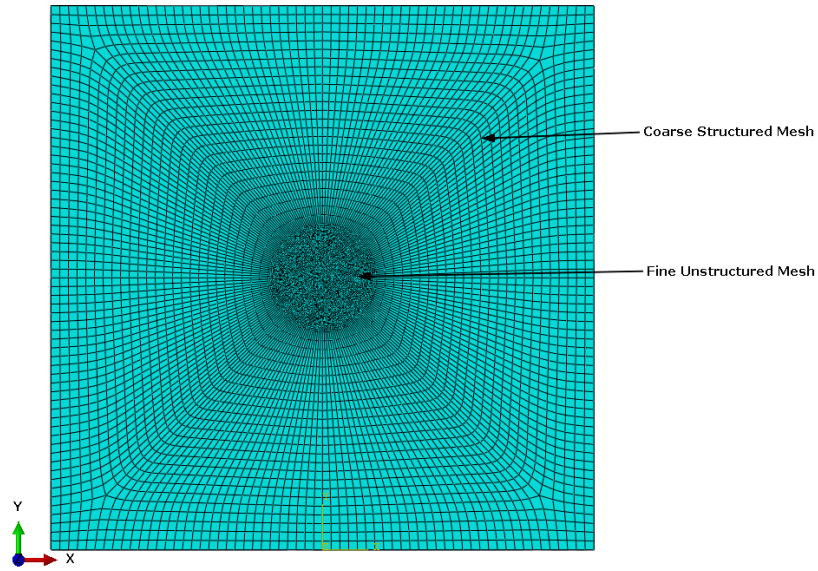

Fig. 7.10 Armour Plate 500x500 mm and 40 mm thickness Meshing

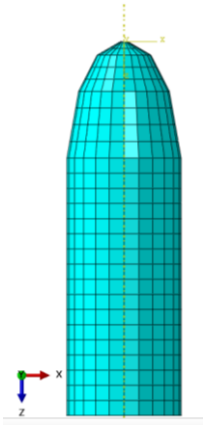

Fig. 7.11 Projectile Meshing

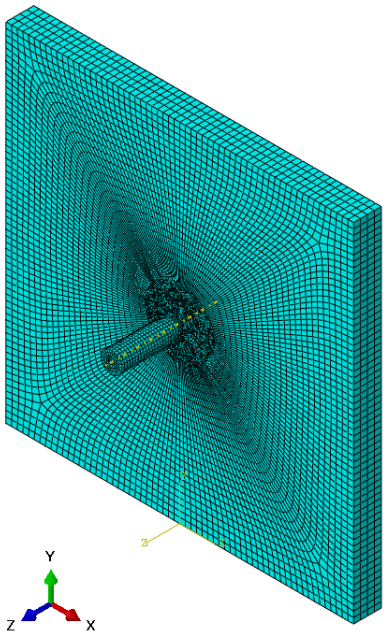

Fig. 7.12 Assembly of Projectile and armour Plate

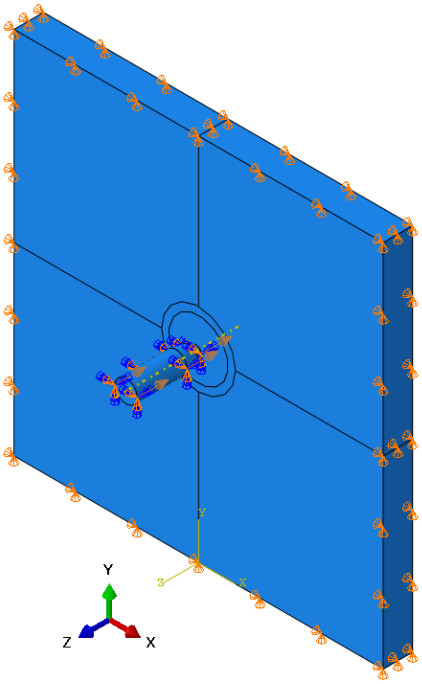

Fig. 7.13 Boundary conditions in armour plate and projectile

7.6.5 Modelling of crack

Different no. of cracks of different length 4, 6, 8, 10, and 12 mm are modelled through VUMAT subroutine. First the fracture toughness value of 96.9 $MPa\sqrt{m}$ was is used in simulation. The cracks are considered brittle in nature. The fracture toughness values are assigned to these cracks only and rest of the plate behviour are considered as ductile. The simulation of intact plate without crack with rigid projectile of striking velocity 800 m/s is performed. The residual velcoity of the intact plate is considered as a reference with which the performances of all the cracked plate in term of residual velocity are compared.

Fig. 7.14 shows the plate with two cracks of length 6mm at a striking velcoity 800 ms^{-1} while in Fig. 7.15 four cracks of length 12 mm are simulated with same striking velocity and in Fig. 7.16 four cracks of length 6 mm are simulated. At striking veloicty 1200 ms^{-1} and 1800 ms^{-1} four cracks of 6 mm in length is shown in Fig. 7.17 & 7.18 respectively. The fine broken elements (brittle in nature) ahead of the projectile are armor plate elements. At the rear side of the plate the petals are formed, these petals are originated from the crack. From Fig. 7.19 to 7.23 the crack length and number of cracks originated on the plate are shown.

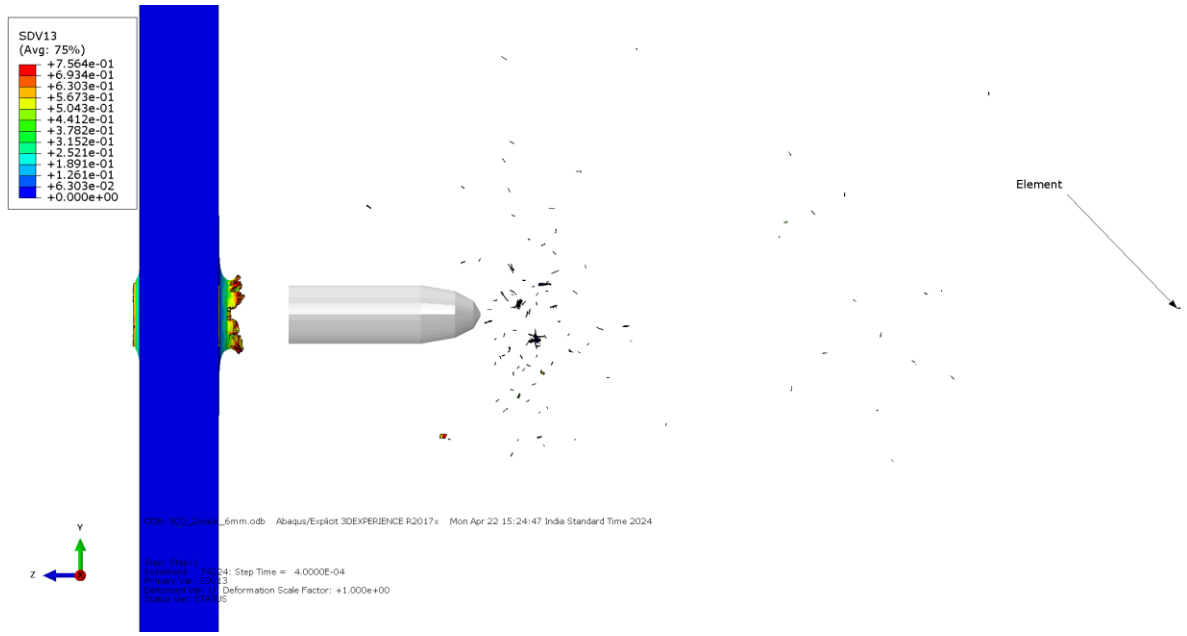

Fig. 7.14 Striking velocity 800 ms^{-1}, 40 mm thick armour plate, 2 cracks, each 6 mm in length

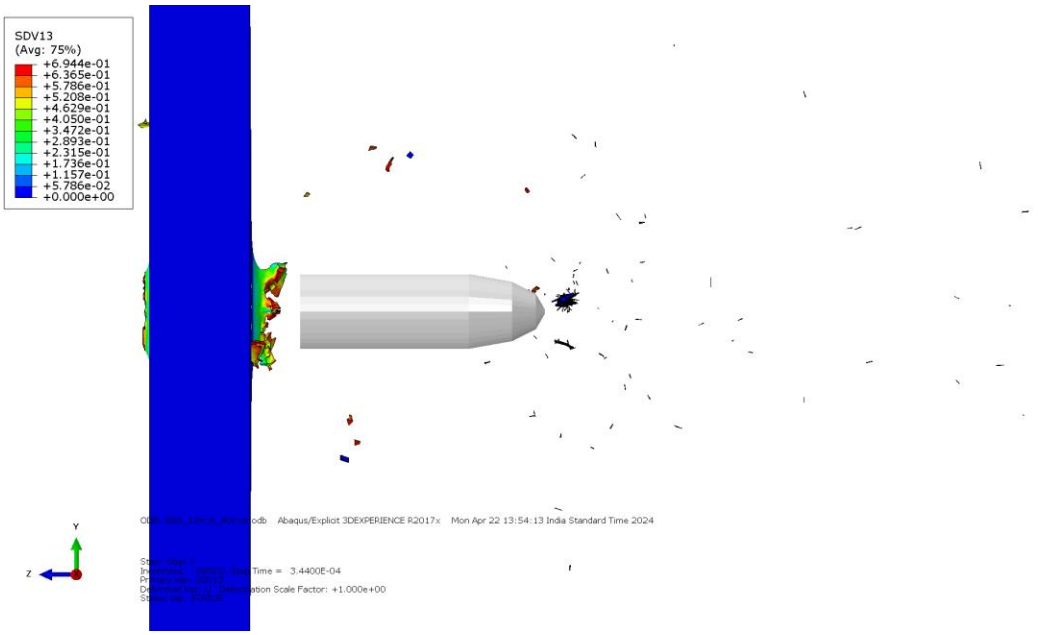

Fig. 7.15 Striking velocity 800 ms^{-1}, 40 mm thick armour plate, 4 cracks, each 12 mm in length

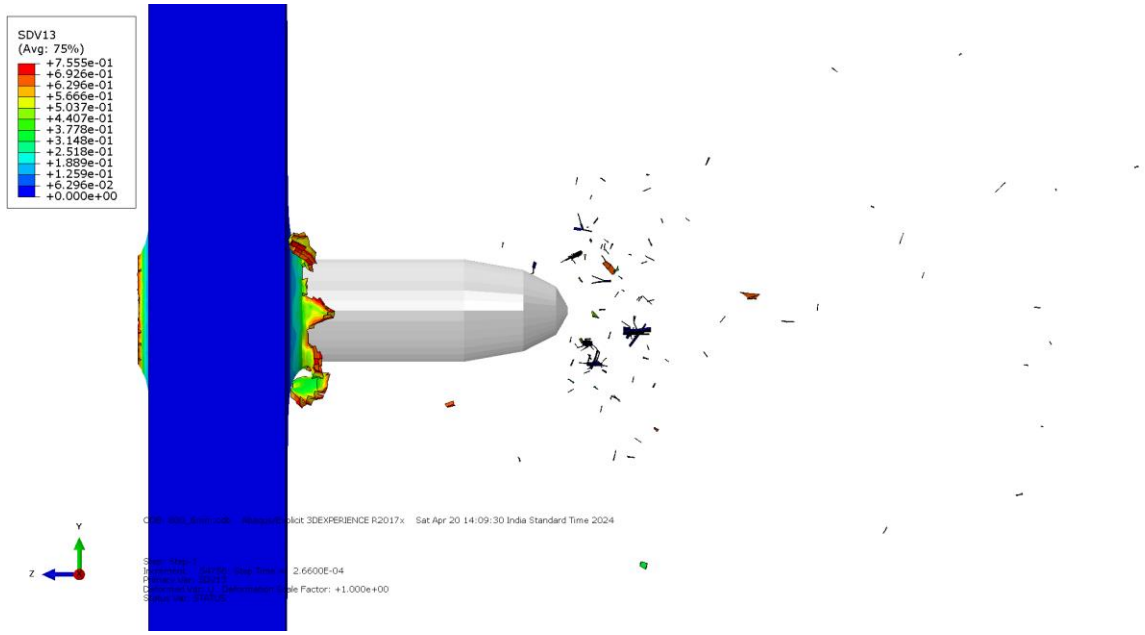

Fig. 7.16 Striking velocity 800 ms^{-1}, 40 mm thick armour plate, 4 cracks, each 6 mm in length

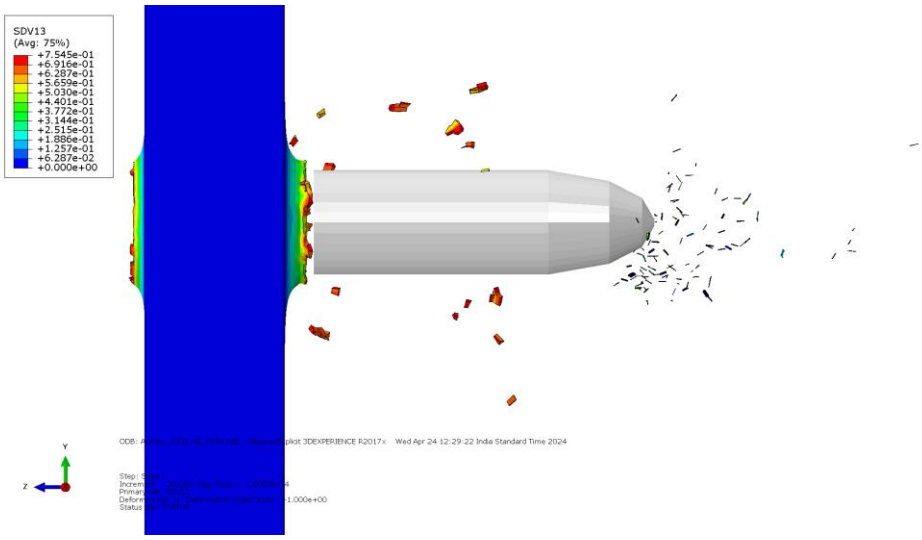

Fig. 7.17 Striking velocity 1200 ms^{-1}, 40 mm thick armour plate, 4 cracks, each 6 mm in length

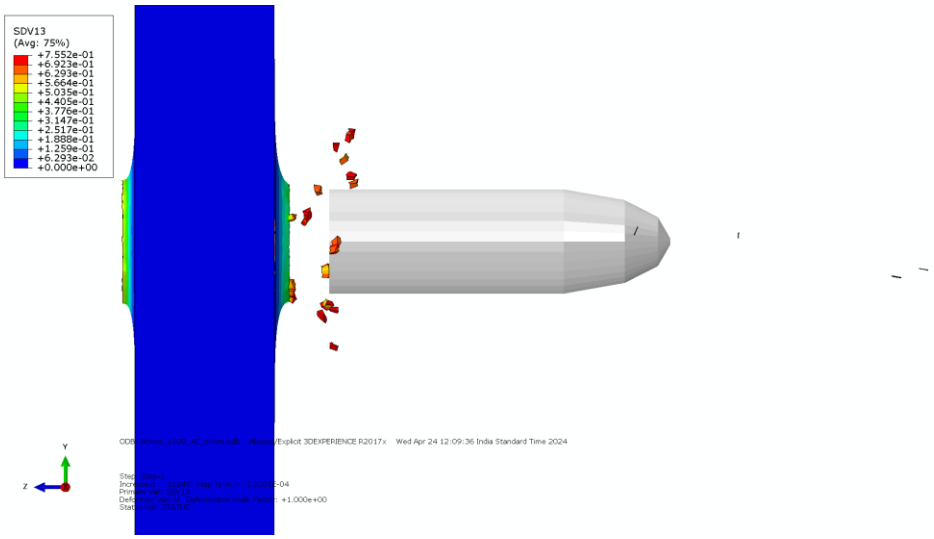

Fig. 7.18 Striking velocity 1800 ms^{-1}, 40 mm thick armour plate, 4 cracks, each 6 mm in length

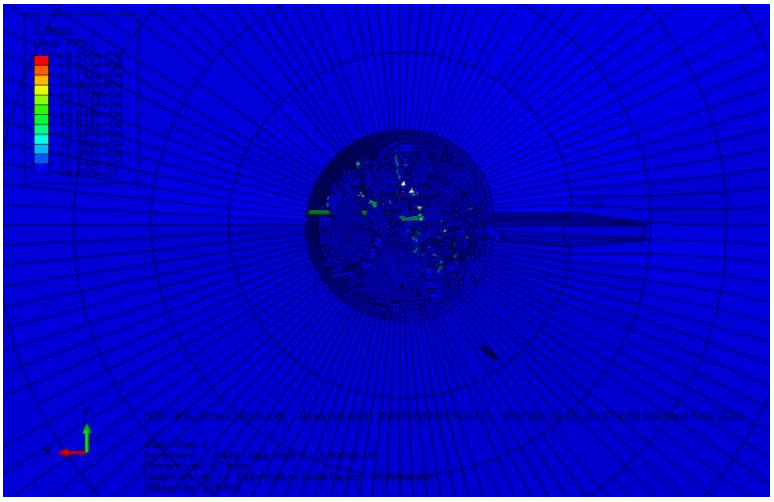

Fig. 7.19 2 cracks, each 6 mm

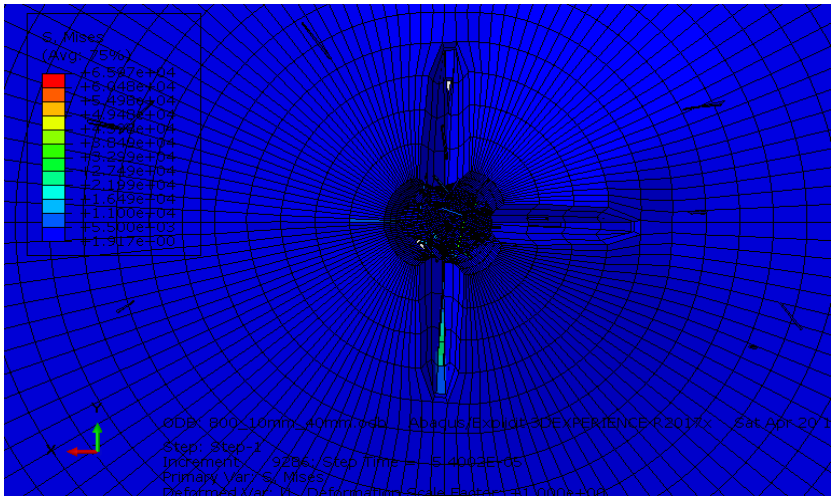

Fig. 7.20 4 cracks, each 10 mm

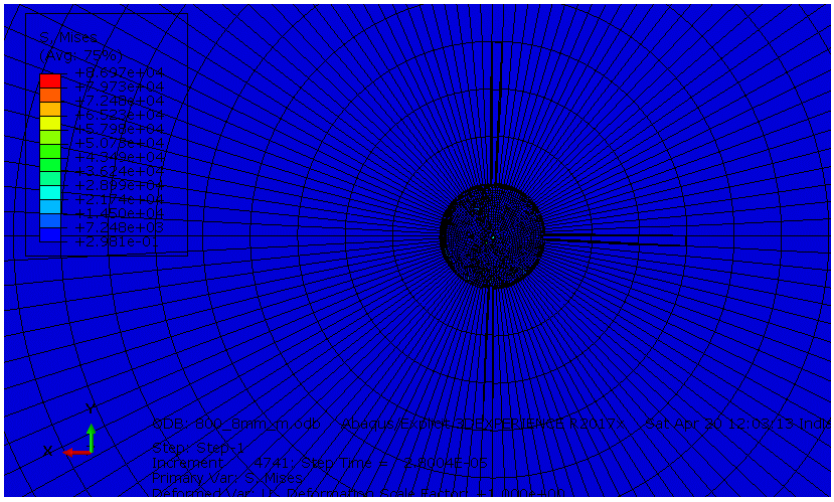

Fig. 7.21 4 cracks, each 8 mm

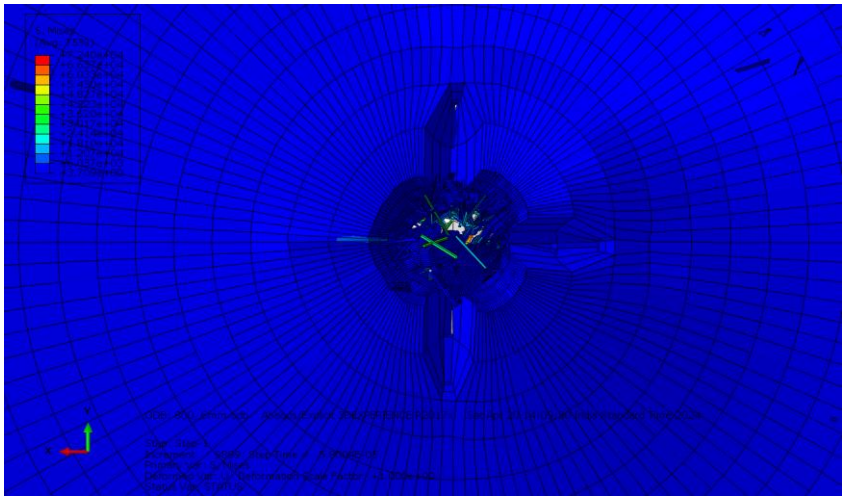

Fig. 7.22 4 cracks, each 6 mm

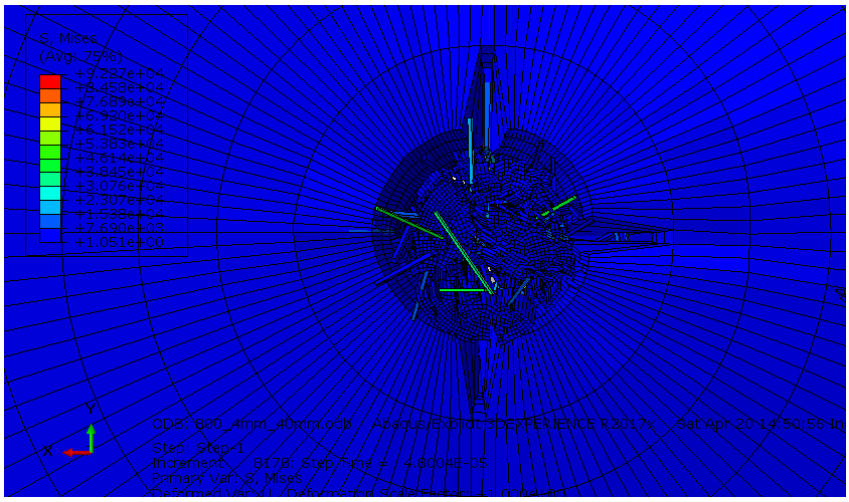

Fig. 7.23 4 cracks, each 4 mm

7.7 Results and discussion

- Figs. 7.14 to 7.18 clearly show how the material fragments under impact. The armour steel plate is inherently a ductile material, meaning it can undergo significant plastic deformation before breaking. However, when brittle inserts are introduced within the plate, the material behaves differently compared to a fully ductile structure. In a fully ductile material (without brittle inserts), the projectile velocity decreases gradually due to plastic deformation, where the material stretches and bends without immediate failure. In contrast, when brittle inserts are present, the velocity reduction happens much more quickly because cracks spread rapidly and fail. This leads to material fragmentation, where pieces break away to release fracture energy rather than just deforming.

  The failure pattern across Figs. 7.14 to 7.18 varies due to the combined influence of both ductile and brittle failure modes:

  - Brittle failure: The spreading and breaking of material fragments suggest a sudden and catastrophic type of failure, common in brittle materials.
  - Ductile failure: The bending of material and the formation of a necked region (where the material deforms before breaking) indicate gradual deformation before failure, a characteristic of ductile behaviour.

  At high striking velocity (1800 m/sec) the crack propagation speed is high which requires the rate of energy release though surface energy is also high. Thus, there will be rapid fragmentation giving less scope for plastic deformation (Fig 7.18).

  The overall fragmentation behaviour depends on:

- Number of cracks present in the material.
- Crack length, which influences how quickly the structure weakens.
- Striking velocity, determining the intensity of the impact and how the material absorbs energy.
- Fracture toughness

This analysis highlights the complex interaction between ductile and brittle behaviors in impact mechanics, demonstrating how material properties influence the way structures break under extreme conditions.

Figs 7.24 (a) & (b) show the change in residual velocity with crack parameters (crack length and number of cracks). Cracks makes the armour plate weaker and hence the less capability of absorbing energy. Both the plots show higher residual velocity with increasing crack length and more number of cracks. The ballistic performance (BPI) is the capability of the armour plate to absorb kinetic energy of the projectile and calculated as

$$\text{B.P.I} = \frac{\frac{1}{2}mv_i^2 - \frac{1}{2}mv_f^2}{\frac{1}{2}mv_i^2} \text{ x } 100$$

Table shows the BPI of the armour plate for different crack conditions

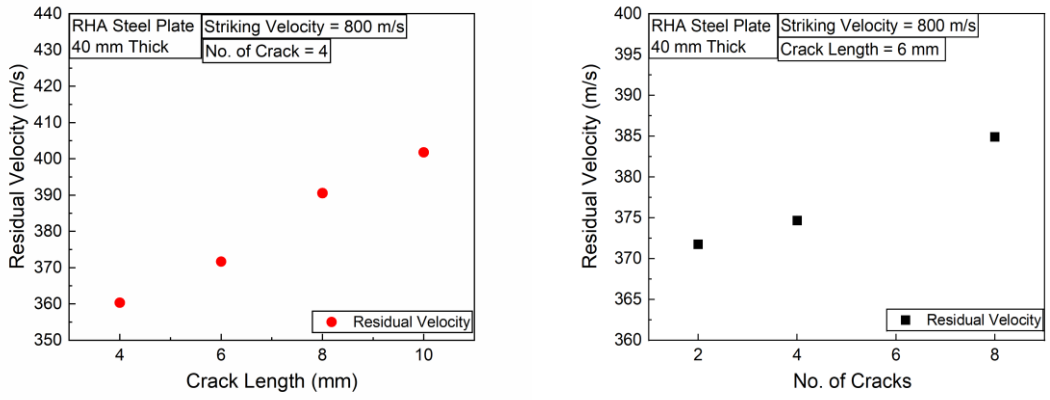

(a) (b)

Fig. 7.24 Variation of residual velocity with crack parameters

Table 7.3 B.P.I of plate for different crack conditions

Crack Length	4 mm	6 mm		8 mm	Uncracked
Crack No.	04	04	06	04	
B.P.I (%)	78.06	79.711	77.47	76.16	85.93

Figs 7.25 (a) & (b) show loss of kinetic energy of the projectile for crack parameters of the armour plate. Both the figures show the loss of K.E of the projectile decreases with long crack length and more number of cracks. It is evident that the armour plate weakens due to cracks and loses the energy absorbing capacity.

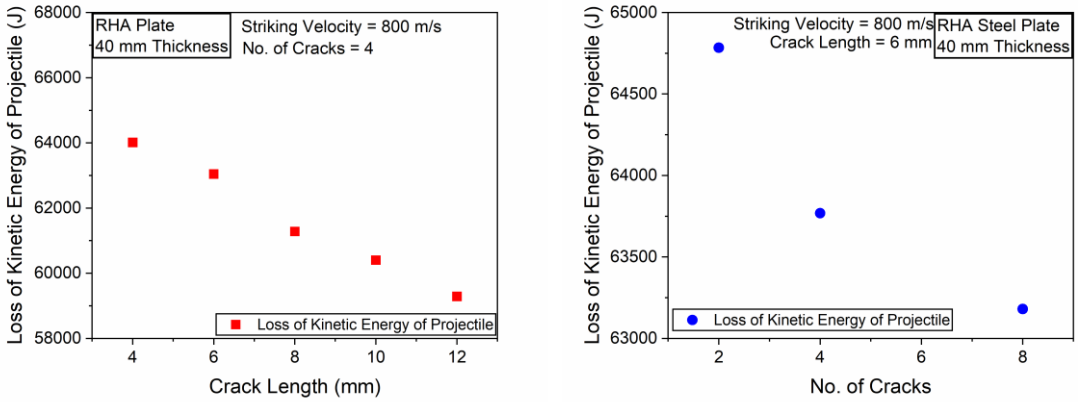

(a) (b)

Fig. 7.25 Varation of loss of K.E of the projectile with crack parameters

Fig 7.26 shows the variation of loss of kinetic energy with striking velocity. Figure shows that there is not much variation in loss of kinetic energy of the projectile for moderate velocities (upto 1200 m/sec). But, the loss of K.E of the projectile is much more at high velocity (1800 m/sec). This is because the failure mode changes with lot of fragmentations (Fig 7.18) which creates more surfaces and more surface energy derived from the K.E of the projectile.

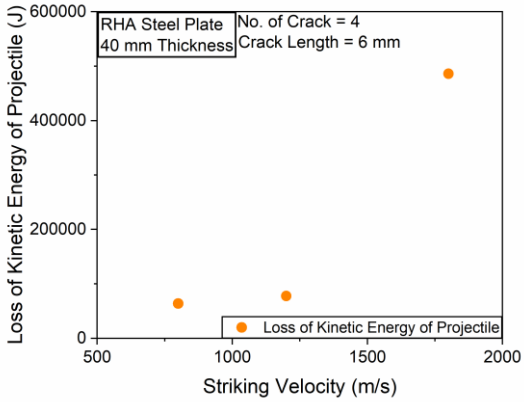

Fig. 7.26 Variation of loss of K.E of the projectile with striking velocity

Fig 7.27 shows the total energy variation of the plate and the projectile with time. The total energy consists of elastic energy, plastic energy of the plate, kinetic energy of the projectile, frictional dissipation and fracture energy. Fracture energy goes out of the system. Thus, reduces the total energy of the plate. In transition the projectile loses its kinetic energy due to friction unless it stabilizes at 0.1 ms. There after the total energy remains almost.

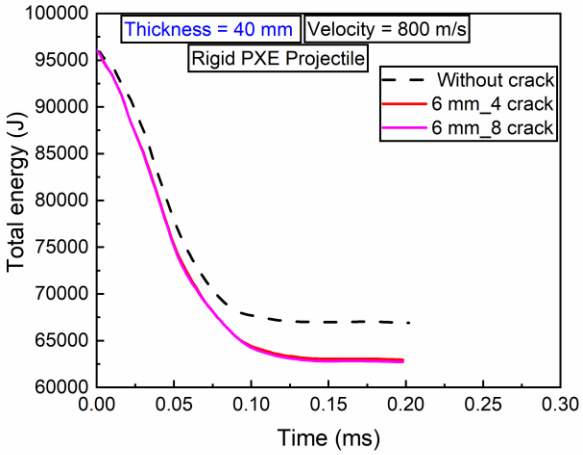

Fig. 7.27 Total energy variation with time for crack and uncracked plate struck by rigid projectile.

Constant with a saturated plastic deformation The figure compares the crack and uncrack plates. The crack plates stabilizes at lower value of energy shows less plastic deformation due to crack growth. This shows that the crack influences the energy absorbing capacity of the plate.

- The Fig. 7.28 illustrates the velocity variation in a 40 mm thick plate with different crack sizes (4 mm, 6 mm, 8 mm, 10 mm, and 12 mm) under impact conditions. The velocity of the projectile gradually decreases over time for all cases, indicating energy absorption through deformation and fracture mechanisms. Plates with smaller cracks (4 mm, 6 mm) experience a slower velocity drop, suggesting better resistance to impact, whereas larger cracks (10 mm, 12 mm) result in a faster velocity decline**,** indicating weakened structural integrity and increased energy dissipation. The presence of longer cracks amplifies stress concentration, accelerating fracture initiation and propagation**,** leading to premature failure. This behaviour highlights a progressive failure mechanism**,** where smaller cracks allow for better energy absorption, while larger cracks significantly weaken the material, resulting in rapid structural breakdown. The findings align with fracture mechanics principles, demonstrating that crack length directly influences impact resistance and material failure dynamics. As crack length increases, the ability of the material to resist impact decreases, leading to higher residual velocity. However, when the crack length approaches the projectile diameter (around 10-12 mm), the residual velocity becomes almost constant because the material structural integrity is already significantly weakened, and additional crack growth has a diminishing effect on impact resistance.

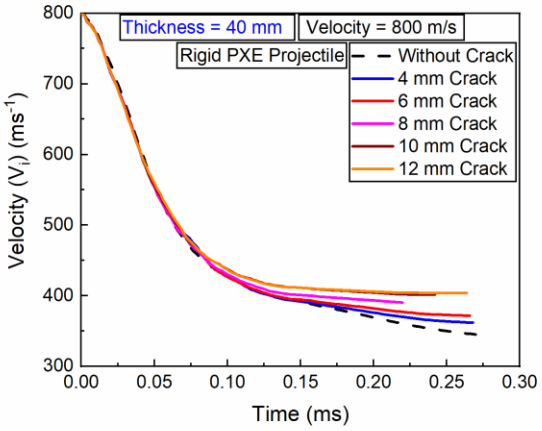

Fig. 7.28 40 mm thickness plate

- Fig. 7.29 illustrates the energy variation in a 40 mm thick plate impacted by a rigid projectile at 800 m/s, comparing cases with different crack sizes (4 mm, 6 mm, 8 mm, 10 mm, and 12 mm) to an uncracked plate. The uncracked plate retains the highest energy throughout the impact, indicating greater structural resistance to deformation and fracture. As crack length increases, energy dissipation occurs more rapidly due to stress

concentration at crack tips, leading to earlier material failure and lower retained energy. The energy stabilizes after 0.15 ms, suggesting that most of the impact energy has already been dissipated through plastic deformation, crack growth, and fragmentation. The total energy absorbed by the system depends on crack size. Comparatively the intact plate absorbs and retains more energy due to its higher plastic deformation before failure. In contrast, larger cracks (10 mm, 12 mm) cause earlier structural failure, leading to rapid energy dissipation and reduced total energy absorption compared to smaller cracks. This confirms that crack length directly influences impact resistance, with larger cracks reducing the plate ability to retain energy effectively, leading to rapid structural failure.

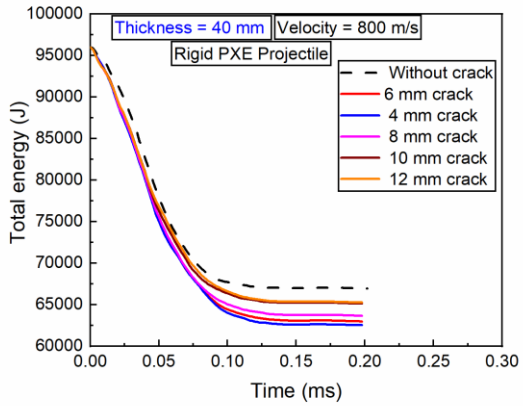

Fig. 7.29 40 mm thickness plate residual energy

- The Fig. 7.30 illustrates the crack growth behaviour in a material under impact conditions, showing how initial crack size (8 mm, 10 mm, 12 mm, 14 mm) influences final crack growth**.** The results indicate that larger initial cracks lead to significantly higher crack propagation**,** confirming that stress concentration at crack tips accelerates failure. The growth pattern is nonlinear, meaning that once a crack reaches a critical size, it expands rapidly, leading to unstable fracture propagation. Smaller cracks require more impact energy to initiate growth**,** while larger cracks grow more easily due to higher stress intensity factors. This behaviour aligns with fracture mechanics principles, specifically Griffith's Criterion, which states that crack growth accelerates when the energy release rate exceeds a critical threshold. The presence of a threshold crack length suggests that materials with pre-existing cracks beyond this point are highly susceptible to sudden failure. To improve structural integrity and impact resistance, it is crucial to limit initial crack sizes and implement reinforcement techniques such as crack arrestors or residual compressive stresses to prevent unstable crack growth.

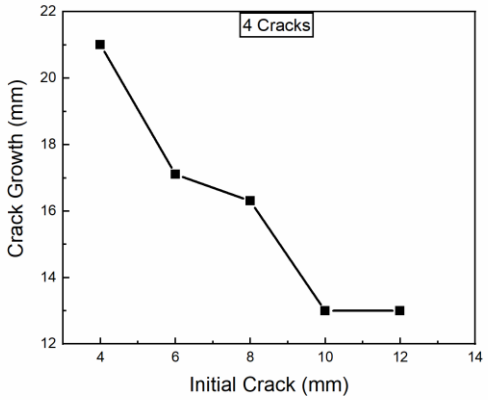

Fig. 7.30 Variation of crack growth vs initial crack

- The simulation results for a 20 mm thick plate with a 10 mm crack length indicate that the plate provides minimal resistance at all striking velocities, as shown in Fig. 7.31 and 7.32. The presence of the cracks significantly weakens the plate structural integrity, allowing for rapid failure upon impact. This suggests that larger cracks drastically reduce the plate ability to absorb impact energy, making it highly vulnerable to fracture under high-velocity conditions.

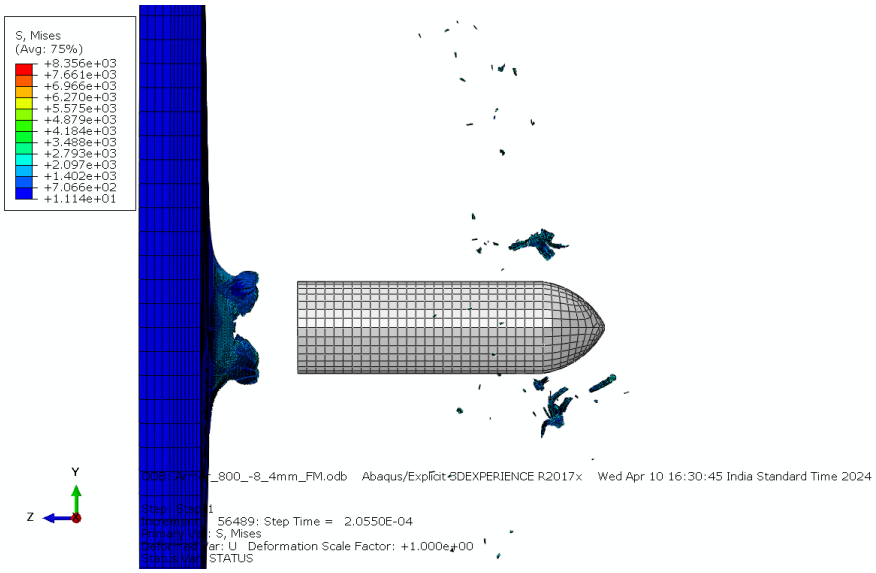

Fig. 7.31 20 mm thickness plate, rigid ogive projectile

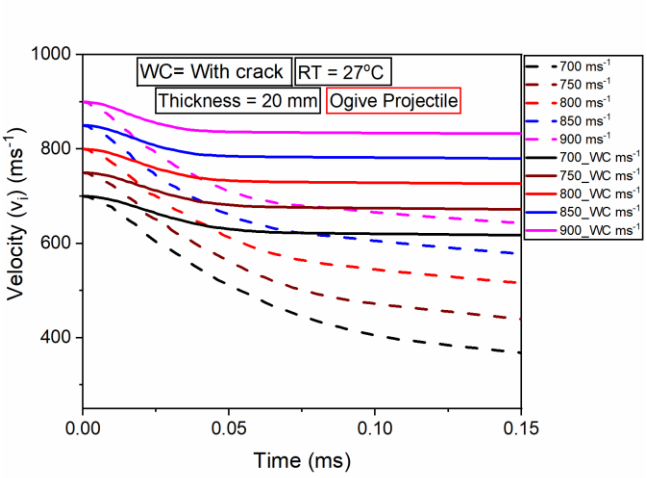

Fig. 7.32 20 mm thickness plate of 8 mm crack

- The Fig. 7.33 illustrates the velocity variation in a 40 mm thick plate impacted by a rigid projectile at 800 m/s, highlighting the influence of fracture toughness on velocity reduction over time. The velocity steadily decreases from 800 m/s to below 400 m/s, indicating energy dissipation through plastic deformation, crack propagation, and fracture initiation. Materials with higher fracture toughness exhibit slower velocity reduction, as they can withstand greater stresses before failure, while those with lower fracture toughness experience a faster velocity drop due to rapid crack propagation and structural failure. The velocity curve stabilizes around 0.30–0.35 ms, suggesting that most of the fracture processes and energy dissipation occur within this time frame. This behaviour aligns with fracture mechanics principles, where the ability to resist crack initiation and propagation determines impact resistance. The findings emphasize the importance of fracture toughness in material design, as tougher materials can absorb more energy before fracturing, thereby improving structural integrity under high-velocity impact conditions. The residual velocity with different fracture toughness value are shown in Fig. 7.32. When the fracture toughness value is 60 MPa√m, the material absorbs less energy, resulting in a higher residual velocity. Conversely, at 100 MPa√m**,** the material absorbs more impact energy, leading to a lower residual velocity as compared to other fracture toughness values.

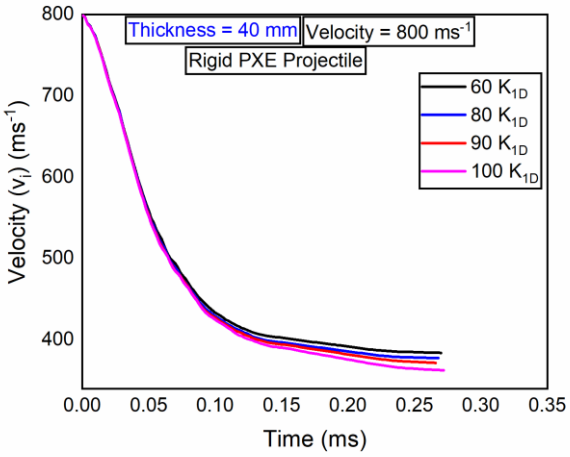

Fig. 7.33 Residual velocity at different fracture toughness

7.8 Conclusion

This study examines how the presence of cracks in a target plate affects its impact resistance. Cracks can form due to manufacturing defects or multiple low-velocity impacts, eventually leading to catastrophic failure, even under lower impact forces. The study successfully simulates the ballistic resistance of 40 mm and 20 mm thick plates under different crack sizes. The results confirm that cracks significantly weaken the plate's ability to resist impact, reducing its overall strength. To better understand how crack growth changes with impact velocity, experimental data is needed.

The findings show that material inhomogeneity plays a major role in impact resistance, fragmentation, and structural failure. When brittle inserts are present in RHA steel plates, they help crack propagation, causing faster material fragmentation. In contrast, fully ductile materials absorb more energy by deforming gradually and helps in velocity reduction before failure. The length of cracks is also critical—larger cracks lead to faster failure due to unstable crack propagation causing quicker energy dissipation and weaker structural integrity. More number of cracks also weaken the plate because of more stress concentration spots. Notably, when the crack length reaches approximately the projectile diameter (10–12 mm), the weakening effect stabilizes, meaning additional crack growth has less impact on resistance.

In terms of energy absorption, plates with smaller cracks (4 mm, 6 mm) absorb more energy and fail more slowly, whereas larger cracks (10 mm, 12 mm) cause earlier failure and lower energy retention. Additionally, fracture toughness directly affects impact resistance. Materials with higher

fracture toughness show slower velocity reduction because they absorb more impact energy. For example, for K_{Id} = 60 MPa√m, the material absorbs less energy, leading to higher residual velocity, whereas at 100 MPa√m, it absorbs more energy lowering the residual velocity.

Further simulations on 20 mm thick plates with 8 mm cracks reveal that these plates offer very little resistance at all impact velocities, emphasizing the importance of material thickness and crack control. Experiments also show that fracture toughness changes with loading rate and temperature, proving that materials behave differently under different impact conditions. The simulation results confirm that cracks significantly lower the ballistic performance and hence the ballistic limit, which is a critical factor in armour design. The presence of cracks not only weakens the material but, in some cases, can cause sudden brittle failure, further reducing structural integrity.

These findings provide valuable insights for armour design, aerospace engineering, and impact-resistant materials, helping engineers develop stronger and more durable materials that perform better under high-velocity impacts.

References

[1] Gailly B, Petit J. Influence of the microstructure on armor steel spalling 2008;635:635–8. https://doi.org/10.1063/1.50639.

[2] Gailly B, Pineau A. Dynamic fracture of armor steel. Mech Mech Damage Fail n.d.

[3] Ravi-Chandar K, Knauss WG. An experimental investigation into dynamic fracture: I. Crack initiation and arrest. Int J Fract 1984;25:247–62. https://doi.org/10.1007/BF00963460.

[4] Ravi-Chandar K, Knauss WG. An experimental investigation into dynamic fracture: III. On steady-state crack propagation and crack branching. Int J Fract 1984;26:141–54. https://doi.org/10.1007/BF01157550.

[5] Kazarinov N, Bratov V, Petrov Y. Simulation of dynamic crack propagation under quasistatic loading. Appl Mech Mater 2014;532:337–41. https://doi.org/10.4028/www.scientific.net/AMM.532.337.

[6] Ravi-Chandar K. An experimental investigation into the mechanics of dynamic fracture 1982;Ph.D.

[7] Ravi-Chandar K, Knauss WG. An experimental investigation into dynamic fracture: II. Microstructural aspects. Int J Fract 1984;26:65–80. https://doi.org/10.1007/BF01152313.

[8] Kalthoff JF. Fracture behavior under high rates of loading. Eng Fract Mech 1986;23:289–98. https://doi.org/10.1016/0013-7944(86)90193-1.

[9] Kobayashi T, Toda H, Masuda T. Analysis of test data obtained from Charpy V and impact tensile test. Eur Struct Integr Soc 2002;30:173–80. https://doi.org/10.1016/S1566-1369(02)80018-8.

[10] Fengchun J, Ruitang L, Xiaoxin Z, Vecchio KS, Rohatgi A. Evaluation of dynamic fracture toughness KId by Hopkinson pressure bar loaded instrumented Charpy impact test. Eng Fract Mech 2004;71:279–87. https://doi.org/10.1016/S0013-7944(03)00139-5.

[11] Kazarinov N, Smirnov I, Sudenkov Y, Petrov Y, Slesarenko V. Experimental investigation of dynamic crack propagation in PMMA plates. Procedia Struct Integr 2017;6:83–9. https://doi.org/10.1016/j.prostr.2017.11.013.

[12] Kazarinov NA, Bratov VA, Morozov NF, Petrov Y V., Balandin V V., Iqbal MA, et al. Experimental and numerical analysis of PMMA impact fracture. Int J Impact Eng 2020;143:103597. https://doi.org/10.1016/j.ijimpeng.2020.103597.

[13] Bleyer J, Roux-Langlois C, Molinari JF. Dynamic crack propagation with a variational phase-field model: limiting speed, crack branching and velocity-toughening mechanisms. Int J Fract 2017;204:79–100. https://doi.org/10.1007/s10704-016-0163-1.

[14] D.T. Ngo FLP and DB. Modeling of Dynamic Crack Propagation Under Quasistatic Loading. 15 IACMAG 2017;402 LNNS:577–85. https://doi.org/10.1007/978-3-030-96380-4_63.

[15] Li S, Zhang Y, Wu J, Yu J, Gong X. Modeling of crack propagation with the quasi-static material point method. Eng Fract Mech 2021;245:107602. https://doi.org/10.1016/j.engfracmech.2021.107602.

[16] Bratov V. NUMERICAL SIMULATIONS of DYNAMIC FRACTURE. CRACK PROPAGATION and FRACTURE of INITIALLY INTACT MEDIA. Mater Phys Mech 2021;47:455–74. https://doi.org/10.18149/MPM.4732021_7.

[17] Johnson GR, Cook WH. A Computational Constitutive Model and Data for Metals Subjected to Large Strain, High Strain Rates and High Pressures. 1983.

[18] Banerjee A, Dhar S, Acharyya S, Datta D, Nayak N. Determination of Johnson cook material and failure model constants and numerical modelling of Charpy impact test of armour steel. Mater Sci Eng A 2015;640:200–9. https://doi.org/10.1016/j.msea.2015.05.073.

[19] Borvik T, Hopperstad OS, Berstad T, Langseth M. Perforation of 12mm thick steel plates by 20mm diameter projectiles with flat, hemispherical and conical noses - Part II: Numerical simulations. Int J Impact Eng 2001;27:37–64. https://doi.org/10.1016/S0734-743X(01)00035-5.

[20] Klepaczko JR, Rusinek A, Rodríguez-Martínez JA, Pecherski RB, Arias A. Modelling of thermo-viscoplastic behaviour of DH-36 and Weldox 460-E structural steels at wide ranges

of strain rates and temperatures, comparison of constitutive relations for impact problems. Mech Mater 2009;41:599–621. https://doi.org/10.1016/j.mechmat.2008.11.004.

[21] Whittington WR, Oppedal AL, Turnage S, Hammi Y, Rhee H, Allison PG, et al. Capturing the effect of temperature, strain rate, and stress state on the plasticity and fracture of rolled homogeneous armor (RHA) steel. Mater Sci Eng A 2014;594:82–8. https://doi.org/10.1016/j.msea.2013.11.018.

[22] McDonald B, Bornstein H, Ameri A, Daliri A, Orifici AC. Plasticity and ductile fracture behaviour of four armour steels. Int J Solids Struct 2019;176–177:135–49. https://doi.org/10.1016/j.ijsolstr.2019.05.013.

[23] Bhav Singh B, Sukumar G, Prakasa Rao P, Siva Kumar K, Madhu V, Arockia Kumar R. Superior ballistic performance of high-nitrogen steels against deformable and non-deformable projectiles. Mater Sci Eng A 2019;751:115–27. https://doi.org/10.1016/j.msea.2019.02.044.

[24] Singh BB, Sukumar G, Paman A, Balaji G, Siva Kumar K, Madhu V, et al. A Comparative Study on the Ballistic Performance and Failure Mechanisms of High-Nitrogen Steel and RHA Steel Against Tungsten Heavy Alloy Penetrators. J Dyn Behav Mater 2021;7:60–80. https://doi.org/10.1007/s40870-020-00270-8.

[25] Conshohocken W. Standard Test Method for Measurement of Fracture Toughness 1. Annu B ASTM Stand 2001;i:1–56. https://doi.org/10.1520/E1820-20E01.

[26] 1820. ASTM Standards 1820 2018;i:3–5. https://doi.org/10.1520/E1820-18AE0110.1520/E1820-20.

[27] 1972 Landes Begley The effect of specimen geometry on JIc.pdf n.d.

Chapter 8

Conclusion and Future scope of Work

8.1 Conclusion

This thesis investigated the dynamic behaviour, fracture response, and ballistic resistance of martensitic armour steels, specifically Rolled Homogeneous Armour (RHA) and PHS 1500, under a wide range of strain rates and temperatures. Through a combination of experimental testing, advanced material modelling, and finite element simulations, the work successfully addressed the limitations of conventional constitutive relations in capturing the thermoviscoplastic behaviour of these steels.

A major outcome of this study was the development and validation of a Modified Johnson–Cook (MJ-C) constitutive model, which addressed the limitations of conventional phenomenological models. By incorporating a strain-rate index and temperature-dependent strain-hardening exponent, the MJ-C model demonstrated improved predictive accuracy across a wide range of strain rates (10^{-4}–10^{3} s^{-1}) and temperatures (27–600 °C). This model reliably captured flow stress, failure strain, and post-peak softening, with prediction errors under 3%, thereby offering a robust tool for impact and penetration simulations.

These objectives have been successfully met, leading to the following key conclusions:

1. **Superiority of the Modified Johnson-Cook (MJ-C) Model:** The newly developed Modified Johnson-Cook (MJ-C) constitutive model demonstrably outperforms both the standard phenomenological Johnson-Cook (J-C) model and the semi-physical Rusinek-Klepaczko (R-K) model. By incorporating temperature-dependent strain hardening and a non-linear formulation for strain-rate and thermal softening sensitivity, the MJ-C model achieved a significant reduction in prediction error (often below 3% for both yield and ultimate stress) across the entire tested range of strain rates (10^{-4} s^{-1} to 10^{3} s^{-1}) and temperatures (27°C to 600°C). This makes it the most suitable model for simulating the complex behavior of body-centered tetragonal (BCT) martensitic armor steels.

2. **Validation Through Integrated Experimentation and Simulation:** The research methodology, which combined meticulous experimental testing (including high strain-rate tensile tests, high-temperature tests, Charpy V-notch impact tests, and fracture toughness testing) with rigorous finite element analysis (FEA), proved highly effective. The material parameters extracted from tensile tests were successfully validated by accurately predicting the load-displacement response in tensile simulations and the force-time-energy response

in Charpy impact simulations. This integrated approach ensures the reliability and practical applicability of the developed models.

3. **Critical Influence of Loading Conditions on Material Response:** The experimental data revealed that the mechanical behavior of RHA steel is highly sensitive to both strain rate and temperature. While the material generally exhibits positive strain-rate sensitivity, a window of negative strain-rate and temperature sensitivity was observed between 300°C and 400°C, attributed to dynamic strain aging (DSA) and microstructural changes. This complex, non-monotonic behavior underscores the necessity of using advanced, coupled constitutive models like the MJ-C model for accurate predictions.

4. **Successful Application to Ballistic and Impact Scenarios:** The validated MJ-C model, coupled with a modified Johnson-Cook failure model and a non-linear damage evolution law, was effectively applied to simulate Charpy impact tests and ballistic penetration. The Charpy V-notch impact studies revealed the role of adiabatic heating and microstructural void nucleation in enhancing ductility at high loading rates, while fractographic analyses confirmed that void size decreases but nucleation density increases with strain rate. Finite element simulations validated with experimental energy absorption data further established the superiority of the MJ-C model in reproducing dynamic fracture behavior.

   Ballistic impact investigations showed that the armour plate exhibits a ballistic limit of ~785 m/s against rigid projectiles, with failure modes strongly dependent on projectile nose shape, deformability, and plate microstructure. Blunt projectiles generated severe plugging, hemispherical projectiles produced smaller plugs, while conical projectiles promoted fragmentation and petalling. Parametric studies demonstrated that proper heat treatment and optimized microstructures significantly enhanced ballistic performance indices. The simulations also highlighted the influence of mesh sensitivity, projectile tip stiffness, and dynamic friction on penetration resistance. The simulations provided critical insights into energy absorption, failure patterns, and the influence of projectile nose shape and target microstructure. Furthermore, the study established the significant role of the dynamic fracture toughness parameter (K_{ID}) in determining ballistic performance, demonstrating that pre-existing cracks can substantially degrade an armor plate resistance to penetration. The fracture toughness–based failure model successfully captured crack-driven failure modes such as petalling, validating the importance of incorporating fracture mechanics in ballistic simulations. It was shown that pre-existing cracks and material inhomogeneities drastically reduce ballistic performance, with fracture toughness (K_{IC}) directly controlling residual velocity and energy dissipation. Plates with higher fracture toughness absorbed

more energy before failure, underscoring the need for toughness optimization in armour steels.

5. **Practical Contributions and Methodological Advancements:** Beyond the theoretical development of the MJ-C model, this work offers substantial practical value:
    - It provides a extensive and novel dataset on the high strain-rate and high-temperature properties of RHA and PHS 1500 steels.
    - It presents a cost-effective methodology for conducting intermediate to high strain-rate tensile tests using a drop-weight impact tester, validated against established systems like the Servo-Hydraulic (VHS) and Split Hopkinson Bar (SHB).
    - The findings directly inform armor design, material selection, and heat treatment optimization by clarifying the interplay between microstructure, mechanical properties, and ballistic performance.

In summary, this thesis makes a significant contribution to the field of impact and fracture mechanics of armor materials. By developing, validating, and applying an enhanced material model, it provides a robust computational framework for predicting material behavior under extreme conditions. The findings not only advance the fundamental understanding of martensitic steel performance but also offer practical tools and data for the design of more effective and reliable protective structures in defense and related high-stakes industries. Future work may focus on extending the model to capture the negative strain-rate sensitivity phenomenon and investigating even higher strain-rate regimes and multi-axial stress states.

8.2 Future Scope of Work

While this thesis has addressed critical aspects of the dynamic response of armour steels, further research opportunities remain to expand and strengthen the findings:

1. **Advanced Constitutive Modelling**
    - Extend the MJ-C model by coupling with microstructure-informed approaches (e.g., crystal plasticity, phase-field methods).
    - Employ hybrid machine learning and physics-informed neural networks to improve predictions in unexplored strain rate–temperature regimes.
2. **Ballistic Testing and Multi-Hit Conditions**
    - Conduct controlled ballistic experiments with deformable and fragment-simulating projectiles for further model validation.

- Investigate multiple-hit and oblique-impact scenarios to replicate real battlefield conditions.

3. **Fracture and Damage Evolution**
    - Implement cohesive zone models (CZM) and extended finite element methods (XFEM) for crack initiation and propagation in armour plates.
    - Explore the influence of hydrogen embrittlement, corrosion, and environmental degradation on fracture toughness under dynamic loading.
4. **Material and Microstructural Optimization**
    - Examine advanced heat treatment cycles, alloying strategies, and multiphase steels for improved ballistic resistance.
    - Investigate additive manufacturing (AM) and hybrid composite–metallic armour architectures for lightweight yet high-strength protection.
5. **High-Strain-Rate Testing Methodologies**
    - Develop facilities for ultra-high strain rate testing ($>10^4\ s^{-1}$) using laser-driven or electromagnetic impact techniques.
    - Expand intermediate strain rate test setups to shear, compression, and torsion samples for comprehensive model calibration.
6. **Coupled Multi-Physics Simulations**
    - Integrate thermo-mechanical-chemical models to capture softening, oxidation, and damage during prolonged or high-energy impacts.
    - Investigate coupled blast–impact scenarios, relevant for vehicular and naval armour.
7. **System-Level Applications**
    - Scale validated models to full-vehicle and protective system simulations to assess survivability.
    - Collaborate with defence industries to implement model-driven armour design workflows, reducing reliance on costly full-scale ballistic testing.

This combined conclusion and future scope underscores the scientific and practical significance of the research while laying out a clear roadmap for advancing the field. The thesis thus contributes not only to the fundamental understanding of armour steel behaviour but also to its engineering application in defence and safety-critical industries.